RUHR-UNIVERSITÄT BOCHUM

Pore-Scale Study of Non-Darcian Fluid Flow in Porous Media using Smoothed-Particle Hydrodynamics

Rakulan Sivanesapillai

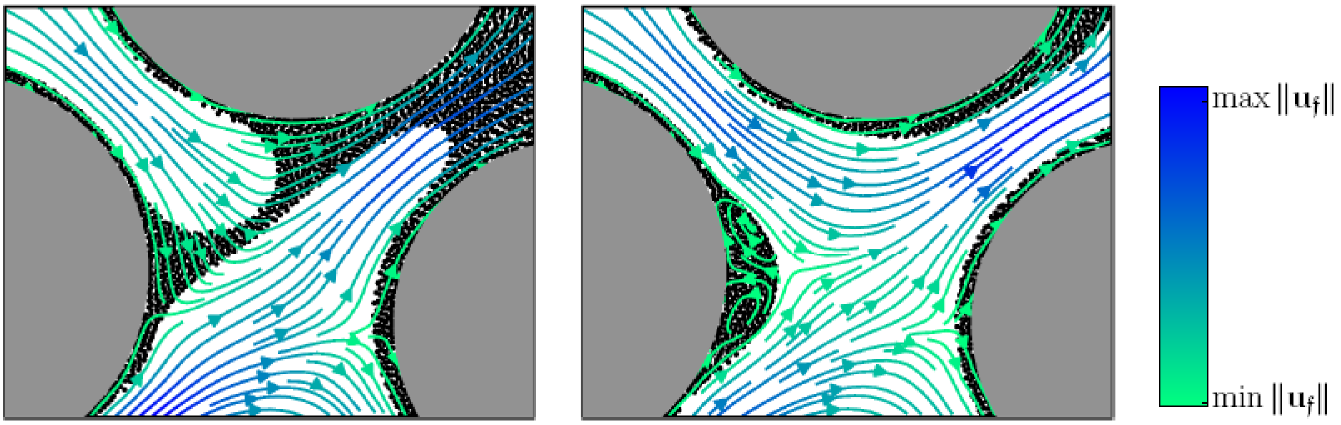

$t_0 + 0.6\,\mathrm{ms}$ $\quad$ $t_0 + 0.9\,\mathrm{ms}$

RUHR-UNIVERSITÄT BOCHUM

Pore-Scale Study of Non-Darcian Fluid Flow in Porous Media using Smoothed-Particle Hydrodynamics

Dissertation
zur
Erlangung des Grades
Doktor-Ingenieur (Dr.-Ing.)

der
Fakultät für Maschinenbau
der Ruhr-Universität Bochum

von

Rakulan Sivanesapillai

aus Herne

Bochum 2016

Einreichung der Dissertation (thesis submission): 20. April 2016
Tag der mündlichen Prüfung (thesis defense): 01. Juli 2016

Erster Referent (first referee): Prof. Dr. rer. nat. Alexander Hartmaier
Zweiter Referent (second referee): Prof. Dr.-Ing. Holger Steeb
Dritter Referent (third referee): Prof. Dr. rer. nat. Insa Neuweiler
Vorsitzender (committee chair): Prof. Dr.-Ing. Franz Peters

Abstract

We study high velocity single-phase as well as immiscible two-phase fluid flow in porous media using pore-scale resolved direct numerical simulations. The effects of inertia and capillarity generally render microscopic flow conditions non-laminar and, as a result, the effective constitutive behavior on the macroscale non-linear. High velocity and two-phase flow conditions are thus subsumed under the term non-Darcian. Despite of their practical relevance, for instance during carbon dioxide sequestration, groundwater contamination remediation or reservoir well testing, the role that microscopic heterogeneities have on the macroscopic non-Darcian behavior remains to a large extent unknown.

To this end, we use the meshfree Lagrangian Smoothed Particle Hydrodynamics (SPH) method to study these effects in numerically fully-resolved heterogeneous porous media of particulate microstructure. On the pore-scale, bulk fluid flow is governed by the incompressible Navier-Stokes equations whereas interfacial balance equations are taken into account for multiphase flow problems. While its meshfree interpolation stencils render spatial discretization of complex pore-spaces comparatively cheap, its Lagrangian nature gives rise to intrinsic stability against the apparent hyperbolicity of convective flows and the fragmentation and coalescence dynamics of interfaces during multiphase flow. We thereby argue that SPH constitutes an attractive simulation tool for the present study. In an attempt to support this statement, the presented SPH model is first subject to an extensive validation procedure.

We subsequently study the transition from low to high Reynolds number flow in porous media with particular focus on the complex array of the emerging microscopic processes. These include streamline rectification, flow tube narrowing and formation and growth of wake eddies, all of which are found sensitive to microstructure and to have decisive influence on the effective hydraulic properties of porous media.

Finally, we study the saturation-controlled displacement of a wetting pore-fluid by non-wetting fluid, i.e. primary drainage. The interplay of viscous and capillary forces is known to result in macroscopic displacement patterns as diverse as viscous fingering, capillary fingering or stable displacement. In this work, we elucidate microscopic flow patterns associated with different displacement mechanisms with particular focus on the evolution of specific interfacial areas. The formation of lubrication layers during viscous fingering on the one hand and the localization of saturation fronts during stable displacement on the other hand evidence the important role of interfacial areas.

Zusammenfassung

Die vorliegende Arbeit befasst sich mit trägheitsdominanten Einphasen- sowie Zweiphasenströmungen nicht-mischbarer Fluide in porösen Medien. Trägheits- und Kapillareffekte haben im Allgemeinen nicht-laminare Strömungsprofile auf der Mikroskala zur Folge. Die daraus folgenden effektiven makroskopischen Eigenschaften bedürfen einer nicht-linearen Konstitutivmodellierung, d.h. solche, die wir als nicht-Darcysche Modelle klassifizieren. Obgleich Prozessen dieser Art eine große praktische Bedeutung zuzusprechen ist, wie bspw. im Rahmen der CO_2-Sequestrierung oder Grundwassersanierung, bleibt der Einfluss mikroskopischer Heterogenitäten auf nicht-Darcysche Strömungsvorgänge weitestgehend unerforscht. Auf Basis der Smoothed-Particle-Hydrodynamics-Methode (SPH) werden Strömungen dieser Art in numerisch vollaufgelösten heterogenen porösen Medien simuliert. Auf der Porenskala sind die zugrunde liegenden Erhaltungsgleichungen die Navier-Stokes-Gleichungen. Darüber hinaus werden Grenzflächen-Bilanzgleichungen im Rahmen der Mehrphasenströmung berücksichtigt. Während der netzfreie Interpolationsansatz der SPH-Methode die räumliche Diskretisierung heterogener Mikrostrukturen vereinfacht, bietet der Lagrange-Lösungsansatz eine besondere Stabilität bei konvektiven Strömungen bzw. bei komplexer Grenzflächendynamik. Darin ist die Attraktivität der SPH-Methode für die vorliegende Studie begründet, die durch eine umfangreiche numerische Validierungsstudie untermauert wird. Es wird der Übergang von laminaren zu trägheitsdominierten Strömungen in porösen Medien studiert. Dies geschieht mit besonderem Augenmerk auf mikroskopische Prozesse, wie bspw. die Ausrichtung der Stromlinien und die Entstehung stationärer Wirbel. Einerseits erweisen sich diese Prozesse als stark mikrostrukurabhängig, andererseits sind sie von entscheidender Bedeutung für das effektive hydraulische Materialverhalten. Anschließend wird die ratenkontrollierte Verdrängung einer benetzenden Porenflüssigkeit durch eine nicht-benetzende Flüssigkeit, d.h. primäre Entwässerungsprozesse, studiert. Durch das Zusammenspiel von Kapillarität und Viskosität können verschiedenste makroskopische Sättigungsmuster entstehen, wie bspw. das viskose Ausfingern, das kapillare Ausfingern oder die sog. stabile Verdrängung. Die vorliegende Arbeit thematisiert die mikroskopischen Strömungsprofile und die Evolution fluider Grenzflächen, die mit eben jenen makroskopischen Sättigungsmustern einhergehen. Während im Rahmen des viskosen Ausfingerns benetzende Schmierungsfilme entstehen, lokalisieren sich fluide Grenzflächen bei stabiler Verdrängung. Auf Basis dieser Beobachtungen wird die besondere Rolle, die spezifischen Grenzflächen im Rahmen der Zweiphasenströmung in porösen Medien zukommt, diskutiert.

Contents

Notation V

1 Introduction 1

1.1 Motivation 1

1.2 Scope 3

1.3 Outline 5

2 Continuum fluid mechanics 7

2.1 Fundamentals of single-phase flow 7

2.1.1 Kinematics 8

2.1.2 Transport theorem 10

2.1.3 General balance equations 11

2.1.4 Constitutive equations 12

2.1.5 Initial boundary value problems 15

2.2 Fundamentals of two-phase flow 17

2.2.1 Geometry and kinematics 18

2.2.2 Transport theorem 22

2.2.3 General balance equations 26

2.2.4 Constitutive equations 30

2.3 Immersed boundary formulation 32

2.3.1 Whole-domain balance of mass 33

2.3.2 Whole-domain balance of linear momentum 33

2.3.3 Whole-domain balance of moment of momentum 35

2.3.4 Governing dimensionless numbers . . . 35
2.3.5 Continuum surface force method . . . 36
2.4 Fundamentals of two-phase flow in porous media . . . 38
2.4.1 Introduction . . . 38
2.4.2 Overview of governing balance equations . . . 39
2.4.3 Initial and boundary conditions . . . 41
2.4.4 Unconstrained contact lines . . . 42
2.4.5 Constrained contact lines . . . 43
2.4.6 Whole-domain formulation . . . 45

3 Smoothed particle hydrodynamics 49
3.1 Numerical principles . . . 49
3.2 Nodal integration . . . 55
3.3 Kernel functions . . . 57
3.4 Numerical errors . . . 61
3.4.1 Discretization errors . . . 61
3.4.2 Boundary inconsistency . . . 67
3.4.3 Corrective approaches . . . 70
3.5 Discrete nodal motion equations . . . 74
3.5.1 Boundary conditions . . . 75
3.5.2 Interparticle pressure forces . . . 82
3.5.3 Interparticle viscous forces . . . 83
3.5.4 Immersed interfacial particle forces . . . 84
3.6 Simulation parameterization . . . 86

4 Model validation 91
4.1 Poiseuille flow between parallel plates . . . 91
4.2 Lid-driven square cavity flow . . . 94
4.3 Permeability of sphere packings . . . 97
4.4 Fully immersed liquid droplet . . . 102
4.5 Layered co-current flow between parallel plates . . . 107
4.6 Capillary rise between parallel plates . . . 111
4.7 Oscillating fluid droplet . . . 117

5 From low to high Reynolds number flow in porous media 121
5.1 Motivation . . . 121
5.2 Methods . . . 123
5.3 Results . . . 125
5.4 Discussion . . . 130
5.5 Summary . . . 135

6 Wetting phase entrapment during primary drainage 137
6.1 Introduction . . . 138
6.2 Methods . . . 140
6.2.1 Methodological benefits and limitations . . . 140
6.2.2 Simulation Setup . . . 143
6.2.3 Macroscopic Quantities . . . 148
6.3 Results . . . 150
6.3.1 Capillary Fingering Regime . . . 150
6.3.2 Viscous Fingering Regime . . . 156
6.3.3 Stable Displacement Regime . . . 162
6.4 Discussion . . . 166
6.5 Summary and Conclusions . . . 171

7 Summary and Outlook 175

List of Figures 179

List of Tables 181

List of Algorithms 181

Bibliography 183

Notation

Symbols and abbreviations that are repetitively used throughout this thesis are listed below. We make use of the convention that second or higher-order tensors, and only those, are denoted by bold characters. The subscripts $(\cdot)_i$ and $(\cdot)_j$ are exclusively used to denote discrete values at numerical collocation points $\mathbf{x}_i$ and $\mathbf{x}_j$, respectively, and not to be confused with Einstein's summation convention. Throughout this text, the term macroscopic is associated with the length scale where coarse-grained models such as Darcy's law are deemed applicable whereas the term microscopic is associated with the characteristic length scale of pores where direct numerical simulations methods are applied herein.

Abbreviations

(I)BVP	(Initial) boundary value problem
BCC	Body-centered cubic
CSF	Continuum surface force method
CSS	Continuum surface stress method
CUC	Computational unit cell
DLA	Diffusion-limited aggregation
EOS	Enhanced oil recovery
FCC	Face-centered cubic
FEM	Finite element method
LB	Lattice Boltzmann method
LHS	Left-hand side
RHS	Right-hand side
RVE	Representative volume element
SC	Simple cubic
SPH	Smoothed Particle Hydrodynamics

Domains, boundaries and surfaces

Γ	Boundary of computation domain Ω
Γ^D	Dirichlet boundary
Γ^P	Periodic boundary
$\Gamma^{\alpha\beta}$	Interface that separates bulk phase domains Ω_α and Ω_β
$\Gamma_\mathfrak{s}, \Gamma_\mathfrak{f}$	Outer boundaries to solid and fluid phase domains
$\Gamma_{\mathfrak{f}\mathfrak{s}}$	Solid surface or solid-fluid interface
Ω	Current configuration of a material body in $\mathbb{R}^3$ (Computation domain)
Ω_0	Reference configuration of a material body in $\mathbb{R}^3$
$\Omega_\mathfrak{s}, \Omega_\mathfrak{f}$	Solid and fluid phase domains
Ω_G	Total ghost domain formed by union $\Omega_{Go} \cup \Omega_{Gi}$
Ω_i	Compact support domain of kernel centered at particle position $\mathbf{x}_i$
$\Omega_\mathbf{x}$	Compact support domain of kernel centered at $\mathbf{x}$
Ω_{Gi}	Inner ghost domain adjacent to solid surface $\Gamma_{\mathfrak{f}\mathfrak{s}}$
Ω_{Go}	Outer ghost domain adjacent to computation domain boundary Γ
Ω_G^D	Ghost domain adjacent to a Dirichlet boundary
Σ	Current configuration of surface embedded in $\mathbb{R}^3$
Σ_0	Reference configuration of surface embedded in $\mathbb{R}^3$
Υ	Contact line domain in current configuration
U	Current configuration of a surface in $\mathbb{R}^2$
U_0	Reference configuration of a surface in $\mathbb{R}^2$

Sub- and superscripts

$(\cdot)^\mathfrak{f}, (\cdot)_\mathfrak{f}$	Bulk fluid phase property
$(\cdot)^\mathfrak{n}, (\cdot)_\mathfrak{n}$	Bulk non-wetting fluid phase property
$(\cdot)^\mathfrak{s}, (\cdot)_\mathfrak{s}$	Bulk solid phase property
$(\cdot)^\mathfrak{w}, (\cdot)_\mathfrak{w}$	Bulk wetting fluid phase property
$(\cdot)^{\mathrm{ASn}}$	Number density weighted antisymmetric reproducing approximation
$(\cdot)^{\mathrm{AS}}$	Antisymmetric discrete reproducing approximation
$(\cdot)^{\mathrm{Cm}}$	m-th order complete discrete reproducing approximation
$(\cdot)^T$	Transpose
$(\cdot)^{-1}$	Inverse
$(\cdot)^{\alpha\beta}$	Interface-excess quantity or surface-bound operator of interface $\Gamma^{\alpha\beta}$
$(\cdot)^*$	Prescribed property of a boundary ghost particle
$(\cdot)_0$	Reference value or initial condition

$(\cdot)_\Gamma$	Prescribed value on Dirichlet boundary Γ^D
$(\cdot)_{\mathrm{eq}}$	Equilibrium part
$(\cdot)_{\mathrm{neq}}$	Non-equilibrium part
$(\cdot)_{\mathrm{ref}}$	Characteristic value
$(\cdot)_g$	Property of Gaussian kernel function
$(\cdot)_h$	Reproducing kernel approximation
$(\cdot)_i$	Property of focal particle i at position $\mathbf{x}_i$
$(\cdot)_j$	Property of neighboring particle j at position $\mathbf{x}_j$
$(\cdot)_q$	Property of fifth-order quintic B-spline function
$(\cdot)_S$	General interface-excess quantity or surface-bound operator
$(\cdot)_w$	Property of Wendland kernel
$(\cdot)_{h,dx}$	Discrete reproducing kernel approximation

Miscellaneous

$[[\cdot]]$	Interfacial jump or Hadamard operator
α_n	Kernel normalization constant in n-dimensional space
$\|\cdot\|$	Euclidean norm
$(\bar{\cdot})$	Non-dimensional variable
$\cdot$	Scalar (Inner) product
χ	Motion function
δ	Dirac delta distribution
$\delta_S, (\delta^{\alpha\beta})$	Interface Dirac delta distribution (of interface $\Gamma^{\alpha\beta}$)
$\mathrm{dev}(\cdot)$	Deviatoric part
$\mathrm{div}_S, (\mathrm{div}^{\alpha\beta})$	Surface divergence (of interface $\Gamma^{\alpha\beta}$)
ϵ_D	Discretization error
ϵ_I	Interpolation error
$\epsilon_{D,I}$	Combined discretization and interpolation error
$\mathfrak{M}$	Total mass of a material body
$\mathrm{grad}_S, (\mathrm{grad}^{\alpha\beta})$	Surface gradient (of interface $\Gamma^{\alpha\beta}$)
$\kappa, (\kappa^{\alpha\beta})$	Twice the mean curvature (of interface $\Gamma^{\alpha\beta}$)
λ	Dilatational viscosity
$\langle\cdot\rangle, (\langle\cdot\rangle^\alpha)$	Total (phase-specific) volumetric averaging operator
$\mathcal{F}\left[\cdot\right](s)$	Fourier transform
Ca	Capillary number
$\mathrm{d}/\mathrm{d}t(\cdot), (\dot{\cdot})$	Material time derivative for fixed material point $\mathbf{X}$

$\mathrm{d}_S/\mathrm{d}t(\cdot)$	Material surface time derivative for surface-fixed material point $\mathbf{X}_S$
M	Viscosity ratio
Re	Reynolds number
μ	Dynamic viscosity
$\otimes$	Dyadic (Outer) product
$\partial/\partial t(\cdot)$	Partial time derivative
$\sigma, (\sigma^{\alpha\beta})$	Interfacial tension (of interface $\Gamma^{\alpha\beta}$)
$\boldsymbol{\mathfrak{F}}$	Supply of linear momentum to a material body
$\boldsymbol{\mathfrak{I}}$	Total linear momentum of a material body
Θ	Contact angle
$\tilde{(\cdot)}$	Diffuse-interface approximation of a field
$\tilde{W}$	Non-dimensional smoothing kernel function
$\times$	Cross (Vector) product
ϱ	Mass density
$\mathrm{vol}(\cdot)$	Volumetric part
$A_{\alpha\beta}$	Total interfacial area of interface $\Gamma^{\alpha\beta}$
c	Speed of sound
$C, (C^{\alpha\beta})$	Phase indicator field (of phase domains Ω^α and Ω^β)
d	Number of spatial dimensions
F	Helmholtz free energy
h	Smoothing length
J	Jacobian
K	Bulk modulus
k	Kernel compactness factor
N	Total number of SPH particles
N_α	Total number of particles of phase α
N_n	Number of nearest neighbors
p	Local pressure
$p_C, (P_C)$	Microscopic (Coarse-grained macroscopic) capillary pressure
q	Non-dimensional radius
S^1, S^2	Curvilinear surface coordinates that parameterize U_0
s^1, s^2	Curvilinear surface coordinates that parameterize U
t	Time
$V, (V_\alpha)$	Total volume (of phase α)
W	Smoothing kernel function
$\boldsymbol{\Pi}$	Interfacial Cauchy stress tensor

$\mathbf{a}$	Acceleration
$\mathbf{b}$	Volumetric force density
$\mathbf{b}_S, (\mathbf{b}^{\alpha\beta})$	Unit vector tangent to boundary curve $\partial\Sigma$ (or $\partial\Gamma^{\alpha\beta}$)
$\mathbf{D}$	Strain-rate tensor, Symmetric part of spatial velocity gradient
$\mathbf{e}_a$	Standard basis vectors
$\mathbf{F}$	Deformation gradient
$\mathbf{F}_i^G$	Volumetric force acting on lumped mass of particle i
$\mathbf{F}_{ij}^P$	Pressure interaction forces acting between particles i and j
$\mathbf{F}_i^S$	Immersed interfacial force acting of particle i
$\mathbf{F}_{ij}^V$	Viscous interaction forces acting between particles i and j
$\mathbf{G}_1, \mathbf{G}_1$	Covariant basis vectors tangent to Σ_0
$\mathbf{g}_1, \mathbf{g}_1$	Covariant basis vectors tangent to Σ
$\mathbf{I}$	Identity tensor
$\mathbf{I}_S$	Surface identity tensor
$\mathbf{L}$	Spatial velocity gradient
$\mathbf{n}$	Unit outward normal to a boundary
$\mathbf{O}$	Point of origin
$\mathbf{T}, (\mathbf{T}_E)$	Cauchy (extra) stress tensor
$\mathbf{t}_b$	Boundary curve traction
$\mathbf{t}_s$	Surface traction vector
$\mathbf{u}$	Velocity
$\mathbf{W}$	Spin tensor, Skew-symmetric part of spatial velocity gradient
$\mathbf{X}, X_a$	Position vector and material coordinates in reference configuration
$\mathbf{x}, x_a$	Position vector and spatial coordinates in current configuration

Notation specific to coarse-grained models of porous flow

γ	Blending coefficient in Churchill-Usagi asymptotic correlation [45]
$\hat{\mathbf{p}}^{\mathfrak{f}}$	Momentum interaction between pore-fluid and solid skeleton
ϕ	Porosity
ζ	Coefficient to cubic term in cubic filtration model
$a_{\alpha\beta}$	Specific interfacial area of $\Gamma^{\alpha\beta}$ (normalized by total volume V)
c_F	Forchheimer coefficient
$k_I, (k_A)$	Intrinsic (Apparent) permeability
L_C	Width of capillary dispersion zone
m_F	Average grain-size diameter

m_N	Mean pore-throat size
S_α	Pore-space saturation by phase α
$T, (T_M)$	Hydraulic tortuosity (estimate based on Duda et al. [60])
v_F	Standard deviation of grain-size diameter distribution
v_N	Standard deviation of pore-throat size distribution
$\mathbf{F}^D$	Total drag force
$\mathbf{F}^D_P$	Total form drag
$\mathbf{F}^D_V$	Total viscous skin friction
$\mathbf{J}$	Driving force due to pressure head and volumetric acceleration
$\mathbf{q}$	Darcy or filter velocity
$\mathbf{v}_\mathfrak{f}$	Macroscopic fluid velocity, i.e. volume-average fluid velocity in Ω_{RVE}
$\mathbf{v}_\mathfrak{s}$	Macroscopic solid velocity, i.e. volume-average solid velocity in Ω_{RVE}
$\mathbf{w}_\mathfrak{f}$	Relative or seepage velocity

CHAPTER 1

Introduction

1.1 Motivation

Transport processes in porous media and, in particular, fluid flow in porous media are ubiquitous in many fields of engineering, biomechanics and subsurface sciences. Examples of ongoing relevance include flow in porous catalysts, blood flow through a network of capillaries, groundwater flow or enhanced oil recovery. Effective hydraulic properties of porous materials as defined on the length and time scale of a macroscopic observer are decisively influenced by microscopic heterogeneities that appear on the characteristic length scale of the pore space, e.g. the average pore diameter. Despite of the apparent multiphase and multiscale nature of fluid flow in porous media, numerical modeling of these processes by means of resolving the microstructure, generally comprised of a complex distribution of bulk phases and interfaces, is computationally restricted to the length scale of several pores only. It is for that reason effective transport models, the continuum Mixture Theory and the Theory of Porous Media (see [28, 29, 64, 84–86] and references therein) remain subjects of ongoing research.

A concept that is fundamental to the formulation of macroscopic continuum balance equations is that of the Representative Volume Element (RVE). The RVE serves as averaging volume to bridge the gap between the microscopic and macroscopic scale. The microscopically discontinuous distribution of phases is averaged over the volume of the RVE to form a coarse-grained macroscopic space in which constituent phases form superimposed continua. Microscopic physical processes that give rise to mass, momentum or energy exchange between the various discontinuous phases are subsequently taken into account using constitutive models for the interaction of macroscopically superimposed continua. The most anticipated constitutive model for fluid flow in porous media is Darcy's law which was proposed in 1856 by Henry Darcy. For incompressible phases, Darcy's law postulates that the relative velocity between pore-fluid and solid skeleton as averaged over the volume of an RVE, i.e. the so-called seepage velocity, is proportional to the driving hydraulic gradient. The coefficient of proportionality, which is a second-order tensor for anisotropic porous media, is referred to as permeability tensor and represents an effective material parameter. In continuum Mixture Theory, Darcy's law can be shown equivalent to the assumption that the non-equilibrium momentum exchange between coarse-grained fluid phase and solid skeleton is proportional to seepage velocity. The linearity as postulated by Darcy, however, has been semi-empirically found to only hold provided that the microscopic flow field is reminiscent of laminar flow through undeformable conduits, i.e. the creeping flow of a viscous fluid with parabolic flow profiles in the absence of inertia. On the contrary, appropriate modifications to the constitutive models that represent the interaction of constituent phases are necessary to account for non-Darcian flow.

In this thesis, we study two situations of practical relevance where the condition of laminar flow on the microscale is generally not met: high-velocity single-phase and two-phase immiscible flow in porous media. During high-velocity flow, non-Darcian effects occur due to the dominant role of inertia that cause the microscopic flow fields to deviate from parabolic flow profiles. The transition from low to high velocity flow is accommodated by the gradual microscopic processes of streamline rectification, flow tube narrowing, formation and growth of wake eddies and the increasing relevance of secondary flow [4, 40, 71, 133, 147, 175, 186, 189]. Such effects have been reported relevant for inertial flow in narrow fractures, e.g. during well-testing of hydrocarbon reservoirs when production rates are high or if flow path obstacles in narrow conduits exert a considerable amount of form drag on the pore-fluid [41, 109, 172, 182]. For two-phase immiscible flow, on the other hand, microscopic effects at interfaces that separate bulk phases, in particular capillary and wettability effects, constitute the main reasons causing the effective behavior to deviate from the classical Darcian solutions. When, for instance, a non-wetting fluid displaces a wetting fluid that initially saturates the entire void-space of a porous medium, i.e. primary drainage as observed during sequestration of carbon dioxide in sedimentary formations [150], relative dominance of capillary forces over viscous forces implies a microscopic mean curvature flow. The characteristic feature of mean curvature flows is that microscopic fluid-fluid interfaces are of constant mean curvature and fluid percolation only occurs through preferential flow paths that exhibit the lowest interfacial energy barriers [3, 68, 69, 122, 154, 160, 161, 165, 210, 214]. Preferential flow of the non-wetting fluid ultimately implies hydraulic isolation of wetting phase clusters that remain trapped in inaccessible void-space [49, 112, 165, 214]. These effects strongly affect sweeping efficiency reduction during hydrocarbon production or groundwater contamination by non-aqueous phase liquids.

Despite of the fact that microscopic flow patterns that emerge during high velocity and two-phase immiscible flow considerably deviate from laminar flow conditions, phenomenological, heuristic or semi-empirical extensions of Darcy's law remain the tools engineers rely on to model such processes. The most prominent model to account for the effects of inertia during high velocity flow in porous media is a quadratic extension of Darcy's law due to Forchheimer [72]. While volumetric homogenization and dimensional analysis support that the upper limit to the non-equilibrium momentum interaction between coarse-grained pore-fluid and solid skeleton is quadratic in seepage velocity [164, 188], the transition from linear to quadratic flow remains unknown. Indeed, the hydraulic gradient has been observed to vary with the cube of the flow rate when inertia forces are weak [4, 44, 71, 116, 130, 133, 147, 175, 188]. Such inconsistencies occur since inertial transition is decisively influenced by the morphology of flow conduits, e.g. the laminar to turbulent transition is known rather discrete in straight conduits while more gradual in tortuous flow paths. For two-phase immiscible flow, on the other hand, Darcy's law is assumed applicable to each constituent phase separately. Apart from the implicit assumption of microscopically laminar flow, constituent pore-fluids are thereby thought to occupy and flow through distinct conduits and their microscopic distribution is assumed continuous, i.e. path-connected, throughout the entire pore-space at all times. In an attempt to account for varying saturation states and fluid immiscibility, the permeability tensors and the pore-fluid pressure difference, i.e. macroscopic capillary pressure, are considered functions of constituent saturations [14]. Non-Darcian effects related, for instance, to hydraulic isolation of wetting fluid, formation of lubrication layers on solid surfaces or interfacial energy driven spontaneous events (Haines jumps [6, 54, 81, 135], Melrose events [97, 142]), are thus lumped into permeability and capillary pressure functions. As a result, these constitutive functions are typically rendered non-linear, hysteretic and sensitive to boundary conditions [75, 80, 103, 144]. While contemporary macroscopic models for two-phase flow explicitly acknowledge the role of interfacial areas [78, 87–89] or take into account path-disconnection due to trapping [91, 93], the lack of constitutive calibration of these models hampers their use in practice.

1.2 Scope

In an attempt to further elucidate the underlying pore-scale mechanisms during high-velocity and two-phase flow, to assess effective hydraulic properties of porous materials and to calibrate constitutive models for flow processes beyond the limits of Darcy's law, this work promotes the use of pore-scale resolved simulations as a numerical tool complementary to physical experiments. In particular, we perform pore-scale resolved numerical simulations using direct numerical methods, i.e. solving the Navier-Stokes equations for bulk pore-fluid phases and interfacial balance equations on interfaces between immiscible bulk phases. Use of direct numerical simulations (DNS) implies that the resulting nodal equations represent a discretization of the governing microscopic conservation equations and thus inherit a reduced set of modeling assumptions. This is in contrast to traditional pore-scale simulation approaches, such as percolation theory [18] or pore-network models [20, 105, 171], that require a larger set of modeling assumptions since the pore space is represented by an idealized network of pore-bodies and pore-throats. DNS methods, however, imply increased computational costs which restricts numerical analysis to length scales considerably smaller than the macroscale. Despite of the latter, access to the pore-scale hydrodynamics enables the identification of microscopic processes that affect the effective macroscopic behavior.

Our approach to pore-scale resolved simulations of non-Darcian flow is a weakly-compressible Smoothed Particle Hydrodynamics (SPH) method. Following its first use to simulate astrophysical fluid dynamics [77, 128], SPH is attracting an ever increasing interest as a simulation tool in engineering and applied sciences (see reviews [126, 136, 204] and textbook [203]). This is largely due to the fact that SPH constitutes a mesh-free Lagrangian particle method. Using SPH, discretization of the governing partial differential equations (PDE) gives rise to a set of interacting collocation points (particles) with lumped masses that are advected in space according to the local advection velocity (updated-Lagrangian method). Upon discretization, internal forces and fluxes take the form of particles that exchange mass, momentum or energy with neighboring particles. Nodal motion equations are thus formally reminiscent of a system of colloidal particles interacting with each other. Due to its Lagrangian nature, problems that involve large deformations, contact discontinuities, free surfaces or a pronounced hyperbolic character of the governing PDEs can be approached without the need of stability treatments, such as the upwind scheme, or adaptivity, e.g. mesh refinement in Finite Element methods (FEM). Nonetheless, the freedom of SPH regarding spatial discretization has its disadvantages. First and foremost, SPH methods generally lack a consistent way to account for Dirichlet and Neumann boundary conditions. This is due to the fact that the reproducing kernel approximation of SPH naturally regularizes nodal constraints and boundary conditions. Moreover, nodal integration in SPH implies that field variables and their spatial derivatives are evaluated on the same set of collocation points which, in particular situations, gives rise to spurious zero energy modes. Moreover, only rarely does the use of time-implicit methods constitute a feasible approach on an unstructured set of collocation points. Due to explicit time integration, rather restrictive stability constraints with respect to time-stepping have to be taken into account.

It is for that reason, numerical validation and the assessment of SPH regarding pore-scale simulations is considered an additional scope of this thesis.

Having the advantages and limitations of SPH methods in mind, we consider pore-scale resolved simulation of non-Darcian flow a problem where we can exploit both, the mesh-free and the Lagrangian nature of SPH. Due to its mesh-free nature, spatial discretization of complex pore spaces is less computationally expensive as compared to traditional grid or mesh-based methods. Furthermore, its Lagrangian nature, due to which non-linear convective terms are not required to be modeled, enhances stability for locally large Reynolds numbers. The Lagrangian nature of SPH reveals to be particularly useful for two-phase flow simulations since the phase indicator field - a binary field that indicates the phase membership of a particle - is intrinsically advected through particle motion. Hence, no additional advection equation for the phase indicator field that is potentially prone to numerical diffusion, as used in the Eulerian Volume-of-Fluid (VOF) method [68, 69, 178, 201], is required. It is moreover possible to derive SPH equations that are compliant to Galilean invariance and conserve total mass and linear momentum.

1.3 Outline

The present thesis is organized as follows.

In **Chapter 2** we first concisely introduce the relevant kinematics and balance equations for bulk volumes with and without internal discontinuities, i.e. interfaces. In formulating interfacial balance equations, we make use of the well-known Gibbs convention by which interfaces are regarded as singular diving surfaces. In this context, constitutive equations are introduced for quasi-incompressible, non-polar Newtonian fluids as well as for interfaces with negligible interfacial excess mass-density. We further discuss the immersed boundary method by means of which interfacial balance equations are reformulated into singular sources for mass and momentum density of adjacent bulk phases. Subsequently, we formulate the initial boundary value problems (IBVP) that govern the analyzed pore-scale fluid flow problems.

Chapter 3 constitutes a general introduction to the SPH method. Special attention is paid to the discussion of interpolation and discretization errors as well as basic corrective approaches that recover a certain order of completeness of the discrete interpolation stencils in spite of boundary truncation or irregular particle distributions. We complete this chapter by presenting the discrete particle motion equations and a schematic discussion of simulation algorithms.

In **Chapter 4**, the numerical model is subject to an extensive validation study. Not only do we discuss suitable numerical parameterizations, but also the predictive capability of SPH regarding the particular flow problems that are of interest in this work. Numerical computations are benchmarked against reference data or closed form solutions for creeping flow, inertial flow and capillary flow problems.

Chapter 5 and 6 constitute self-contained parts discussing high velocity and two-phase flow in porous media, respectively. In particular, we study the apparent non-linearity between macroscopic hydraulic gradient and seepage velocity in **chapter 5**. The critical question of interest in this chapter is: How does the micro-morphology of the porous medium influence the laminar-turbulent inertial transition on the effective scale ? Based on our numerical results, we are able to correlate the effective macroscopic non-linearity to the microscopic causes in terms of eddy-formation, streamline rectification and microscopic dragforces. Closing this chapter, we present a phenomenological estimate of the Forchheimer coefficient based on the morphological properties porosity and tortuosity.

In **Chapter 6**, we present pore-scale resolved DNS of primary drainage in porous media of particulate microstructure for various capillary numbers and viscosity ratios. The capillary number describes the relative dominance of capillary forces over viscous forces and macroscopic displacement patterns are known sensitive to these non-dimensional numbers. In an attempt to meet the question, whether or not pore-scale flow topologies associated with different displacement patterns are equivalent, we characterize the entrapment of wetting phase. We report pronounced differences in pore-scale flow patterns and wetting phase trapping mechanisms that are shown to affect the effective macroscopic behavior significantly.

It is noted that parts of this thesis have been published or submitted for publication in scientific peer-reviewed journals. The results of chapter 5 have been published in *Geophysical Research Letters* by Sivanesapillai et al. [186]. The content of section 3.5 and chapter 4 has been accepted for publication in *Advances in Water Resources* and available online in Sivanesapillai et al. [187]. Chapter 6 has been submitted for publication in *Water Resources Research.* Pre-release of the above publications was approved in accordance with §7(1) of the “Promotionsordnung der Fakultät für Maschinenbau der Ruhr-Universität Bochum” as of 6 December 2002.

CHAPTER 2

Continuum fluid mechanics

The following chapter constitutes a concise introduction to the classical continuum description of fluid transport. In addition to the model equations that govern the flow of Newtonian fluids (section 2.1), this chapter covers the introduction to interfacial balance equations that are required in the presence of multiple fluid phases (section 2.2). The employed computational approach to simulate interfacial fluid dynamics is the immersed boundary method (section 2.3). All of the above furthermore serve as input to model two-phase flow in porous media (section 2.4). The chapter title "continuum fluid mechanics" shall imply that we restrict ourselves to formulations where the primary variable in the governing momentum balance equation is velocity, rather than displacement, and the local stress state is considered to exclusively depend on the kinematics of the fluid in its current configuration.

2.1 Fundamentals of single-phase flow

In the following section, we introduce the kinematic, balance and constitutive equations that govern isothermal, single-phase fluid flow through a porous medium comprised of a rigid solid phase and a fluid-saturated pore-space. Throughout the text, we restrict ourselves to the well-established group of non-polar, quasi-incompressible Newtonian fluids. The textbooks Batchelor [13] and Aris [5] have served as valuable references.

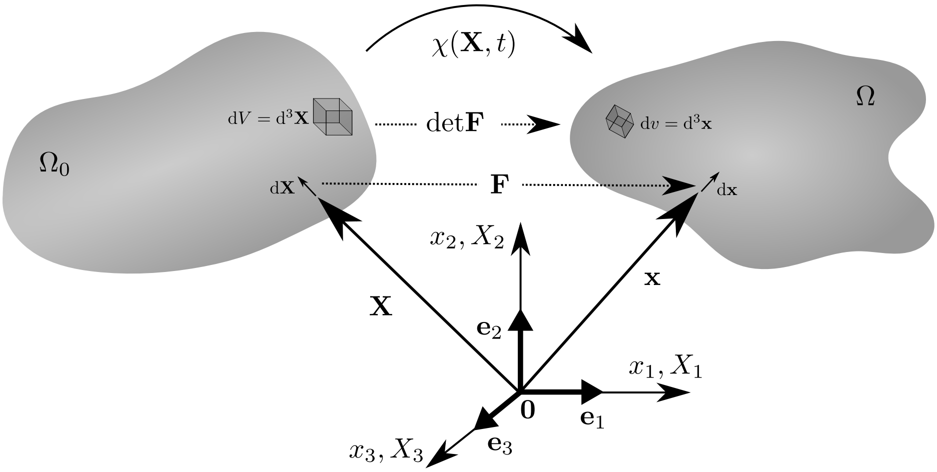
$\chi(\mathbf{X},t)$
Ω_0
$\mathrm{d}V = \mathrm{d}^3\mathbf{X}$
det**F**
$\mathrm{d}v = \mathrm{d}^3\mathbf{x}$
Ω
$\mathrm{d}\mathbf{X}$
F
$\mathrm{d}\mathbf{x}$
x_2, X_2
X
x
$\mathbf{e}_2$
x_1, X_1
0
$\mathbf{e}_1$
$\mathbf{e}_3$
x_3, X_3

Figure 2.1: Schematic representation of motion of a material body, its reference and current configurations as well as the concept of mapping.

2.1.1 Kinematics

The material body is a compact set of material points and its reference configuration Ω_0 at time $t = 0$ in a 3-dimensional Cartesian coordinate system with unit vectors $\mathbf{e}_a$ and time-invariant origin **O** is parametrized by the position vector **X**. We write $\mathbf{X} = \sum_{a=1}^{3} X_a \mathbf{e}_a$ using the material coordinates X_a. We follow the motion of a material point in terms of the continuous mapping $\chi : \Omega_0 \subset \mathbb{R}^3 \to \Omega \subset \mathbb{R}^3$ which maps points **X** of the reference configuration onto points $\mathbf{x} = \sum_{a=1}^{3} x_a \mathbf{e}_a$ of the current configuration Ω (Fig. 2.1), such that

$$\mathbf{x} = \chi\left(\mathbf{X}, t\right), \qquad \mathbf{X} \in \Omega_0 \subset \mathbb{R}^3 \quad \text{and} \quad \mathbf{x} \in \Omega \subset \mathbb{R}^3.$$

We refer to x_a as spatial coordinates. The mapping χ is assumed continuous, differentiable and invertible such that its inverse χ^{-1} exists. The referential position may hence be written $\mathbf{X} = \chi^{-1}\left(\mathbf{x}, t\right)$. The latter implies that the Jacobian

$$J = \det \frac{\partial \mathbf{x}}{\partial \mathbf{X}}$$

is non-zero. The square Jacobian matrix

$$\mathbf{F} = \frac{\partial \mathbf{x}}{\partial \mathbf{X}}$$

is referred to as deformation gradient and is observed to map an infinitesimal line element $\mathrm{d}\mathbf{X}$ of the referential configuration to an infinitesimal line element $\mathrm{d}\mathbf{x}$ of the current configuration, since

$$\mathrm{d}\mathbf{x} = \frac{\partial \mathbf{x}}{\partial \mathbf{X}} \cdot \mathrm{d}\mathbf{X} = \mathbf{F} \cdot \mathrm{d}\mathbf{X}. \tag{2.1}$$

The volume element $\mathrm{d}V$ of the referential configuration in $\mathbb{R}^3$ is given as the volume of the parallelepiped $\mathrm{d}V = \mathrm{d}\mathbf{X}_1 \cdot \mathrm{d}\mathbf{X}_2 \times \mathrm{d}\mathbf{X}_3$, where the three line elements $\mathrm{d}\mathbf{X}_1$, $\mathrm{d}\mathbf{X}_2$ and $\mathrm{d}\mathbf{X}_3$ form a right-handed system in the reference configuration. Using Eq. (2.1) we find

$$\mathrm{d}v = \mathbf{F} \cdot \mathrm{d}\mathbf{X}_1 \cdot (\mathbf{F} \cdot \mathrm{d}\mathbf{X}_2 \times \mathbf{F} \cdot \mathrm{d}\mathbf{X}_3) = \det \mathbf{F} \mathrm{d}V = J \mathrm{d}V, \tag{2.2}$$

which implies that the Jacobian J maps volume elements from reference to current configurations and thus subject to the physical constraint $J > 0$.

Partial derivatives with respect to time for fixed material coordinates $\mathbf{X}$, or, also referred to as material time derivatives, are denoted $\mathrm{d}/\mathrm{d}t := (\partial/\partial t)_{\mathbf{X}}$. Velocity and acceleration at time t for a fixed material point that is initially located at $\mathbf{X}$ are thus defined

$$\mathbf{u} := \frac{\mathrm{d}}{\mathrm{d}t}\mathbf{x} = \frac{\mathrm{d}}{\mathrm{d}t}\chi\left(\mathbf{X}, t\right), \quad \text{and} \quad \mathbf{a} := \frac{\mathrm{d}^2}{\mathrm{d}t^2}\mathbf{x} = \frac{\mathrm{d}^2}{\mathrm{d}t^2}\chi\left(\mathbf{X}, t\right),$$

respectively. Using the short-hand notation $\dot{(\bullet)} := \mathrm{d}/\mathrm{d}t(\bullet)$, we equivalently write $\mathbf{u} = \dot{\mathbf{x}}$ and $\mathbf{a} = \dot{\mathbf{u}}$.

Introducing a generic field $\mathbf{\Phi}$ of arbitrary rank, the expression $\mathbf{\Phi} = \mathbf{\Phi}\left(\mathbf{x}, t\right)$ is referred to as spatial description or Eulerian description, whereas the expression $\mathbf{\Phi} = \hat{\mathbf{\Phi}}\left(\mathbf{X}, t\right)$ is denoted material description or Lagrangian description. Applying the chain rule, the material time derivative of $\mathbf{\Phi}\left(\mathbf{x}, t\right)$ for a fixed parameter $\mathbf{X}$ reads

$$\frac{\mathrm{d}}{\mathrm{d}t}\mathbf{\Phi}\left(\mathbf{x}, t\right) = \dot{\mathbf{\Phi}} = \frac{\partial}{\partial t}\mathbf{\Phi}\left(\mathbf{x}, t\right) + \operatorname{grad} \mathbf{\Phi}\left(\mathbf{x}, t\right) \cdot \mathbf{u}, \tag{2.3}$$

where the gradient of a vector is given as $\operatorname{grad} \mathbf{\Phi} := \sum_{a=1}^{3} \mathbf{e}_a (\partial/\partial x_a) \otimes \mathbf{\Phi}$ in Cartesian coordinates. The first term on the RHS of Eq. (2.3) is referred to as local time derivative whereas the second term accounts for material point advection and referred to as convective term.

The spatial velocity gradient

$$\mathbf{L} := \operatorname{grad} \mathbf{u}$$

can be additively split into the symmetric and skew-symmetric parts

$$\mathbf{D} \coloneqq \frac{1}{2}\left(\mathbf{L} + \mathbf{L}^T\right), \quad \text{and} \quad \mathbf{W} \coloneqq \frac{1}{2}\left(\mathbf{L} - \mathbf{L}^T\right), \tag{2.4}$$

respectively, and we refer to $\mathbf{D}$ as strain-rate tensor. Moreover, the additive split of the strain-rate tensor $\mathbf{D} = \operatorname{dev}(\mathbf{D}) + \operatorname{vol}(\mathbf{D})$ into the traceless deviatoric part $\operatorname{dev}(\mathbf{D})$ and the volumetric part $\operatorname{vol}(\mathbf{D})$ is useful in light of the constitutive modeling of fluids. The volumetric part is given as

$$\operatorname{vol}(\mathbf{D}) \coloneqq \frac{1}{3}\operatorname{tr}(\mathbf{D})\,\mathbf{I} = \operatorname{div}\mathbf{u}\,\mathbf{I},$$

where the divergence of a vector is given as $\operatorname{div}\boldsymbol{\Phi} \coloneqq \sum_{a=1}^{3} \partial\Phi_a/\partial x_a$ in Cartesian coordinates. Cartesian components of $\boldsymbol{\Phi}$ are denoted Φ_a such that $\boldsymbol{\Phi} = \sum_{a=1}^{3} \Phi_a \mathbf{e}_a$. The identity tensor is denoted $\mathbf{I}$.

2.1.2 Transport theorem

The Reynolds transport theorem is an essential calculus operation to formulate local balance equations in continuum mechanics. We again consider a generic density field $\boldsymbol{\Phi}$ of arbitrary rank which is continuously defined over Ω. The temporal rate of change of the total amount of $\boldsymbol{\Phi}$ contained within the time-dependent region Ω with boundary $\Gamma = \partial\Omega$ is written

$$\frac{\mathrm{d}}{\mathrm{d}t}\int_{\Omega} \boldsymbol{\Phi}\left(\mathbf{x}, t\right)\mathrm{d}v = \int_{\Omega_0} \frac{\mathrm{d}}{\mathrm{d}t}\left[\hat{\boldsymbol{\Phi}}\left(\mathbf{X}, t\right) J\left(\mathbf{X}, t\right)\right]\mathrm{d}V, \tag{2.5}$$

where Eq. (2.2) has been used together with the fact that the reference configuration Ω_0 is time invariant. Using the product rule and Euler's formula

$$\frac{\mathrm{d}}{\mathrm{d}t} J\left(\mathbf{X}, t\right) = \operatorname{div}\mathbf{u}\left(\mathbf{x}, t\right) J\left(\mathbf{X}, t\right),$$

we rewrite Eq. (2.5) to yield

$$\frac{\mathrm{d}}{\mathrm{d}t}\int_{\Omega} \boldsymbol{\Phi}\,\mathrm{d}v = \int_{\Omega} \dot{\boldsymbol{\Phi}} + \boldsymbol{\Phi}\operatorname{div}\mathbf{u}\,\mathrm{d}v. \tag{2.6}$$

Invoking the definition (2.3) of the material time derivative yields

$$\frac{\mathrm{d}}{\mathrm{d}t}\int_{\Omega} \boldsymbol{\Phi}\,\mathrm{d}v = \int_{\Omega} \frac{\partial\boldsymbol{\Phi}}{\partial t} + \operatorname{div}(\boldsymbol{\Phi}\otimes\mathbf{u})\,\mathrm{d}v, \tag{2.7}$$

where the calculus identity

$$\operatorname{div}(\boldsymbol{\Phi} \otimes \mathbf{u}) = \boldsymbol{\Phi} \operatorname{div} \mathbf{u} + \operatorname{grad} \boldsymbol{\Phi} \cdot \mathbf{u}$$

has been used. Furthermore, using the divergence theorem

$$\int_\Omega \operatorname{div}(\boldsymbol{\Phi} \otimes \mathbf{u})\, \mathrm{d}v = \int_\Gamma (\boldsymbol{\Phi} \otimes \mathbf{u})^T \mathbf{n}\, \mathrm{d}a = \int_\Gamma (\boldsymbol{\Phi} \cdot \mathbf{n})\, \mathbf{u}\, \mathrm{d}a, \tag{2.8}$$

where $\mathbf{n}$ denotes the unit outward normal to the surface Γ with surface element $\mathrm{d}a$, an alternative form of the transport theorem is given as

$$\frac{\mathrm{d}}{\mathrm{d}t} \int_\Omega \boldsymbol{\Phi}\, \mathrm{d}v = \int_\Omega \frac{\partial \boldsymbol{\Phi}}{\partial t}\, \mathrm{d}v + \int_\Gamma (\boldsymbol{\Phi} \cdot \mathbf{n})\, \mathbf{u}\, \mathrm{d}a. \tag{2.9}$$

The temporal rate of change of the total amount of a density $\boldsymbol{\Phi}$ contained within Ω is thus observed equal to the sum of the volume integral of the local time derivative of $\boldsymbol{\Phi}$ and the convective flux of $\boldsymbol{\Phi}$ across the surface Γ.

2.1.3 General balance equations

We axiomatically require the total mass $\mathfrak{M}$ of a material body to remain constant during deformation and motion, i.e.

$$\mathfrak{M} := \int_\Omega \mathrm{d}m = \int_\Omega \varrho\, \mathrm{d}v = \text{const.}.$$

The mass density $\varrho = \mathrm{d}m/\mathrm{d}v$ is defined as the ratio of infinitesimal mass $\mathrm{d}m$ to the volume element $\mathrm{d}v$. Application of the transport theorem (2.6) yields

$$\frac{\mathrm{d}}{\mathrm{d}t} \int_\Omega \varrho\, \mathrm{d}v = \int_\Omega \dot{\varrho} + \varrho \operatorname{div} \mathbf{u}\, \mathrm{d}v = 0. \tag{2.10}$$

Since the integral statement (2.10) has to hold true for any arbitrary domain of integration Ω, the localized balance of mass, hereinafter referred to as continuity equation, reads

$$\dot{\varrho} + \varrho \operatorname{div} \mathbf{u} = 0. \tag{2.11}$$

Assuming an incompressible flow, i.e. $\dot{\varrho} = 0$, implies that the corresponding velocity field has to be divergence free, i.e. $\operatorname{div} \mathbf{u} = 0$, such that $\operatorname{vol}(\mathbf{D}) = \mathbf{0}$.

The rate of change $\mathrm{d}\mathfrak{J}/\mathrm{d}t$ of total linear momentum

$$\mathfrak{J} := \int_\Omega \varrho \mathbf{u}\, \mathrm{d}v$$

is axiomatically required equal to the sum $\mathfrak{F}_\Omega + \mathfrak{F}_\Gamma$ of total volume force

$$\mathfrak{F}_\Omega := \int_\Omega \varrho \mathbf{b} \, \mathrm{d}v, \tag{2.12}$$

where **b** denotes volumetric force density, and total contact force

$$\mathfrak{F}_\Gamma := \int_\Gamma \mathbf{t}_s \, \mathrm{d}a = \int_\Gamma \mathbf{n} \cdot \mathbf{T} \, \mathrm{d}a. \tag{2.13}$$

The contact force $\mathfrak{F}_\Gamma$ arises due to surface tractions $\mathbf{t}_s$ acting on the surface $\Gamma = \partial\Omega$. Surface tractions are related to the Cauchy stress tensor $\mathbf{T}$ by means of the Cauchy theorem $\mathbf{t}_s := \mathbf{n} \cdot \mathbf{T}$. The particular structure of the second-order Cauchy stress tensor $\mathbf{T}$ remains to be introduced using a constitutive material model.

Applying the divergence theorem (2.8) to Eq. (2.13) and taking into account the transport theorem as well as the continuity equation yields the local balance of linear momentum

$$\varrho \dot{\mathbf{u}} = \operatorname{div} \mathbf{T} + \varrho \mathbf{b}. \tag{2.14}$$

In accordance with the classical fluid dynamics of non-polar fluids, the stress tensor is assumed symmetric, such that

$$\mathbf{T} = \mathbf{T}^T. \tag{2.15}$$

While a formal proof is omitted here for the sake of brevity, the symmetry (2.15) is equivalent to the localized balance of moment of momentum provided that couple stresses are absent and the balances (2.11) and (2.14) hold as well.

The forthcoming analysis of transport processes in porous media assumes thermal effects to be negligible. In particular, sources of specific heat supply or heat flux across the surface Γ are considered absent and the temperature field to be uniform. As a consequence, the mechanical problem can be formulated by the set of balance equations (2.11), (2.14) and (2.15) together with initial and boundary conditions with respect to the primary variables ϱ and $\mathbf{u}$ as well as closing constitutive equations. Therefore, the balance of energy is not considered within this thesis.

2.1.4 Constitutive equations

In order to close the system of equations that the mechanical problem is comprised of, constitutive relations are required for the six unique components of the symmetric Cauchy stress tensor $\mathbf{T}$. While the kinematic relationships and balance equations that were introduced in the preceding sections apply to general classical continua, in the following, we restrict ourselves to the constitutive modeling of quasi-incompressible, Newtonian fluid phases.

In particular, the Cauchy stress tensor is physically required to satisfy the invariance under superposed rigid body motion $\mathbf{T} = \mathbf{Q}\mathbf{T}\mathbf{Q}^T$, where $\mathbf{Q}$ denotes a generic proper orthogonal tensor. In other words, the local stress states may not change when the material body is subject to a rigid body motion. A further physical requirement is that the stress state is isotropic when the fluid is at rest. The latter implies that the equilibrium part of $\mathbf{T}$ must be of general form

$$\mathbf{T}_{\mathrm{eq}} = -p\mathbf{I}, \tag{2.16}$$

where p, with unit of force per unit area, is referred to as pressure. While a formal thermodynamic discussion of pressure is considered out of scope of this text, for a thermodynamically closed system, pressure is defined as the negative rate of change of free energy with volume at constant temperature. A closure relation for pressure p is denoted equation of state and a fluid is referred to as barotropic if the equation of state has the form $p = p(\varrho)$. Since we consider isothermal processes for which the dependency of pressure on temperature is neglected, only barotropic fluids are modeled hereinafter. In order to introduce a specific form of the equation of state, we follow Murnaghan [146] and consider the bulk modulus

$$K = \varrho \frac{\partial p}{\partial \varrho} \tag{2.17}$$

to be a linear function of pressure by truncating the Taylor series expansion of K about $p = 0$ after the first order term, i.e.

$$K = K(0) + \left(\frac{\partial K}{\partial p}\right)\bigg|_{p=0} p + \mathcal{O}(p^2) = K_0 + \gamma p + \mathcal{O}(p^2), \tag{2.18}$$

where the parameter $\gamma \coloneqq (\partial K/\partial p)\big|_{p=0}$. Truncation of the Taylor series is reasonable in light of the fact that we restrict ourselves to quasi-incompressible fluids. Rearranging Eq. (2.18) and using Eq. (2.17) we obtain

$$\frac{1}{K_0 + \gamma p}\mathrm{d}p = \frac{1}{\varrho}\mathrm{d}\varrho. \tag{2.19}$$

Since pressure must vanish for a reference density ϱ_0, the boundary condition $p(\varrho_0) = 0$ is taken into account. The latter yields a closed-form solution of Eq. (2.19) which reads

$$p(\varrho) = \frac{\varrho_0 c^2}{\gamma}\left[\left(\frac{\varrho}{\varrho_0}\right)^{\gamma} - 1\right], \tag{2.20}$$

where the speed of sound

$$c := \sqrt{\frac{K_0}{\varrho_0}}.$$

We may refer to p as thermodynamic pressure if it is a dependent variable that is given in terms of an equation of state. For a truly incompressible fluid on the other hand, where p can be identified as a Lagrange multiplier which accounts for the incompressibility constraint $\operatorname{div} \mathbf{u} = 0$, p is referred to as non-thermodynamic pressure. Hereinafter we compute pressure as function of density according to an equation of state. The parameters c and γ are calibrated such that density fluctuations relative to initial fluid density can be neglected (see section 3.6). With respect to the equation of state (2.20), the assumption $\gamma = 7$ is common for quasi-incompressible fluids [see 13, § 1.8]. A further very commonly used equation of state is the linearization of Eq. (2.20) about $\varrho = \varrho_0$ with $\gamma = 1$, i.e.

$$p(\varrho) = c^2 (\varrho - \varrho_0). \tag{2.21}$$

While Eq. (2.16) together with a suitable equation of state determines the equilibrium stress state, a constitutive equation for the non-equilibrium stress $\mathbf{T}_{\text{neq}}$ remains to be introduced. As a result of the entropy inequality, the total stress can be additively decomposed to read

$$\mathbf{T} = \mathbf{T}_{\text{eq}} + \mathbf{T}_{\text{neq}}. \tag{2.22}$$

While omitting a formal derivation, we reconstruct the chain of reasoning leading towards the constitutive equation that determines the non-equilibrium stress state of a Newtonian fluid. We begin from the initial assumption that the non-equilibrium stress state of a homogeneous fluid may only depend on density, velocity and velocity gradient of the current configuration - the so-called non-equilibrium process variables. For reasons of isotropy, $\mathbf{T}_{\text{neq}}$ can be reduced to a continuous function of density and the symmetric strain-rate tensor only, i.e. $\mathbf{T}_{\text{neq}} = \mathbf{T}_{\text{neq}}(\varrho, \mathbf{D})$. The simplest constitutive form for the non-equilibrium stress compliant with the dissipation inequality is the linear relationship $\mathbf{T}_{\text{neq}} = \mathbb{M}\mathbf{D}$, where $\mathbb{M}$ is a forth-order tensor function of density. The latter assumption of linearity is the defining property of Newtonian fluids. In the linear theory of elasticity for isotropic and homogeneous materials, the forth order stiffness tensor relating stresses and strains can be reduced to two material parameters, the so-called Lamé coefficients. In equivalence to the latter, the tensor $\mathbb{M}$ for isotropic and homogeneous Newtonian fluids can be reduced to two material parameters λ and μ as well to yield

$$\mathbf{T}_{\text{neq}} = \lambda(\operatorname{tr} \mathbf{D})\mathbf{I} + 2\mu\mathbf{D}. \tag{2.23}$$

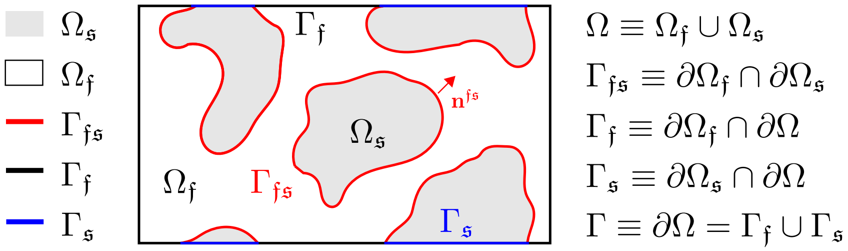
$\Omega_{\mathfrak{s}}$
$\Omega_{\mathfrak{f}}$
$\Gamma_{\mathfrak{fs}}$
$\Gamma_{\mathfrak{f}}$
$\Gamma_{\mathfrak{s}}$
$\Gamma_{\mathfrak{f}}$
$\mathbf{n}^{\mathfrak{fs}}$
$\Omega_{\mathfrak{s}}$
$\Omega_{\mathfrak{f}}$
$\Gamma_{\mathfrak{fs}}$
$\Gamma_{\mathfrak{s}}$
$\Omega \equiv \Omega_{\mathfrak{f}} \cup \Omega_{\mathfrak{s}}$
$\Gamma_{\mathfrak{fs}} \equiv \partial\Omega_{\mathfrak{f}} \cap \partial\Omega_{\mathfrak{s}}$
$\Gamma_{\mathfrak{f}} \equiv \partial\Omega_{\mathfrak{f}} \cap \partial\Omega$
$\Gamma_{\mathfrak{s}} \equiv \partial\Omega_{\mathfrak{s}} \cap \partial\Omega$
$\Gamma \equiv \partial\Omega = \Gamma_{\mathfrak{f}} \cup \Gamma_{\mathfrak{s}}$

Figure 2.2: Schematic representation of domains, boundaries and relations among them for single phase flow in porous media.

The coefficient μ is referred to as dynamic viscosity, whereas λ is the dilatational viscosity. Since $\operatorname{tr}\mathbf{D} = 3\operatorname{div}\mathbf{u}$, the first term on the RHS of Eq. (2.23) is typically neglected for quasi-incompressible fluids. Using Eq. (2.4), the non-equilibrium stress tensor of quasi-incompressible fluids, or, hereafter referred to as viscous extra stress, is given by

$$\mathbf{T}_{\text{neq}}^{\text{incom.}} = \mu\left(\operatorname{grad}\mathbf{u} + \operatorname{grad}^{T}\mathbf{u}\right). \tag{2.24}$$

2.1.5 Initial boundary value problems

In order to formulate the mechanical problem of isothermal, single phase fluid transport through a porous medium within a bounded domain $\Omega \subset \mathbb{R}^d$, $d = 2, 3$, and a time interval $(0, T)$, we subdivide $\Omega = \Omega_{\mathfrak{s}} \cup \Omega_{\mathfrak{f}}$ into a domain $\Omega_{\mathfrak{s}}$ occupied by material points of the solid phase and a domain $\Omega_{\mathfrak{f}}$ occupied by material points of the fluid phase (Fig. 2.2). The subscripts $(\cdot)_{\mathfrak{f}}$ and $(\cdot)_{\mathfrak{s}}$ are introduced to differentiate the properties of the fluid phase from those of the solid phase. We take into account the physical constraint $\Omega_{\mathfrak{s}} \cap \Omega_{\mathfrak{f}} = \emptyset$. The interface $\Gamma_{\mathfrak{fs}} := \partial\Omega_{\mathfrak{s}} \cap \partial\Omega_{\mathfrak{f}}$ is referred to as solid-fluid interface. We introduce $\mathbf{u}_{\mathfrak{f}}(\mathbf{x}, t), \forall\mathbf{x} \in \Omega_{\mathfrak{f}}$ as fluid velocity, whereas $\mathbf{u}_{\mathfrak{s}}(\mathbf{x}, t), \forall\mathbf{x} \in \Omega_{\mathfrak{s}}$ is referred to as solid velocity. For all flow processes analyzed herein we consider the solid phase to be static and rigid such that $\mathbf{u}_{\mathfrak{s}} = \mathbf{0}$, which implies that the governing balance equations for the solid phase reduce to

$$\dot{\mathbf{u}}_{\mathfrak{s}} = \mathbf{0}, \quad \text{and} \quad \dot{\varrho}^{\mathfrak{s}} = 0, \qquad \forall\mathbf{x} \in \Omega_{\mathfrak{s}}.$$

Consequently, we omit the explicit physical modeling of the deformation of the bulk solid phase. However, the model needs to account for momentum exchange between solid and fluid phases at the interface $\Gamma_{\mathfrak{fs}}$. The latter is achieved by introducing inner boundary conditions on $\Gamma_{\mathfrak{fs}}$. We incorporate a kinematic condition, denoted no-penetration boundary condition, by which the fluid velocity component normal to the solid-fluid interface is required to be zero, i.e.

$$\mathbf{u}_{\mathfrak{f}} \cdot \mathbf{n}^{\mathfrak{fs}} = 0, \qquad \forall\,(t, \mathbf{x}) \in (0, T) \times \Gamma_{\mathfrak{fs}}, \tag{2.25}$$

where $\mathbf{n}^{\mathfrak{fs}}$ is the unit outward normal of the interface $\Gamma_{\mathfrak{fs}}$. As shown in section 2.2.3, the latter results from the interfacial balance of mass at points of the interface $\Gamma_{\mathfrak{fs}}$. Additionally, we assume fluid velocities at points of the solid-fluid interface in directions tangent to the interface to be zero. The latter implies the well-known no-slip boundary condition

$$\mathbf{u}_{\mathfrak{f}} - \left(\mathbf{u}_{\mathfrak{f}} \cdot \mathbf{n}^{\mathfrak{fs}}\right) \mathbf{n}^{\mathfrak{fs}} = \mathbf{0}, \qquad \forall\,(t, \mathbf{x}) \in (0, T) \times \Gamma_{\mathfrak{fs}}. \tag{2.26}$$

While the no-penetration condition is required for mass conservation, the no-slip condition constitutes a physical assumption. Together, the no-slip and no-penetration boundary conditions result in the inner Dirichlet boundary condition

$$\mathbf{u}_{\mathfrak{f}}\,(\mathbf{x}, t) = \mathbf{0}, \qquad \forall\,(t, \mathbf{x}) \in (0, T) \times \Gamma_{\mathfrak{fs}}.$$

The more general case that the solid phase is subject to a rigid body translation or rotation, i.e. $\mathbf{u}_{\mathfrak{s}} \neq \mathbf{0}$, requires the relative motion between solid and fluid phases at points of the interface to be zero, hence

$$\mathbf{u}_{\mathfrak{f}}\,(\mathbf{x}, t) = \mathbf{u}_{\mathfrak{s}}\,(\mathbf{x}, t)\,, \qquad \forall\,(t, \mathbf{x}) \in (0, T) \times \Gamma_{\mathfrak{fs}}.$$

The set of governing balance equations for the fluid phase is comprised of

$$\dot{\varrho}^{\mathfrak{f}} + \varrho^{\mathfrak{f}} \operatorname{div} \mathbf{u}_{\mathfrak{f}} = 0, \quad \varrho^{\mathfrak{f}} \dot{\mathbf{u}}_{\mathfrak{f}} = \operatorname{div} \mathbf{T}^{\mathfrak{f}} + \varrho^{\mathfrak{f}} \mathbf{b}, \quad \text{and} \quad \mathbf{T}^{\mathfrak{f}} = \mathbf{T}^{\mathfrak{f}^T}, \qquad \forall\,\mathbf{x} \in \Omega_{\mathfrak{f}}, \tag{2.27}$$

where the body forces $\mathbf{b}$ have to be specified for all $(t, \mathbf{x}) \in (0, T) \times \Omega_{\mathfrak{f}}$. Using Eqs. (2.22), (2.16),(2.24) as well as the relation

$$\operatorname{div}\left(\operatorname{grad}^T \mathbf{u}\right) = \operatorname{grad}\left(\operatorname{div} \mathbf{u}\right),$$

the general balance of linear momentum (2.14) for a homogeneous, quasi-incompressible fluid ($\operatorname{div} \mathbf{u} \approx 0$) with constant dynamic viscosity $\mu^{\mathfrak{f}}$ is reformulated to give

$$\varrho^{\mathfrak{f}} \dot{\mathbf{u}}_{\mathfrak{f}} = \mu^{\mathfrak{f}} \operatorname{div}\left(\operatorname{grad} \mathbf{u}_{\mathfrak{f}}\right) - \operatorname{grad} p + \varrho^{\mathfrak{f}} \mathbf{b}, \qquad \forall\,\mathbf{x} \in \Omega_{\mathfrak{f}}. \tag{2.28}$$

Eq. (2.28) is denoted incompressible Navier-Stokes equation. We complete the formulation of the mechanical problem by specifying initial conditions for $t = 0$ with respect to the primary variables, i.e.

$$\mathbf{u}_{\mathfrak{f}}(\mathbf{x}, t) = \mathbf{u}_0(\mathbf{x}), \qquad \varrho^{\mathfrak{f}}(\mathbf{x}, t) = \varrho_0^{\mathfrak{f}}, \qquad \forall \mathbf{x} \in \Omega_{\mathfrak{f}},\ t = 0.$$

Furthermore, since the fluid phase $\Omega_{\mathfrak{f}}$ is not entirely contained in Ω, there exists an outer boundary to the fluid phase $\Gamma_{\mathfrak{f}} \coloneqq \partial\Omega_{\mathfrak{f}} \cap \partial\Omega = \partial\Omega_{\mathfrak{f}} \setminus \Gamma_{\mathfrak{f}\mathfrak{s}}$ on which boundary conditions with respect to velocity are required. Throughout this work, outer boundaries to the fluid domain are either subject to the Dirichlet boundary condition

$$\mathbf{u}_{\mathfrak{f}}(\mathbf{x}, t) = \mathbf{u}_{\Gamma}(\mathbf{x}, t) \qquad \forall (t, \mathbf{x}) \in (0, T) \times \Gamma_{\mathfrak{f}}^{D}$$

or periodic boundary conditions on $\Gamma_{\mathfrak{f}}^{P}$ that are introduced in section 3.5.1.

2.2 Fundamentals of two-phase flow

We proceed by introducing the kinematic, balance and constitutive equations that govern the mechanical problem of multi-phase flow of immiscible bulk fluid phases. The distinctive property of multi-phase flow is the presence of interfaces that separate bulk fluid phases. From a geometrical point of view, the interface is represented by a surface embedded in Euclidean space. Hence, referring to its geometric properties, an interface is also referred to as surface. The textbooks Aris [5], Edwards et al. [63] and the overview Dziubek [62] have served as valuable references. In contrast to Dziubek [62], however, the following introduction is simplified since we consider interfaces to be impermeable due to bulk fluid phases being mutually immiscible; such interfaces being referred to as material interfaces. The latter assumption is invalid when, for instance, evaporation or condensation phenomena appear at interfaces that separate a bulk liquid and its vapor phase. Furthermore, mass density of the interface, i.e. interface-excess mass density, is considered negligible compared to the mass density of the bulk fluid phases. The latter assumption is invalid when, for instance, studying foam films that separate gas phases. On the other hand, the application of the Gibbs convention by which interfaces are regarded singular boundaries to the adjacent bulk phases is common to the majority of continuum approaches to modeling multi-phase transport processes. In the following section, discussion of the differential geometry and kinematics of surfaces embedded in Euclidean space are kept to a minimum; the interested reader with focus on the mechanics of interfaces is referred to the above references.

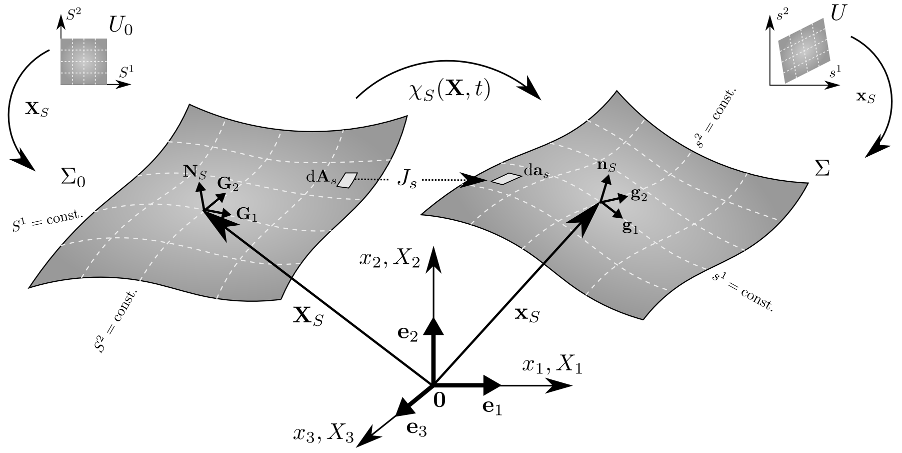
S^2
U_0
S^1
$\mathbf{X}_S$
$\chi_S(\mathbf{X},t)$
s^2
U
s^1
$\mathbf{x}_S$
Σ_0
$\mathbf{N}_S$
$\mathbf{G}_2$
$\mathbf{G}_1$
$\mathrm{d}\mathbf{A}_s$
J_s
$\mathrm{d}\mathbf{a}_s$
$\mathbf{n}_S$
$\mathbf{g}_2$
$\mathbf{g}_1$
Σ
$S^1 = \text{const.}$
$S^2 = \text{const.}$
$s^2 = \text{const.}$
$s^1 = \text{const.}$
x_2, X_2
$\mathbf{e}_2$
$\mathbf{X}_S$
$\mathbf{x}_S$
x_1, X_1
$\mathbf{0}$
$\mathbf{e}_1$
$\mathbf{e}_3$
x_3, X_3

Figure 2.3: Schematic representation of motion of a surface through three-dimensional space, its reference and current configurations as well as the concept of mapping. The oriented differential surface area element of the reference configuration $\mathrm{d}\mathbf{A}_S = \mathbf{N}_S \cdot [\mathrm{d}\mathbf{G}_1 \times \mathrm{d}\mathbf{G}_2]$, whereas in the current configuration $\mathrm{d}\mathbf{a}_S = \mathbf{n}_S \cdot [\mathrm{d}\mathbf{g}_1 \times \mathrm{d}\mathbf{g}_2]$. Moreover, $\mathrm{d}A_S = \|\mathrm{d}\mathbf{G}_1 \times \mathrm{d}\mathbf{G}_2\| \mathrm{d}S^1 \mathrm{d}S^2$ and $\mathrm{d}a_S = \|\mathrm{d}\mathbf{g}_1 \times \mathrm{d}\mathbf{g}_2\| \mathrm{d}s^1 \mathrm{d}s^2$

2.2.1 Geometry and kinematics

We consider a set of material points that represent an interface. Since we consider material interfaces such that there is no mass exchange between interfaces and bulk phases, the interface shall always be comprised of the same set of surface-fixed material points. The referential position of material points fixed to the two-dimensional smooth interface U_0 can be *intrinsically* given in terms of the curvilinear surface coordinates S^1 and S^2. In the context of coupling bulk phases and interfaces, however, we are interested in an *extrinsic* description considering the surface to be embedded in a 3-dimensional Euclidean space with Cartesian coordinates, unit vectors $\mathbf{e}_a$ and time-invariant origin $\mathbf{O}$. The extrinsic description of the position of a material point fixed to a smooth interface Σ_0 in referential configuration at time $t = 0$ is given by the parameterization $\mathbf{X}_S : U_0 \subset \mathbb{R}^2 \rightarrow \Sigma_0 \subset \mathbb{R}^3$ as $\mathbf{X}_S = \sum_{a=1}^{3} X_a(S^1, S^2)\, \mathbf{e}_a$ (Fig. 2.3, left). The covariant basis vectors that are tangent to the curvilinear S^1 and S^2 coordinate curves and local to a referential position $\mathbf{X}_S$ are

$$\mathbf{G}_1 = \frac{\partial \mathbf{X}_S}{\partial S^1} = \sum_{a=1}^{3} \frac{\partial X_a}{\partial S^1} \mathbf{e}_a \quad \text{and} \quad \mathbf{G}_2 = \frac{\partial \mathbf{X}_S}{\partial S^2} = \sum_{a=1}^{3} \frac{\partial X_a}{\partial S^2} \mathbf{e}_a,$$

such that the local surface unit normal vector at $\mathbf{X}_S$ is expressed

$$\mathbf{N}_S = \frac{\mathbf{G}_1 \times \mathbf{G}_2}{\|\mathbf{G}_1 \times \mathbf{G}_2\|}.$$

In equivalence to the description of motion of bulk phase material points, we follow the motion of a surface-fixed material point in terms of the continuous mapping $\chi_S : \Sigma_0 \subset \mathbb{R}^3 \to \Sigma \subset \mathbb{R}^3$ which maps points $\mathbf{X}_S$ of the reference configuration Σ_0 onto points $\mathbf{x}_S = \sum_{a=1}^{3} x_a(s^1, s^2)\mathbf{e}_a$ of the current configuration Σ (Fig. 2.3, right), such that

$$\mathbf{x}_S = \chi_S\left(\mathbf{X}_S, t\right), \qquad \mathbf{X}_S \in \Sigma_0 \subset \mathbb{R}^3 \quad \text{and} \quad \mathbf{x}_S \in \Sigma \subset \mathbb{R}^3.$$

The spatial coordinates x_a represent a parameterization $\mathbf{x}_S : U \subset \mathbb{R}^2 \to \Sigma \subset \mathbb{R}^3$ of the surface Σ in its current configuration. The covariant basis vectors at spatial position $\mathbf{x}_S$ with respect to the curvilinear surface coordinates s^1 and s^2 of U are

$$\mathbf{g}_1 = \frac{\partial \mathbf{x}_S}{\partial s^1} = \sum_{a=1}^{3} \frac{\partial x_a}{\partial s^1} \mathbf{e}_a \quad \text{and} \quad \mathbf{g}_2 = \frac{\partial \mathbf{x}_S}{\partial s^2} = \sum_{a=1}^{3} \frac{\partial x_a}{\partial s^2} \mathbf{e}_a,$$

such that the surface unit normal vector

$$\mathbf{n}_S = \frac{\mathbf{g}_1 \times \mathbf{g}_2}{\|\mathbf{g}_1 \times \mathbf{g}_2\|}.$$

Introducing the surface identity tensor

$$\mathbf{I}_S := \mathbf{I} - \mathbf{n}_S \otimes \mathbf{n}_S, \tag{2.29}$$

the surface gradient[1] is defined by removing components of the spatial gradient field that act in direction of the surface normal [62, see Eq. (10)], i.e.

$$\operatorname{grad}_S(\bullet) := \operatorname{grad}(\bullet) \cdot \Big[\mathbf{I} - \mathbf{n}_S \otimes \mathbf{n}_S\Big] = \operatorname{grad}(\bullet) \cdot \mathbf{I}_S. \tag{2.30}$$

Consequently, the surface divergence

$$\operatorname{div}_S(\bullet) := \operatorname{grad}_S(\bullet) : \mathbf{I}_S.$$

The local curvature tensor for the surface is defined

$$\mathbf{K} := -\operatorname{grad}_S \mathbf{n}_S,$$

where the minus sign invokes the convention that curvatures are measured positive when at point $\mathbf{x}_S$ the surface is curved concave in direction of $\mathbf{n}_S(\mathbf{x}_S)$. Due to reasons of symmetry, $\mathbf{K}$ can be decomposed to $\mathbf{K} = \kappa_1 \mathbf{k}_1 \otimes \mathbf{k}_1 + \kappa_2 \mathbf{k}_2 \otimes \mathbf{k}_2$. The vectors $\mathbf{k}_1$ and $\mathbf{k}_2$ are eigenvectors of $\mathbf{K}$ with eigenvalues, or, also referred to as principal curvatures, κ_1 and κ_2, respectively. For reasons apparent later, the total curvature κ, which we define twice the mean curvature $\frac{1}{2}(\kappa_1 + \kappa_2)$, i.e.

$$\kappa := \kappa_1 + \kappa_2 = -\operatorname{div}_S \mathbf{n}_S, \tag{2.31}$$

is a useful scalar measure of curvature. The term total curvature often refers to the Gaussian curvature $\kappa_1\kappa_2$, however, the definition of total curvature in terms of Eq. (2.31) is common in engineering literature [114, 193]. We furthermore introduce the general identity

$$\operatorname{div}_S \mathbf{I}_S = \kappa \mathbf{n}_S. \tag{2.32}$$

For the purpose of this treatise, the characterization of surfaces embedded in $\mathbb{R}^3$ in terms of their extrinsic geometric properties as given above suffices for the description of interfacial effects.

Partial derivatives with respect to time for fixed material surface coordinates $\mathbf{X}_S$, or, also referred to as material surface time derivatives, are denoted $\mathrm{d}_S/\mathrm{d}t := (\partial/\partial t)_{\mathbf{X}_S} = (\partial/\partial t)_{S^1,S^2}$. For a surface-fixed material point initially located at $\mathbf{X}_S$, velocity at time t is thus defined

---

[1] Introducing the contravariant basis vectors

$$\mathbf{g}^1 = \sum_{a=1}^{3} \frac{\partial s^1}{\partial x_a} \mathbf{e}_a \quad \text{and} \quad \mathbf{g}^2 = \sum_{a=1}^{3} \frac{\partial s^2}{\partial x_a} \mathbf{e}_a,$$

the surface identity tensor can be written

$$\mathbf{I}_S = \mathbf{g}^1 \otimes \mathbf{g}_1 + \mathbf{g}^2 \otimes \mathbf{g}_2,$$

whereas the surface gradient and surface divergence may be expressed as

$$\operatorname{grad}_S(\bullet) = \sum_{a=1}^{2} \frac{\partial}{\partial s^a} \mathbf{g}^a \otimes (\bullet) \quad \text{and} \quad \operatorname{div}_S(\bullet) = \sum_{a=1}^{2} \frac{\partial(\bullet)_a}{\partial s^a}.$$

In the above expressions, the intrinsic, surface-bound nature of grad_S and div_S becomes more apparent.

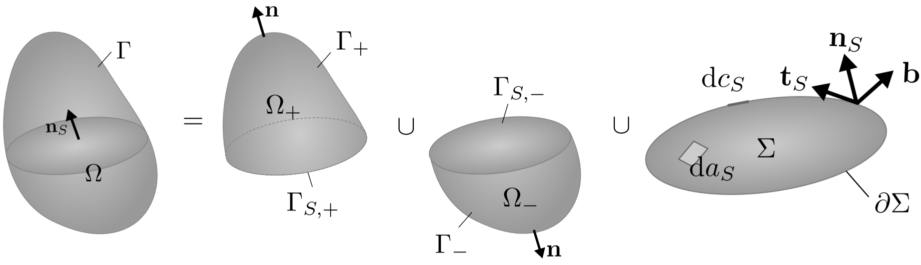

Figure 2.4: Schematic representation of a material domain Ω comprised of two bulk phases Ω_+ and Ω_- with outer unit normal **n** and a surface Σ representing an internal interface. The surface Σ is bounded by the boundary curve ∂Σ with unit tangent vector $\mathbf{t}_S$ and unit vector $\mathbf{b}_S = \mathbf{n}_S \times \mathbf{t}_S$ perpendicular to ∂Σ.

$$\mathbf{u}_S := \frac{\mathrm{d}_S}{\mathrm{d}t}\mathbf{x}_S = \frac{\mathrm{d}_S}{\mathrm{d}t}\chi_S\left(\mathbf{X}_S, t\right).$$

Introducing a generic surface field $\boldsymbol{\Phi}_S$ of arbitrary rank, the material surface time derivative of $\boldsymbol{\Phi}_S\left(\mathbf{x}_S, t\right)$ in spatial description for a fixed parameter $\mathbf{X}_S$ reads [see 63, § 3.4]

$$\frac{\mathrm{d}_S}{\mathrm{d}t}\boldsymbol{\Phi}_S\left(\mathbf{x}_S, t\right) = \frac{\partial}{\partial t}\boldsymbol{\Phi}_S\left(\mathbf{x}_S, t\right) + \operatorname{grad}_S \boldsymbol{\Phi}_S\left(\mathbf{x}_S, t\right) \cdot \mathbf{u}_S. \tag{2.33}$$

We denote the bounded domains occupied by material points of the bulk phases that are adjacent to the interface as Ω_+ and Ω_-, where the interface unit normal $\mathbf{n}_S$ points from Ω_- to Ω_+ (Fig. 2.4). Considering material interfaces, i.e. impermeable interfaces separating immiscible bulk phases, a kinematic constraint is incorporated by which we consider the areal domains

$$\begin{aligned}\Gamma_{S,+} &:= \partial\Omega_+ \cap \Sigma \overset{!}{=} \Sigma, \quad \text{and} \\ \Gamma_{S,-} &:= \partial\Omega_- \cap \Sigma \overset{!}{=} \Sigma,\end{aligned} \tag{2.34}$$

where $\Gamma_{S,+}$ and $\Gamma_{S,-}$ are referred to as internal interfaces whereas $\Gamma_+ := \partial\Omega_+ \setminus \Gamma_{S,+}$ and $\Gamma_- := \partial\Omega_- \setminus \Gamma_{S,-}$ are referred to as outer boundaries to Ω_+ and Ω_-, respectively.

We use the notation

$$\begin{aligned}(\bullet)^+ &:= (\bullet)|_{\mathbf{x}=\mathbf{x}_S}\,, \quad \forall\,\mathbf{x} \in \Omega_+, \mathbf{x}_S \in \Sigma \quad \text{and}\\ (\bullet)^- &:= (\bullet)|_{\mathbf{x}=\mathbf{x}_S}\,, \quad \forall\,\mathbf{x} \in \Omega_-, \mathbf{x}_S \in \Sigma,\end{aligned}$$

to indicate the values of bulk field variables evaluated at points of the internal interface. The surface unit normals to the internal interfaces are thus denoted

$$\begin{aligned}\mathbf{n}^+ &:= -\mathbf{n}_S\left(\mathbf{x}_S\right), \quad \text{and}\\ \mathbf{n}^- &:= +\mathbf{n}_S\left(\mathbf{x}_S\right).\end{aligned} \tag{2.35}$$

2.2.2 Transport theorem

We consider a generic density field $\mathbf{\Phi}_{\text{micro}}$ of arbitrary rank which is, from a microscopic point of view, continuously defined over the entire domain Ω. In contrast to section 2.1.2, hereinafter, Ω shall be comprised of two immiscible bulk phases. If $\mathbf{\Phi}_{\text{micro}}$ is for instance taken to be mass density, the microscopic density field may exhibit large gradients in interfacial transition zones, e.g. a zone separating a gas and a liquid phase. In this section, the length scale we associate with the microscopic description shall be in the order of the length scale of the interfacial transition zone. In the context of applying the continuum approach to model multiphase phenomena at considerably larger length scales on the other hand, it is most common to substitute the microscopic density field with a macroscopic density field $\mathbf{\Phi} = \mathbf{\Phi}_{\text{macro}}$ that exhibits a discontinuity at points of a singular interface - the so-called Gibbs convention. The residual difference $\int_\Sigma \mathbf{\Phi}_S \mathrm{d}a_S := \int_\Omega \mathbf{\Phi}_{\text{micro}} \mathrm{d}v - \int_\Omega \mathbf{\Phi}_{\text{macro}} \mathrm{d}v$, which has non-zero contributions only within the interfacial transition region, is subsequently assigned to a singular interface (Fig. 2.5) and we refer to $\mathbf{\Phi}_S$ as interface-excess density[1]. While the macroscopic density field $\mathbf{\Phi}$ is defined with respect a unit of volume of the bulk phases, the interface-excess density field is defined with respect to a unit of area of the singular interface.

Consequently, we consider a material volume comprised of two bulk phases and an internal, singular interface such that $\Omega = \Omega_+ \cup \Omega_- \cup \Sigma$, or, using the short-hand notation $\Omega_\pm := \Omega_+ \cup \Omega_-$, we equivalently write $\Omega = \Omega_\pm \cup \Sigma$ (Fig. 2.4). In an attempt to derive a transport theorem for a material volume with an internal interface, we use the additive decomposition

---

[1] A singular interface with interface-excess density is often referred to as Gibbs dividing plane or Gibbs model following the pioneering work of J.W.Gibbs. For a rigorous definition of interface-excess density, the interested reader is referred to Edwards et al. [63, § 15].

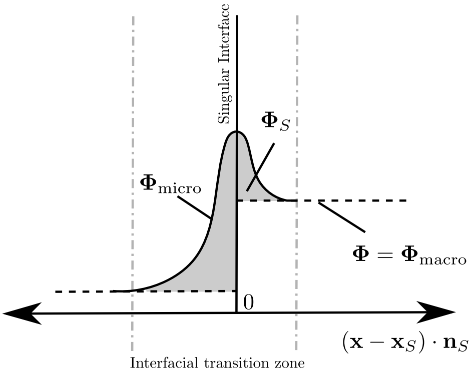
Singular Interface
$\mathbf{\Phi}_S$
$\mathbf{\Phi}_{\mathrm{micro}}$
$\mathbf{\Phi} = \mathbf{\Phi}_{\mathrm{macro}}$
0
$(\mathbf{x} - \mathbf{x}_S) \cdot \mathbf{n}_S$
Interfacial transition zone

Figure 2.5: Schematic of a microscopic, continuous density field $\mathbf{\Phi}_{\mathrm{micro}}$ and a macroscopic, discontinuous representation $\mathbf{\Phi}_{\mathrm{macro}}$ in the vicinity of an interface plotted in direction of the normal $\mathbf{n}_S$ according to Edwards et al. [63, see Fig. (3.6-3)]. In continuum models, the integral of the shaded region, termed interface-excess density $\mathbf{\Phi}_S$, is assigned to a singular interface.

$$
\begin{aligned}
\frac{\mathrm{d}}{\mathrm{d}t}\left[\int_{\Omega} \mathbf{\Phi}_{\mathrm{micro}} \mathrm{d}v\right] &= \frac{\mathrm{d}}{\mathrm{d}t}\left[\int_{\Omega_\pm} \mathbf{\Phi}\,\mathrm{d}v + \int_{\Sigma} \mathbf{\Phi}_S\,\mathrm{d}a_S\right] \\
&= \frac{\mathrm{d}}{\mathrm{d}t}\int_{\Omega_\pm} \mathbf{\Phi}\,\mathrm{d}v + \frac{\mathrm{d}_S}{\mathrm{d}t}\int_{\Sigma} \mathbf{\Phi}_S\,\mathrm{d}a_S, \qquad (2.36)
\end{aligned}
$$

where it has been taken into account that the material time derivative $\mathrm{d}/\mathrm{d}t$ is equivalent to the material surface time derivative $\mathrm{d}_S/\mathrm{d}t$ when the operator acts on surface-fixed material points. For the sake of clarity, in the following, each term on the RHS of Eq. (2.36) is reformulated individually. To start with, the rate of change in $\Omega_\pm$ is further decomposed into

$$
\frac{\mathrm{d}}{\mathrm{d}t}\int_{\Omega_\pm} \mathbf{\Phi}\,\mathrm{d}v = \frac{\mathrm{d}}{\mathrm{d}t}\int_{\Omega_+} \mathbf{\Phi}\,\mathrm{d}v + \frac{\mathrm{d}}{\mathrm{d}t}\int_{\Omega_-} \mathbf{\Phi}\,\mathrm{d}v. \qquad (2.37)
$$

Application of the single-phase transport theorem (2.9) to each of the terms on the RHS of Eq. (2.37) yields

$$
\begin{aligned}
\frac{\mathrm{d}}{\mathrm{d}t}\int_{\Omega_\pm} \mathbf{\Phi}\mathrm{d}v = &\int_{\Omega_+} \frac{\partial \mathbf{\Phi}}{\partial t}\,\mathrm{d}v + \int_{\Gamma_+} (\mathbf{\Phi}\cdot\mathbf{n})\,\mathbf{u}\,\mathrm{d}a + \int_{\Gamma_{S,+}} (\mathbf{\Phi}\cdot\mathbf{n})\,\mathbf{u}\,\mathrm{d}a \\
&+ \int_{\Omega_-} \frac{\partial \mathbf{\Phi}}{\partial t}\,\mathrm{d}v + \int_{\Gamma_-} (\mathbf{\Phi}\cdot\mathbf{n})\,\mathbf{u}\,\mathrm{d}a + \int_{\Gamma_{S,-}} (\mathbf{\Phi}\cdot\mathbf{n})\,\mathbf{u}\,\mathrm{d}a, \qquad (2.38)
\end{aligned}
$$

where surface fluxes across $\partial\Omega_+$ and $\partial\Omega_-$ have been decomposed into fluxes across the outer boundaries Γ_+ and Γ_- as well as fluxes across the internal interfaces $\Gamma_{S,+}$ and $\Gamma_{S,-}$. Considering the relations (2.34)-(2.35) and incorporating the interface velocity $\mathbf{u}_S$, Eq. (2.38) is alternatively written

$$\begin{aligned}\frac{\mathrm{d}}{\mathrm{d}t}\int_{\Omega_\pm}\mathbf{\Phi}\mathrm{d}v = \int_{\Omega_+}\frac{\partial\mathbf{\Phi}}{\partial t}\,\mathrm{d}v + \int_{\Gamma_+}(\mathbf{\Phi}\cdot\mathbf{n})\,\mathbf{u}\,\mathrm{d}a - \int_\Sigma\left(\mathbf{\Phi}^+\cdot\mathbf{n}_S\right)\mathbf{u}_S\,\mathrm{d}a_S \\ + \int_{\Omega_-}\frac{\partial\mathbf{\Phi}}{\partial t}\,\mathrm{d}v + \int_{\Gamma_-}(\mathbf{\Phi}\cdot\mathbf{n})\,\mathbf{u}\,\mathrm{d}a + \int_\Sigma\left(\mathbf{\Phi}^-\cdot\mathbf{n}_S\right)\mathbf{u}_S\,\mathrm{d}a_S,\end{aligned}$$

To adopt a concise notation, we may introduce the Hadamard jump operator

$$[\![\mathbf{\Phi}(\mathbf{x}_S,t)]\!] \coloneqq \lim_{\epsilon\to 0}\Big[\mathbf{\Phi}(\mathbf{x}_S+\epsilon\,\mathbf{n}_S,t)-\mathbf{\Phi}(\mathbf{x}_S-\epsilon\,\mathbf{n}_S,t)\Big] = \mathbf{\Phi}^+-\mathbf{\Phi}^-. \tag{2.39}$$

Using the jump operator, we finally write

$$\frac{\mathrm{d}}{\mathrm{d}t}\int_{\Omega_\pm}\mathbf{\Phi}\mathrm{d}v = \int_{\Omega_\pm}\frac{\partial\mathbf{\Phi}}{\partial t}\,\mathrm{d}v + \int_{\Gamma_\pm}(\mathbf{\Phi}\cdot\mathbf{n})\,\mathbf{u}\,\mathrm{d}a - \int_\Sigma[\![(\mathbf{\Phi}\cdot\mathbf{n}_S)\,\mathbf{u}_S]\!]\,\mathrm{d}a_S, \tag{2.40}$$

where the short-hand notation $\Gamma_\pm = \Gamma_+\cup\Gamma_-$.

Comparing Eq. (2.40) to its single-phase equivalent (2.9), an additional term is observed that accounts for the motion of the interfacial discontinuity within $\Omega_\pm$. In particular, it can be shown that Eq. (2.40) can be derived from the transport equation (2.7), when, instead of using the divergence theorem (2.8), the modified divergence theorem for material bodies with internal interfacial discontinuity

$$\int_{\Omega_\pm}\mathrm{div}\,(\bullet)\;\mathrm{d}v = \int_{\Gamma_\pm}(\bullet)^T\,\mathbf{n}\,\mathrm{d}a - \int_\Sigma[\![(\bullet)^T\,\mathbf{n}_S]\!]\,\mathrm{d}a_S \tag{2.41}$$

is used. The validity of Eq. (2.41) can be shown by applying a procedure analogous to what was used in Eqs. (2.38)-(2.40), i.e. additively decomposing surface integrals into integrals over outer surfaces and internal interface.

The second term on the RHS of Eq. (2.36) denotes the temporal rate of change of the total amount of interface-excess density $\mathbf{\Phi}_S$ contained within an interface Σ. The derivation of the surface transport theorem is conceptually analogous to the approach outlined in section 2.1.2. Introducing the non-zero surface Jacobian[1] J_S that maps areal elements of the referential configuration to areal elements of the current configuration, i.e. $\mathrm{d}a_S = J_S\mathrm{d}A_S$, the total amount of interface-excess density can be expressed with respect to the time-invariant reference configuration such that

$$\frac{\mathrm{d}_S}{\mathrm{d}t}\int_\Sigma\mathbf{\Phi}_S(\mathbf{x}_S,t)\,\mathrm{d}a_S = \int_{\Sigma_0}\frac{\mathrm{d}_S}{\mathrm{d}t}\Big[\hat{\mathbf{\Phi}}_S(\mathbf{X}_S)\,J_S(\mathbf{X}_S,t)\Big]\,\mathrm{d}A_S, \tag{2.42}$$

where $\hat{\mathbf{\Phi}}_S\left(\mathbf{X}_S, t\right) = \mathbf{\Phi}_S\left(\chi_S\left(\mathbf{X}_S, t\right), t\right) = \mathbf{\Phi}_S\left(\mathbf{x}_S, t\right)$ is referred to as material description of interface-excess density.

Using the product rule and the material surface time derivative of the surface Jacobian [see 63, Eq. (3.4-14)]

$$\frac{\mathrm{d}_S}{\mathrm{d}t} J_S\left(\mathbf{X}_S, t\right) = \operatorname{div}_S \mathbf{u}_S\left(\mathbf{x}_S, t\right) J_S\left(\mathbf{X}_S, t\right),$$

we rewrite Eq. (2.42) to yield

$$\frac{\mathrm{d}_S}{\mathrm{d}t} \int_\Sigma \mathbf{\Phi}_S \,\mathrm{d}a_S = \int_\Sigma \frac{\mathrm{d}_S}{\mathrm{d}t} \mathbf{\Phi}_S + \mathbf{\Phi}_S \operatorname{div}_S \mathbf{u}_S \,\mathrm{d}a_S. \tag{2.43}$$

Reformulating the material surface time derivative on the RHS of Eq. (2.43) according to Eq. (2.33), using the calculus identity

$$\operatorname{div}_S\left(\mathbf{\Phi}_S \otimes \mathbf{u}_S\right) = \mathbf{\Phi}_S \operatorname{div}_S \mathbf{u}_S + \operatorname{grad}_S \mathbf{\Phi}_S \cdot \mathbf{u}_S$$

as well as the divergence theorem for surfaces [see 62, § 3.4]

$$\begin{aligned}\int_\Sigma \operatorname{div}_S\left(\mathbf{\Phi}_S \otimes \mathbf{u}_S\right) \mathrm{d}a_S &= \int_{\partial\Sigma} \left(\mathbf{\Phi}_S \cdot \mathbf{b}_S\right) \mathbf{u}_S \,\mathrm{d}c_S + \int_\Sigma \operatorname{div}_S \mathbf{n}_S \left(\mathbf{\Phi}_S \cdot \mathbf{n}_S\right) \mathbf{u}_S \,\mathrm{d}a_S \\ &= \int_{\partial\Sigma} \left(\mathbf{\Phi}_S \cdot \mathbf{b}_S\right) \mathbf{u}_S \,\mathrm{d}c_S - \int_\Sigma \kappa \left(\mathbf{\Phi}_S \cdot \mathbf{n}_S\right) \mathbf{u}_S \,\mathrm{d}a_S, \quad (2.44)\end{aligned}$$

where the definition of the total curvature (2.31) has been used, an alternative form of the transport theorem is given as

---

[1] The surface Jacobian is defined $J_S \coloneqq \det_S \mathbf{F}_S$, where

$$\det{}_S \mathbf{F}_S \coloneqq \frac{\|\mathbf{F}_S \cdot \mathbf{G}_1 \times \mathbf{F}_S \cdot \mathbf{G}_2\|}{\|\mathbf{G}_1 \times \mathbf{G}_2\|},$$

and the surface Jacobian matrix

$$\mathbf{F}_S = \frac{\partial \mathbf{x}_S}{\partial \mathbf{X}_S} = \operatorname{Grad}_S \mathbf{x}_S$$

using

$$\operatorname{Grad}_S(\bullet) \coloneqq \operatorname{Grad}(\bullet) \cdot \left[\mathbf{I} - \mathbf{N}_S \otimes \mathbf{N}_S\right] = \sum_{a=1}^{3} \mathbf{e}_a \frac{\partial}{\partial X_a} \cdot \left[\mathbf{I} - \mathbf{N}_S \otimes \mathbf{N}_S\right] \otimes (\bullet).$$

For proofs of the above stated definitions, which are omitted herein for the sake of brevity, the reader is referred to Steinmann [193, § 3.1].

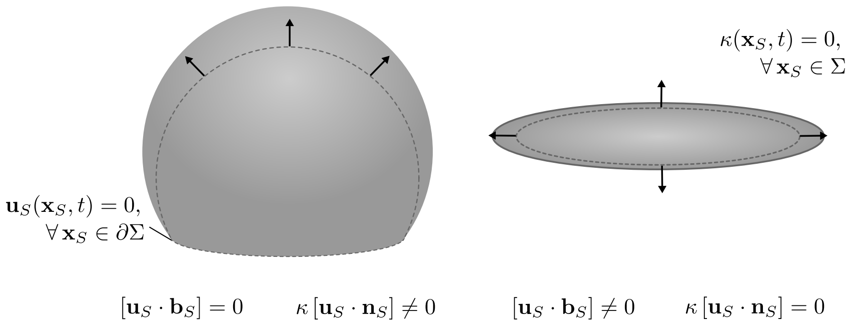
$\kappa(\mathbf{x}_S,t)=0,$
$\forall\,\mathbf{x}_S\in\Sigma$
$\mathbf{u}_S(\mathbf{x}_S,t)=0,$
$\forall\,\mathbf{x}_S\in\partial\Sigma$
$[\mathbf{u}_S\cdot\mathbf{b}_S]=0$
$\kappa\,[\mathbf{u}_S\cdot\mathbf{n}_S]\neq 0$
$[\mathbf{u}_S\cdot\mathbf{b}_S]\neq 0$
$\kappa\,[\mathbf{u}_S\cdot\mathbf{n}_S]=0$

Figure 2.6: Interpretation of flux terms occurring in the transport theorem for surfaces. For the deformation mode depicted on the LHS, the boundary curve integral in Eq. (2.45) vanishes. For the deformation mode depicted on the RHS, the second surface integral in Eq. (2.45) vanishes.

$$\frac{\mathrm{d}_S}{\mathrm{d}t}\int_\Sigma \mathbf{\Phi}_S\,\mathrm{d}a_S=\int_\Sigma\frac{\partial\mathbf{\Phi}_S}{\partial t}\,\mathrm{d}a_S-\int_\Sigma\kappa\,(\mathbf{\Phi}_S\cdot\mathbf{n}_S)\,\mathbf{u}_S\,\mathrm{d}a_S+\int_{\partial\Sigma}(\mathbf{\Phi}_S\cdot\mathbf{b}_S)\,\mathbf{u}_S\,\mathrm{d}c_S. \tag{2.45}$$

For a surface Σ bounded by the boundary curve $\partial\Sigma$, $\mathrm{d}c_S$ denotes the differential line element of the contour $\partial\Sigma$ and $\mathbf{b}_S$ denotes an outwardly directed, unit vector that is tangent to Σ and perpendicular to $\partial\Sigma$ (Fig. 2.4).

The convective flux terms occurring on the RHS of Eq. (2.45) can be geometrically interpreted. Indeed, the second term on the RHS of Eq. (2.45) is related to fluxes that appear normal to the interface Σ while the third term is related to fluxes that appear normal to the boundary curve $\partial\Sigma$ (Fig. 2.6). The temporal rate of change of the total amount of a density $\mathbf{\Phi}_S$ contained within Σ is thus observed equal to the sum of the surface integral of the local time derivative of $\mathbf{\Phi}_S$ and the convective fluxes in direction normal to the interface and tangent to the boundary curve $\partial\Sigma$.

2.2.3 General balance equations

As indicated earlier, for all multi-phase transport processes studied within this treatise, thermal effects are neglected and bulk liquid phases are considered non-polar. The set of balance equations is thus reduced to a balance of mass and a balance of linear momentum, i.e. we explicitly take into account transport of mass density ϱ and density of linear momentum $\varrho\,\mathbf{u}$. A crucial assumption which shall be applied hereinafter is that interface-excess mass density ϱ_S, i.e. the

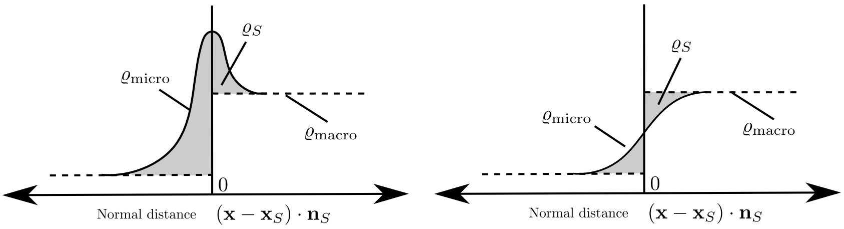
ϱ_S
ϱ_{micro}
ϱ_{macro}
0
Normal distance $(\mathbf{x}-\mathbf{x}_S)\cdot\mathbf{n}_S$
ϱ_S
ϱ_{micro}
ϱ_{macro}
0
Normal distance $(\mathbf{x}-\mathbf{x}_S)\cdot\mathbf{n}_S$

Figure 2.7: Schematic mass density concentration profiles plotted in direction of the normal $\mathbf{n}_S$ for a multi-phase system with non-negligible concentration of surfactants (left) and a system with negligible interface-excess mass density (right).

surface-specific residual difference between total microscopic mass density and discontinuous mass density representation $\int_\Omega \varrho_{\text{micro}}\mathrm{d}v - \int_\Omega \varrho_{\text{macro}}\mathrm{d}v$, is considered negligible. Absence of interface-excess mass density is motivated by assuming negligible concentration of any type of surface active material (surfactants) that might segregate to or be absorbed by internal interfaces (Fig. 2.7). Independent of the surfactant concentration, the latter assumption is expected to hold valid for transport processes that might be characterized as being quasi-static, i.e. negligible inertial effects as well as negligible dynamic perturbations from thermodynamic equilibrium.

The axiomatic requirement of conservation of total mass within an arbitrary material volume comprised of two bulk phases and an internal interface implies

$$\frac{\mathrm{d}}{\mathrm{d}t}\int_{\Omega_\pm} \varrho \mathrm{d}v + \frac{\mathrm{d}_S}{\mathrm{d}t}\int_\Sigma \varrho_S \,\mathrm{d}a_S = 0.$$

Using Eq. (2.40) and taking into account negligible interface-excess mass density, i.e. $\varrho_S = 0$, subsequently yields

$$\int_{\Omega_\pm} \frac{\partial \varrho}{\partial t}\,\mathrm{d}v + \int_{\Gamma_\pm} (\varrho\mathbf{u})\cdot\mathbf{n}\,\mathrm{d}a - \int_\Sigma [\![(\varrho\mathbf{u}_S)\cdot\mathbf{n}_S]\!]\,\mathrm{d}a_S = 0.$$

Reformulating the integral over the outer surface $\Gamma_\pm$ using the divergence theorem (2.41) for material volumes with internal interface yields

$$\int_{\Omega_\pm} \frac{\partial \varrho}{\partial t} + \operatorname{div}(\varrho\mathbf{u})\;\mathrm{d}v - \int_\Sigma [\![\varrho\,(\mathbf{u}-\mathbf{u}_S)\cdot\mathbf{n}_S]\!]\,\mathrm{d}a_S = 0. \tag{2.46}$$

Since Eq. (2.46) must be satisfied for any arbitrary surface Σ and volume $\Omega_\pm$, it may be localized, provided that mass density ϱ and velocity $\mathbf{u}$ are continuously defined in $\Omega_\pm$ and on Σ, respectively, such that

$$[\![\varrho\,(\mathbf{u}-\mathbf{u}_S)\cdot\mathbf{n}_S]\!]=0,\qquad\forall\,\mathbf{x}_S\in\Sigma,\tag{2.47}$$

and

$$\frac{\partial\varrho}{\partial t}+\operatorname{div}(\varrho\mathbf{u})=\dot{\varrho}+\varrho\operatorname{div}\mathbf{u}=0,\qquad\forall\,\mathbf{x}\in\Omega_{\pm}.\tag{2.48}$$

Equation (2.47) can be interpreted as the interface condition of vanishing mass transfer across the internal interface, or, in other words, the impermeable, material interface is neither a source nor a sink for mass density with respect to either of the adjacent bulk phases. We may reduce equation (2.47) to

$$\mathbf{u}_S\cdot\mathbf{n}_S=\mathbf{u}^+\cdot\mathbf{n}_S=\mathbf{u}^-\cdot\mathbf{n}_S,\qquad\forall\,\mathbf{x}_S\in\Sigma\tag{2.49}$$

which implies interfacial coupling of bulk fluid velocities in direction normal to the interface. Clearly, the latter leads to a no-penetration condition at static solid-fluid interfaces as introduced in section 2.1.5. Moreover, the local balance of mass (2.48) that applies to points of both adjacent bulk phases is equivalent to the single-phase continuity equation (2.11).

For the temporal rate of change of total linear momentum contained within a material volume with internal interface we axiomatically require

$$\frac{\mathrm{d}}{\mathrm{d}t}\int_{\Omega_\pm}\varrho\mathbf{u}\,\mathrm{d}v+\frac{\mathrm{d}}{\mathrm{d}t}\int_{\Sigma}\varrho_S\mathbf{u}_S\,\mathrm{d}a_S=\mathfrak{F}_{\Omega_\pm}+\mathfrak{F}_{\Gamma_\pm}+\mathfrak{F}_{\Sigma}+\mathfrak{F}_{\partial\Sigma}.\tag{2.50}$$

In equivalence to Eq. (2.12), $\mathfrak{F}_{\Omega_\pm}$ represents the total volume force acting on material points of the bulk phases. In equivalence to Eq. (2.13), $\mathfrak{F}_{\Gamma_\pm}$ represents the total contact force due to surface tractions acting on the outer surface $\Gamma_\pm$. Due to the presence of an internal interface, we additionally take into account the total contact force

$$\mathfrak{F}_{\partial\Sigma}:=\int_{\partial\Sigma}\mathbf{t}_b\,\mathrm{d}c_S=\int_{\partial\Sigma}\mathbf{b}_S\cdot\mathbf{\Pi}\,\mathrm{d}c_S.\tag{2.51}$$

The contact force $\mathfrak{F}_{\partial\Sigma}$ represents the flux of linear momentum across the boundary curve $\partial\Sigma$ of the internal interface, or, in other words, the effect of boundary curve tractions $\mathbf{t}_b$ acting on $\partial\Sigma$ (Fig. 2.4). Boundary curve tractions are related to the interfacial Cauchy stress tensor $\mathbf{\Pi}$ by means of the interfacial Cauchy theorem $\mathbf{t}_b:=\mathbf{b}_S\cdot\mathbf{\Pi}$. The particular structure of the second-order interfacial Cauchy stress tensor $\mathbf{\Pi}$ remains to be introduced using a constitutive material model. Equation (2.51) is the interface analog of the total bulk contact force (2.13).

Due to assuming negligible interface-excess mass density, total far field, or, volume forces $\mathfrak{F}_\Sigma$ that take effect at points of the interface are considered absent, i.e. $\mathfrak{F}_\Sigma = \mathbf{0}$. In the presence of surfactants and a resulting high mass concentration at points of the interface for instance, interfacial volume forces due to gravity have to be taken into account. In the presence of electrically charged surfactants, a far field magnetic field might render interfacial volume forces non-negligible as well. For negligible interface-excess mass density, the temporal rate of change of total interface-excess linear momentum, i.e. the second term on the LHS of Eq. (2.50), vanishes as well.

We reformulate the LHS of Eq. (2.50) to a form in which it is accessible to material point localization, i.e.

$$\begin{aligned}
\frac{\mathrm{d}}{\mathrm{d}t}\int_{\Omega_\pm} \varrho\mathbf{u}\,\mathrm{d}v &\overset{(2.40)}{=} \int_{\Omega_\pm} \frac{\partial(\varrho\mathbf{u})}{\partial t}\,\mathrm{d}v + \int_{\Gamma_\pm} (\varrho\mathbf{u}\otimes\mathbf{u})^T\,\mathbf{n}\,\mathrm{d}a - \int_\Sigma [\![(\varrho\mathbf{u}\cdot\mathbf{n}_S)\,\mathbf{u}_S]\!]\,\mathrm{d}a_S \\
&\overset{(2.41)}{=} \int_{\Omega_\pm} \frac{\partial(\varrho\mathbf{u})}{\partial t} + \operatorname{div}(\varrho\mathbf{u}\otimes\mathbf{u})\,\mathrm{d}v + \int_\Sigma [\![(\varrho\mathbf{u}\cdot\mathbf{n}_S)\,\mathbf{u}]\!] - [\![(\varrho\mathbf{u}\cdot\mathbf{n}_S)\,\mathbf{u}_S]\!]\,\mathrm{d}a_S \\
&= \int_{\Omega_\pm} \frac{\partial(\varrho\mathbf{u})}{\partial t} + \operatorname{div}(\varrho\mathbf{u}\otimes\mathbf{u})\,\mathrm{d}v + \int_\Sigma [\![\varrho\mathbf{u}\,(\mathbf{u}-\mathbf{u}_S)\cdot\mathbf{n}_S]\!]\,\mathrm{d}a_S \\
&\overset{(2.47)}{=} \int_{\Omega_\pm} \frac{\partial(\varrho\mathbf{u})}{\partial t} + \operatorname{div}(\varrho\mathbf{u}\otimes\mathbf{u})\,\mathrm{d}v \\
&\overset{(2.3)}{=} \int_{\Omega_\pm} \frac{\mathrm{d}(\varrho\mathbf{u})}{\mathrm{d}t} + \varrho\mathbf{u}\operatorname{div}\mathbf{u}\,\mathrm{d}v \\
&\overset{(2.48)}{=} \int_{\Omega_\pm} \varrho\dot{\mathbf{u}}\,\mathrm{d}v.
\end{aligned}$$

Reformulating the surface integral $\mathfrak{F}_{\Gamma_\pm}$ using the divergence theorem (2.41) and the boundary curve integral $\mathfrak{F}_{\partial\Sigma}$ using the divergence theorem for surfaces (2.44), the temporal rate of change of total linear momentum reads

$$\begin{aligned}
\int_{\Omega_\pm} \varrho\dot{\mathbf{u}}\,\mathrm{d}v = \int_{\Omega_\pm} \varrho\mathbf{b}\,\mathrm{d}v + \int_{\Omega_\pm} \operatorname{div}\mathbf{T}\,\mathrm{d}v \\
+ \int_\Sigma [\![\mathbf{T}\cdot\mathbf{n}_S]\!]\,\mathrm{d}a_S + \int_\Sigma \operatorname{div}_S\boldsymbol{\Pi}\,\mathrm{d}a_S + \int_\Sigma \kappa\boldsymbol{\Pi}\cdot\mathbf{n}_S\,\mathrm{d}a_S. \qquad (2.52)
\end{aligned}$$

Since Eq. (2.52) must be satisfied for any arbitrary choice of Σ and $\Omega_\pm$, it may be localized, provided that mass density ϱ, velocity $\mathbf{u}$ and volumetric force density $\mathbf{b}$ are continuously defined in $\Omega_\pm$ and on Σ, respectively, such that

$$-[\![\mathbf{T}\cdot\mathbf{n}_S]\!] = \operatorname{div}_S\boldsymbol{\Pi} + \kappa\boldsymbol{\Pi}\cdot\mathbf{n}_S, \qquad \forall\,\mathbf{x}_S\in\Sigma, \qquad (2.53)$$

and

$$\varrho\dot{\mathbf{u}} = \operatorname{div}\mathbf{T} + \varrho\mathbf{b}, \qquad \forall\,\mathbf{x} \in \Omega_{\pm}. \tag{2.54}$$

As expected, the local balance of linear momentum (2.54) applicable to all points of both bulk fluid phases is equivalent to the single-phase balance of linear momentum. On the other hand, in the presence of internal interfacial stresses, the interfacial balance of linear momentum (2.53) constitutes an interfacial jump in surface tractions exerted by bulk fluid phases onto each other that is balanced by internal interfacial forces.

The set of unknown scalar values at the interface is comprised of the unique components of the bulk Cauchy stress tensors $(\mathbf{T}^{+}, \mathbf{T}^{-})$, interfacial Cauchy stress tensor $\mathbf{\Pi}$ and velocities $(\mathbf{u}^{+}, \mathbf{u}^{-})$. Equating the number of unknowns at the interface to the number of available interfacial balance equations, it is realized that, on the one hand, a constitutive equation is required for the unknown interfacial Cauchy stress tensor $\mathbf{\Pi}$, and, on the other hand, two additional scalar boundary conditions are required [see 185, § 2.4.2]. The missing two scalar equations relate components of bulk fluid velocities tangent to the interface to each other. We recall that the coupling (2.49) of components of bulk fluid velocities normal to the interface results from local mass balance at material interfaces. On the contrary, the interfacial jump condition

$$[\![\mathbf{u} \cdot \mathbf{I}_S]\!] = \mathbf{0}, \qquad \forall\,\mathbf{x}_S \in \Sigma, \tag{2.55}$$

which requires tangential components of bulk velocities to be continuous across the interface, represents a kinematic assumption. For justification of the assumption (2.55), the reader is referred to Shikhmurzaev [see 185, § 4.3] and Barenblatt & Chernyi [11] where Eq. (2.55) is shown equivalent to the assumption that the interface is neither a source nor a sink for moment of momentum density of bulk fluid phases.

2.2.4 Constitutive equations

We introduce the constitutive equation that determines the interfacial Cauchy stress tensor $\mathbf{\Pi}$. We first consider the interface to be in a state in which there is no intrinsic motion of surface-fixed material points, i.e. we consider the relative motion $\mathbf{u}_S(\mathbf{x}_{S,1}) - \mathbf{u}_S(\mathbf{x}_{S,2}) = \mathbf{0}$ for all arbitrary points $\mathbf{x}_{S,1}$ and $\mathbf{x}_{S,2}$ of Σ. For such a state of intrinsic hydrodynamic equilibrium, the stress tensor $\mathbf{\Pi}$ is physically required homogeneous, isotropic with respect to all directions tangent to the interface and invariant under rigid body motion of the interface. Hence, in equivalence to Eq. (2.16), the equilibrium part of $\mathbf{\Pi}$ must be of general form

$$\boldsymbol{\Pi}_{\mathrm{eq}} = \sigma \mathbf{I}_S, \tag{2.56}$$

where σ, with unit of force per unit length, is referred to as interfacial tension. Recalling the definition (2.29) of the surface identity tensor $\mathbf{I}_S$, the equilibrium part $\boldsymbol{\Pi}_{\mathrm{eq}}$ is observed to induce a tension of magnitude σ at all points of the interface Σ acting in every direction tangent to it. In other words, if $\mathbf{g}_t$ is a normalized, but otherwise arbitrary linear combination of the covariant basis vectors $\mathbf{g}_1$ and $\mathbf{g}_2$, i.e. a unit vector tangent to the interface, the stress $\mathbf{g}_t \cdot \boldsymbol{\Pi}_{\mathrm{eq}} \cdot \mathbf{g}_t$ is equal to σ. For the isothermal processes considered herein, a dependency of σ on temperature is not considered. Moreover, in the absence of surfactants, which tend to accumulate at interfaces and decrease the effective interfacial tension, σ is considered constant in time and of equal magnitude for all points of a common interface.

While pressure can be interpreted a force per unit area that opposes local volumetric compression, interfacial tension can be interpreted a force per unit length that opposes local increase of interfacial area. In contrast to molecules of bulk phases that experience a vanishing net cohesive force due to isotropic interaction with neighboring molecules of the same phase only, molecules in the vicinity of material interfaces experience an asymmetric action of cohesive forces due to interaction with bulk molecules of different phases. The latter forms the molecular origin of interfacial tension.

In analogy to the additive split of the Cauchy stress tensor into an equilibrium and non-equilibrium part, we may additively split the interfacial Cauchy stress tensor $\boldsymbol{\Pi} = \boldsymbol{\Pi}_{\mathrm{eq}} + \boldsymbol{\Pi}_{\mathrm{neq}}$. However, for negligible interface-excess mass density, the non-equilibrium interfacial stress tensor $\boldsymbol{\Pi}_{\mathrm{neq}}$ is generally considered negligible. Setting $\boldsymbol{\Pi} = \boldsymbol{\Pi}_{\mathrm{eq}}$, we reformulate the interfacial balance of linear momentum (2.53). In particular, taking into account that, by definition, $\boldsymbol{\Pi}_{\mathrm{eq}} \cdot \mathbf{n}_S = \mathbf{0}$ and using the identity (2.32), Eq. (2.53) reads

$$-[\![\mathbf{T} \cdot \mathbf{n}_S]\!] = \operatorname{div}_S \boldsymbol{\Pi} = \operatorname{grad}_S \sigma + \sigma \kappa \mathbf{n}_S, \qquad \forall\, \mathbf{x}_S \in \Sigma, \tag{2.57}$$

The interfacial jump in tractions is thus observed to be comprised of two parts: The first term on the RHS of Eq. (2.57), the so-called Marangoni force, represents a force that, by definition (2.30) of grad_S, acts entirely in a direction tangent to the interface and vanishes for spatially constant values of σ. On the other hand, the second term on the RHS of Eq. (2.57), the so-called Young-Laplace force, represents a force that acts entirely in direction of the unit normal to the interface. Assuming interfacial tension constant in space and substituting the definitions (2.22), (2.16) and (2.39) into Eq. (2.57) finally yields

$$\left(\mathbf{T}^{+}_{\text{neq}} - \mathbf{T}^{-}_{\text{neq}}\right) \cdot \mathbf{n}_S + \left(p^{-} - p^{+} + \sigma\kappa\right) \mathbf{n}_S = \mathbf{0}, \qquad \forall\, \mathbf{x}_S \in \Sigma. \tag{2.58}$$

The first term in Eq. (2.58) implies continuity of tangential viscous stresses across the interface. The second term in Eq. (2.58) introduces a pressure jump condition across the interface due to the concentrated interfacial force per unit area $\sigma\kappa\mathbf{n}_S$ acting normal to the interface. In equilibrium, viscous stresses are absent and Eq. (2.58) reduces to the Young-Laplace equation

$$p^{+}_{\text{eq}} - p^{-}_{\text{eq}} = \sigma\kappa, \qquad \forall\, \mathbf{x}_S \in \Sigma, \tag{2.59}$$

which relates the equilibrium pressure discontinuity at interfaces between two bulk fluid phases to total curvature κ of the interface. The pressure jump in Eq. (2.59) is referred to as microscopic capillary pressure $p_C := p^{+} - p^{-}$. Since in hydrostatic equilibrium pressure fields must be homogeneous within each bulk phase, Eq. (2.59) implies that geometric properties of interfaces in equilibrium are such that total curvatures are equal for all points of the interface, i.e. $\kappa = 1/R =$ const., where R is referred to as radius of curvature. Considering a droplet fully immersed in another fluid, the latter gives rise to the spherical shape of droplets in equilibrium.

2.3 Immersed boundary formulation

The Gibbs convention of singular interfaces leads to interfacial balance equations that may be regarded boundary conditions with respect to the primary variables of the bulk phase balance equations. Hereafter, interfacial balance equations are also referred to as interfacial jump conditions to indicate that the interface resembles a singular source or sink for the considered density field. As apparent later, from a numerical point of view, it is convenient to immerse interfacial jump conditions into the bulk balance equations in terms of a singular source term that is localized to points of the interface. The resulting balance equations with immersed singular sources are referred to as whole-domain balance equations and apply to points of the entire domain $\Omega = \Omega_{\pm} \cup \Sigma$. For all points $\mathbf{x} \in \Omega$ we define their normal distance to the interface

$$n_S\left(\mathbf{x}\right) := \left(\mathbf{x} - \mathbf{x}_S\right) \cdot \mathbf{n}_S\left(\mathbf{x}_S\right),$$

such that $\mathbf{x} = \mathbf{x}_S + n_S\mathbf{n}_S$. Immersion of singular sources is subsequently achieved using a Dirac delta distribution that is supported on points of the interface only, i.e.

$$\delta_S(\mathbf{x}) := \delta(n_S) = \begin{cases} 1 & \text{if } \mathbf{x} \in \Sigma \\ 0 & \text{if } \mathbf{x} \in \Omega_\pm \end{cases} . \tag{2.60}$$

The key property of the interface Dirac delta distribution (2.60) for its use regarding jump condition immersion is that we may relate surface integrals over Σ to volume integrals over the entire domain Ω [178], such that

$$\int_\Omega \mathbf{\Phi}(\mathbf{x})\, \delta_S(\mathbf{x})\, \mathrm{d}v = \int_\Sigma \mathbf{\Phi}(\mathbf{x})\, \mathrm{d}a_S, \tag{2.61}$$

where $\mathbf{\Phi}$ denotes a generic field of arbitrary rank. The method of immersing boundary conditions in fluid mechanics using a Dirac delta distribution is called immersed boundary method following the pioneering work Peskin [158]. For the volume integral on the LHS of Eq. (2.61) to be accessible to numerical quadrature, the Dirac distribution δ_S is typically replaced with a regularized, smooth distribution as defined in section 2.3.5.

2.3.1 Whole-domain balance of mass

The whole-domain balance of mass is formulated by immersion of the interfacial mass density jump condition (2.47) such that

$$\int_{\Omega_\pm} \frac{\partial \varrho}{\partial t} + \operatorname{div}(\varrho \mathbf{u})\, \mathrm{d}v = -\int_\Omega [\![\varrho(\mathbf{u} - \mathbf{u}_S) \cdot \mathbf{n}_S]\!] \delta_S\, \mathrm{d}v = 0. \tag{2.62}$$

Since the material interface is neither a source nor a sink for mass density localization of Eq. (2.62) yields

$$\dot{\varrho} + \varrho \operatorname{div} \mathbf{u} = 0, \qquad \forall\, \mathbf{x} \in \Omega, \tag{2.63}$$

which implies that, for material interfaces, the general continuity equation (2.11) applies to all points of the whole-domain.

2.3.2 Whole-domain balance of linear momentum

The whole-domain balance of linear momentum is formulated by immersion of the interfacial linear momentum density jump condition (2.53) such that

$$\begin{aligned} \int_{\Omega_\pm} \varrho \dot{\mathbf{u}} - \varrho \mathbf{b} - \operatorname{div} \mathbf{T}\, \mathrm{d}v &= -\int_\Omega [\![\mathbf{T} \cdot \mathbf{n}_S]\!] \delta_S\, \mathrm{d}v \\ &= \int_\Omega (\operatorname{div}_S \mathbf{\Pi} + \kappa \mathbf{\Pi} \cdot \mathbf{n}_S)\, \delta_S\, \mathrm{d}v. \end{aligned}$$

Incorporating the constitutive relation (2.56) and localizing to a material point yields

$$\varrho\dot{\mathbf{u}} = \operatorname{div}\mathbf{T} + \varrho\mathbf{b} + \operatorname{div}\left(\mathbf{\Pi}\delta_S\right), \qquad \forall\,\mathbf{x} \in \Omega, \tag{2.64}$$

or, for an interfacial tension σ constant in space and time,

$$\varrho\dot{\mathbf{u}} = \operatorname{div}\mathbf{T} + \varrho\mathbf{b} + \sigma\kappa\mathbf{n}_S\delta_S, \qquad \forall\,\mathbf{x} \in \Omega. \tag{2.65}$$

In the above, the surface divergence of the interfacial stress tensor has been rewritten

$$\operatorname{div}_S\left(\mathbf{\Pi}\right)\delta_S = \operatorname{div}\left(\mathbf{\Pi}\delta_S\right), \tag{2.66}$$

which holds since the normal projection of the interfacial Cauchy stress tensor $(\sigma\mathbf{I}_S)\cdot\mathbf{n}_S$ vanishes and, furthermore, the distribution δ_S is only supported on Σ.

Hence, the interfacial jump in tractions takes the form of the volumetric force density

$$\mathbf{f}_S \coloneqq \operatorname{div}\left(\mathbf{\Pi}\delta_S\right), \tag{2.67}$$

or, alternatively,

$$\mathbf{f}_S \coloneqq \sigma\kappa\mathbf{n}_S\delta_S. \tag{2.68}$$

The action of the force density $\mathbf{f}_S$ is restricted to the interface Σ by virtue of the distribution δ_S.

The use of Eq. (2.67) rather than Eq. (2.68) avoids the computation of the total curvature κ, which otherwise would require the evaluation of higher order spatial derivatives potentially prone to numerical noise [30, 141]. Moreover, errors that arise in the numerical estimation of total curvature lead to violation of local linear momentum conservation. In particular, for erroneous curvature computations, the microscopic capillary pressure p_C is locally not equilibrated by interfacial tension. Unbalanced pressure gradients subsequently cause unphysical fluid motion, also referred to as spurious or parasitic currents [83, 212].

On the other hand, the interfacial stress tensor $\mathbf{\Pi}$ can be conveniently embedded into the conservation form

$$\frac{\partial\left(\varrho\mathbf{u}\right)}{\partial t} + \operatorname{div}\left(\varrho\mathbf{u}\otimes\mathbf{u} - \mathbf{T} + \mathbf{\Pi}\delta_S\right) = \mathbf{0}, \tag{2.69}$$

where the volumetric force density $\mathbf{b}$ has been omitted. Using Eq. (2.69), the computation of curvature is avoided. Furthermore, using the above conservation form, it is possible to construct numerical quadrature schemes that are compliant with linear momentum conservation.

2.3.3 Whole-domain balance of moment of momentum

We consider the interface to be neither a source nor a sink for moment of momentum density of bulk fluid phases. As a result, for which a rigorous derivation is omitted herein, the whole-domain balance of moment of momentum requires bulk Cauchy stress tensors to be symmetric, i.e. $\mathbf{T} = \mathbf{T}^T$. Furthermore, if the evolution of fluid flow governed by the above whole-domain balance equations (2.63) and (2.64) is free of shear stress singularities, the kinematic assumption (2.55) is intrinsically satisfied [see 185, § 4.3].

2.3.4 Governing dimensionless numbers

Introducing the set of dimensionless variables

$$\bar{\mathbf{u}} = \frac{\mathbf{u}}{U_{\mathrm{ref}}},\ \bar{\mathbf{x}} = \frac{\mathbf{x}}{L_{\mathrm{ref}}},\ \bar{t} = \frac{t}{L_{\mathrm{ref}}/U_{\mathrm{ref}}},\ \bar{\mu} = \frac{\mu}{\mu_{\mathrm{ref}}},\ \bar{\varrho} = \frac{\varrho}{\varrho_{\mathrm{ref}}},\ \bar{p} = \frac{p}{\varrho_{\mathrm{ref}} U_{\mathrm{ref}}^2},$$

where characteristic velocity U_{ref}, characteristic length scale L_{ref}, reference viscosity μ_{ref} and reference mass density ϱ_{ref} must be suitably chosen regarding the boundary value problem at hand, the non-dimensional whole-domain balance of linear momentum (2.65) with volume forces omitted is written [83]

$$\frac{\partial\left(\bar{\varrho}\bar{\mathbf{u}}\right)}{\partial t} + \operatorname{div}\left(\bar{\varrho}\bar{\mathbf{u}} \otimes \bar{\mathbf{u}}\right) = \frac{1}{\mathrm{Re}} \operatorname{div}\left(\bar{\mu}\operatorname{grad}\bar{\mathbf{u}} + \bar{\mu}\operatorname{grad}^T\bar{\mathbf{u}}\right) + \frac{1}{\mathrm{ReCa}}\kappa\mathbf{n}_S\delta_S - \operatorname{grad}\bar{p}.$$

It is emphasized that the pressure field has been non-dimensionalized with the characteristic pressure $\varrho_{\mathrm{ref}} U_{\mathrm{ref}}^2$, whereas for creeping flow absent of inertia forces a more suitable choice for the characteristic pressure is $L_{\mathrm{ref}}/(\mu_{\mathrm{ref}} U_{\mathrm{ref}})$. For non-vanishing effects of inertia, however, dimensionless numbers governing capillary flow are the Reynolds number

$$\mathrm{Re} := \frac{\varrho_{\mathrm{ref}} U_{\mathrm{ref}} L_{\mathrm{ref}}}{\mu_{\mathrm{ref}}} \tag{2.70}$$

and the capillary number

$$\mathrm{Ca} := \frac{\mu_{\mathrm{ref}} U_{\mathrm{ref}}}{\sigma}.$$

While the Reynolds number represents the ratio of inertia to viscous forces, the capillary number represents the ratio of viscous to interfacial tension forces. In the limit of Re → 0 and Ca → 0, interfacial effects dominate resulting in a so-called mean curvature flow, i.e. the flow field evolves such that the curvature κ of an interface is constant and always compliant with the Young-Laplace equation (2.77). The evolution of mean curvature flows can be described as a surface minimization problem if the homogeneous bulk pressures are known and boundary conditions can be specified with respect to the boundary curve $\partial\Sigma$. In the limit of $\mathrm{Re} \to \infty$, inertia effects dominate resulting in an inviscid flow governed by the conservative Euler equations $\varrho\dot{\mathbf{u}} = -\operatorname{grad} p + \mathbf{b}$. In the limit of $\mathrm{Re} \to 0$ and $\mathrm{Ca} \to \infty$, viscous momentum diffusion dominates resulting in a laminar, creeping flow governed by the Stokes equations which are obtained by omitting the non-linear convective term $\operatorname{div}(\varrho\mathbf{u} \otimes \mathbf{u})$ from Eq. (2.28).

2.3.5 Continuum surface force method

The continuum surface force method (CSF) as introduced by Brackbill et al. [30] and the continuum surface stress method (CSS) as introduced by Lafaurie et al. [115] are computational methods to incorporate the interfacial force density $\mathbf{f}_S$ into the discrete, numerical quadrature scheme. While the CSF method represents $\mathbf{f}_S$ by the non-conservation form (2.68), the CSS method represents $\mathbf{f}_S$ by the conservation form (2.67). Despite the latter distinction, the underlying concept of introducing a smooth distribution $\tilde{\delta}_S$ to replace the singular surface Dirac distribution δ_S is common to both methods. In particular, the modified surface Dirac distribution $\tilde{\delta}_S$ is constructed such that it is compactly supported on a bounded domain $\tilde{\Sigma}$ that encloses the interface, i.e. $\Sigma \subset \tilde{\Sigma}$. Applications of the CSF and CSS method can be found in the context of various numerical methods including Finite Differences [30, 115], Finite Volumes [68, 69, 167, 168, 178], Finite Elements [157] and Smoothed Particle Hydrodynamics [1, 31, 99, 141].

We define a Heaviside step function $C(\mathbf{x})$, or, hereafter referred to as phase indicator field, that exhibits a unit jump across the interface Σ following

$$C\left(\mathbf{x}\right) = \begin{cases} 0, & \text{if } \mathbf{x} \in \Omega_-, \\ 1, & \text{if } \mathbf{x} \in \Omega_+, \\ 0.5, & \text{if } \mathbf{x} \in \Sigma. \end{cases}$$

For the purpose of regularization, the phase indicator field is typically smoothed by means of a convolution interpolation [30, 115, 178] or linearly interpolated [68, 69] between collocation points of the numerical method. In particular, the convolution-based, smooth approximation $\tilde{C}(\mathbf{x})$ is given as

$$\tilde{C}\left(\mathbf{x}\right) = \int_{\Omega} C\left(\mathbf{x}'\right) W\left(\mathbf{x} - \mathbf{x}', h\right) \mathrm{d}v, \quad \forall\, \mathbf{x} \in \Omega, \tag{2.71}$$

where the smooth kernel function W is required to have compact support with h representing a characteristic finite width of the compact support. Furthermore,

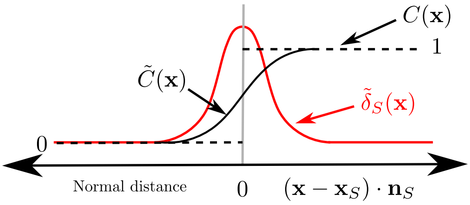
$C(\mathbf{x})$
1
$\tilde{C}(\mathbf{x})$
$\tilde{\delta}_S(\mathbf{x})$
0
Normal distance
0
$(\mathbf{x}-\mathbf{x}_S)\cdot\mathbf{n}_S$

Figure 2.8: Schematic representation of the phase indicator field $C(\mathbf{x})$, its smooth approximation $\tilde{C}(\mathbf{x})$ and modified surface Dirac distribution $\tilde{\delta}_S(\mathbf{x})$.

the kernel function shall satisfy the Dirac delta property

$$\lim_{h\to 0} W(\mathbf{x},h) = \delta(\mathbf{x}),$$

such that the sharp interface limit is recovered for increasing numerical resolution. For a finite length h, on the other hand, the kernel function shall moreover satisfy the normalization condition $\int_\Omega W(\mathbf{x},h)\,\mathrm{d}v = 1$ as to reproduce the step function. For computational purposes, the length scale h is in the order of the length scale of numerical resolution. Due to the equivalence of the above convolution-based approximation to the reproducing kernel approximation of the Smoothed Particle Hydrodynamics method, the reader is referred to chapter 3 for further discussion on the properties of Eq. (2.71).

By virtue of Eq. (2.71), the unit jump is extended to the length scale of numerical resolution, turning the sharp interface into a numerically diffuse interface (Fig. 2.8). The modified surface Dirac distribution is then defined

$$\tilde{\delta}_S := \|\operatorname{grad}\tilde{C}(\mathbf{x})\|,$$

and the unit normal to the interface is approximated as

$$\mathbf{n}_S \approx \frac{\operatorname{grad}\tilde{C}(\mathbf{x})}{\|\operatorname{grad}\tilde{C}(\mathbf{x})\|}.$$

An approximation of the interfacial force density $\tilde{\mathbf{f}}_S \approx \mathbf{f}_S$ that is suitable for numerical quadrature is subsequently given as

$$\tilde{\mathbf{f}}_S := \operatorname{div}\left(\frac{\sigma}{\|\operatorname{grad}\tilde{C}(\mathbf{x})\|}\left[\mathbf{I}\|\operatorname{grad}\tilde{C}(\mathbf{x})\|^2 - \operatorname{grad}\tilde{C}(\mathbf{x})\otimes\operatorname{grad}\tilde{C}(\mathbf{x})\right]\right),$$

where the definition (2.29) of the surface identity tensor $\mathbf{I}_S$ has been substituted. The sharp interface limit is reached in the limit of increasing numerical resolution, i.e. $\lim_{h\to 0}\tilde{(\bullet)} = (\bullet)$ for all approximations $\tilde{(\bullet)} \in \{\tilde{\mathbf{f}}_S, \tilde{C}, \tilde{\delta}_S\}$. Hence, in an attempt to simplify notation, the tilde symbol that highlights smooth approximations is omitted hereafter.

2.4 Fundamentals of wetting and two-phase flow in porous media

In the following section, we introduce the balance equations that govern the isothermal flow of two immiscible Newtonian fluid phases through the pore space of a porous material. To this end, we make use of bulk balance equations as introduced in section 2.1, interfacial balance equations as introduced in section 2.2 and the immersed boundary formulation as introduced in section 2.3. For the purpose of introducing the specific notation for two-phase flow in porous media as used throughout the remainder of this thesis, however, the complete set of balance equations is shortly summarized hereafter. In the preceding sections 2.2 and 2.3, interface-excess quantities and interface-bound operators for a general surface Σ were highlighted by the subscript $(\cdot)_S$. In the following, on the other hand, the subscript $(\cdot)_{\alpha\beta}$ is instead used to highlight interfacial quantities for a specific interface $\Gamma_{\alpha\beta}$.

2.4.1 Introduction

The total domain of the porous material $\Omega \subseteq \mathbb{R}^d$, where d denotes the number of spatial dimensions, can be expressed as the union of the total fluid domain $\Omega_\mathfrak{f}$ and solid matrix domain $\Omega_\mathfrak{s}$, i.e. $\Omega := \Omega_\mathfrak{f} \cup \Omega_\mathfrak{s}$. The total fluid domain is further expressed as the union of both fluid phase domains, i.e $\Omega_\mathfrak{f} := \Omega_\mathfrak{n} \cup \Omega_\mathfrak{w}$, where $\Omega_\mathfrak{w}$ and $\Omega_\mathfrak{n}$ denote domains of wetting and non-wetting fluid phase, respectively. The internal boundary $\Gamma_{\mathfrak{f}\mathfrak{s}}$ between solid matrix and fluid domain is defined as the intersection $\Gamma_{\mathfrak{f}\mathfrak{s}} := \partial\Omega_\mathfrak{f} \cap \partial\Omega_\mathfrak{s}$. The distinctive property of two-phase flow is the presence of the interface $\Gamma_{\mathfrak{w}\mathfrak{n}} := \partial\Omega_\mathfrak{n} \cap \partial\Omega_\mathfrak{w}$ that separates both fluid phases (see Fig. 2.9). We hereafter refer to $\Gamma_{\mathfrak{w}\mathfrak{n}}$ as fluid-fluid interface or meniscus, whereas $\Gamma_{\mathfrak{f}\mathfrak{s}}$ is referred to as solid surface. The solid surface is furthermore expressed as the union $\Gamma_{\mathfrak{f}\mathfrak{s}} := \Gamma_{\mathfrak{w}\mathfrak{s}} \cup \Gamma_{\mathfrak{n}\mathfrak{s}}$, where the interfaces that are formed between each of the fluid phases and solid matrix $\Gamma_{\mathfrak{w}\mathfrak{s}} := \partial\Omega_\mathfrak{w} \cap \partial\Omega_\mathfrak{s}$ and $\Gamma_{\mathfrak{n}\mathfrak{s}} := \partial\Omega_\mathfrak{n} \cap \partial\Omega_\mathfrak{s}$ are differentiated from each other as to account for interfacial balance equations separately. Due to mutual immiscibility of bulk phases, all of the above interfaces represent impermeable material interfaces. We finally introduce the intersection of interfaces

$$\Upsilon := \partial\Gamma_{\mathfrak{w}\mathfrak{s}} \cap \partial\Gamma_{\mathfrak{n}\mathfrak{s}} \cap \partial\Gamma_{\mathfrak{w}\mathfrak{n}}$$

that defines the domain of three-phase contact lines. In analogy to the assumptions that were incorporated in section 2.2, for all material interfaces, we consider impermeability, interface-excess mass density negligible, interfacial far-

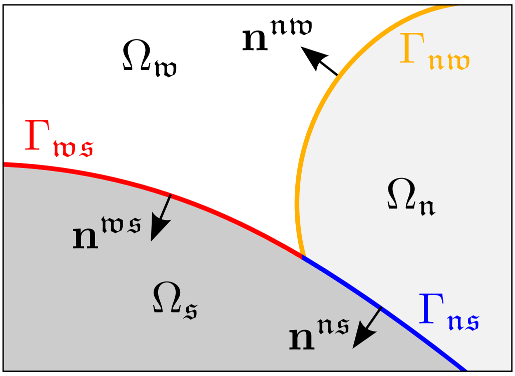

Figure 2.9: Schematic diagram introducing the notation for bulk phases, interfaces $\Gamma_{\alpha\beta}$ and interfacial unit normals $\mathbf{n}^{\alpha\beta}$ with respect to a three-phase system as encountered during multi-phase flow in porous media. The indicator $\alpha\beta \in \{\mathfrak{nw}, \mathfrak{ns}, \mathfrak{ws}\}$, whereas $\mathfrak{s}$ denotes the bulk solid phase and $\mathfrak{n}$ and $\mathfrak{w}$ denote bulk fluid phases.

field forces absent, boundary curve tractions to be given by Eq. (2.51) and interfacial Cauchy stress tensors equivalent to Eq. (2.56).

2.4.2 Overview of governing balance equations

Following Eqs. (2.27), mass and linear momentum balances that apply to points of both fluid phase domains $\Omega_\alpha \in \{\Omega_{\mathfrak{n}}, \Omega_{\mathfrak{w}}\}$ read

$$\dot{\varrho}^\alpha = -\varrho^\alpha \operatorname{div} \mathbf{u}_\alpha, \quad \forall \mathbf{x} \in \Omega_\alpha, \tag{2.72}$$

and

$$\varrho^\alpha \, \dot{\mathbf{u}}_\alpha = \operatorname{div} \mathbf{T}^\alpha = \operatorname{div} \mathbf{T}^\alpha_E - \operatorname{grad} p^\alpha \quad \forall \mathbf{x} \in \Omega_\alpha, \tag{2.73}$$

respectively, where ϱ^α denotes mass density, p^α denotes local pressure, $\mathbf{T}^\alpha_E$ denotes the viscous extra stress tensor, $\mathbf{T}^\alpha := -p^\alpha \mathbf{I} + \mathbf{T}^\alpha_E$ denotes the fluid Cauchy stress tensor and $\mathbf{u}_\alpha$ denotes local velocity. In the present work, simulations of two-phase flow in porous media are performed for negligible volumetric force densities $\mathbf{b}$. The latter is therefor omitted in the above balance of linear momentum (2.73). We model barotropic, quasi-incompressible fluid phases by taking into account the numerically stiff equation of state (2.20) that is parameterized in such a way that density fluctuations relative to initial fluid density ϱ^α_0 can be neglected (less than 5 %). Furthermore, both fluid phases are considered Newtonian fluids such that $\mathbf{T}^\alpha_E = \mu^\alpha (\operatorname{grad} \mathbf{u}_\alpha + \operatorname{grad}^T \mathbf{u}_\alpha)$ according to Eq. (2.24), where μ^α denotes dynamic viscosity.

Following the Gibbs convention introduced in section 2.2, interfaces are considered surfaces of vanishing thickness that divide bulk phases. The assumption of negligible interface-excess mass density is hereafter applied to the complete set of interfaces $\Gamma_{\alpha\beta} \in \{\Gamma_{\mathfrak{wn}}, \Gamma_{\mathfrak{ns}}, \Gamma_{\mathfrak{ws}}\}$. Following Eq. (2.39), we use the jump operator

$$[\![\bullet]\!] := (\bullet)^{\beta} - (\bullet)^{\alpha}, \quad \forall \mathbf{x}_S \in \Gamma_{\alpha\beta}$$

for a concise notation of the interfacial balance equations, where $(\bullet)^{\alpha}$ and $(\bullet)^{\beta}$ represent bulk properties at intersecting surfaces $\partial\Omega_{\alpha} \in \{\partial\Omega_{\mathfrak{n}}, \partial\Omega_{\mathfrak{w}}\}$ and $\partial\Omega_{\beta} \in \{\partial\Omega_{\mathfrak{n}}, \partial\Omega_{\mathfrak{s}}\}$, respectively, with $\beta \neq \alpha$. The spatial position $\mathbf{x}_S$ is occupied by a material point that is bound to the interface $\Gamma_{\alpha\beta}$ and the velocity of a fixed interfacial material point $\mathbf{u}_S := \dot{\mathbf{x}}_S$. Following Eq. (2.47), the interfacial balances of mass read

$$[\![\varrho\,(\mathbf{u} - \mathbf{u}_S) \cdot \mathbf{n}^{\alpha\beta}]\!] = 0, \quad \forall \mathbf{x}_S \in \Gamma_{\alpha\beta}, \tag{2.74}$$

where the unit normal $\mathbf{n}^{\alpha\beta}$ to the interface $\Gamma_{\alpha\beta}$ points from bulk phase Ω_{α} to bulk phase Ω_{β} (see Fig. 2.9). As discussed in section 2.2.3, Eq. (2.74) implies kinematic coupling of fluid velocities normal to the fluid-fluid interface such that $\mathbf{u}_{\mathfrak{n}} \cdot \mathbf{n}^{\mathfrak{wn}} = \mathbf{u}_{\mathfrak{w}} \cdot \mathbf{n}^{\mathfrak{wn}}, \forall \mathbf{x}_S \in \Gamma_{\mathfrak{wn}}$.

Following Eq. (2.57), interfacial balances of linear momentum

$$-[\![\mathbf{T} \cdot \mathbf{n}^{\alpha\beta}]\!] = \mathrm{div}^{\alpha\beta}\boldsymbol{\Pi}^{\alpha\beta}, \quad \forall \mathbf{x}_S \in \Gamma_{\alpha\beta} \tag{2.75}$$

constitute discontinuities in surface tractions exerted by adjacent bulk phases onto each other that are balanced by internal interfacial forces. Internal interfacial forces are expressed by the divergence of the interfacial Cauchy stress tensor $\boldsymbol{\Pi}^{\alpha\beta}$. As introduced in section 2.2.1, the surface divergence $\mathrm{div}^{\alpha\beta}$ is defined as the trace of the gradient matrix with the component normal to the interface being removed, i.e. $\mathrm{div}^{\alpha\beta}(\bullet) := \mathrm{grad}\,(\bullet) : \mathbf{I}^{\alpha\beta}$, where the surface identity tensor $\mathbf{I}^{\alpha\beta} := \mathbf{I} - \mathbf{n}^{\alpha\beta} \otimes \mathbf{n}^{\alpha\beta}$. Far field forces that take effect at points of the interface are considered absent. For negligible interface-excess mass density, the usual constitutive assumption is $\boldsymbol{\Pi}^{\alpha\beta} := \sigma^{\alpha\beta}\mathbf{I}^{\alpha\beta}$, which induces an interfacial tension of magnitude $\sigma^{\alpha\beta}$ at any point of the interface $\Gamma_{\alpha\beta}$ acting in every direction tangent to it (see section 2.2.4). Due to the absence of surfactants and thermal effects, interfacial tensions $\sigma^{\alpha\beta}(\mathbf{x}_S) = \sigma^{\alpha\beta}$ are considered constant in time and of equal magnitude for all points of a common interface. According to Eq. (2.31), the curvature measure $\kappa^{\alpha\beta} := -\mathrm{div}^{\alpha\beta}\,\mathbf{n}^{\alpha\beta}$, i.e. twice the mean curvature.

In equivalence to Eq. (2.58), an alternative expression of the interfacial balance of linear momentum (2.75) that is applicable to points of the fluid-fluid interface reads

$$\left(\mathbf{T}_E^{\mathfrak{n}} - \mathbf{T}_E^{\mathfrak{w}}\right) \cdot \mathbf{n}^{\alpha\beta} + \left(p^{\mathfrak{w}} - p^{\mathfrak{n}} + \sigma^{\mathfrak{wn}}\kappa^{\mathfrak{wn}}\right)\mathbf{n}^{\mathfrak{wn}} = \mathbf{0}, \quad \forall \mathbf{x}_S \in \Gamma_{\mathfrak{wn}}. \tag{2.76}$$

The first term in Eq. (2.76) implies continuity of tangential viscous extra stresses across the interface, hereafter referred to as interfacial viscous coupling. The second term in Eq. (2.76) introduces a pressure jump condition across the interface. In equilibrium, viscous stresses are absent and Eq. (2.76) reduces to the Young-Laplace equation

$$p^{\mathfrak{n}}_{\mathrm{eq}} - p^{\mathfrak{w}}_{\mathrm{eq}} = \sigma^{\mathfrak{wn}} \kappa^{\mathfrak{wn}}, \quad \forall \, \mathbf{x}_S \in \Gamma_{\mathfrak{wn}}. \tag{2.77}$$

The pressure jump in Eq. (2.77) is referred to as microscopic capillary pressure $p^{\mathrm{eq}}_C := p^{\mathfrak{n}}_{\mathrm{eq}} - p^{\mathfrak{w}}_{\mathrm{eq}}$. All interfaces are assumed sufficiently smooth and differentiable such that curvatures $\kappa^{\alpha\beta}$ are well-defined.

Following section 2.1.5, we consider the solid matrix static and rigid such that

$$\mathbf{u}_{\mathfrak{s}} = \mathbf{0}, \, \dot{\mathbf{u}}_{\mathfrak{s}} = \mathbf{0}, \text{ and } \dot{\varrho}^{\mathfrak{s}} = 0, \quad \forall \, (t, \mathbf{x}) \in (0, t_{\max}) \times \Omega_{\mathfrak{s}}. \tag{2.78}$$

As a result, shape and velocity of the solid surface are known and, together with interfacial balance equations, serve to prescribe boundary conditions with respect to fluid velocity. For a static solid surface, the interfacial balances of linear momentum (2.75) with respect to $\Gamma_{\mathfrak{ws}}$ and $\Gamma_{\mathfrak{ns}}$ can be used to determine the solid surface traction $\mathbf{T}^{\mathfrak{s}} \cdot \mathbf{n}^{\mathfrak{fs}}$ that constitutes a reaction force per unit of surface due to momentum exchange with fluid phase and solid-fluid interface. Despite the latter being irrelevant when solving for the unknown velocities of the fluid phase, our computational procedure indeed takes into account all interfacial balances (2.75) as to model the effects at points of contact lines $\mathbf{x}_C \in \Upsilon$ where all interfaces meet.

2.4.3 Initial and boundary conditions

Formulating an initial boundary value problem (IBVP) for the unknown fluid densities, fluid velocities and fluid-fluid interface velocities, we use the initial conditions

$$\mathbf{u}_\alpha(\mathbf{x}, t) = \mathbf{0}, \, \varrho^\alpha(\mathbf{x}, t) = \varrho^\alpha_0 \quad \forall \, \mathbf{x} \in \Omega_\alpha, t = 0, \tag{2.79}$$

as well as

$$\mathbf{u}_S(\mathbf{x}_S, t) = \mathbf{0} \quad \forall \, \mathbf{x}_S \in \Gamma_{\mathfrak{wn}}, t = 0. \tag{2.80}$$

Boundary conditions with respect to fluid velocity on $\partial\Omega_{\mathfrak{f}}$ are specified according to section 2.1.5. In particular, inner boundary conditions on solid surface $\Gamma_{\mathfrak{fs}}$ are comprised of no-penetration (2.25) and no-slip condition (2.26). Together, we require zero velocity magnitudes

$$\mathbf{u}_{\mathfrak{f}} = \mathbf{0}, \quad \forall \, (t, \mathbf{x}_S) \in (0, t_{\max}) \times \Gamma_{\mathfrak{fs}}. \tag{2.81}$$

Following Eq. (2.55), we assume tangential components of bulk fluid velocities continuous across the fluid-fluid interface such that

$$[\![\mathbf{u}\cdot\mathbf{I}^{\mathfrak{wn}}]\!] = \mathbf{0}, \quad \forall\,\mathbf{x}_S \in \Gamma_{\mathfrak{wn}}. \tag{2.82}$$

Boundary conditions with respect to velocity at points of the contact line Υ have to be modified since the no-slip assumption at points of a moving contact line results in diverging tangential stresses and unphysical energy dissipation as first shown by Huh & Scriven [101]. The latter singularity represents a limit to the continuum assumptions. Many continuum models have been proposed to resolve Huh and Scriven's paradox (see Bonn et al. [26, § 1]). In this work, we allow for a certain degree of tangential slip, as discussed in section 3.5 and Sivanesapillai et al. [187, § 2.9].

2.4.4 Unconstrained contact lines

The local balance of linear momentum at points of an unconstrained contact line implies that boundary curve tractions (2.51) of all adjacent interfaces are in mutual balance. The set of boundary curve tractions acting on a common point of the contact line form a concurrent force system. The balance of concurrent forces acting on an unconstrained contact line reads Kurzeja & Steeb [cf. 114, § 4]

$$\mathbf{b}^{\mathfrak{nw}}\cdot[\sigma^{\mathfrak{nw}}\mathbf{I}^{\mathfrak{nw}}] + \mathbf{b}^{\mathfrak{ns}}\cdot[\sigma^{\mathfrak{ns}}\mathbf{I}^{\mathfrak{ns}}] + \mathbf{b}^{\mathfrak{ws}}\cdot[\sigma^{\mathfrak{ws}}\mathbf{I}^{\mathfrak{ws}}] = \mathbf{0}, \qquad \forall\,\mathbf{x}\in\Upsilon, \tag{2.83}$$

where $\mathbf{b}^{\alpha\beta}$ denote outwardly directed, unit vectors, tangent to $\Gamma_{\alpha\beta}$ and perpendicular to $\partial\Gamma_{\alpha\beta}$ such that $\mathbf{b}^{\alpha\beta}\cdot\mathbf{n}^{\alpha\beta} = 0$ for all $\Gamma_{\alpha\beta}$. The identity $\mathbf{b}^{\alpha\beta}\cdot\mathbf{I}^{\alpha\beta} = \mathbf{b}^{\alpha\beta}$ holds since the unit normal $\mathbf{b}^{\alpha\beta}$ to the boundary curve is tangent to the interface $\Gamma_{\alpha\beta}$. Hence, Eq. (2.83) reduces to the intuitive balance of interfacial tensions

$$\sigma^{\mathfrak{nw}}\mathbf{b}^{\mathfrak{nw}} + \sigma^{\mathfrak{ns}}\mathbf{b}^{\mathfrak{ns}} + \sigma^{\mathfrak{ws}}\mathbf{b}^{\mathfrak{ws}} = \mathbf{0}, \qquad \forall\,\mathbf{x}\in\Upsilon \tag{2.84}$$

for an unconstrained contact line. For a formal derivation of the above, one may consider a control volume $\Omega_C \subset \Omega$ that encloses a subset of the contact line Υ such that $\Omega_C \cap \Upsilon \neq \emptyset$ (as depicted in Fig. 2.9). Omitting volumetric sources, the rate of change of total linear momentum contained within Ω_C is equal to the flux of momentum density across the surface of the control volume $\partial\Omega_C$ and boundary curves $\partial\Gamma^{\alpha\beta}$. Localizing the latter to a point $\mathbf{x}_C$ of the contact line, whereby all surface fluxes vanish due to being distributed on area elements, yields the above balance (2.83) of boundary curve tractions.

2.4.5 Constrained contact lines

It is emphasized that Eqs. (2.83) and (2.84) apply to unconstrained contact lines only. For a static solid surface on the other hand, the motion of the contact line is restricted to planes tangent to the solid surface. The latter gives rise to a constraining force[1] $F_C\mathbf{n}^{\mathfrak{fs}}$ understood as being exerted on the contact line by the solid phase [see 185, § 2.4.4]. The resulting balance of concurrent forces acting on a contact line that is constrained to a rigid solid surface thus reads (Fig. 2.10)

$$\sigma^{\mathfrak{wn}}\mathbf{b}^{\mathfrak{wn}} - \sigma^{\mathfrak{ns}}\mathbf{b}^{\mathfrak{ws}} + \sigma^{\mathfrak{ws}}\mathbf{b}^{\mathfrak{ws}} = F_C\mathbf{n}^{\mathfrak{fs}}, \quad \forall\, \mathbf{x}_C \in \Upsilon, \tag{2.85}$$

where $\sigma^{\alpha\beta}\mathbf{I}^{\alpha\beta} \cdot \mathbf{b}^{\alpha\beta} = \sigma^{\alpha\beta}\mathbf{b}^{\alpha\beta}$ has been taken into account as well as the geometric relations

$$\mathbf{n}^{\mathfrak{ns}} = \mathbf{n}^{\mathfrak{ws}} \quad \text{and} \quad \mathbf{b}^{\mathfrak{ns}} = -\mathbf{b}^{\mathfrak{ws}}, \qquad \forall\, \mathbf{x}_C \in \Upsilon,$$

applicable to points of a smooth and rigid solid surface. The contact angle Θ is defined as the angle formed between the local tangent to interface $\Gamma_{\mathfrak{wn}}$ and solid surface such that

$$\cos\Theta = \mathbf{b}^{\mathfrak{wn}} \cdot \mathbf{b}^{\mathfrak{ws}}, \qquad \forall\, \mathbf{x}_C \in \Upsilon.$$

Multiplying Eq. (2.85) with $-\mathbf{b}^{\mathfrak{ws}}$, i.e. considering the projection onto a plane tangent to the solid surface, and accounting for $\mathbf{n}^{\mathfrak{fs}} \cdot \mathbf{b}^{\mathfrak{ws}} = 0$ yields

$$\sigma^{\mathfrak{wn}}\cos\Theta = \sigma^{\mathfrak{ns}} - \sigma^{\mathfrak{ws}}, \quad \forall\, \mathbf{x}_C \in \Upsilon. \tag{2.86}$$

Equation (2.86) is referred to as Young's equation. In equilibrium and assuming solid phase rigidity, the geometric shape of the interface $\Gamma_{\mathfrak{nw}}$ in the vicinity of a contact line can thus be determined by Young-Laplace Eq. (2.77) and Young's Eq. (2.86) if microscopic capillary pressure p_C and the 2-tuple of material parameters $(\sigma^{\mathfrak{nw}}, \sigma^{\mathfrak{ws}} - \sigma^{\mathfrak{ns}})$ are known. Hence, only the difference in interfacial tensions $\sigma^{\mathfrak{ws}} - \sigma^{\mathfrak{ns}}$, rather than their separate values, is required. In the following, we restrict ourselves to partially wetting cases where the magnitude $\|\cos\Theta\| < 1$ and, to be consistent with our notation for wetting ($\mathfrak{w}$) and non-wetting phase ($\mathfrak{n}$), $\Theta < 90°$. The special cases $\Theta = 0°$ and $\Theta = 180°$, which imply complete wetting by either of the bulk fluid phases, are not considered within this treatise.

---

[1] The kinematic constraint that gives rise to the constraining force $\mathbf{F}_C$ is given as $\mathbf{u}_C \cdot \mathbf{n}^{\mathfrak{fs}} = 0\,\forall\, \mathbf{x}_C \in \Upsilon$, where contact line velocity $\mathbf{u}_C := \dot{\mathbf{x}}_C$. The equality constraint restricts the instantaneous velocity $\mathbf{u}_C$ of the contact line to the local tangent plane of the solid surface. The constraining force may be formally derived by defining the Lagrange function for the contact line and using the method of Lagrange multipliers to incorporate the above equality constraint.

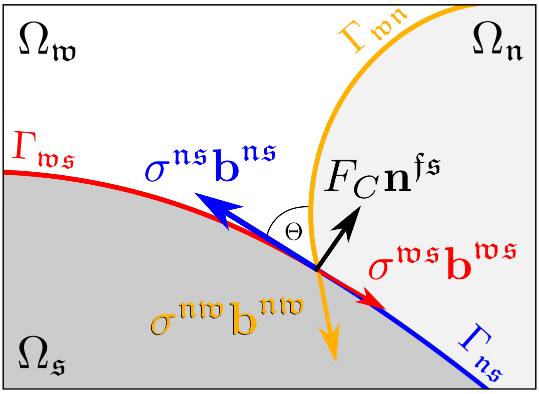
$\Omega_{\mathfrak{w}}$
$\Gamma_{\mathfrak{wn}}$
$\Omega_{\mathfrak{n}}$
$\Gamma_{\mathfrak{ws}}$
$\sigma^{\mathfrak{ns}}\mathbf{b}^{\mathfrak{ns}}$
$F_C\mathbf{n}^{\mathfrak{fs}}$
Θ
$\sigma^{\mathfrak{ws}}\mathbf{b}^{\mathfrak{ws}}$
$\sigma^{\mathfrak{nw}}\mathbf{b}^{\mathfrak{nw}}$
$\Gamma_{\mathfrak{ns}}$
$\Omega_{\mathfrak{s}}$

Figure 2.10: Schematic representation of concurrent forces comprised of boundary curve tractions $\sigma^{\alpha\beta}\mathbf{b}^{\alpha\beta}$ and contact line constraining force $F_C\mathbf{n}^{\mathfrak{fs}}$ acting on common point of contact line that is constrained to the solid-fluid interface.

In the case of complete wetting, the wetting fluid spreads over the solid-fluid interface to eventually form thin wetting films and contact lines are absent in equilibrium.

Multiplying Eq. (2.85) with $\mathbf{n}^{\mathfrak{fs}}$ yields the balance of contact line forces projected onto the direction normal to the solid surface as

$$\sigma^{\mathfrak{wn}} \sin\Theta = F_C, \quad \forall\, \mathbf{x}_C \in \Upsilon, \tag{2.87}$$

which implies that the contact line constraining force $F_C\mathbf{n}^{\mathfrak{fs}}$ is non-zero for the case of partial wetting, i.e. $0° < \Theta < 180°$. The assumption of negligible contact line energy and contact line tension is inherent in the above.

The above balance equations are only applicable to ideal solid surfaces absent of chemical imperfections, surface roughness or dust particles. In the presence of inhomogeneous solid surfaces on the other hand, a phenomenon referred to as contact line hysteresis has to be taken into account. In particular, as a result of surface inhomogeneities, a contact line may be pinned and resist motion unless a threshold force acting on the contact line is overcome. The apparent contact angle of a pinned contact line may thus differ from Young's contact angle Θ and fall into an interval bounded by static receding and advancing contact angles $\Theta_{\mathrm{r,st}}$ and $\Theta_{\mathrm{a,st}}$, respectively, which constitute material parameters. Once the threshold force is overcome, dynamic receding and advancing contact angles may further differ from respective static values. Typical effective continuum models that account for this behavior are reminiscent of static and kinetic friction models as encountered in mechanics of solid materials (see Kurzeja & Steeb [114, § 4] and references therein). It is emphasized that the given approach, however, does not account for inhomogeneous solid surfaces and assumes the validity of Young's Eq. (2.86), i.e. we restrict ourselves to ideal solid surfaces.

2.4.6 Whole-domain formulation

For the numerical solution of the IBVP comprised of bulk balance equations (2.72)-(2.73), interfacial balance equations (2.74)-(2.75), initial conditions (2.79)-(2.80) and boundary conditions (2.81)-(2.82), we adopt the formalism of immersed boundaries (section 2.3) as well as the continuum surface stress method (section 2.3.5). Due to solid phase rigidity, balance equations for material points of $\Omega_{\mathfrak{s}}$ are given by Eqs. (2.78) and the explicit modeling of the bulk solid phase is omitted. Immersion of interfacial balance equations using the immersed boundary method gives rise to whole-domain balance equations applicable to the entire fluid domain $\Omega_{\mathfrak{f}}$ with primary variables being fluid density $\varrho^{\mathfrak{f}}$ and fluid velocity $\mathbf{u}_{\mathfrak{f}}$. The latter is achieved using interface Dirac delta distributions. Hence, we introduce the phase indicator fields

$$C^{\alpha\beta}\left(\mathbf{x}\right) = \begin{cases} 0, & \text{if } \mathbf{x} \in \Omega_{\alpha}, \\ 1, & \text{if } \mathbf{x} \in \Omega_{\beta}, \\ 0.5, & \text{if } \mathbf{x} \in \Gamma_{\alpha\beta}. \end{cases}$$

The modified surface Dirac distributions and surface unit normals are subsequently given as

$$\tilde{\delta}^{\alpha\beta} := \|\operatorname{grad}\tilde{C}^{\alpha\beta}(\mathbf{x})\|, \quad \text{and} \quad \tilde{\mathbf{n}}^{\alpha\beta} := \frac{\operatorname{grad}\tilde{C}^{\alpha\beta}(\mathbf{x})}{\|\operatorname{grad}\tilde{C}^{\alpha\beta}(\mathbf{x})\|}. \tag{2.88}$$

We further introduce a solid-fluid phase indicator field

$$C^{\mathfrak{f}\mathfrak{s}}\left(\mathbf{x}\right) = \begin{cases} 0, & \text{if } \mathbf{x} \in \Omega_{\mathfrak{f}}, \\ 1, & \text{if } \mathbf{x} \in \Omega_{\mathfrak{s}}, \\ 0.5, & \text{if } \mathbf{x} \in \Gamma_{\mathfrak{f}\mathfrak{s}}, \end{cases} \quad \text{such that} \quad \tilde{\mathbf{n}}^{\mathfrak{f}\mathfrak{s}} \approx \frac{\operatorname{grad}\tilde{C}^{\mathfrak{f}\mathfrak{s}}(\mathbf{x})}{\|\operatorname{grad}\tilde{C}^{\mathfrak{f}\mathfrak{s}}(\mathbf{x})\|}.$$

As in section 2.3.5, the superimposed tilde symbol $\tilde{(\bullet)}$ highlights smooth, convolution-based approximations (2.71) of fields that are otherwise singular or discontinuous at the interface.

The rate of change of total mass density contained within $\Omega_{\mathfrak{f}}$ with interfacial balances being immersed reads

$$\int_{\Omega_{\mathfrak{f}}} \dot{\varrho}^{\mathfrak{f}} + \varrho^{\mathfrak{f}} \operatorname{div}\mathbf{u}_{\mathfrak{f}} \, \mathrm{d}v = -\int_{\Omega_{\mathfrak{f}}} \sum_{\alpha\beta} [\![\varrho\left(\mathbf{u} - \mathbf{u}_{S}\right) \cdot \mathbf{n}^{\alpha\beta}]\!] \delta^{\alpha\beta} \, \mathrm{d}v,$$

which, substituting Eqs. (2.74), can be trivially localized to yield the whole-domain balance of mass

$$\dot{\varrho}^{\mathfrak{f}} = -\varrho^{\mathfrak{f}} \operatorname{div} \mathbf{u}_{\mathfrak{f}}, \quad \forall\, \mathbf{x} \in \Omega_{\mathfrak{f}}.$$

In other words, since material interfaces of negligible interface-excess mass density are neither sources nor sinks for bulk mass density, the continuity equation is applicable to the entire fluid domain.

The assumption (2.82) of fluid velocity continuity tangent to the fluid-fluid interface is satisfied by considering $\Gamma_{\mathfrak{wn}}$ neither a source nor a sink for moment of momentum density, i.e. the whole-domain balance of moment of momentum requires the symmetry $\mathbf{T}^{\mathfrak{f}} = (\mathbf{T}^{\mathfrak{f}})^T$.

The current approach to incorporating Young's equation (2.86) is the immersion of interfacial balances (2.75) of all three interfaces into a whole-domain balance of linear momentum. Since explicit modeling of the solid phase is omitted, the constraining force F_C as required by Eq. (2.87) is not accounted for. Interface balances of linear momentum are thus modified in such a way that the action of interfacial forces at points of the solid surface is restricted to planes tangent to the solid surface only. As implied by Eqs. (2.85) and (2.86), the latter reproduces Young's equation. Components of interfacial forces normal to the solid surface are removed using the solid surface identity tensor $\mathbf{I}^{\mathfrak{fs}} := \mathbf{I} - \mathbf{n}^{\mathfrak{fs}} \otimes \mathbf{n}^{\mathfrak{fs}}$. As $\mathbf{n}^{\mathfrak{fs}}$ is only defined for points $\mathbf{x} \in \Gamma_{\mathfrak{fs}}$, the latter modification only takes effect at points of the solid surface since $\mathbf{I}^{\mathfrak{fs}} = \mathbf{I}$ for all $\mathbf{x} \in \Omega_{\mathfrak{f}} \setminus \Gamma_{\mathfrak{fs}}$. As shown further below, the latter modification, which constitutes the main difference of our model to what was proposed earlier in Hu & Adams [99], reduces spurious currents associated with the otherwise unbalanced contact line stress $\sigma^{\mathfrak{wn}} \sin\Theta$ normal to the solid surface.

The rate of change of total linear momentum density contained within $\Omega_{\mathfrak{f}}$ with interfacial balances being immersed hence reads

$$\int\limits_{\Omega_{\mathfrak{f}}} \varrho^{\mathfrak{f}} \dot{\mathbf{u}}_{\mathfrak{f}} - \operatorname{div} \mathbf{T}^{\mathfrak{f}} \, \mathrm{d}v = \int\limits_{\Omega_{\mathfrak{f}}} \sum_{\alpha\beta} \left[\operatorname{div}^{\alpha\beta} \mathbf{\Pi}^{\alpha\beta} \right] \delta^{\alpha\beta} \cdot \mathbf{I}^{\mathfrak{fs}} \, \mathrm{d}v, \tag{2.89}$$

where Eqs. (2.75) have been substituted and the above discussed modification incorporated. In equivalence to Eq. (2.66), the surface divergence $[\operatorname{div}^{\alpha\beta} \mathbf{\Pi}^{\alpha\beta}] \delta^{\alpha\beta} = \operatorname{div}(\mathbf{\Pi}^{\alpha\beta} \delta^{\alpha\beta})$. Localization of Eq. (2.89) thus yields the whole-domain balance of linear momentum

$$\varrho^{\mathfrak{f}} \dot{\mathbf{u}}_{\mathfrak{f}} = \operatorname{div} \mathbf{T}^{\mathfrak{f}} + \sum_{\alpha\beta} \operatorname{div} \left(\mathbf{\Pi}^{\alpha\beta} \delta^{\alpha\beta} \right) \cdot \mathbf{I}^{\mathfrak{fs}}, \qquad \forall\, \mathbf{x} \in \Omega_{\mathfrak{f}}. \tag{2.90}$$

Use of the whole-domain formulation (2.90) is considered computationally more attractive as compared to formulating a moving boundary problem. We emphasize that away from the solid surface, Eq. (2.90) reduces to the previously introduced whole-domain balance (2.64), i.e.

$$\varrho^{\mathfrak{f}}\dot{\mathbf{u}}_{\mathfrak{f}} = \operatorname{div}\mathbf{T}^{\mathfrak{f}}_{E} - \operatorname{grad} p^{\mathfrak{f}} + \operatorname{div}\left(\boldsymbol{\Pi}^{\mathfrak{wn}}\delta^{\mathfrak{wn}}\right) \quad \forall\,\mathbf{x} \in \Omega_{\mathfrak{f}} \setminus \Gamma_{\mathfrak{fs}}, \tag{2.91}$$

or, considering $\sigma^{\mathfrak{wn}}$ a constant,

$$\varrho^{\mathfrak{f}}\dot{\mathbf{u}}_{\mathfrak{f}} = \operatorname{div}\mathbf{T}^{\mathfrak{f}}_{E} - \operatorname{grad} p^{\mathfrak{f}} + \sigma^{\mathfrak{wn}}\kappa^{\mathfrak{wn}}\mathbf{n}^{\mathfrak{wn}}\delta^{\mathfrak{wn}} \quad \forall\,\mathbf{x} \in \Omega_{\mathfrak{f}} \setminus \Gamma_{\mathfrak{fs}}. \tag{2.92}$$

While Eq. (2.91) constitutes a conservation form, Eq. (2.92) constitutes a non-conservation form. In the presence of discontinuities, conservation forms are typically preferred with the purpose to minimize numerical errors that may give rise to spurious currents.

We discuss the consequences of removing interfacial forces normal to the solid surface by means of studying equilibrium SPH solutions of a wetting fluid droplet on a planar solid substrate (Fig. 2.11). The interfacial tensions are chosen such that the equilibrium contact angle $\Theta = 60°$. We denote the reduced interfacial force density, i.e. the second term on the RHS of Eq. (2.90),

$$\tilde{\mathbf{f}} = \sum_{\alpha\beta} \operatorname{div}\left(\boldsymbol{\Pi}^{\alpha\beta}\delta^{\alpha\beta}\right) \cdot \mathbf{I}^{\mathfrak{fs}}, \tag{2.93}$$

whereas the total interfacial force density is denoted

$$\mathbf{f} = \sum_{\alpha\beta} \operatorname{div}\left(\boldsymbol{\Pi}^{\alpha\beta}\delta^{\alpha\beta}\right). \tag{2.94}$$

Both interfacial force densities yield comparable phase distributions and reproduce the prescribed contact angle in equilibrium. However, while the reduced interfacial force density $\tilde{\mathbf{f}}$ only yields interfacial forces normal to the meniscus $\Gamma_{\mathfrak{nw}}$, which are balanced by the pressure jump at the interface, the total interfacial force density $\mathbf{f}$ induces an unbalanced interfacial force of magnitude $\sigma^{\mathfrak{wn}} \sin\Theta$ in the vicinity of the contact line acting normal to the solid-fluid interfaces. We emphasize that the latter is an artifact due to inappropriate immersion of the volumetric force density in light of the solid rigidity assumption. The evolution of the total kinetic energy E_{kin} over time iterations (Fig. 2.11, right) shows that the equilibrium states differ by one order of magnitude. We conclude that unbalanced interfacial forces lead to spurious velocities which are drastically reduced by means of using $\tilde{\mathbf{f}}$.

Rather than incorporating interfacial balance equations of all three interfaces, alternative approaches to account for Young's equation exist. In the context of SPH, Breinlinger et al. [31] considered the non-conservation form (2.92) and prescribed the contact angle on Υ by means of the boundary condition

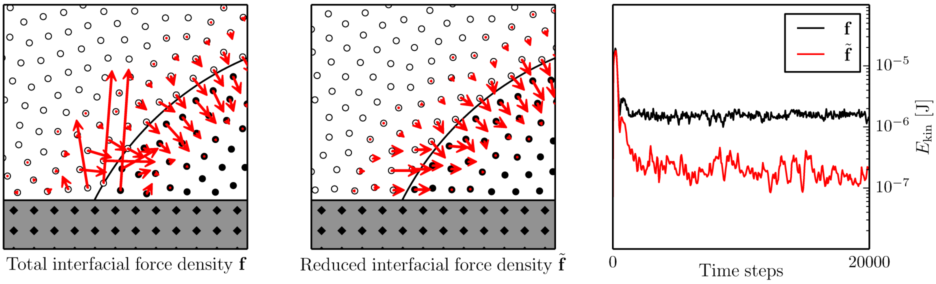

Total interfacial force density $\mathbf{f}$ Reduced interfacial force density $\tilde{\mathbf{f}}$

Figure 2.11: Close-up of equilibrium SPH solutions of a wetting fluid droplet on a planar solid substrate. Open circle, filled circle and filled diamond markers represent the SPH particle positions of the non-wetting phase, wetting phase and solid phase, respectively. Lengths and directions of the arrows represent the magnitude and direction of the interfacial force density field, respectively. (left) Solution using the total interfacial force density $\mathbf{f}$ following Eq. (2.94). (middle) Solution using the reduced interfacial force density $\tilde{\mathbf{f}}$ following Eq. (2.93). (right) Evolution of total kinetic energy over the number of time steps.

$\mathbf{n}^{\mathfrak{wn}} \cdot \mathbf{n}^{\mathfrak{fs}} = -\cos\Theta$ for the normal vector field $\mathbf{n}^{\mathfrak{wn}}$; an approach which is also commonly used in the context of mesh and grid-based methods. However, as to be indicated in section 3.2, kernel shape functions in SPH do not satisfy the Kronecker delta property by virtue of which the application of boundary conditions is regarded cumbersome. On the other hand, Huber et al. [100], Kunz et al. [113] and Hirschler et al. [95] used the non-conservation form (2.92) together with a contact line force

$$\mathbf{f}_C := \left[\sigma^{\mathfrak{ns}} - \sigma^{\mathfrak{ws}} - \sigma^{\mathfrak{wn}} \cos\Theta_{\text{app}}\right] \mathbf{b}^{\mathfrak{ns}} \delta^{\mathfrak{wns}}, \quad \forall\, \mathbf{x}_C \in \Upsilon,$$

that acts in direction $\mathbf{b}^{\mathfrak{ns}}$ tangent to the solid surface. They localize the contact line force to points of the contact line Υ by virtue of the contact line Dirac delta distribution $\delta^{\mathfrak{wns}}$. Recalling Young's equation (2.86), the latter contact line force takes effect if the cosine of the apparent contact angle $\cos\Theta_{\text{app}} := \mathbf{b}^{\mathfrak{wn}} \cdot \mathbf{b}^{\mathfrak{ws}}$ differs from $\cos\Theta$. While the contact line force approach is regarded computationally efficient, whether use of the non-conservation form compromises long-term stability remains to be shown. Moreover, the non-conservation form requires computation of curvature $\kappa^{\mathfrak{wn}}$ and hence computation of higher order spatial derivatives potentially prone to numerical noise [30, 141]. Rather than incorporating governing interfacial mass and momentum balances, further notable approaches to modeling the effects of capillarity in SPH include the use of atomistically motivated interaction forces between SPH particles [151, 195–197].

CHAPTER 3

Smoothed particle hydrodynamics

We implement a Smoothed Particle Hydrodynamics (SPH) model to perform direct numerical simulations of pore-scale resolved, incompressible flow of single or multiple fluid phases through porous media. The governing linear momentum balance equations are the Navier-Stokes equations with interfacial balance equations taken into account when modeling immiscible multiphase flows. It is our interest to assess effective transport properties of porous materials and to evaluate the potential application of SPH methods in digital rock physics. In the following chapter, the numerical principles of SPH and algorithmic computation approaches are covered to the extend to which it is considered necessary for the derivation and solution of the nodal motion equations. For a more extensive study on the subject, the reader is referred to the pioneering works Lucy [128] and Gingold & Monaghan [77], the reviews [126, 136], the textbook [203] and further surveys on fundamental numerical properties of SPH [15, 24, 139, 194].

3.1 Numerical principles

The spatial convolution product of an arbitrary scalar tensor field Φ with the Dirac delta distribution δ reads

$$\Phi\left(\mathbf{x}\right) = \int_\Omega \Phi\left(\mathbf{x}'\right) \delta\left(\mathbf{x} - \mathbf{x}'\right) \mathrm{d}v, \tag{3.1}$$

where Φ is continuously defined in the computation domain Ω and $\mathbf{x}$ denotes the position vector of a focal point. We refer to Eq. (3.1) as integral representation of Φ with the Dirac delta distribution representing the identity with respect to convolution. During the course of this section, the temporal variability of the field $\Phi = \Phi\left(\mathbf{x}, t\right)$ will be omitted for brevity of notation.

The basis of SPH is the convolution product

$$\Phi_h\left(\mathbf{x}\right) = \int_{\Omega} \Phi\left(\mathbf{x}'\right) W\left(\mathbf{x} - \mathbf{x}', h\right) \mathrm{d}v, \tag{3.2}$$

where the Dirac delta distribution in Eq. (3.1) has been replaced with a continuously differentiable kernel function W. In the context of numerical computations the kernel function W is required to have compact support with h representing a characteristic finite width of the compact support. Following common practice, we refer to W as smoothing kernel and h is referred to as smoothing length. The integral representation Φ_h is considered to be a reproducing kernel approximation of Φ if W satisfies the Dirac delta condition

$$\lim_{h \to 0} W\left(\mathbf{x}, h\right) = \delta\left(\mathbf{x}\right), \tag{3.3}$$

by virtue of which

$$\lim_{h \to 0} \Phi_h = \Phi.$$

In order to quantify the order of completeness of the reproducing kernel approximation, that is the ability of Φ_h to exactly reproduce a given polynomial Φ of degree m for finite width h, we introduce the Taylor expansion of $\Phi\left(\mathbf{x}'\right)$ about point $\mathbf{x}$ given as

$$\Phi\left(\mathbf{x}'\right) = \Phi\left(\mathbf{x}\right) + \frac{\partial \Phi}{\partial \mathbf{x}} \cdot \left(\mathbf{x}' - \mathbf{x}\right) + \frac{1}{2}\left(\mathbf{x}' - \mathbf{x}\right)^T \frac{\partial^2 \Phi}{\partial \mathbf{x}^2}\left(\mathbf{x}' - \mathbf{x}\right) + \mathcal{O}\left(h^3\right), \tag{3.4}$$

noting that $\mathcal{O}\left(h^3\right) = \mathcal{O}\left(\|\mathbf{x}' - \mathbf{x}\|^3\right)$, where $\| \bullet \|$ denotes the Euclidean norm and $\Phi\left(\mathbf{x}'\right)$ is assumed smooth over the finite interval $\left(\mathbf{x}', \mathbf{x}\right)$. Substituting the expression in Eq. (3.4) into Eq. (3.2) leads to

$$\begin{aligned}\Phi_h\left(\mathbf{x}'\right) = \Phi\left(\mathbf{x}\right)\int_\Omega W\left(\mathbf{x}-\mathbf{x}',h\right)\mathrm{d}v + \frac{\partial\Phi}{\partial\mathbf{x}}\cdot\int_\Omega\left(\mathbf{x}'-\mathbf{x}\right)W\left(\mathbf{x}-\mathbf{x}',h\right)\mathrm{d}v \\ +\frac{1}{2}\frac{\partial^2\Phi}{\partial\mathbf{x}^2}:\int_\Omega\left(\mathbf{x}'-\mathbf{x}\right)\left(\mathbf{x}'-\mathbf{x}\right)^T W\left(\mathbf{x}-\mathbf{x}',h\right)\mathrm{d}v + \mathcal{O}\left(h^3\right).\end{aligned} \tag{3.5}$$

It is evident from Eq. (3.5) that for Φ_h to be complete to zeroth order, W has to satisfy the zeroth order completeness condition, hereafter referred to as normalization condition,

$$\int_\Omega W\left(\mathbf{x},h\right)\ \mathrm{d}v = 1. \tag{3.6}$$

The second term on the RHS of Eq. (3.5) implies that first order completeness requires the first-order moment condition, hereafter referred to as symmetry condition,

$$\int_\Omega \mathbf{x}\,W\left(\mathbf{x},h\right)\mathrm{d}v = \mathbf{0} \tag{3.7}$$

to be satisfied. Both, Eqs. (3.6) and (3.7) are satisfied by employing radially symmetric kernel functions that have the general form

$$W\left(\mathbf{x},h\right) \overset{\text{radial symmetry}}{=} W\left(r,h\right) \overset{\text{normalization}}{=} \frac{\alpha_n}{h^n}\tilde{W}\left(r,h\right), \tag{3.8}$$

where the scalar normalization constant α_n is chosen such that W satisfies the normalization condition (3.6) and $r := \|\mathbf{x}\|$. Due to kernel radial symmetry, i.e. W is an even function, all terms in Eq. (3.5) of odd powers of the argument $(\mathbf{x}'-\mathbf{x})$ vanish. Thus, radially symmetric kernel functions intrinsically satisfy the symmetry condition (3.7). Moreover, radial symmetry of a kernel with compact support implies

$$W\left(r,h\right) = 0,\ \forall\, r > kh,$$

introducing the compactness factor k. The compactness factor k is a constant positive real number that depends on the particular form of the kernel function. We conclude that the approximation (3.2) is subject to an interpolation error

$$\epsilon_I(\Phi_h) = \|\Phi-\Phi_h\| = \mathcal{O}\left(h^2\right),$$

if W has compact support and exhibits radial symmetry as well as normalization.

Higher order completeness conditions are typically not taken into account arguing that the algorithmically achievable order of completeness is upper limited by the accuracy of the discrete nodal integration [166]. Furthermore, the second-order moment condition

$$\int_\Omega \mathbf{x}^T \mathbf{x}\, W(\mathbf{x}, h)\, \mathrm{d}v = \mathbf{0}$$

requires the kernel to be negative in a subset of its compact support which potentially leads to unphysical interpolations [see 136, § 2.4]. The symmetry condition (3.7) is also satisfied when using anisotropic kernel functions that merely exhibit the symmetry $W(\mathbf{x}, h) = W(-\mathbf{x}, h)$, rather than the more restrictive isotropic radial symmetry (3.8). However, the latter is not considered in this text although anisotropic kernel functions may be useful to account for local adaptivity [183].

It is our interest to approximate spatial differential operators that are inherent in balance equations on the basis of the reproducing kernel approximation. We evaluate the approximation of the gradient of a scalar field Φ by means of applying Eq. (3.2) to $\operatorname{grad} \Phi$, which leads to

$$\operatorname{grad}_h \Phi(\mathbf{x}) = \int_\Omega \frac{\partial \Phi(\mathbf{x}')}{\partial \mathbf{x}'} W(\mathbf{x} - \mathbf{x}', h)\, \mathrm{d}v. \tag{3.9}$$

We reformulate using integration by parts, such that

$$\begin{aligned}\operatorname{grad}_h \Phi(\mathbf{x}) = \int_\Omega \frac{\partial}{\partial \mathbf{x}'} \Big[\Phi(\mathbf{x}')\, W(\mathbf{x} - \mathbf{x}', h)\Big] \mathrm{d}v& \\ - \int_\Omega \Phi(\mathbf{x}')\, \frac{\partial W(\mathbf{x} - \mathbf{x}', h)}{\partial \mathbf{x}'} \mathrm{d}v.&\end{aligned} \tag{3.10}$$

Application of Gauss theorem to the first term on the RHS of Eq. (3.10) gives

$$\begin{aligned}\operatorname{grad}_h \Phi(\mathbf{x}) = \int_\Gamma \Big[\Phi(\mathbf{x}')\, W(\mathbf{x} - \mathbf{x}', h)\Big] \mathbf{n}(\mathbf{x}')\, \mathrm{d}a& \\ - \int_\Omega \Phi(\mathbf{x}')\, \frac{\partial W(\mathbf{x} - \mathbf{x}', h)}{\partial \mathbf{x}'} \mathrm{d}v,&\end{aligned} \tag{3.11}$$

where $\mathbf{n}$ denotes the unit normal vector to the boundary of the computation domain $\Gamma = \partial\Omega$. Since the kernel W has a compact support, the boundary integral in Eq. (3.11) evaluates to zero if the focal point $\mathbf{x}$ lies at some distance $\|\mathbf{x}_B - \mathbf{x}\| > kh, \forall \mathbf{x}_B \in \Gamma$ from the boundary Γ. If the bulk volume of Ω is sufficiently large, the latter condition applies to the majority of focal points. Neglecting the boundary integral and taking into account kernel radial symmetry, which implies the antisymmetry

$$\frac{\partial W\left(\mathbf{x}-\mathbf{x}', h\right)}{\partial \mathbf{x}'} = -\frac{\partial W\left(\mathbf{x}-\mathbf{x}', h\right)}{\partial \mathbf{x}}, \tag{3.12}$$

yields the approximative expression for the gradient of a scalar field

$$\begin{aligned}\operatorname{grad}_h \Phi\left(\mathbf{x}\right) &= \int_\Omega \Phi\left(\mathbf{x}'\right) \frac{\partial W\left(\mathbf{x}-\mathbf{x}', h\right)}{\partial \mathbf{x}} \mathrm{d}v \\ &= \int_\Omega \Phi\left(\mathbf{x}'\right) \operatorname{grad} W\left(\mathbf{x}-\mathbf{x}', h\right) \mathrm{d}v,\end{aligned} \tag{3.13}$$

where the spatial gradient operator is now observed to act on the continuously differentiable kernel function. The approach outlined in Eqs. (3.9)-(3.13) is fundamental to the approximation of spatial differential operators using SPH.

The approach to quantify the order of completeness of the approximation $\operatorname{grad}_h \Phi$ is equivalent to Eq. (3.5) in that the Taylor series expansion (3.4) is substituted into Eq. (3.13) to give

$$\begin{aligned}\operatorname{grad}_h \Phi\left(\mathbf{x}\right) = \Phi\left(\mathbf{x}\right) &\int_\Omega \operatorname{grad} W\left(\mathbf{x}-\mathbf{x}', h\right) \mathrm{d}v \\ + \frac{\partial \Phi}{\partial \mathbf{x}} &\int_\Omega \operatorname{grad} W\left(\mathbf{x}-\mathbf{x}', h\right) \otimes \left(\mathbf{x}'-\mathbf{x}\right) \mathrm{d}v \\ + \frac{1}{2}\frac{\partial^2 \Phi}{\partial \mathbf{x}^2} : &\int_\Omega \operatorname{grad} W\left(\mathbf{x}-\mathbf{x}', h\right) \otimes \left(\mathbf{x}'-\mathbf{x}\right)\left(\mathbf{x}'-\mathbf{x}\right)^T \mathrm{d}v \\ + \mathcal{O}\left(h^3\right) &\cdot \mathcal{O}\left(\operatorname{grad} W \mathrm{d}v\right).\end{aligned} \tag{3.14}$$

All terms in Eq. (3.14) containing integrands of even powers of the argument $(\mathbf{x}' - \mathbf{x})$, i.e. the first and third term on the RHS, evaluate to zero since $\operatorname{grad} W$ is an odd function according to Eq. (3.12). The integral in the second term of the RHS is reformulated using integration by parts to give

$$\int_\Omega \frac{\partial W\left(\mathbf{x}-\mathbf{x}',h\right)}{\partial \mathbf{x}} \otimes \left(\mathbf{x}'-\mathbf{x}\right) \mathrm{d}v = \int_\Omega \frac{\partial}{\partial \mathbf{x}} \Big[W\left(\mathbf{x}-\mathbf{x}',h\right)\left(\mathbf{x}'-\mathbf{x}\right) \Big] \mathrm{d}v - \int_\Omega W\left(\mathbf{x}-\mathbf{x}',h\right) \frac{\partial \left(\mathbf{x}'-\mathbf{x}\right)}{\partial \mathbf{x}} \mathrm{d}v. \quad (3.15)$$

The first integral on the RHS of Eq. (3.15) can be neglected since W has compact support (see Eqs. (3.10) and (3.11)). Moreover, the second integral on the RHS of Eq. (3.15) is equal to the n-dimensional identity tensor $\mathbf{I}$ since W satisfies the normalization condition (3.6) and $-\partial\mathbf{x}/\partial\mathbf{x} = -\mathbf{I}$. As a result

$$\operatorname{grad}_h \Phi\left(\mathbf{x}\right) = \frac{\partial \Phi}{\partial \mathbf{x}} \cdot \mathbf{I} + \mathcal{O}\left(h^3\right) \cdot \mathcal{O}\left(\operatorname{grad} W \mathrm{d}v\right).$$

Since $\mathcal{O}\left(\operatorname{grad} W \mathrm{d}v\right) = \mathcal{O}\left(1/h\right)$, the resulting interpolation error is written

$$\epsilon_I(\operatorname{grad}_h \Phi) = \| \operatorname{grad} \Phi - \operatorname{grad}_h \Phi \| = \mathcal{O}\left(h^2\right),$$

indicating that for compactly supported, normalized and symmetric kernels first-order completeness applies to both, Φ_h and $\operatorname{grad}_h \Phi$.

The reproducing approximation of spatial differential operators acting on tensor fields of arbitrary order can be derived in equivalence to Eqs. (3.9) to (3.13). Within the course of this text, we will make particular use of the reproducing approximation of the divergence of a first-order tensor field $\boldsymbol{\Phi}$, which reads

$$\operatorname{div}_h \boldsymbol{\Phi}\left(\mathbf{x}\right) = \int_\Omega \boldsymbol{\Phi}\left(\mathbf{x}'\right) \cdot \operatorname{grad} W\left(\mathbf{x}-\mathbf{x}',h\right) \mathrm{d}v. \quad (3.16)$$

Although in principle the approximation ansatz (3.2) can be readily extended to approximate second-order spatial operators, such as the Laplacian div[grad (•)], numerical quadrature of convolution integrals involving the second-order derivate of W exhibits an undesirable amount of sensitivity with respect to the arrangement of nodal integration points [33, 136]. An alternative approach to approximate higher-order derivatives is discussed in section 3.5.3.

It is furthermore possible to account for spatial and temporal variability of the smoothing length, i.e. $h = h(\mathbf{x}, t)$, which implies that the partial derivative $\partial h/\partial \mathbf{x}'$ needs to be taken into account in Eqs. (3.9) to (3.13). However, as it will be apparent later, we apply the SPH method to model incompressible flow resulting in near-equispaced configurations of nodal integration points for which spatial adaptivity of the smoothing length is omitted. In the course of this text, we thus consider h to be constant in space and time.

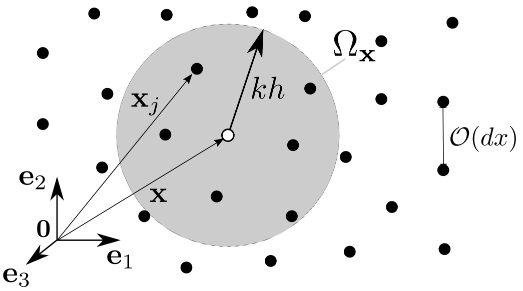

Figure 3.1: Schematic of the nodal integration scheme covering the compact support domain $\Omega_{\mathbf{x}}$ of focal point $\mathbf{x}$.

3.2 Nodal integration

Reproducing kernel approximations (3.2), (3.13) and (3.16) are numerically integrated using a quadrature rule over N integration points. The quadrature rule that comes to use in the overwhelming majority of SPH methods is a nodal integration equivalent to a middle Riemann sum which, in the case of Eq. (3.2), reads

$$\Phi_{h,dx}\left(\mathbf{x}\right) = \sum_{j:\mathbf{x}_j \in \Omega}^{N} \Phi\left(\mathbf{x}_j\right) W\left(\mathbf{x}-\mathbf{x}_j, h\right) V_j. \tag{3.17}$$

The subscript $(\bullet)_{h,dx}$ is introduced to indicate that the smoothing length h as well as the characteristic discretization length scale dx are involved in the approximation $\Phi_{h,dx}$. Equation (3.17) further introduces the volume V_j of a point centered at position $\mathbf{x}_j$; the volume V_j being interpreted as the discrete equivalent of the volume element dv. For two-dimensional simulations, i.e. for $n=2$, V_j shall denote a volume per unit of length. Using the density $\varrho_j = \varrho\left(\mathbf{x}_j\right)$, a focal point at $\mathbf{x}_j$ is carrying matter of lumped mass m_j such that $V_j = m_j/\varrho_j$. Given that W has a compact support, the summation operator in Eq. (3.17) can be algorithmically restricted to the nearest neighbors $N_n(\mathbf{x})$ of focal point $\mathbf{x}$ which satisfy $\|\mathbf{x}-\mathbf{x}_j\| < kh$. We thus introduce the compact support domain $\Omega_{\mathbf{x}}$ of the kernel function centered at $\mathbf{x}$ (Fig. 3.1) and write

$$\Phi_{h,dx}\left(\mathbf{x}\right) = \sum_{j:\mathbf{x}_j \in \Omega_{\mathbf{x}}}^{N_n(\mathbf{x})} \Phi\left(\mathbf{x}_j\right) W\left(\mathbf{x}-\mathbf{x}_j, h\right) V_j. \tag{3.18}$$

Nodal integration of the approximated spatial differential operators (3.13) and (3.16) implies

$$\operatorname{grad}_{h,dx} \Phi\left(\mathbf{x}\right) = \sum_{j:\mathbf{x}_j \in \Omega_{\mathbf{x}}}^{N_n(\mathbf{x})} \Phi\left(\mathbf{x}_j\right) \operatorname{grad} W\left(\mathbf{x} - \mathbf{x}_j, h\right) V_j, \tag{3.19}$$

and

$$\operatorname{div}_{h,dx} \mathbf{\Phi}\left(\mathbf{x}\right) = \sum_{j:\mathbf{x}_j \in \Omega_{\mathbf{x}}}^{N_n(\mathbf{x})} \mathbf{\Phi}\left(\mathbf{x}_j\right) \cdot \operatorname{grad} W\left(\mathbf{x} - \mathbf{x}_j, h\right) V_j. \tag{3.20}$$

For simplicity, the set of focal points where we evaluate the above approximations coincides with the set of points where the field functions are sampled. Hereafter, the subscript $i = 1, \ldots, N$ is used to denote the focal points whereas the index of summation $j = 1, \ldots, N_n(\mathbf{x}_i)$ applies to the sampling points. We introduce the shorthand notations

$$W_{ij} = W\left(\mathbf{x}_i - \mathbf{x}_j, h\right) \quad \text{and} \quad r_{ij} = \|\mathbf{x}_i - \mathbf{x}_j\|.$$

Due to radial symmetry, the spatial gradient of the kernel may be evaluated as

$$\operatorname{grad} W\left(\mathbf{x}_i - \mathbf{x}_j, h\right) = \frac{\partial W_{ij}}{\partial r_{ij}} \frac{\mathbf{x}_i - \mathbf{x}_j}{r_{ij}}, \quad \text{where} \quad \frac{\partial W_{ij}}{\partial r_{ij}} := \left.\frac{\partial W(r,h)}{\partial r}\right|_{r=r_{ij}}.$$

Let us further define

$$\Phi_i := \left.\Phi_{h,dx}\right|_{\mathbf{x}=\mathbf{x}_i}, \quad \operatorname{grad}_i \Phi := \left.\operatorname{grad}_{h,dx} \Phi\right|_{\mathbf{x}=\mathbf{x}_i} \quad \text{and} \quad \operatorname{div}_i \mathbf{\Phi} := \left.\operatorname{div}_{h,dx} \mathbf{\Phi}\right|_{\mathbf{x}=\mathbf{x}_i}.$$

The shorthand notations of Eqs. (3.18), (3.19) and (3.20), which are broadly used in literature, are subsequently introduced to read

$$\Phi_i = \sum_{j:\mathbf{x}_j \in \Omega_i} \Phi_j W_{ij} V_j, \tag{3.21}$$

$$\operatorname{grad}_i \Phi = \sum_{j:\mathbf{x}_j \in \Omega_i} \Phi_j \frac{\partial W_{ij}}{\partial r_{ij}} \frac{\mathbf{x}_i - \mathbf{x}_j}{r_{ij}}, \tag{3.22}$$

$$\operatorname{div}_i \mathbf{\Phi} = \sum_{j:\mathbf{x}_j \in \Omega_i} \mathbf{\Phi}_j \cdot \frac{\partial W_{ij}}{\partial r_{ij}} \frac{\mathbf{x}_i - \mathbf{x}_j}{r_{ij}}. \tag{3.23}$$

The compact support domain of the kernel function centered at point $\mathbf{x}_i$ is denoted Ω_i. Closing this section on nodal integration, we discuss two distinct interpretations of the presented discretization scheme:

SPH: A mesoscopic particle method

> In a physical interpretation, the sampling points $\mathbf{x}_j$ can be considered mesoscopic entities of a continuum, or, hereafter particles. A particle j with discrete volume V_j is carrying matter of lumped mass m_j and density $\varrho_j = \varrho(\mathbf{x}_j)$, which implies that $\mathbf{x}_j$ represents the position of its center of mass. There is a length scale $\mathcal{O}(V_j^{1/n})$ associated with the size of particle j. In the context of solving continuum balance equations subject to boundary conditions, the resulting nodal SPH balance equations take the form of a focal particle i exchanging mass, momentum and energy with neighboring particles that are elements of the influence domain Ω_i. It is for that reason the unstructured set of SPH collocation points is reminiscent of a system of colloidal particles interacting with each other.

SPH: A point collocation method

> Introducing the shape functions $W_V(\mathbf{x}_i) = W(\mathbf{x}_i - \mathbf{x}_j, h)\, V_j$ we may write Eq. (3.17) as $\Phi_{h,dx}(\mathbf{x}_i) = \sum_j \Phi_j W_V(\mathbf{x}_i)$, which has the form of a classical finite element ansatz. We may consider SPH a point collocation method considering that $W_V(\mathbf{x}_i)$ span a functional sub-space of finite dimensions $N * \sum_i N_n(i)$ (Total number of interactions), in which we seek a solution to an initial boundary value problem requiring that the balance equations may be satisfied at the focal points only. However, in contrast to finite element shape functions, $W_V(\mathbf{x}_i)$ are not piecewise polynomials that interpolate between nodal points. Furthermore, they are not required to satisfy the Kronecker delta property $W_V(\mathbf{x}_i) \neq \delta_{ij}$, where $\delta_{ij} = \{1 \text{ if } i = j \text{ and } 0 \text{ if } i \neq j\}$. Since the latter implies $\Phi_{h,dx}(\mathbf{x}_i) \neq \Phi_i W_V(\mathbf{x}_i)$, the application of boundary conditions is non-trivial in SPH methods [25].

3.3 Kernel functions

One may construct an infinite number of kernel functions that satisfy the Dirac delta condition (3.3), normalization (3.6) and symmetry (3.7) [see 126, § 3.2]. In addition, all kernel functions that come to use hereafter exhibit radial symmetry (3.8) as well. Introducing the non-dimensional distance $q \coloneqq r/h$, the kernel function and its gradient are written

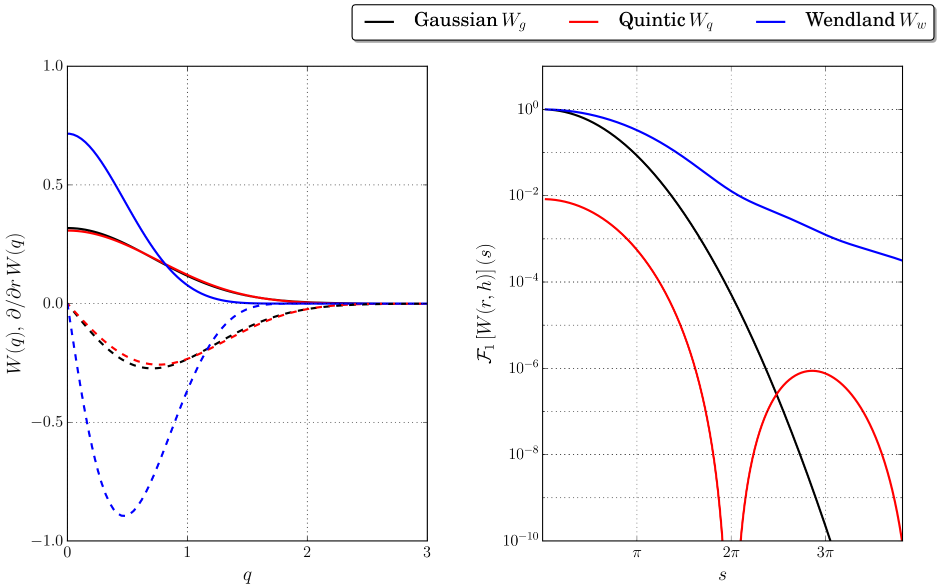

Figure 3.2: One-dimensional kernel functions $W(q)$ with smoothing lengths set to unity $h = 1$ (left, Solid lines), their derivatives $\partial/\partial r\, W(q)$ (left, Dashed lines) and respective one-dimensional Fourier transforms $\mathcal{F}_1\left[W(r,h)\right](s)$ (right).

$$W\left(\mathbf{x}-\mathbf{x}',h\right) = \frac{\alpha_n}{h^n}\tilde{W}\left(q\right) \quad \text{and}$$

$$\operatorname{grad} W\left(\mathbf{x}-\mathbf{x}',h\right) = \frac{\alpha_n}{h^{n+1}}\frac{\partial\tilde{W}\left(q\right)}{\partial q}\frac{\mathbf{x}-\mathbf{x}'}{r},$$

respectively. Hence, a kernel function can be uniquely defined by the dimension-dependent scalar normalization constant α_n and the dimensionless scalar function $\tilde{W}\left(q\right)$. With $q_{ij} \coloneqq r_{ij}/h$, we write

$$W_{ij} = \frac{\alpha_n}{h^n}\tilde{W}\left(q_{ij}\right) \qquad \text{and} \qquad \frac{\partial W_{ij}}{\partial r_{ij}} = \frac{\alpha_n}{h^{n+1}}\left.\frac{\partial\tilde{W}(q)}{\partial q}\right|_{q=q_{ij}}$$

in light of the notation that has been introduced in Eqs. (3.21)-(3.23).

The Gaussian kernel

$$\tilde{W}_g\left(q\right) = \exp\left(-q^2\right),$$

with $\alpha_{g,n} = \pi^{-n/2}$, was among the first kernels to be used in SPH methods, including the pioneering work Gingold & Monaghan [77]. Despite its attractive property of being infinitely differentiable, computational costs associated with using the Gaussian are excessively large given that it is not compactly supported. In the context of nodal integration, the latter implies that the computational costs associated with the Gaussian kernel scale with $\mathcal{O}(N^2)$. On the other hand, for compactly supported kernel functions, computational costs can be drastically reduced to $\mathcal{O}(N \cdot \bar{N}_n)$, where $\bar{N}_n$ is the average number of sampling particles neighboring the set of focal particles. Both kernel functions that are introduced in the following are piecewise polynomial, compactly supported and radial functions.

Among the most commonly used alternatives to the Gaussian kernel are the Schoenberg [181] B-splines, in particular the fifth-order quintic B-spline, hereafter referred to as quintic kernel,

$$\tilde{W}_q(q) = (3-q)_+^5 - 6(2-q)_+^5 + 15(1-q)_+^5 ,$$

where the operator $(\bullet)_+ = \max\{0, \bullet\}$ is used for abbreviation and the normalization constants $\alpha_{q,1} = 1/120$, $\alpha_{q,2} = 7/(478\pi)$ and $\alpha_{q,3} = 1/(120\pi)$ in one, two and three-dimensional space, respectively. Since $W_q = 0$, $\forall q > 3$, the compactness factor $k_q = 3$. Following common practice and the validation computations presented in section 4 we choose the smoothing length of the quintic kernel to be $h_q = 1.45\ dx_0$, where dx_0 denotes the initial particle spacing. The Gaussian kernel and the quintic kernel exhibit profound similarities to each other in real space (Fig. 3.2, left), and the same holds true for derivatives $\partial/\partial r\, W(q)$.

We furthermore use the Wendland [207] C4 kernel

$$\tilde{W}_w(q) = \left(1 - \frac{1}{2}q\right)_+^6 \left(3 + 9q + \frac{35}{4}q^2\right),$$

which has a compactness factor $k_w = 2$ and normalization constants $\alpha_{w,1} = 9/32$, $\alpha_{w,2} = 3/(4\pi)$ and $\alpha_{w,3} = 165/(256\pi)$ in one, two and three-dimensional space, respectively. The smoothing length of the Wendland kernel is chosen to be $h_w = 1.7\ dx_0$. Since $k_w < k_q$, the number of neighbors N_n for a given integration point number density and smoothing length h is smaller in the case of W_w as compared to W_q, leading to further reduction in computation costs. The magnitude of W_w is comparatively high at $q = 0$, which implies that more weight is put to the close vicinity of the focal point as compared to W_q and W_g.

While the above kernel functions exhibit qualitative similarities in real space, i.e. a smooth bell-shaped character, pronounced differences are observed in

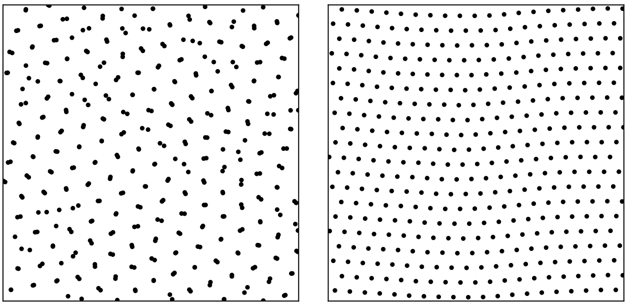

Figure 3.3: Typical equilibrium particle distributions as observed for the quintic kernel (left), which exhibits the pairing instability, and Wendland-C4 kernel (right).

Fourier space. We resort ourselves to the one-dimensional Fourier transform of $W(r,h)$, which, since the kernel is an even function, is equal to the real-valued cosine transform

$$\mathcal{F}\left[W(r,h)\right](s) = 2\int_0^\infty W(r,h)\cos(sr)\,\mathrm{d}r. \tag{3.24}$$

Introducing the dimensionless frequency $\bar{s} = sh$, $\mathcal{F}\left[W(r,h)\right](s)$ can be rewritten as the Fourier transform of the dimensionless kernel $\tilde{W}\,(q)$ to yield

$$\mathcal{F}\left[W(r,h)\right](s) = 2\alpha_1\int_0^\infty \tilde{W}(q)\cos(\bar{s}q)\,\mathrm{d}q,$$

where α_1 denotes the normalization constant in one-dimensional space. The one-dimensional Fourier transforms of the above kernel functions read

$$\mathcal{F}\left[W_g(r,h)\right](s) = \exp\left(-\frac{\bar{s}^2}{4}\right), \tag{3.25}$$

$$\mathcal{F}\left[W_q(r,h)\right](s) = \frac{1}{120}\left[\frac{2}{\bar{s}}\sin\left(\frac{\bar{s}}{2}\right)\right]^6$$

and

$$\mathcal{F}\left[W_w(r,h)\right](s) = \frac{945}{32\bar{s}^9}\Big[16\bar{s}\left(9-2\bar{s}^2\right) + 3\left(4\bar{s}^2-35\right)\sin\left(2\bar{s}\right) + 66\bar{s}\cos\left(2\bar{s}\right)\Big]. \tag{3.26}$$

We observe that the Fourier transforms of the Gaussian and Wendland-C4 kernels are positive for all frequencies (Fig. 3.2, right). In contrast to $\mathcal{F}\left[W_w\right]$, which exhibits comparatively large power at high frequencies due to its high weight in the vicinity of the focal point, $\mathcal{F}\left[W_g\right]$ and $\mathcal{F}\left[W_q\right]$ quickly loose power with increasing frequency. Despite their similarities in real space, the Fourier transform of the quintic kernel, in contrast to the Fourier transform of the Gaussian, has roots at integer multiples of 2π. The latter reveals to be important since, according to Dehnen & Aly [51], non-negativity of the multidimensional kernel Fourier transform is a necessary requirement to avoid the pairing instability. In the context of using SPH to solve fluid dynamical equations, pairing instabilities lead to particles experiencing a spurious force driving the formation of particle pairs (Fig. 3.3, left). Particles form pairs in an attempt to decrease total internal energy. In summary, despite its often asserted interpolation accuracy [98], the quintic kernel, in contrast to the Wendland-C4 and Gaussian kernels, is prone to the pairing instability. In the context of multiphase simulations, where we study localized effects at interfaces, non-uniform particle distributions that result from the pairing instability are undesirable.

3.4 Numerical errors

As shown in section 3.1, interpolation errors inherent in the reproducing kernel approximations Φ_h and $\operatorname{grad}_h \Phi$ are of second-order in the smoothing length h. Considering nodal integration, the average distance $\mathcal{O}(dx)$ between neighboring particles introduces an additional numerical length scale. Errors that arise due to nodal integration of the reproducing kernel approximations are referred to as discretization errors and expected to be dependent on dx. In the following section, we analytically study discretization errors on regular grids following the approach of Monaghan [136] and empirically study the effect of particle disorder on numerical errors. Apart from discretization errors, boundary inconsistencies that arise if the computation domain Ω is bounded motivate the use of corrective discretization schemes.

3.4.1 Discretization errors

Quantifying the discretization errors $\epsilon_D(\Phi) = \|\Phi_h - \Phi_{h,dx}\|$ and $\epsilon_D(\operatorname{grad}_h \Phi) = \|\operatorname{grad}_h - \operatorname{grad}_{h,dx}\|$ is non-trivial since they are expected to depend on the distribution of particles in Ω, for which assumptions have to be made since mesh- or grid-related constraints, such as in finite element or finite difference methods, are absent. A natural approach to quantify ϵ_D is to assume particles to be distributed on a structured grid for which accurate closed-form error expressions can be derived [136, 166, 203]. On the other hand, statistical error estimates equivalent to Monte Carlo error estimates are suitable for a random distribution.

In the context of modeling fluid transport, particles are typically advected according to the local advection velocity, i.e. in the sense of an updated Lagrangian method. As a result, the distribution of particles depends on the governing balance equations. As indicated earlier, when considering near-incompressible flow, particles are typically distributed in a close-packing, glass-like arrangement that exhibits a global regularity (Fig. 3.3, right). We therefor consider discretization error estimates based on regular grids more representative of the applications that are considered in the following. While an extensive study of discretization errors is beyond the scope of this text, we shall however concisely discuss the main findings of Monaghan [136] and Quinlan et al. [166] in this section.

In his illustrative approach to quantify discretization errors, Monaghan [136] considered the discrete representation (3.21) of a linear scalar function $\Phi^1(X) = a + bX$ in one dimensional space with spatial coordinate X using an equidistant distribution of sampling points. Since Φ^1 is a linear function, the second-order interpolation error $\epsilon_I(\Phi_h^1)$ vanishes. We denote the regular grid spacing ΔX and evaluate Eq. (3.21) at an arbitrary point $X_i = i\Delta X$ which reads

$$\Phi^1_{h,dx}\left(X_i\right) = \sum_{j=-\infty}^{\infty} \left[a + bX_j\right] W\left(X_i - X_j, h\right) \Delta X, \tag{3.27}$$

where i and j are elements of the set of integers $\mathbb{Z}$ such that $X_i = i\Delta X$ and $X_j = j\Delta X$. If we shift the origin of the coordinate system to the focal point X_i by applying the translation operator $\mathcal{T}_{X_i} f(X) = f(X_i - X)$, Eq. (3.27) can be rewritten to

$$\begin{aligned} \mathcal{T}_{X_i}\left(\Phi^1_{h,dx}\right)(0) &= \sum_{j=-\infty}^{\infty} \left[a + bX_i - bX_j\right] W\left(X_j, h\right) \Delta X \\ &= \left[a + bi\Delta X\right] \sum_{j=-\infty}^{\infty} W\left(X_j, h\right) \Delta X - b \sum_{j=-\infty}^{\infty} j\Delta X W\left(X_j, h\right) \Delta X. \end{aligned} \tag{3.28}$$

By shifting the origin, we can exploit radial symmetry of the kernel function, i.e. $W\left(X_j, h\right) = W\left(-X_j, h\right)$, which implies that the second term on the RHS of Eq. (3.28) vanishes. As a result

$$\mathcal{T}_{X_i}\left(\Phi^1_{h,dx}\right)(0) = \left[a + bi\Delta X\right] \sum_{j=-\infty}^{\infty} W\left(X_j, h\right) \Delta X.$$

We observe that $\Phi^1\left(X_i\right) = a + bi\Delta X$ is only equal to the discrete approximation $\Phi^1_{h,dx}\left(X_i\right)$ if the discrete equivalent of the normalization condition (3.6), which reads

$$\sum_{j=-\infty}^{\infty} W\left(X_j, h\right) \Delta X \overset{!}{=} 1, \tag{3.29}$$

is satisfied.

The summation (3.29) in real space can be converted to a summation in Fourier space using the Poisson summation formula [192]

$$\sum_{j\in\mathbb{Z}} W\left(j\Delta X, h\right) \Delta X = \sum_{l\in\mathbb{Z}} \mathcal{F}\Big[W\Big]\left(l\hat{s}\right), \tag{3.30}$$

where the wavenumber $\hat{s} = 2\pi/\Delta X$. Using the one-dimensional Fourier transform (3.24) of even functions, Eq. (3.30) can be rewritten to

$$\sum_{j\in\mathbb{Z}} W\left(j\Delta X, h\right) \Delta X = \int_{-\infty}^{\infty} W(X,h) dX + 2\sum_{l=1}^{\infty}\int_{0}^{\infty} W(X,h)\cos(l\hat{s}X)\ \mathrm{d}X,$$

where the first term on the RHS is equal to unity due to normalization (3.6). Since the proposed compactly supported and bell-shaped kernel functions quickly lose power with increasing frequency (Fig. 3.2, right), the summation in Fourier space is expected to converge quickly. We thus truncate the Poisson summation for $l > 2$, such that

$$\sum_{j=-\infty}^{\infty} W\left(j\Delta X, h\right) \Delta X \approx 1 + 2\int_{0}^{\infty} W(X,h)\cos(\hat{s}X)\ \mathrm{d}X.$$

In other words, the discretization error is inherently related to the kernel Fourier transform.

Substituting the normalized frequency $\bar{s} = 2\pi h/\Delta X$ into the Fourier transforms (3.25)-(3.26) finally gives

$$\Phi^1_{h,dx,g}\left(X_i\right) \approx \Phi^1(X_i) \cdot \left[1 + \exp\left(-\frac{\pi^2 h^2}{(\Delta X)^2}\right)\right]$$

for the Gaussian and

$$\Phi^1_{h,dx,q}\left(X_i\right) \approx \Phi^1(X_i) \cdot \left[1 + \frac{1}{120}\left(\frac{\Delta X}{\pi h}\sin\left(\frac{\pi h}{\Delta}\right)\right)\right] \tag{3.31}$$

for the quintic kernel. The error expression for the Wendland-C4 kernel is omitted for brevity but can be easily constructed using Eq. (3.26). The immediately apparent result from the above is that, while the continuous approximation (3.2) satisfies first-order completeness, the discrete equivalent (3.17) does generally not satisfy zeroth-order completeness. The latter can be directly related to the fact that the discrete normalization condition (3.29) is generally not satisfied. Applying the Gaussian kernel on one-dimensional regular grids, discretization errors are observed to be non-zero for all ratios $h/\Delta X$, however, negligibly small for $h > \Delta X$. Using the quintic kernel, on the other hand, discretization errors evaluate to zero if h is an integer multiple of ΔX and small for $h > \Delta X$.

Within the course of this text, the following statements have only been shown to hold true for regular grids in one-dimensional space, however, they apply to regular grids in multidimensional space as well, as shown in Quinlan et al. [166] and Violeau [203]. While interpolation errors $\epsilon_I = \mathcal{O}(h^2)$ increase with increasing smoothing length, discretization errors decrease with increasing smoothing length. However, at fixed smoothing length, decreasing the grid spacing ΔX will invoke a convergence behavior. Following Quinlan et al. [166] and Violeau [203], discretization errors satisfy the general form $\epsilon_D = \mathcal{O}(\Delta X/h)^\zeta$, where the real-valued scalar ζ is expected to depend on the kernel function and the nodal integration stencil. The latter implies that $h > \Delta X$ is a condition that should preferably be met for all simulation parameterizations.

We proceed to discuss discretization errors that arise due to nodal integration of the gradient approximation. Applying the discrete approximation (3.22) to the derivative $\partial\Phi^1/\partial X$ in analogy to the approach outlined in Eqs. (3.27)-(3.28), i.e. shifting the origin and taking into account the antisymmetry (3.12), results in

$$\mathcal{T}_{X_i}\left(\frac{\partial}{\partial X}\Phi^1_{h,dx}(X)\right)(0) = -b\sum_{j=-\infty}^{\infty} X_j \frac{\partial}{\partial X} W\left(X_j, h\right)\Delta X.$$

Using the Poisson summation formula, one may show that the Fourier transform of the derivative of the kernel is related to discretization errors in Eq. (3.22). Moreover, we observe that discretization errors arise if the discrete first-order moment of the derivative of the kernel is not equal to -1, i.e.

$$\sum_{j=-\infty}^{\infty} X_j \frac{\partial}{\partial X} W\left(X_j, h\right)\Delta X \overset{!}{=} -1. \tag{3.32}$$

Upon taking the derivative of the symmetry condition (3.7) and reformulating it using integration by parts, i.e.

$$\begin{aligned}\frac{\partial}{\partial \mathbf{x}} \int_{-\infty}^{\infty} \mathbf{x}\, W\left(\mathbf{x}, h\right) \mathrm{d}v &= \int_{-\infty}^{\infty} \mathbf{x} \frac{\partial W\left(\mathbf{x}, h\right)}{\partial \mathbf{x}} \mathrm{d}v + \int_{-\infty}^{\infty} \mathbf{I} : W\left(\mathbf{x}, h\right) \mathrm{d}v \\ &= \int_{-\infty}^{\infty} \mathbf{x} \frac{\partial W\left(\mathbf{x}, h\right)}{\partial \mathbf{x}} \mathrm{d}v + 1 \overset{!}{=} 0,\end{aligned}$$

the condition (3.32) is found a discrete analogue of the symmetry condition.

We conclude that total numerical errors $\epsilon_{D,I}$ in SPH methods that employ normalized and symmetric kernel functions can be decomposed into interpolation errors and discretization errors having the form [110]

$$\begin{aligned}\epsilon_{D,I}\left(\Phi_{h,dx}\right) \coloneqq \|\Phi - \Phi_{h,dx}\| \leq \|\Phi - \Phi_h\| + \|\Phi_h - \Phi_{h,dx}\| \\ = \mathcal{O}\left(h^2\right) + \mathcal{O}\left(\frac{dx}{h}\right)^{\zeta},\end{aligned}$$

where dx denotes the grid spacing between equidistant particles. Discretization errors arise due to the numerical violation of the discrete equivalents of the normalization and symmetry condition

$$\sum_{j:\mathbf{x}_j \in \Omega_i} W\left(\mathbf{x}_j, h\right)\, V_j = 1, \qquad \text{and} \tag{3.33}$$

$$\sum_{j:\mathbf{x}_j \in \Omega_i} \mathbf{x}_j\, W\left(\mathbf{x}_j, h\right)\, V_j = \mathbf{0}, \tag{3.34}$$

respectively.

Since the preceding analysis of numerical errors was restricted to equidistant particles in one-dimensional space only, an empirical study of the L^2 error norms

$$\begin{aligned}\left[\epsilon_{D,I}^{L2}\left(\Phi_{h,dx}\right)\right]^2 &\coloneqq \frac{1}{N} \sum_{i:\mathbf{x}_i \in \Omega}^{N} \|\, \Phi_i - \Phi\left(\mathbf{x}_i\right) \|^2 \qquad \text{and} \\ \left[\epsilon_{D,I}^{L2}\left(\mathrm{grad}_{h,dx}\, \Phi\right)\right]^2 &\coloneqq \frac{1}{N} \sum_{i:\mathbf{x}_i \in \Omega}^{N} \left\| \left(\mathrm{grad}_i\, \Phi - \mathrm{grad}\, \Phi\big|_{\mathbf{x}=\mathbf{x}_i}\right) \right\|^2\end{aligned} \tag{3.35}$$

was performed in two-dimensional space using the harmonic function $\Phi = \sin(2\pi X_1 \lambda_h^{-1}) \cos(2\pi X_2 \lambda_h^{-1})$ with $\lambda_h = 1$ as input (Fig. 3.4). In an attempt to quantify total numerical errors that arise due to non-uniform particle distribu-

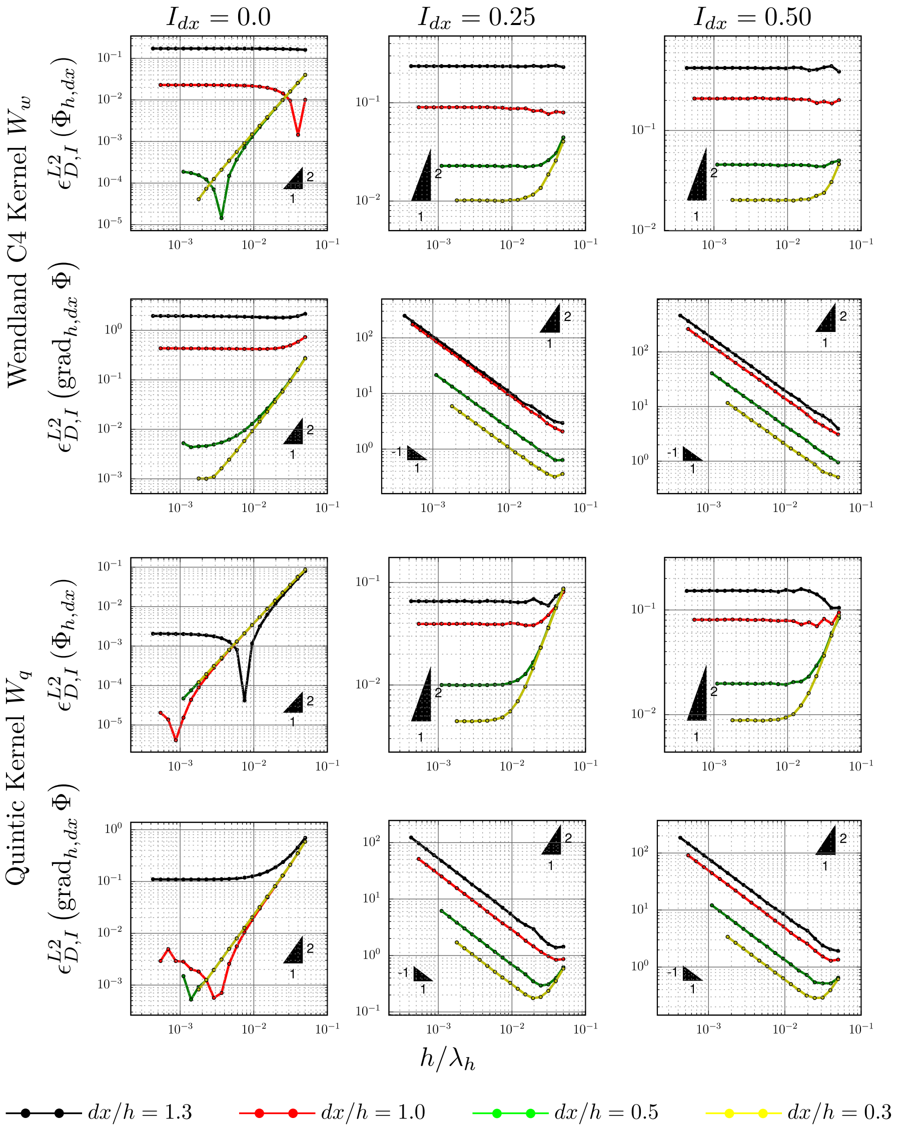

Figure 3.4: Empirical study of L^2 error convergence of the discrete reproducing approximations $\Phi_{h,dx}$ and $\mathrm{grad}_{h,dx}\,\Phi$ in two dimensional space as a function of non-dimensional smoothing length h/λ_h, numerical length scale ratio dx/h, grid point perturbation factor I_{dx} and kernel functions W_w and W_q.

tions, an initially uniform grid with spacing dx was perturbed by adding a random scalar drawn from a uniform distribution on the open interval $(-I_{dx}dx, I_{dx}dx)$ to each of the coordinates $X_{1,i}$ and $X_{2,i}$ for all focal points $\mathbf{x}_i \in \Omega$. The scalar I_{dx} is referred to as grid point perturbation factor. In an attempt to avoid boundary inconsistencies (section 3.4.2), periodic boundary conditions were applied with respect to the direction of $\mathbf{e}_1$ and $\mathbf{e}_2$. Particle volumes $V_i = dx^2$ in all cases.

For the unperturbed grid (Fig. 3.4, left column), results are in qualitative agreement with the preceding analysis in that interpolation errors ($\mathcal{O}\left(h^2\right)$) are dominant at large h, whereas a lower limit interrupting h-convergence is observed due to the discretization error ($\mathcal{O}\left(dx/h\right)^{\zeta}$). Since convergence was studied for constant ratios dx/h, the latter yields lower asymptotes independent of h. For special values of h/λ_h, local minima that correspond to roots of the corresponding error expression, in analogy to the properties of Eq. (3.31), are observed. As expected, errors are considerably larger for the cases $dx > h$ as compared to $h > dx$.

Increasing the perturbation factor results in larger numerical errors as compared to the unperturbed reference results. While numerical errors with respect to $\Phi_{h,dx}$ qualitatively behave equivalent to those of the unperturbed grid, i.e. lower asymptotes at small h and $\mathcal{O}\left(h^2\right)$-scaling at large h, below a threshold value for h, numerical errors for perturbed grids with respect to $\operatorname{grad}_{h,dx}\Phi$ are observed to linearly increase for decreasing values of h. In other words, SPH lacks error convergence for increasing resolution if the distribution of collocation points is non-uniform. The latter $\mathcal{O}\left(1/h\right)$-scaling for non-uniform grids at low h was theoretically confirmed in Quinlan et al. [166]. Clearly, the latter constitutes a critical constraint that must be tackled using corrective approaches as discussed in section 3.4.3. Numerical errors produced by both kernel functions exhibit equivalent qualitative characteristics, however, discretization errors for small values of h are consistently larger using the Wendland C4 kernel as compared to the quintic kernel which results from the smaller support radius of W_w, i.e. $k_w < k_q$.

3.4.2 Boundary inconsistency

In the preceding sections 3.1-3.4.1, we have consistently neglected effects related to spatial boundedness of general computation domains. For instance, let us recall that we have neglected the boundary integral in Eq. (3.11) arguing that the compact support domain $\Omega_{\mathbf{x}}$ of a kernel that is centered at point $\mathbf{x}$ is typically contained in the computational domain, i.e. $\Omega_{\mathbf{x}} \subset \Omega$ (Fig. 3.5). Furthermore, quantifying discretization errors in section 3.4.1, all summation operators in real and Fourier space have been applied to unbounded domains. As a consequence, the validity of the interpolation and discretization error estimates (3.34) is only

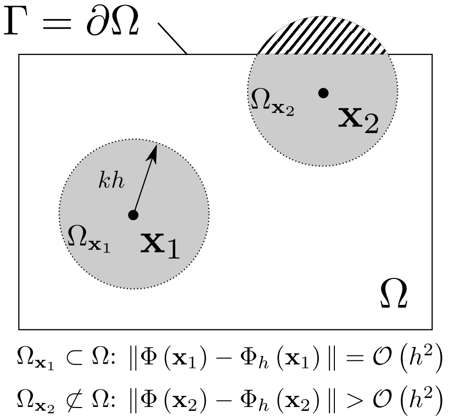
$\Gamma = \partial\Omega$
$\Omega_{\mathbf{x}_2}$
$\mathbf{x}_2$
kh
$\Omega_{\mathbf{x}_1}$
$\mathbf{x}_1$
Ω
$\Omega_{\mathbf{x}_1} \subset \Omega$: $\|\Phi(\mathbf{x}_1) - \Phi_h(\mathbf{x}_1)\| = \mathcal{O}(h^2)$
$\Omega_{\mathbf{x}_2} \not\subset \Omega$: $\|\Phi(\mathbf{x}_2) - \Phi_h(\mathbf{x}_2)\| > \mathcal{O}(h^2)$

Figure 3.5: Schematic of truncation of the compact kernel support domain $\Omega_{\mathbf{x}}$ by the computation domain boundary Γ leading to boundary inconsistency errors.

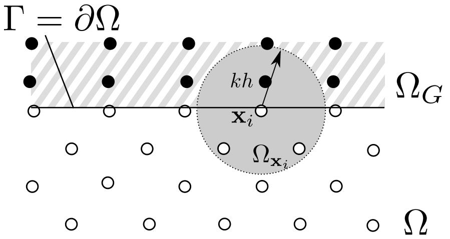
$\Gamma = \partial\Omega$
kh
Ω_G
$\mathbf{x}_i$
$\Omega_{\mathbf{x}_i}$
Ω

Figure 3.6: Schematic of the ghost particle approach whereby the set of sampling points is extended by spatially fixed ghost particles (closed markers) that are elements of the ghost domain Ω_G.

granted for bulk particles that are located at a distance kh from the boundary Γ. On the other hand, continuous completeness conditions (3.6)-(3.7) as well as their discrete counterparts in Eqs. (3.34) are violated if the compact support domain $\Omega_{\mathbf{x}}$ of the kernel is truncated by the computation domain boundary $\Gamma = \partial\Omega$, i.e. $\Omega_{\mathbf{x}} \not\subset \Omega$. The latter applies to boundary particles. Due to lack of completeness in the vicinity of Γ, boundary particles are prone to boundary inconsistency errors (Fig. 3.7). Since boundary particles lack sampling points that populate their compact support domains, boundary inconsistency errors are commonly also referred to as particle deficiency errors.

The condition of unbounded domains is typically not met by the initial boundary value problems that are considered in this work and suitable corrective approaches are thus required to account for boundary inconsistency errors. The most common approach to reduce boundary inconsistencies involves the use of so-called ghost particles that are elements of an artificial ghost domain Ω_G. The ghost domain extends the physical computation domain Ω (Fig. 3.6) and can be thought of as a layer of constant thickness kh that coats Ω at all points of its boundary Γ. The purpose of Ω_G is to recover completeness of the reproducing approximations at points of Γ. Upon discretization, ghost particles that are dis-

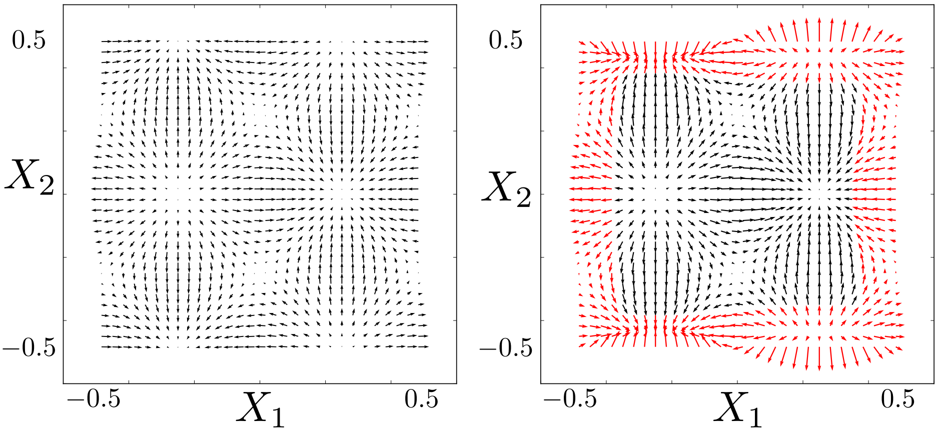

Figure 3.7: Analytic evaluation of the gradient field $\operatorname{grad}\Phi$ (left) and discrete reproducing approximation $\operatorname{grad}_{h,dx}\Phi$ (right) for $\Phi = \sin(2\pi X_1)\cos(2\pi X_2)$ within the bounded domain $\Omega = \{\mathbf{x} \in \mathbb{R}^2 \mid -0.5 \leq X_2, X_1 \leq 0.5\}$. Red arrows highlight boundary particles that are prone to boundary inconsistency errors.

crete nodal elements of Ω_G serve as sampling points for focal points in Ω. The properties of ghost particles are assigned at the beginning of a time step in such a way that the flux of a field variable across the boundary Γ^N takes a desired value (Neumann boundary condition) or such that the value of a field variable takes a desired value at Γ^D (Dirichlet boundary condition). The latter approach is conceptually equivalent to the ghost-cell approach in finite volume methods [see 123, § 7] and the ghost-point approach in finite difference methods [see 200, § 1.4]. The application of boundary conditions using ghost particles, in particular Dirichlet boundary conditions with respect to fluid velocity, is discussed in section 3.5.1.

However, the application of the ghost particle approach is cumbersome for deforming boundaries, e.g. free surfaces in fluid dynamics, due to their spatial and temporal variability. Furthermore, when taking the assumptions into account that boundary particles at free surfaces do not exchange mass, momentum or energy with the surrounding gas atmosphere, the use of ghost particles at free surfaces must be considered overly computationally expensive. The alternative approach to reduce boundary inconsistency errors at free surfaces involves the use of corrective reproducing approximations (section 3.4.3) that satisfy a given degree of completeness even when subject to truncated kernel supports.

Following section 2.1.5 and in the context of studying transport processes through porous media comprised of a rigid solid phase, the computation domain is restricted to the fluid phase $\Omega_\mathfrak{f}$ only and additional boundary conditions are specified on the solid surface $\Gamma_{\mathfrak{fs}}$. As a result, kernel truncation at the inner boundary $\Gamma_{\mathfrak{fs}}$ has to be prevented as well. Hence, not only do we take into account ghost particles at the system boundary $\partial\Omega$, but also at the solid surface $\Gamma_{\mathfrak{fs}}$. The latter are differentiated from each other by denoting the outer ghost domain adjacent to the system boundary Ω_{Go} and the inner ghost domain adjacent to the solid surface Ω_{Gi}. Despite the formal distinction, ghost particle properties of both ghost domains are assigned in similar manner.

3.4.3 Corrective approaches

The fundamental discrete reproducing approximations (3.21)-(3.23) are rarely used. This is due to the circumstance that even if the continuous completeness conditions (3.6) and (3.7) are satisfied in the absence of boundary inconsistency errors, the discrete equivalents in Eq. (3.33) and (3.34) may not. As shown in preceding sections, errors with respect to the discrete completeness conditions are large if particle distributions are highly non-uniform. Particle disorder even leads to error divergence as discretization errors increase with $\mathcal{O}(1/h)$ for decreasing smoothing lengths (Fig. 3.4). Corrective discrete reproducing approximations have been proposed in Liu et al. [127], Belytschko et al. [15], Bonet [24] and Bonet & Kulasegaram [25], among others, and a concise overview of corrective approaches is given in the following.

The most intuitive example of corrective approaches involves the correction of the discrete reproducing approximation $\Phi_{h,dx}$ to satisfy zeroth order completeness even if subject to nodal integration and boundary inconsistency. For that reason, we introduce the zeroth order complete kernel

$$W^{\mathrm{C0}}\left(\mathbf{x}_j, h\right) \coloneqq W\left(\mathbf{x}_j, h\right) K_0\left(\mathbf{x}_i\right),$$

where $K_0\left(\mathbf{x}_i\right)$ is a correction coefficient that is specific to a focal point $\mathbf{x}_i$ and chosen such that the normalization constraint

$$\sum_{j:\mathbf{x}_j\in\Omega_i} W^{\mathrm{C0}}\left(\mathbf{x}_j, h\right) V_j = \sum_{j:\mathbf{x}_j\in\Omega_i} W\left(\mathbf{x}_j, h\right) K_0\left(\mathbf{x}_i\right) V_j \overset{!}{=} 1,$$

is enforced. The resulting renormalized reproducing approximation [184]

$$\Phi_i^{\mathrm{C0}} \coloneqq \sum_{j:\mathbf{x}_j\in\Omega_i} \Phi_j W_{ij}^{\mathrm{C0}} V_j = \frac{\sum\limits_{j:\mathbf{x}_j\in\Omega_i} \Phi_j W_{ij} V_j}{\sum\limits_{j:\mathbf{x}_j\in\Omega_i} W_{ij} V_j}, \tag{3.36}$$

is commonly used as an alternative to Eq. (3.21). For constant scalar fields, Eq. (3.36) is exactly reproducing even if the completeness condition (3.33) is not satisfied and thus referred to as strictly zeroth order complete reproducing approximation. The preceding approach to enforce zeroth order completeness can be generalized to enforce an arbitrary number of completeness constraints. In particular, the m'th-order complete kernel [15, 127] is given as

$$W^{\mathrm{Cm}}\left(\mathbf{x}_j, h\right) := \mathbf{P}\left(\mathbf{x}_i - \mathbf{x}_j\right) \cdot \mathbf{K}_N\left(\mathbf{x}_i\right) W\left(\mathbf{x}_j, h\right),$$

where $\mathbf{P}\left(\mathbf{x}_i - \mathbf{x}_j\right) = \left\{1, \mathbf{x}_i - \mathbf{x}_j, \left(\mathbf{x}_i - \mathbf{x}_j\right) \otimes \left(\mathbf{x}_i - \mathbf{x}_j\right), \dots\right\}$ represents a polynomial basis and $\mathbf{K}_m$ is a vector of m free coefficients chosen such that a number m of completeness constraints are enforced. For $m = 0$, the latter can be reduced to the zeroth order complete kernel W^{C0}.

While the latter approach can be equivalently applied to derive corrective versions of the discrete gradient operator $\mathrm{grad}_{h,dx}$ as well, the computationally least expensive approach to enforce zeroth order completeness of the discrete gradient operator involves the trivial identity [137]

$$\mathrm{grad}\ \Phi = \mathrm{grad}\ \Phi - \Phi\ \mathrm{grad}\ 1.$$

Application of the reproducing approximation (3.22) to the above identity yields

$$\mathrm{grad}_i^{\mathrm{C0}}\ \Phi = \sum_{j:\mathbf{x}_j \in \Omega_i} \left[\Phi_j - \Phi_i\right] \frac{\partial W_{ij}}{\partial r_{ij}} \frac{\mathbf{x}_i - \mathbf{x}_j}{r_{ij}} V_j. \tag{3.37}$$

The discrete gradient operator (3.37) is strictly zeroth order complete since the gradient of constant fields Φ, for which the bracket term $\Phi_j - \Phi_i$ is zero, is exactly reproduced. Reproducing approximations of type Eq. (3.37) are therefor often used for boundary value problems involving free surfaces to reduce boundary inconsistency errors.

We empirically study the effect of using the discrete, zeroth order complete gradient operator (3.37) on convergence of the L^2 error norm (3.35). The parameters of the error analysis, in particular the input function as well as the grid point distribution, are chosen in equivalence to the error analysis discussed in section 3.4.1. For regular grids, i.e. $I_{dx} = 0$, and within the range of analyzed smoothing lengths, numerical errors that arise using the fundamental operator $\mathrm{grad}_{h,dx}$ are identical to those that arise using the zeroth order complete operator $\mathrm{grad}_{h,dx}^{C0}$ (Fig. 3.8, left column). On the other hand, for perturbed grids, the divergent behavior of $\mathrm{grad}_{h,dx}$, by which numerical errors increase with $\mathcal{O}(1/h)$ for decreasing smoothing lengths, is absent for all values of the ratio dx/h and grid point perturbation factor I_{dx} (Fig. 3.8, center and right column). Specifically, the resulting convergence behavior is in line with the preceding analytical error

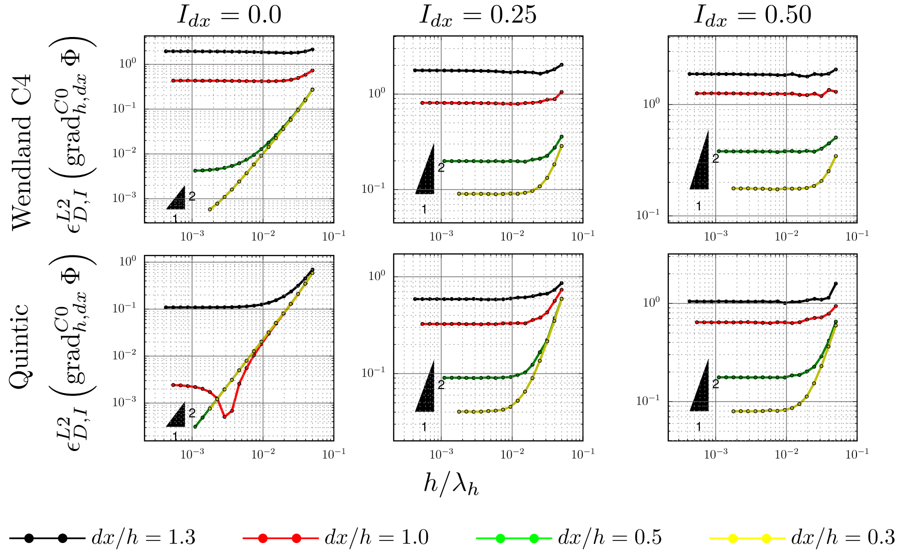

Figure 3.8: Empirical study of L^2 error convergence of the discrete, zeroth order complete gradient operator $\mathrm{grad}^{\mathrm{C0}}_{h,dx}\,\Phi$ in two dimensional space as a function of non-dimensional smoothing length h/λ_h, numerical length scale ratio dx/h, grid point perturbation factor I_{dx} and kernel functions W_w and W_q.

analysis for regular grids in that numerical errors scale with $\mathcal{O}(h^2)$ for large h and with $\mathcal{O}(dx/h)^{\zeta}$ for small h. Consequently, we assert that the use of the computationally inexpensive gradient operator (3.37) yields dramatic improvement of error convergence with respect to non-uniform particle distributions.

In contrast to the above corrective approaches where we enforce a certain degree of completeness, a conceptually different corrective approach is introduced using the calculus identity

$$\mathrm{grad}\ \Phi = \varrho\,\mathrm{grad}\left(\frac{\Phi}{\varrho}\right) + \frac{\Phi}{\varrho}\,\mathrm{grad}\left(\varrho\right), \tag{3.38}$$

where $\varrho = \varrho(\mathbf{x}, t)$ denotes the local mass density. Application of the reproducing approximation (3.22) to the above identity and taking into account $V_j = m_j/\varrho_j$ yields

$$\mathrm{grad}^{\mathrm{AS}}_i\,\Phi = \varrho_i \sum_{j:\mathbf{x}_j\in\Omega_i}\left[\frac{\Phi_i}{\varrho_i^2} + \frac{\Phi_j}{\varrho_j^2}\right]\frac{\partial W_{ij}}{\partial r_{ij}}\frac{\mathbf{x}_i - \mathbf{x}_j}{r_{ij}}m_j. \tag{3.39}$$

Given that $\mathbf{x}_i - \mathbf{x}_j = -(\mathbf{x}_j - \mathbf{x}_i)$ and the particle indices in the bracket term can be exchanged, the discrete gradient operator (3.39) is referred to as antisymmetric gradient operator $\text{grad}_i^{\text{AS}}$. Using antisymmetric operators, it is possible to construct discrete nodal motion equations which are globally conservative. Following Bonet [24], a simple illustration is provided considering the rate of change of total linear momentum in a closed system comprised of N particles in the absence of volumetric sources. The latter is given as

$$\dot{\mathfrak{J}}_N = \sum_{i:\mathbf{x}_i \in \Omega}^{N} m_i \dot{\mathbf{u}}_i = \sum_{i:\mathbf{x}_i \in \Omega}^{N} \mathbf{F}_i = \sum_{i:\mathbf{x}_i \in \Omega}^{N} \sum_{j:\mathbf{x}_j \in \Omega_i}^{N_n(\mathbf{x}_i)} \mathbf{F}_{ij}^I \overset{!}{=} 0,$$

where $\mathbf{F}_i$ denotes the total force acting on a particle i resulting from forces $\mathbf{F}_{ij}^I$ due to interaction with neighboring particles j. Total linear momentum is conserved if $\mathbf{F}_{ij}^I = -\mathbf{F}_{ji}^I$ which can be achieved using antisymmetric operators. In conclusion, rather than enforcing completeness, antisymmetric operators can be used to enforce conservation. Hereafter, we employ antisymmetric operators to derive nodal motion equations. We argue that conservative operators are more appropriate for the present simulations since, on the one hand, free surfaces which would otherwise motivate the use of zeroth-order complete stencils are absent such that particle deficiency errors are less critical, and, on the other hand, particle distributions exhibit uniformity due to quasi-incompressibility of the considered fluid phases.

Due to lack of completeness, however, antisymmetric operators are sensitive to truncation at domain boundaries and non-uniform particle distributions. Corresponding discretization errors are amplified in the case of discontinuous density fields $\varrho(\mathbf{x}, t)$ which are considered as weights in the identity (3.38). Considering multiphase problems where the density field might exhibit discontinuities, e.g. at a liquid-gas interface, the particle number density SPH variant, which was originally proposed in Ott & Schnetter [153] and further developed in [99, 195, 196], is often preferred.

The particle number density n_i of particle i is defined as

$$n_i \coloneqq \sum_{j:\mathbf{x}_j \in \Omega_i} W_{ij} \tag{3.40}$$

and is a measure of local particle concentration within the compact support domain Ω_i. Using Eq. (3.21), n_i can be interpreted as the reproducing kernel approximation of specific volume $n(\mathbf{x}, t) \coloneqq 1/V(\mathbf{x}, t)$ and, therefor, $n_i \approx 1/V_i$. While the density field $\varrho(\mathbf{x}, t)$ may be discontinuous at the interface between immiscible fluids, the particle number density is approximately constant for quasi-incompressible bulk phases by virtue of repulsive pressure forces acting between particles which tend to keep particle concentrations homogeneous. Hence, antisymmetric operators are derived on the basis of the identity

$$\text{grad}\ \Phi = n\,\text{grad}\left(\frac{\Phi}{n}\right) + \frac{\Phi}{n}\,\text{grad}\,(n)\,,$$

which yields

$$\text{grad}_i^{\text{ASn}}\ \Phi = n_i \sum_{j:\mathbf{x}_j\in\Omega_i}\left[\frac{\Phi_i}{n_i^2}+\frac{\Phi_j}{n_j^2}\right]\frac{\partial W_{ij}}{\partial r_{ij}}\frac{\mathbf{x}_i-\mathbf{x}_j}{r_{ij}}, \tag{3.41}$$

The antisymmetric operator (3.41) is independent of particle masses and densities, which leads to improved stability in the presence of high density contrast interfaces. However, if the density field is constant throughout the computation domain, Eq. (3.41) and Eq. (3.39) are equivalent to each other.

The above corrective approaches can be equivalently applied to the divergence operator (3.23). In particular, the discrete, zeroth order complete divergence operator is given as

$$\text{div}_i^{\text{C0}}\ \mathbf{\Phi} = \sum_{j:\mathbf{x}_j\in\Omega_i}\left[\mathbf{\Phi}_j-\mathbf{\Phi}_i\right]\cdot\frac{\partial W_{ij}}{\partial r_{ij}}\frac{\mathbf{x}_i-\mathbf{x}_j}{r_{ij}},$$

whereas density and number density weighted antisymmetric divergence operators are given as

$$\text{div}_i^{\text{AS}}\ \mathbf{\Phi} = \varrho_i \sum_{j:\mathbf{x}_j\in\Omega_i}\left[\frac{\mathbf{\Phi}_i}{\varrho_i^2}+\frac{\mathbf{\Phi}_j}{\varrho_j^2}\right]\cdot\frac{\partial W_{ij}}{\partial r_{ij}}\frac{\mathbf{x}_i-\mathbf{x}_j}{r_{ij}}m_j, \quad \text{and}$$

$$\text{div}_i^{\text{ASn}}\ \mathbf{\Phi} = n_i \sum_{j:\mathbf{x}_j\in\Omega_i}\left[\frac{\mathbf{\Phi}_i}{n_i^2}+\frac{\mathbf{\Phi}_j}{n_j^2}\right]\cdot\frac{\partial W_{ij}}{\partial r_{ij}}\frac{\mathbf{x}_i-\mathbf{x}_j}{r_{ij}}, \tag{3.42}$$

respectively.

3.5 Discrete nodal motion equations

For the derivation of the motion equations of SPH particles, we discretize spatial differential operators that are inherent in the governing balance equations using the discrete stencils introduced in the preceding sections. As a result, we compute discrete forces that act on lumped particle masses.

We model incompressible, single-phase flow with constant viscosity $\mu^{\mathfrak{f}}$ using the balance of linear momentum introduced in section 2.1, i.e.

$$\varrho^{\mathfrak{f}}\dot{\mathbf{u}}_{\mathfrak{f}} = \mu^{\mathfrak{f}}\operatorname{div}\left(\operatorname{grad}\mathbf{u}_{\mathfrak{f}}\right) - \operatorname{grad}p + \varrho^{\mathfrak{f}}\mathbf{b}, \qquad \forall\,\mathbf{x}\in\Omega_{\mathfrak{f}}. \tag{3.43}$$

For two-phase flow, on the other hand, we take into account immersed interfacial force densities as introduced in section 2.4, such that the whole-domain balance of linear momentum reads

$$\varrho^{\mathfrak{f}}\dot{\mathbf{u}}_{\mathfrak{f}} = \operatorname{div}\left[\mu^{\mathfrak{f}}\left(\operatorname{grad}\mathbf{u}_{\mathfrak{f}}\right) + \mu^{\mathfrak{f}}\left(\operatorname{grad}\mathbf{u}_{\mathfrak{f}}\right)^{T}\right] - \operatorname{grad}p + \varrho^{\mathfrak{f}}\mathbf{b} + \sum_{\alpha\beta}\operatorname{div}\left(\boldsymbol{\Pi}^{\alpha\beta}\delta^{\alpha\beta}\right)\cdot\mathbf{I}^{\mathfrak{fs}}, \quad \forall\,\mathbf{x}\in\Omega_{\mathfrak{f}}, \tag{3.44}$$

where non-constant fluid viscosities $\mu^{\mathfrak{f}}$ have been taken into account. Discretization of the two-phase balance equation (3.44) using the SPH method yields the intuitive motion equation

$$m_i\dot{\mathbf{u}}_i = \sum_{j:\mathbf{x}_j\in\Omega_i}\mathbf{F}^{V}_{ij} - \sum_{j:\mathbf{x}_j\in\Omega_i}\mathbf{F}^{P}_{ij} + \mathbf{F}^{G}_{i} + \tilde{\mathbf{F}}^{S}_{i}, \qquad \forall\,\mathbf{x}_i\in\Omega_{\mathfrak{f}}. \tag{3.45}$$

For single-phase flow, i.e. Eq. (3.43), the discrete immersed interfacial forces $\tilde{\mathbf{F}}^{S}_{i}$ can be omitted. Upon discretization, we hence find local balances of momentum transformed into a system of ordinary differential equations for the unknown particle velocities $\mathbf{u}_i$. A particle i is subject to force interaction with neighboring particles j that are located within its kernel compact support domain Ω_i. The total force acting on a fluid particle i is the sum of the volumetric force $\mathbf{F}^{G}_{i} = m_i\mathbf{b}$, the pressure interaction forces $\mathbf{F}^{P}_{ij}$ (see section 3.5.2), the viscous interaction forces $\mathbf{F}^{V}_{ij}$ (see section 3.5.3) and the reduced interfacial force $\tilde{\mathbf{F}}^{S}_{i}$ (see section 3.5.4).

We recall that the kernel compact support domain of boundary particles not only covers neighboring fluid particles $j:\mathbf{x}_j\in\Omega_{\mathfrak{f}}$, but also neighboring ghost particles $j:\mathbf{x}_j\in\Omega_G$. Hence, force interactions $\mathbf{F}^{P}_{ij}$ and $\mathbf{F}^{V}_{ij}$ may occur between two fluid particles or between a fluid particle and a ghost particle. In deriving the force interactions, we thus have to consider a case differentiation. As to be introduced in section 3.5.1, interaction forces that act between fluid particles and ghost particles are designed in such a way that boundary conditions are enforced.

3.5.1 Boundary conditions

Following section 2.1.5, boundary conditions are required on the inner solid-fluid interface $\Gamma_{\mathfrak{fs}}$ as well as on the outer boundary Γ. Incorporating boundary conditions into SPH, two crucial aspects have to be taken into account:

1. The compact support domain of boundary particles must be populated with sampling particles as to minimize particle deficiency errors, i.e. boundary inconsistency errors. In this work, the latter is achieved by introducing ghost particles with prescribed properties as elements of a ghost domain Ω_G that coats the physical boundaries Γ and $\Gamma_{\mathfrak{fs}}$ (see section 3.4.2). Alternative methods to incorporate boundary conditions in SPH other than using ghost particles exist (see review Violeau & Rogers [204] and references therein). However, the use of spatiotemporally fixed ghost particles as proposed by Adami et al. [2] constitutes a computationally efficient and conceptually simple approach in light of complex boundaries in porous media. We highlight prescribed properties of ghost particles with an asterisk character in the superscript, i.e. $(\bullet)^*$.

2. The interpolants $W_V(\mathbf{x}_i) = W(\mathbf{x}_i - \mathbf{x}_j, h)\, V_j$ do not satisfy the Kronecker delta property due to which $\Phi_{h,dx}(\mathbf{x}_i) \neq \Phi_i W_V(\mathbf{x}_i)$ (see section 3.2). The latter implies that trivially setting the ghost particle properties $\mathbf{\Phi}^*(\mathbf{x}, t) = \mathbf{\Phi}_\Gamma(\mathbf{x}, t)$ for a generic field $\mathbf{\Phi}$ fails to reproduce the Dirichlet boundary condition $\mathbf{\Phi} = \mathbf{\Phi}_\Gamma(\mathbf{x}, t)$, $\forall\, \mathbf{x} \in \Gamma^D$.

In the context of simulating flow through porous media, we commonly apply periodic boundary conditions at system boundaries as to avoid effects that otherwise arise due to spatial boundedness and, furthermore, no-slip and no-penetration boundary conditions at solid surfaces. The prescription of ghost particle properties at periodic and Dirichlet boundaries is discussed in the following.

Periodic boundary conditions on Γ^P

In the predominant number of simulations that are presented in this treatise, periodic boundary conditions are applied with respect to the outer boundary, i.e. $\Gamma^P = \Gamma$. The aim is to reduce computational efforts in studying effective transport properties of porous materials that can be described in terms of a representative volume element (RVE). Although not unambiguous, the most common definition of RVEs is that of the smallest unit of microstructure periodicity. Implementing periodic boundary conditions using the well-known minimum image convention [134], the domain of computation can be reduced to the size of a single RVE only while computation results remain representative of an unbounded domain. Boundary effects that would otherwise result in the context of using bounded domains are hence absent.

From a schematic point of view, the unit of computation Ω is replicated multiple times and each copy is subsequently translated with respect to all Cartesian directions along which periodicity is prescribed. As a result, a periodic unbounded domain tiled with copies of Ω is generated. Taking into account the compact support of the smoothing kernel, the periodic unbounded domain can

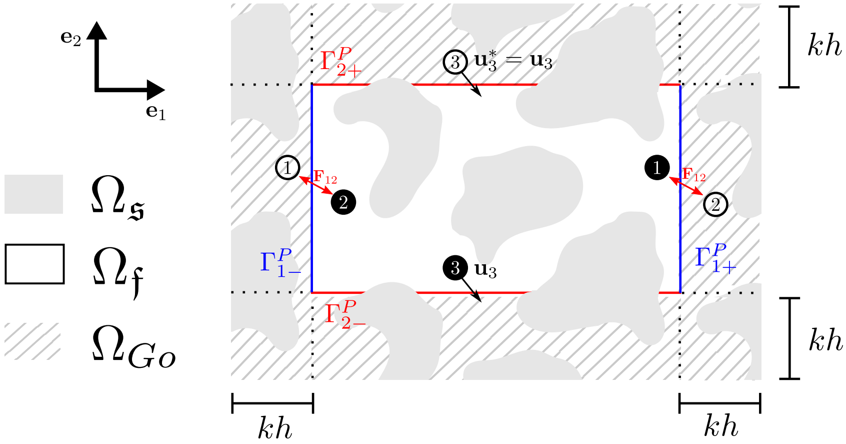

Figure 3.9: Schematic representation of periodic boundary conditions applied to a rectangular domain in two dimensions using the minimum image convention. The outer ghost domain Ω_{Go}, the width of which is equal to the compact support radius kh, is populated with replicating ghost particles (open markers) that are replications of fluid points located in Ω (closed markers).

be computationally reduced to the domain of computation Ω and the outer ghost domain Ω_{Go} only. The outer ghost domain Ω_{Go} is populated with replicating ghost particles as a result of replicating and translating fluid particles that are elements of Ω (Fig. 3.9). Considering a ghost particle $j : \mathbf{x}_j^* \in \Omega_{Go}$ to be a replication of a fluid particle $i : \mathbf{x}_i \in \Omega$ implies that for all field variables Φ we prescribe $\Phi_j^* = \Phi_i$. The latter includes mass, momentum, energy, stress state as well as material properties.

If a fluid particle i is located in the vicinity of the periodic boundary, it may exchange mass, momentum or energy with neighboring replicating ghost particles that are elements of its compact support domain Ω_i. The latter is illustrated in Fig. 3.9, where particles labeled ① and ② interact with each others replicating ghost particles. Furthermore, a fluid particle that leaves the unit of computation Ω reappears through the opposite face (e.g. Fig. 3.9, particle labeled ③). From a computational point of view, an efficient implementation of periodic boundary conditions does not require allocation of additional memory space since the properties of a replicating ghost particle are identical to those of a fluid particle. Instead, a replicating particle is typically implemented as pointer to the original fluid particle with its position being shifted by the size of the computation domain in direction of periodicity. The latter reduces computational costs since the generation of replicating particles must be performed for each time iteration.

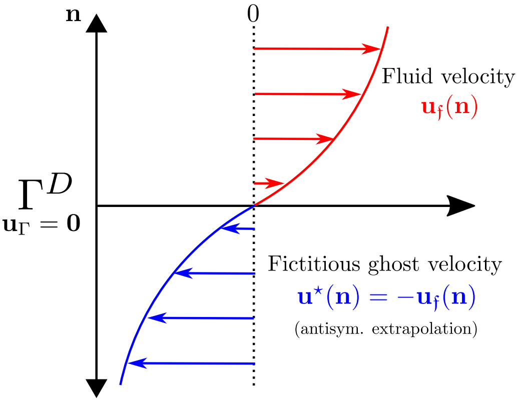
n
0
Fluid velocity
$\mathbf{u}_{\mathfrak{f}}(\mathbf{n})$
Γ^D
$\mathbf{u}_\Gamma = \mathbf{0}$
Fictitious ghost velocity
$\mathbf{u}^\star(\mathbf{n}) = -\mathbf{u}_{\mathfrak{f}}(\mathbf{n})$
(antisym. extrapolation)

Figure 3.10: Schematic of fictitious velocity field (blue line) that is prescribed to ghost particles plotted in direction $\mathbf{n}$ normal to the Dirichlet boundary. Fictitious velocities exhibit antisymmetry with respect to the fluid velocity field (red line) about the plane of symmetry Γ^D. Accounting for viscous momentum exchange between ghost particles and fluid particles subsequently reproduces the no-slip condition.

No-slip and no-penetration boundary conditions on Γ^D

No-slip and no-penetration at points of the Dirichlet boundary Γ^D implies the kinematic constraint

$$\mathbf{u}_{\mathfrak{f}}\left(\mathbf{x}, t\right) = \mathbf{u}_\Gamma\left(\mathbf{x}, t\right), \quad \forall \left(t, \mathbf{x}\right) \in \left(0, T\right) \times \Gamma^D, \tag{3.46}$$

where $\mathbf{u}_\Gamma$ denotes the prescribed boundary velocity. Following Adami et al. [2], we proceed to introduce a computational approach to account for such Dirichlet boundary conditions. For flow in porous media, Dirichlet boundary conditions are prescribed on the solid surface $\Gamma_{\mathfrak{f}\mathfrak{s}}$ whereas periodic boundary conditions are applied on the outer domain boundaries Γ. For most of the validation simulations presented in section 4, however, Dirichlet boundary conditions are prescribed on Γ as well.

We model no-slip and no-penetration boundary conditions by prescribing velocities and pressures of ghost particles such that mutual force interactions $\mathbf{F}_{ij}^P$ and $\mathbf{F}_{ij}^V$ between ghost particles and fluid particles constraints the dynamics of fluid particles close to Dirichlet boundaries. In particular, ghost particle pressures $p^\star$ are prescribed such that the boundary exerts a repulsive pressure force onto fluid particles. Moreover, ghost particle velocities $\mathbf{u}^\star$ are prescribed such that the viscous momentum exchange between fluid particles and ghost particles prevents relative movement of Dirichlet boundaries and adjacent fluid particles. Since it is important to differentiate ghost particle velocities $\mathbf{u}^\star$ from the prescribed advection velocity $\mathbf{u}_\Gamma$ of the boundary, the former are hereafter referred to as fictitious velocities.

In the course of this treatise, Dirichlet boundaries are most commonly considered static and impermeable such that we first discuss the special case of zero velocities $\mathbf{u}_{\mathfrak{f}} = \mathbf{u}_\Gamma = \mathbf{0}$ for all $(t, \mathbf{x}) \in (0, T) \times \Gamma^D$. A computationally efficient method to satisfy the zero velocity boundary condition is to extrapolate fluid velocities onto particles of the ghost domain. The extrapolation is performed such that fictitious particle velocities are antisymmetric with respect to the fluid velocity field about the plane of symmetry Γ^D in direction $\mathbf{n}$ normal to the Dirichlet boundary (Fig. 3.10). The latter is achieved by prescribing

$$\mathbf{u}_i^\star = -\frac{\sum\limits_{j:\mathbf{x}_j \in \Omega_i \cap \Omega_f} \mathbf{u}_j W_{ij} V_j}{\sum\limits_{j:\mathbf{x}_j \in \Omega_i \cap \Omega_f} W_{ij} V_j}, \quad \forall \mathbf{x}_i \in \Omega_G^D, \tag{3.47}$$

where Ω_G^D denotes the ghost domain adjacent to the static boundary (Fig. 3.11). Note that the interpolation (3.47) is supported on the truncated kernel domain $\Omega_i \cap \Omega_f$ only (see Fig. 3.11). For that reason, use of the zeroth order complete approximation (3.36) rather than the fundamental interpolation (3.17) is crucial as to reduce particle deficiency errors. Due to zeroth order consistency, Eq. (3.47) is indeed observed to yield $\mathbf{u}_i^\star = -\mathbf{u}_j$ irrespective of particle distribution when fluid velocities $\mathbf{u}_j = \text{const.}$.

Equation (3.47) constitutes a simple approach to account for no-slip when boundaries are static. On the other hand, for the more general case of moving boundaries $\mathbf{u}_\Gamma \neq \mathbf{0}$ fictitious velocities are prescribed according to

$$\mathbf{u}_i^\star = 2\mathbf{u}_\Gamma - \frac{\sum\limits_{j:\mathbf{x}_j \in \Omega_i \cap \Omega_f} \mathbf{u}_j W_{ij} V_j}{\sum\limits_{j:\mathbf{x}_j \in \Omega_i \cap \Omega_f} W_{ij} V_j}, \quad \forall \mathbf{x}_i \in \Omega_G^D. \tag{3.48}$$

Equation (3.48) was originally proposed in Pozorski & Wawrenczuk [162] and later revisited in Adami et al. [2].

It is crucial to note that upon domain discretization an uncertainty naturally exists in the exact position of the interface Γ^D (see Fig. 3.11). The magnitude of spatial uncertainty is in the order of the domain discretization length scale $\mathcal{O}(dx_0)$, which subsequently takes the role of a slip length. Hence, application of the fictitious velocity approach will yield an apparent slip boundary condition with a slip length dx_0, rather than a no-slip boundary condition. If, however, the discretization length scale dx_0 is smaller than the viscous boundary layer thickness, the viscous force interaction $\mathbf{F}_{ij}^V$ between the fluid and ghost particles accurately reproduces the effect of no-slip boundary conditions. In chapter 4, the latter is demonstrated using numerical validation computations. On the other hand, the apparent slip is desired to account for moving contact lines, where the no-slip boundary condition would otherwise result in singular tangential stresses at the contact line [101, 185]. An undesired effect of the apparent numerical slip is, however, the discretization dependency of the slip length. As a result,

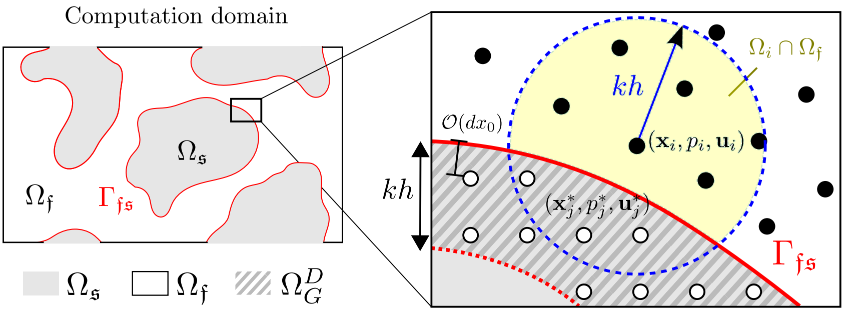
Computation domain
$\Omega_{\mathfrak{s}}$
$\Omega_{\mathfrak{f}}$
$\Gamma_{\mathfrak{fs}}$
$\Omega_{\mathfrak{s}}$
$\Omega_{\mathfrak{f}}$
Ω_G^D
$\Omega_i \cap \Omega_{\mathfrak{f}}$
kh
$\mathcal{O}(dx_0)$
$(\mathbf{x}_i, p_i, \mathbf{u}_i)$
kh
$(\mathbf{x}_j^*, p_j^*, \mathbf{u}_j^*)$
$\Gamma_{\mathfrak{fs}}$

Figure 3.11: Schematic representation of fixed ghost particles (open markers) that populate the ghost domain (shaded region) adjacent to a solid surface (red line). Ghost particles serve as sampling points for fluid particles $\mathbf{x}_i \in \Omega_{\mathfrak{f}}$ (closed markers). Fictitious ghost particle properties $p_j^\star$ and $\mathbf{u}_j^\star$ enforce essential boundary conditions. Upon discretization, the spatial uncertainty with respect to the exact position of the boundary $\Gamma_{\mathfrak{fs}}$ is of order $\mathcal{O}(dx_0)$.

local non-equilibrium processes in the vicinity of a moving contact line must be considered artificial.

Fictitious pressures $p^\star$ of ghost particles are prescribed as to prevent penetration of impermeable Dirichlet boundaries. We first discuss the special case of static boundaries. Evaluating the balance of linear momentum (2.28) at points of the Dirichlet boundary in direction normal to the surface while considering volumetric forces absent and accounting for zero boundary velocities yields

$$-\operatorname{grad} p \cdot \mathbf{n} = 0, \quad \forall\, (t, \mathbf{x}) \in (0, T) \times \Gamma^D,$$

where $\mathbf{n}$ denotes the normal vector to Γ^D. In other words, pressure gradients normal to static and impermeable boundaries vanish, or, introducing a coordinate $n_\perp$ that is aligned along $\mathbf{n}$, we introduce the well-known notation

$$\frac{\partial p}{\partial n_\perp} = 0, \quad \forall\, (t, \mathbf{x}) \in (0, T) \times \Gamma^D. \tag{3.49}$$

Besides Eq. (3.46), Eq. (3.49) must thus be satisfied for consistent implementation of the no-penetration boundary condition. To account for Eq. (3.49) in the numerical scheme, we follow Adami et al. [2] and compute $p^\star$ by means of interpolating fluid pressures using the normalized reproducing approximation (3.36), i.e.

$$p_i^\star = \frac{\sum\limits_{j:\mathbf{x}_j \in \Omega_i \cap \Omega_f} p_j W_{ij} V_j}{\sum\limits_{j:\mathbf{x}_j \in \Omega_i \cap \Omega_f} W_{ij} V_j}, \quad \forall\, \mathbf{x}_i \in \Omega_G^D. \tag{3.50}$$

Assuming a homogeneous fluid pressure field $p_j = \text{const.}$ for all $\mathbf{x}_j \in \Omega_f$, e.g. in thermal equilibrium, yields $p_i^\star = p_j$ for all $\mathbf{x}_i \in \Omega_G^D$ irrespective of particle distribution which is consistent with Eq. (3.49). While Eq. (3.50) suffices when boundaries are static and volumetric force densities $\mathbf{b}$ absent, modified fictitious pressures are necessary when the latter conditions do not apply. In particular, the more general case of accelerating boundaries ($\dot{\mathbf{u}}_\Gamma \neq \mathbf{0}$) as well as non-negligible volumetric force densities ($\mathbf{b} \neq \mathbf{0}$) renders momentum balances normal to impermeable boundaries to read

$$\operatorname{grad} p \cdot \mathbf{n} = \frac{\partial p}{\partial n_\perp} = \varrho^\mathfrak{f} \left(\mathbf{b} - \dot{\mathbf{u}}_\Gamma\right) \cdot \mathbf{n}, \quad \forall\, (t, \mathbf{x}) \in (0, T) \times \Gamma^D. \tag{3.51}$$

To account for Eq. (3.51) in the numerical scheme, we consider the first-order truncated Taylor series expansion of the pressure field about a point $\mathbf{x} \in \Gamma^D$ such that

$$p(\mathbf{x}') = p(\mathbf{x}) + \operatorname{grad} p \cdot (\mathbf{x}' - \mathbf{x}) + \mathcal{O}(h^2).$$

Evaluating the series along the direction of the normal $\mathbf{n}$ such that $(\mathbf{x}' - \mathbf{x})/\|\mathbf{x}' - \mathbf{x}\| = \mathbf{n}$ yields

$$\frac{p(\mathbf{x}') - p(\mathbf{x})}{\|\mathbf{x}' - \mathbf{x}\|} \approx \operatorname{grad} p \cdot \mathbf{n}. \tag{3.52}$$

Substituting Eq. (3.52) into Eq. (3.51) we find

$$p(\mathbf{x}') \approx p(\mathbf{x}) + \varrho^\mathfrak{f} \left(\mathbf{b} - \dot{\mathbf{u}}_\Gamma\right) \cdot \left(\mathbf{x}' - \mathbf{x}\right), \quad \forall\, (t, \mathbf{x}) \in (0, T) \times \Gamma^D. \tag{3.53}$$

We prescribe fictitious pressures $p^\star$ of ghost particles adjacent to a moving boundary by means of interpolating the RHS of Eq. (3.53) using the zeroth order complete reproducing approximation (3.36), such that

$$p_i^\star = \frac{\sum\limits_{j:\mathbf{x}_j \in \Omega_i \cap \Omega_f} p_j W_{ij} V_j}{\sum\limits_{j:\mathbf{x}_j \in \Omega_i \cap \Omega_f} W_{ij} V_j} + (\mathbf{b} - \dot{\mathbf{u}}_\Gamma) \cdot \frac{\sum\limits_{j:\mathbf{x}_j \in \Omega_i \cap \Omega_f} m_j (\mathbf{x}_i - \mathbf{x}_j) W_{ij}}{\sum\limits_{j:\mathbf{x}_j \in \Omega_i \cap \Omega_f} W_{ij} V_j}, \quad \forall \mathbf{x}_i \in \Omega_G^D, \tag{3.54}$$

where $\varrho_j V_j = m_j$ has been accounted for. Clearly, for vanishing volumetric force densities and static boundaries Eq. (3.54) reduces to Eq. (3.50). In particular, the first term on the RHS of Eq. (3.54) is the kernel interpolation of fluid pressures p_j, evaluated at the point of the ghost particle $\mathbf{x}_i$. In the presence of a gravity force density $\mathbf{b} = \mathbf{g} = \text{const.}$, the balancing hydrostatic equilibrium pressure field is linear along the direction of $\mathbf{g}$, which is accounted for by the second term on the RHS of Eq. (3.54). Hence, unbalanced pressure gradients and related spurious volumetric fluxes across the impermeable Dirichlet boundary are absent. Equation (3.54) constitutes the main result of Adami et al. [2]. As fluid velocities and pressures evolve in time, fictitious properties of ghost particles according to Eqs. (3.48) and (3.54) have to be recomputed for every time iteration.

3.5.2 Interparticle pressure forces

Introducing the pressure interaction force $\mathbf{F}_{ij}^P$ we differentiate whether the fluid particle i interacts with a neighboring fluid particle $j : \mathbf{x}_j \in \Omega_\mathfrak{f}$ or with a neighboring ghost particle $j : \mathbf{x}_j \in \Omega_G$. In the case of the latter, the fictitious pressure $p^\star$ is either given by Eq. (3.54) adjacent to an impermeable Dirichlet boundary Γ^D or $p^\star$ is equal to the pressure of a replicated fluid particle adjacent to a periodic boundary Γ^P (see section 3.5.1).

Application of the number-density weighted antisymmetric gradient stencil (3.41) to $\{\text{grad}\, p\}$ will yield the pressure interaction forces

$$\mathbf{F}_{ij}^P = \begin{cases} \left[\dfrac{p_i}{n_i^2} + \dfrac{p_j}{n_j^2}\right] \dfrac{\partial W_{ij}}{\partial r_{ij}} \dfrac{\mathbf{x}_i - \mathbf{x}_j}{r_{ij}}, & \text{if } \mathbf{x}_j \in \Omega_\mathfrak{f} \text{ and } \forall\, \mathbf{x}_i \in \Omega_\mathfrak{f}, \\[2ex] \left[\dfrac{p_i}{n_i^2} + \dfrac{p_j^\star}{n_j^2}\right] \dfrac{\partial W_{ij}}{\partial r_{ij}} \dfrac{\mathbf{x}_i - \mathbf{x}_j}{r_{ij}}, & \text{if } \mathbf{x}_j \in \Omega_G \text{ and } \forall\, \mathbf{x}_i \in \Omega_\mathfrak{f}. \end{cases} \tag{3.55}$$

Since particle indices i and j can be exchanged in the bracket term and taking into account the antisymmetry (3.12) the pressure interaction forces satisfy the conservation criterion $\mathbf{F}_{ij}^P = -\mathbf{F}_{ji}^P$. However, as the stencil (3.55) does not satisfy any order of completeness, the truncation of kernel compact support domains must be avoided. Hence, for flow problems involving free surfaces the strictly zeroth order complete stencil (3.37) constitutes the more favorable choice to discretize pressure gradients. As free surfaces are absent herein, the momentum conserving stencil (3.55) is exclusively used for all simulations presented in this thesis.

3.5.3 Interparticle viscous forces

As discussed in Monaghan [136], the computation of Laplacian operators using an integral SPH approximation that involves the second-order derivative of W is sensitive to particle disorder. Moreover, such formulations may violate the dissipation inequality when modeling viscous flow or thermal conduction if the discrete stencil lacks antisymmetry with respect to particle indices [66, 203]. An alternative formulation is thus derived by applying the number-density weighted antisymmetric divergence stencil (3.42) to the Laplacian term $\{\mu^{\mathfrak{f}}\,\mathrm{div}\,(\mathrm{grad}\,\mathbf{u}_{\mathfrak{f}})\}$, i.e.

$$\mu^{\mathfrak{f}}\,\mathrm{div}_i^{\mathrm{ASn}}\,(\mathrm{grad}\,\mathbf{u}_{\mathfrak{f}}) = n_i\,\mu^{\mathfrak{f}} \sum_{j:\mathbf{x}_j\in\Omega_i} \left[\frac{(\mathrm{grad}\,\mathbf{u}_{\mathfrak{f}})_i}{n_i^2} + \frac{(\mathrm{grad}\,\mathbf{u}_{\mathfrak{f}})_j}{n_j^2}\right] \cdot \frac{\partial W_{ij}}{\partial r_{ij}}\frac{\mathbf{x}_i - \mathbf{x}_j}{r_{ij}}. \tag{3.56}$$

Even though discretization of the gradient operators appearing in Eq. (3.56) using the gradient stencils (3.37), (3.39) or (3.41) would yield an expression of the Laplacian which is free of second-order kernel derivatives, such an approach would imply a computationally expensive two-fold summation over neighboring particles $j : \mathbf{x}_j \in \Omega_i$. For that reason, the gradient operators are typically approximated using a truncated Taylor series expansion of the field variable as initially proposed in Brookshaw [33] and later revised in Morris [139], Cleary [46] and Tartakovsky et al. [198] among others. The Taylor series expansion of $\mathbf{u}$ about point $\mathbf{x}$ reads

$$\mathbf{u}(\mathbf{x}') = \mathbf{u}(\mathbf{x}) + \mathrm{grad}\,\mathbf{u}\cdot(\mathbf{x}' - \mathbf{x}) + \mathcal{O}(h^2),$$

or, upon discretization, we find

$$\begin{aligned}\mathbf{u}_i - \mathbf{u}_j &= (\mathrm{grad}\,\mathbf{u})_i \cdot (\mathbf{x}_i - \mathbf{x}_j) + \mathcal{O}(h^2),\\ \mathbf{u}_i - \mathbf{u}_j &= (\mathrm{grad}\,\mathbf{u})_j \cdot (\mathbf{x}_i - \mathbf{x}_j) + \mathcal{O}(h^2).\end{aligned} \tag{3.57}$$

Substituting Eqs. (3.57) into Eq. (3.56) yields

$$\mu^{\mathfrak{f}}\,\mathrm{div}_i^{\mathrm{ASn}}\left(\mathrm{grad}\,\mathbf{u}_{\mathfrak{f}}\right) \approx n_i\,\mu^{\mathfrak{f}} \sum_{j:\mathbf{x}_j\in\Omega_i} \left[\frac{1}{n_i^2}+\frac{1}{n_j^2}\right] \frac{\mathbf{u}_i-\mathbf{u}_j}{r_{ij}}\frac{\partial W_{ij}}{\partial r_{ij}}, \quad \forall\,\mathbf{x}_i\in\Omega_{\mathfrak{f}} \tag{3.58}$$

for constant viscosity $\mu^{\mathfrak{f}}$. Equation (3.58) exhibits antisymmetry with respect to the particle indices i and j. Moreover, when Eq. (3.58) is applied to model viscous flow, Galilean invariance is inherently satisfied since the viscous interaction forces only depend on relative velocities $\mathbf{u}_i - \mathbf{u}_j$ rather than absolute velocities. The latter further ensures that viscous extra stresses vanish in static equilibrium, i.e. for $\mathbf{u}_i = \mathbf{u}_j$. For two-phase flow, spatial variability of fluid viscosity has to be taken into account. Following Hu & Adams [99], viscous particle interaction forces for non-constant viscosities are approximated as

$$\mathbf{F}_{ij}^{V} = \begin{cases} \left[\frac{1}{n_i^2}+\frac{1}{n_j^2}\right] \frac{2\mu_i\mu_j}{\mu_i+\mu_j}\frac{\mathbf{u}_i-\mathbf{u}_j}{r_{ij}}\frac{\partial W_{ij}}{\partial r_{ij}}, & \text{if } \mathbf{x}_j\in\Omega_{\mathfrak{f}} \text{ and } \forall\,\mathbf{x}_i\in\Omega_{\mathfrak{f}}, \\ \left[\frac{1}{n_i^2}+\frac{1}{n_j^2}\right] \frac{2\mu_i\mu_j^\star}{\mu_i+\mu_j^\star}\frac{\mathbf{u}_i-\mathbf{u}_j^\star}{r_{ij}}\frac{\partial W_{ij}}{\partial r_{ij}}, & \text{if } \mathbf{x}_j\in\Omega_G^P \text{ and } \forall\,\mathbf{x}_i\in\Omega_{\mathfrak{f}}, \\ \left[\frac{1}{n_i^2}+\frac{1}{n_j^2}\right] \mu_i\frac{\mathbf{u}_i-\mathbf{u}_j^\star}{r_{ij}}\frac{\partial W_{ij}}{\partial r_{ij}}, & \text{if } \mathbf{x}_j\in\Omega_G^D \text{ and } \forall\,\mathbf{x}_i\in\Omega_{\mathfrak{f}}. \end{cases} \tag{3.59}$$

In Eq. (3.59), the effective viscosity for two interacting fluid particles i and j is the harmonic mean of particle viscosities μ_i and μ_j. As illustrated in Hu & Adams [99], for locally linear velocity fields the latter ensures continuity of viscous extra stresses across material interfaces. For a ghost particle $j : \mathbf{x}_j \in \Omega_G^P$ adjacent to a periodic boundary, the replicated viscosity $\mu_j^\star$ is used. In order to ensure continuity of fluid velocity across Dirichlet boundaries, on the other hand, the effective viscosity for the mutual interaction of a fluid particle i and a ghost particle $j : \mathbf{x}_j \in \Omega_G^D$ is the viscosity of the focal particle μ_i. The fictitious velocity $\mathbf{u}_j^\star$ of a ghost particle j is either given by Eq. (3.48) adjacent to a Dirichlet boundary, i.e. $\mathbf{x}_j \in \Omega_G^D$, or $\mathbf{u}_j^\star$ is equal to the velocity of a replicated fluid particle at a periodic boundary, i.e. i.e. $\mathbf{x}_j \in \Omega_G^P$.

3.5.4 Immersed interfacial particle forces

We proceed to introduce the reduced interfacial force $\tilde{\mathbf{F}}_i^S$. Following Eq. $(2.88)_1$, we evaluate the interface Dirac distribution of the interface $\Gamma_{\alpha\beta}$ at point $\mathbf{x}_i$ as norm of the spatial gradient of the respective phase indicator field $C^{\alpha\beta}$, i.e. $\delta_i^{\alpha\beta} = \|\mathrm{grad}_i\, C^{\alpha\beta}\|$. Care has to be taken in the computation since the phase indicator field $C^{\alpha\beta}$ is undefined for all $\mathbf{x}_i \notin \{\Omega_\alpha, \Omega_\beta\}$. The latter renders a case differentiation necessary. Evaluating the gradient of the phase indicator field using

$$\operatorname{grad}_i^{\mathrm{ASn}} C^{\alpha\beta} = \begin{cases} \displaystyle\sum_{j:\mathbf{x}_j \in \Omega_i \cap (\Omega_\alpha \cup \Omega_\beta)} n_i \left[\frac{C_i^{\alpha\beta}}{n_i^2} + \frac{C_j^{\alpha\beta}}{n_j^2} \right] \frac{\partial W_{ij}}{\partial r_{ij}} \frac{\mathbf{x}_i - \mathbf{x}_j}{r_{ij}} & \\ \displaystyle\quad + \sum_{j:\mathbf{x}_j \in \Omega_i \setminus (\Omega_\alpha \cup \Omega_\beta)} n_i \left[\frac{C_i^{\alpha\beta}}{n_i^2} + \frac{C_i^{\alpha\beta}}{n_j^2} \right] \frac{\partial W_{ij}}{\partial r_{ij}} \frac{\mathbf{x}_i - \mathbf{x}_j}{r_{ij}}, & \forall \mathbf{x}_i \in \left\{\Omega_\alpha, \Omega_\beta\right\}, \\ \mathbf{0}, & \forall \mathbf{x}_i \notin \left\{\Omega_\alpha, \Omega_\beta\right\}, \end{cases} \tag{3.60}$$

yields interface Dirac distributions $\delta_i^{\alpha\beta}$ that are indeed compactly supported in the vicinity of the interface $\Gamma_{\alpha\beta}$. As in section 2.4, the interfaces $\Gamma_{\alpha\beta} \in \{\Gamma_{\mathfrak{wn}}, \Gamma_{\mathfrak{ns}}, \Gamma_{\mathfrak{ws}}\}$ separate the bulk phases $\Omega_\alpha \in \{\Omega_{\mathfrak{n}}, \Omega_{\mathfrak{w}}\}$ and $\Omega_\beta \in \{\Omega_{\mathfrak{n}}, \Omega_{\mathfrak{s}}\}$. In evaluating (3.60), we take into account that ghost particles adjacent to the fluid-solid interface are elements of the solid domain $\Omega_{\mathfrak{s}}$.

The interfacial stress tensor defined in Eq. (2.56) is subsequently computed as

$$\mathbf{\Pi}_i^{\alpha\beta} = \begin{cases} \sigma^{\alpha\beta} \left(\mathbf{I} - \mathbf{n}_i^{\alpha\beta} \otimes \mathbf{n}_i^{\alpha\beta} \right) \delta_i^{\alpha\beta} & \text{if } \|\operatorname{grad}_i C^{\alpha\beta}\| > 0, \\ \mathbf{0}, & \text{otherwise}, \end{cases} \qquad \forall \mathbf{x}_i \in \Omega_{\mathfrak{f}} \cup \Omega_G, \tag{3.61}$$

where the unit normal $\mathbf{n}_i^{\alpha\beta} := \operatorname{grad}_i C^{\alpha\beta} / \|\operatorname{grad}_i C^{\alpha\beta}\|$ according to Eq. $(2.88)_2$. Note that the interfacial stress tensors $\mathbf{\Pi}_i^{\alpha\beta}$ are computed for all particles including ghost particles that are elements of Ω_G. The latter avoids particle deficiency errors close to solid-fluid interfaces when computing divergences of the immersed interfacial stress tensors. In particular, the discrete equivalent of the interfacial force density (2.67) is the interfacial force $\mathbf{F}_i^{S,\alpha\beta}$ acting on a fluid particle i, which reads

$$\mathbf{F}_i^{S,\alpha\beta} = \sum_{j:\mathbf{x}_j \in \Omega_i} \left[\frac{\mathbf{\Pi}_i^{\alpha\beta}}{n_i^2} + \frac{\mathbf{\Pi}_j^{\alpha\beta}}{n_j^2} \right] \cdot \frac{\partial W_{ij}}{\partial r_{ij}} \frac{\mathbf{x}_i - \mathbf{x}_j}{r_{ij}}, \quad \forall \mathbf{x}_i \in \Omega_{\mathfrak{f}}, \tag{3.62}$$

where the divergence of the interfacial stress tensor is evaluated using the stencil (3.42). As mentioned above, the stencil (3.62) is not prone to particle deficiency errors since the domains Ω_i are fully supported close to solid-fluid interfaces as well. The total interfacial force is the sum of all immersed interfacial forces $\mathbf{F}_i^S = \sum_{\alpha\beta} \mathbf{F}_i^{S,\alpha\beta}$ according to Eq. (2.94). Following what was proposed in section 2.4.6, components of $\mathbf{F}_i^S$ that act in direction normal to the solid-fluid interfaces $\Gamma_{\mathfrak{ns}}$ and $\Gamma_{\mathfrak{ws}}$ are removed such that the action of the total interfacial force at points of the three-phase contact line is reduced to planes tangent to the solid surface only. The latter is achieved using the reduced interfacial force

$$\tilde{\mathbf{F}}_i^S := \begin{cases} \mathbf{F}_i^S - \left(\mathbf{F}_i^S \cdot \mathbf{n}_i^{\mathfrak{ns}}\right) \mathbf{n}_i^{\mathfrak{ns}} & \text{if } \delta_i^{\mathfrak{ns}} > 0, \delta_i^{\mathfrak{ns}} > \delta_i^{\mathfrak{ws}}, \\ \mathbf{F}_i^S - \left(\mathbf{F}_i^S \cdot \mathbf{n}_i^{\mathfrak{ws}}\right) \mathbf{n}_i^{\mathfrak{ws}} & \text{if } \delta_i^{\mathfrak{ws}} > 0, \delta_i^{\mathfrak{ws}} > \delta_i^{\mathfrak{ns}}, \end{cases} \quad \forall\, \mathbf{x}_i \in \Omega_{\mathfrak{f}}, \tag{3.63}$$

according to the modification proposed in Eq. (2.93).

3.6 Simulation parameterization

Initialization

The total computation domain Ω is initially discretized by placing particles on the lattice sites of a uniform Cartesian grid with initial isotropic particle spacing dx_0 and setting initial particle volumes to $V_{0,i} = dx_0^d$ in d-dimensional space. Subsequently, we assign initial conditions for the velocities $\mathbf{u}_{0,i} = \mathbf{u}(\mathbf{x}, t = 0)$ and densities $\varrho_{0,i} := \varrho\left(\mathbf{x}_i, t = 0\right)$ for all particles. Once initialized, the particles properties $C_i^{\alpha\beta}$ and $\mu_i = \mu\left(\mathbf{x}_i\right)$ remain constant during time integration. While the phase fields $C_i^{\alpha\beta}$ are assigned to all particles, viscosities are defined for fluid particles $i : \mathbf{x}_i \in \Omega_{\mathfrak{f}}$ only. Particle masses $m_i := \varrho_{0,i} V_{0,i}$ remain unchanged during simulation as well such that mass conservation is trivially satisfied. Note that in two-dimensional space the unit of $V_{0,i}$ is that of volume per unit of length, which implies that respective particle masses m_i have unit of mass per unit of length. The subscript 0 indicates an initial condition - being a quasi-incompressible method, the evolution of particle densities ϱ_i and particle volumes V_i in time has to be considered. However, the equation of state is calibrated such that relative fluctuations $\Delta\varrho$ of particle densities with respect to initial densities are negligible.

Rather than using uniform initial grids more sophisticated approaches to discretize the computation domain exist [47, 56]. These methods avoid numerical noise at short time scales about the initial time $t = 0$, where the set of fluid particles typically rearranges into an energetically relaxed glass-like close-packing configuration (see Fig. 3.3). We omit the use of more sophisticated discretization schemes, since in this thesis, we analyze effects at times scales at which the effects of particle rearrangement are negligible.

Time integration

Explicit time integration of the particle motion equation (3.45) and position update $\dot{\mathbf{x}}_i = \mathbf{u}_i$ for all $\mathbf{x}_i \in \Omega_{\mathfrak{f}}$ is performed using a modified predictor-corrector scheme of second order accuracy in time due to its often asserted stability [19, 163] when using adaptive time step widths Δt. The predictor step reads

$$\tilde{\mathbf{u}}_i^{1/2} = \mathbf{u}_i^0 + \frac{\Delta t}{2}\dot{\mathbf{u}}_i^0 \text{ and } \tilde{\mathbf{x}}_i^{1/2} = \mathbf{x}_i^0 + \frac{\Delta t}{2}\tilde{\mathbf{u}}_i^{1/2}, \tag{3.64}$$

where the superscripts 0 and 1/2 denote a system at current time t and half-step time $t + (\Delta t/2)$, respectively, and $(\tilde{\bullet})$ indicates predicted half-step time values. The corrector step reads

$$\mathbf{u}_i^{1/2} = \mathbf{u}_i^0 + \frac{\Delta t}{2}\dot{\mathbf{u}}_i^{1/2} \text{ and } \mathbf{x}_i^{1/2} = \mathbf{x}_i^0 + \frac{\Delta t}{2}\mathbf{u}_i^{1/2}, \tag{3.65}$$

where the velocity rates $\dot{\mathbf{u}}_i^{1/2} = \dot{\mathbf{u}}_i(\tilde{\mathbf{x}}_i^{1/2}, \tilde{\mathbf{u}}_i^{1/2})$ are computed for a system at predicted half-step. A time step is finally completed with

$$\mathbf{u}_i^1 = 2\mathbf{u}_i^{1/2} - \mathbf{u}_i^0 \text{ and } \mathbf{x}_i^1 = 2\mathbf{x}_i^{1/2} - \mathbf{x}_i^0, \tag{3.66}$$

where the superscript 1 denotes a system at time $t + \Delta t$. The presented explicit time integration scheme is only conditionally stable. Following Morris [141], the time step size Δt is adaptively limited by the stability conditions

$$\Delta t \leq \min\left\{\frac{0.25h}{\max_i c_i}, \frac{h^2 \min_i \varrho_{0,i}}{8 \max_i \mu_i}, \sqrt{\frac{h}{16\|\mathbf{b}\|}}, \sqrt{\frac{h^3 \min_i \varrho_{0,i}}{32\pi\sigma^{\mathfrak{nw}}}}\right\}, \tag{3.67}$$

which ensures stable time integration in the presence of propagating pressure waves, viscous diffusion fronts, gravity waves and capillary waves, respectively. For single-phase flow, the capillary wave condition in Eq. (3.67) can be disregarded. The operators $\max_i$ and $\min_i$ apply to the total set of fluid particles $\mathbf{x}_i \in \Omega_{\mathfrak{f}}$. In modeling quasi-incompressible bulk fluid phases, the first condition in Eq. (3.67), the well known CFL-condition [48], is typically the dominant one.

Quasi-incompressibility

According to the first condition in Eq. (3.67), the use of physical speed of sounds would yield prohibitively small time steps. It is therefor common practice to use a numerical speed of sound c_i with a magnitude large enough such that relative, dimensionless density fluctuations $\Delta\varrho$ about the initial density $\varrho_{0,i}$ are small, and, on the other hand, with a magnitude small enough such that time step widths are large enough to make numerical computations feasible. Such an approximation is reasonable in the absence of strong shock waves or if acoustic effects play a minor role for the transport problem at hand. We choose $\Delta\varrho = 1\% = 0.01$ and set

$$c_i^2 = \max\left\{\frac{U_{\mathrm{ref}}^2}{\Delta\varrho}, \frac{\mu_i U_{\mathrm{ref}}}{\varrho_{0,i} L_{\mathrm{ref}} \Delta\varrho} \frac{\|\mathbf{b}\| L_{\mathrm{ref}}}{\Delta\varrho}, \frac{\sigma^{\mathfrak{nw}}}{\varrho_{0,i} L_{\mathrm{ref}} \Delta\varrho},\right\}, \tag{3.68}$$

as suggested in Morris [141]. As introduced in section 2.3.4, U_{ref} and L_{ref} denote characteristic velocity and characteristic length scale, respectively, which depend on the particular boundary value problem.

Application of the linear state equation (2.21) will yield the local fluid pressures

$$p_i = c_i^2 \left(m_i n_i - \varrho_{0,i}\right) + p_0, \qquad \forall\, \mathbf{x}_i \in \Omega_{\mathfrak{f}}. \tag{3.69}$$

where the local fluid density ϱ_i is evaluated using the particle number density n_i, which satisfies $n_i = 1/V_i$ in the absence of truncation errors [99, 153, 195, 196]. The background pressure p_0 is introduced to avoid instabilities due to negative pressures [194]. Hence, the magnitude of p_0 should be large enough such that $p_i > 0\ \forall\ \mathbf{x}_i \in \Omega_{\mathfrak{f}}$. However, the background pressure should be small enough such that numerical dispersion effects, which, according to Morris [139], occur for excessively large values of p_0, are negligible. In all our simulations, we set $p_0 = 0.1 \max_i \left(c_i^2 \varrho_{0,i}\right)$.

Computational implementation

The main simulation procedure is summarized in algorithm 1. Even though the computational implementation is not discussed in this thesis, we shall note that time-explicit SPH algorithms can be optimized by performing the particle for-loops, i.e. computations for all $\mathbf{x}_i \in \Omega_{\mathfrak{f}}$, in parallel. Implementing the parallel algorithm on distributed memory machines can be achieved by exploiting the fact that a particle i only interacts with neighboring particles $j : \mathbf{x}_j \in \Omega_i$. Hence, domain decomposition is possible. However, as particles are advected in space, domain decomposition has to be performed dynamically and frequent communication between parallel processes occurs. For an efficient implementation of neighbor for-loops that frequently occur in the force computation function 2, a neighbor searching algorithm is crucial. In the software that was implemented for the purpose of this thesis, we use a cell-linked list method as outlined in Griebel et al. [79]. The cell-linked list is particularly efficient if the kernel radius kh, which determines the edge length of the cells, remains constant in time and space and, furthermore, if the computation domain is homogeneously populated with particles such that load balancing is not required.

Algorithm 1 Pseudocode representing the general structure of two-phase SPH simulations, including initialization and time stepping. For single-phase flow, lines which are highlighted blue can be omitted.

```
procedure SPH SIMULATION(IBVP)

    const $\Omega, \Omega_\mathfrak{f}, \Omega_\mathfrak{s}, \Omega_{\alpha,0}$    ▷ Define simulation domain
    const $U_\text{ref}, L_\text{ref}, \Delta\varrho, \mathbf{b}, h, p_0, dx_0, T_\text{max}, d, \ldots$    ▷ Set simulation parameters
    const $\mu^\alpha, \varrho^\alpha, \sigma^{\alpha\beta}, \Theta_\text{eq}$    ▷ Set material parameters

    for all $\mathbf{x}_i \in \Omega$ do
        $\mathbf{x}_i \leftarrow \mathbf{x}_{0,i}(dx_0)$    ▷ Discretize $\Omega$ and initialize particle positions
        $\mathbf{u}_i \leftarrow \mathbf{u}_{0,i}$    ▷ Initialize particle velocities
        const $C_i^{\mathfrak{fs}} \leftarrow 1$ if $\mathbf{x}_i \in \Omega_G$ else $0$    ▷ Set ghost particle indicator
        const $C_i^{\alpha\beta} \leftarrow 1$ if $\mathbf{x}_i \in \Omega_\beta$, $0$ if $\mathbf{x}_i \in \Omega_\alpha$    ▷ Set phase indicator fields
    end for

    for all $\mathbf{x}_i \in \Omega_\mathfrak{f}$ do
        $\varrho_i \leftarrow \varrho_{0,i}$    ▷ Initialize particle densities
        const $m_i \leftarrow \varrho_{0,i} dx_0^d$    ▷ Set particle masses
        const $\mu_i \leftarrow \mu^\alpha$ if $\mathbf{x}_i \in \Omega_\alpha$    ▷ Set particle viscosities
        const $c_i \leftarrow$ Eq. (3.68)    ▷ Set numerical sound speeds
    end for

    const $\Delta t \leftarrow$ Eq. (3.67)    ▷ Set time step width
    $t \leftarrow t_0$    ▷ Initialize time

    while $t \leq T_\text{max}$ do    ▷ Start time stepping loop

        $\mathbf{x}_i^0 \leftarrow \mathbf{x}_i, \mathbf{u}_i^0 \leftarrow \mathbf{u}_i$    ▷ Store current particle positions and velocities
        $\dot{\mathbf{u}}_i^0 \leftarrow$ COMPUTE PARTICLE ACCELERATIONS($t$)
        $\mathbf{u}_i \leftarrow \tilde{\mathbf{u}}_i^{1/2}, \mathbf{x}_i \leftarrow \tilde{\mathbf{x}}_i^{1/2}$    ▷ Predictor step to $t + \Delta t/2$ with Eqs. (3.64)
        $\dot{\mathbf{u}}_i^{1/2} \leftarrow$ COMPUTE PARTICLE ACCELERATIONS($t + \Delta t/2$)
        $\mathbf{u}_i \leftarrow \mathbf{u}_i^{1/2}, \mathbf{x}_i \leftarrow \mathbf{x}_i^{1/2}$    ▷ Corrector step to $t + \Delta t/2$ with Eqs. (3.65)
        $\mathbf{u}_i \leftarrow \mathbf{u}_i^1, \mathbf{x}_i \leftarrow \mathbf{x}_i^1$    ▷ Complete step to $t + \Delta t$ with Eqs. (3.66)

        File output

    end while

end procedure
```

Algorithm 2 Pseudocode representing the computation of fluid particle accelerations $\dot{\mathbf{u}}_i^t$ at a given time step t. This function is called twice within the time stepping loop outlined in Algorithm 1. For single-phase flow, lines which are highlighted blue can be omitted.

```
function Compute particle accelerations($t$)

    Generate replicating ghost particles in $\Omega_{Go}$ for periodicity adjacent to $\Gamma^P$

    for all $\mathbf{x}_i \in \Omega_\mathfrak{f}$ do
        $n_i \leftarrow$ Eq. (3.40)                    ▷ Update particle number densities
        $p_i \leftarrow$ Eq. (3.69)                    ▷ Update particle pressures
    end for

    for all $\mathbf{x}_i \in \Omega_G^D$ do
        $p_i^\star \leftarrow$ Eq. (3.54)              ▷ Update fictitious pressures adjacent to $\Gamma^D$
        $\mathbf{u}_i^\star \leftarrow$ Eq. (3.48)     ▷ Update fictitious velocities adjacent to $\Gamma^D$
    end for

    for all $\mathbf{x}_i \in \Omega_\mathfrak{f}$ do
        $\dot{\mathbf{u}}_i^t \leftarrow \mathbf{0}$                 ▷ Set particle accelerations to zero
        $\dot{\mathbf{u}}_i^t \mathrel{+}= \mathbf{F}_i^G / m_i$      ▷ Volumetric forces
        for all neighbors $j : \mathbf{x}_j \in \Omega_i$ do
            $\dot{\mathbf{u}}_i^t \mathrel{+}= \mathbf{F}_{ij}^P / m_i$   ▷ Pressure interaction forces (Eq. (3.55))
            $\dot{\mathbf{u}}_i^t \mathrel{+}= \mathbf{F}_{ij}^V / m_i$   ▷ Viscous interaction forces (Eq. (3.59))
        end for
        for all interfaces $\Gamma_{\alpha\beta} \in \{\Gamma_{\mathfrak{wn}}, \Gamma_{\mathfrak{ns}}, \Gamma_{\mathfrak{ws}}\}$ do
            $\delta_i^{\alpha\beta} \leftarrow \|\mathrm{grad}_i\, C^{\alpha\beta}\|$   ▷ Interface Dirac distributions (Eq. (3.60))
            $\mathbf{\Pi}_i^{\alpha\beta} \leftarrow$ Eq. (3.61)        ▷ Interfacial stress tensors
            $\mathbf{F}_i^{S,\alpha\beta} \leftarrow$ Eq. (3.62)        ▷ Immersed interfacial forces
        end for
        $\mathbf{F}_i^S \leftarrow \sum_{\alpha\beta} \mathbf{F}_i^{S,\alpha\beta}$   ▷ Total interfacial forces
        $\tilde{\mathbf{F}}_i^S \leftarrow$ Eq. (3.63)                ▷ Reduced interfacial forces
        $\dot{\mathbf{u}}_i^t \mathrel{+}= \tilde{\mathbf{F}}_i^S / m_i$
    end for

    Shift particles that cross periodic boundaries to opposite edge

    return $\dot{\mathbf{u}}_i^t$

end function
```

CHAPTER 4

Simulation model validation

In the following chapter, we discuss validation simulations and identify appropriate choices of the discretization parameter dx_0 and kernel W. Seven different simulation setups, each of which represent different aspects of single and multi-phase flow, are considered. In section 4.1, we discuss the transient evolution of Poiseuille flow until, eventually, the quasi-static parabolic velocity profile is recovered. In section 4.2, we consider the well-known lid-driven cavity problem for large Reynolds numbers. We proceed to discuss single-phase flow simulations through three-dimensional porous microstructures comprised of regular sphere-packings in section 4.3. In section 4.4, we analyze the capability of the model to reproduce the equilibrium capillary pressure for a system where a droplet is fully immersed in another fluid. In section 4.5, we discuss laminar flow of multiple fluids arranged in layers between parallel plates and focus on modeling accuracy with respect to interfacial viscous coupling. In section 4.6, the capillary rise of a wetting fluid between parallel plates is simulated and we focus on numerical accuracy in predicting equilibrium contact angles, meniscus shapes and meniscus heights. Dynamic and non-equilibrium processes are discussed in section 4.7, where the free oscillation of fully-immersed fluid droplets is discussed. For all validation cases, we have either access to benchmark results or to closed-form solutions.

4.1 Poiseuille flow between parallel plates

The creeping flow of a Newtonian fluid between parallel plates of infinite extension is driven by a volumetric acceleration $\mathbf{b} = g\mathbf{e}_1$. The plates are separated by a

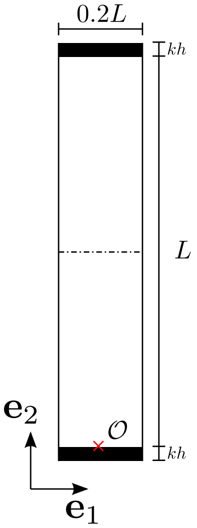

Figure 4.1: Simulation configuration (2-dimensional) for Poiseuille flow. Black area corresponds to fictitious solid phase domain $\Omega_\mathfrak{s}$ and white area corresponds to fluid phase domain $\Omega_\mathfrak{f}$. The dotted line represents a line of symmetry and the point of origin is indicated by the red cross marker. Cartesian coordinates with respect to the unit vectors $\mathbf{e}_1$ and $\mathbf{e}_2$ read X_1 and X_2, respectively. In order to reduce truncation errors, the thickness of the fictitious solid phase domain is chosen to be equal to the compact support radius kh and subsequently populated with ghost particle to account for no-slip and no-penetration at the fluid-solid interface according to section 3.5.1.

distance $L = 1$ m. The computation domain is periodic in direction of $\mathbf{e}_1$ and bounded by ghost particles that represent the static and impermeable plates in direction of $\mathbf{e}_2$. No-slip is modeled for $X_2 = 0$ and $X_2 = L$. Initial particle velocities are set to $\mathbf{u}_{0,i} = \mathbf{0}$. Simulations are based on the quintic kernel W_q. We compute the transient evolution of the velocity profile $U_1(X_2, t)$ in direction of $\mathbf{e}_1$ until steady-state is detected in the evolution of total kinetic energy. The driving volumetric acceleration $g = 0.1$ m/s^2 is chosen small enough such that the Reynolds number Re as defined in Eq. (2.70) is of order $\text{Re} = \mathcal{O}(1)$. Viscosity and initial density are chosen $\mu = 0.01$ Pa s and $\varrho = 1$ kg/m^3, respectively. For the resulting creeping flow, steady-state implies the well-known parabolic velocity profile. A series solution for the transient evolution is given in Morris & Fox [140] as

$$\begin{aligned} U_1(X_2, t) = &\frac{g\varrho}{2\mu} X_2 \left(X_2 - L\right) \\ &+ \sum_{n=0}^{\infty} \frac{4 g \varrho L^2}{\mu \pi^3 (2n+1)^3} \sin\left(\frac{\pi X_2}{L}(2n+1)\right) \exp\left(-\frac{(2n+1)^2 \pi^2 \mu}{\varrho L^2} t\right), \end{aligned}$$

where the second term on the RHS vanishes in steady-state. In the following, the series solution is truncated for $n > 100$. The plate separation L is chosen to be the characteristic length scale $L_\text{ref} = L$ in Eq. (3.68), whereas U_ref is chosen to be the maximum velocity at steady-state, i.e. $U_\text{ref} = \lim_{t\to\infty} U_1(X_2 =$

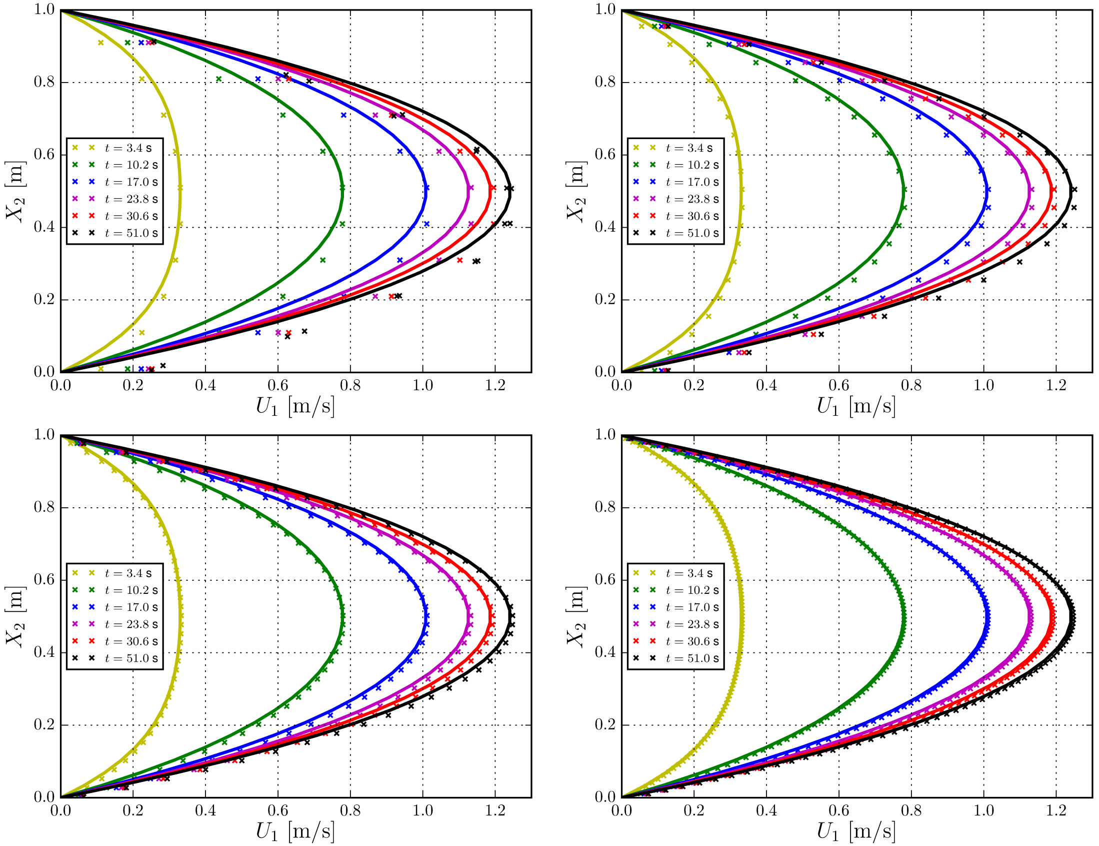

Figure 4.2: Transient evolution of the velocity profile $U_1(X_2, t)$ in direction of $\mathbf{e}_1$ for various numerical resolutions $dx/L = 10, 20, 40, 100$ (from top left to bottom right). SPH solutions are represented by the cross markers whereas the closed-form series solution is represented by the solid lines.

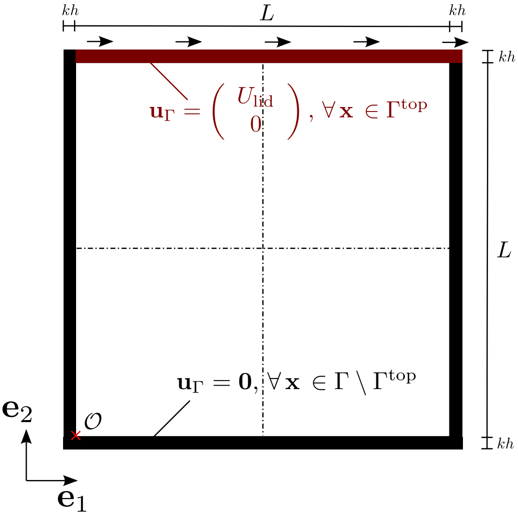
kh
L
kh
kh
$\mathbf{u}_\Gamma = \begin{pmatrix} U_{\text{lid}} \\ 0 \end{pmatrix}, \forall \mathbf{x} \in \Gamma^{\text{top}}$
L
$\mathbf{u}_\Gamma = \mathbf{0}, \forall \mathbf{x} \in \Gamma \setminus \Gamma^{\text{top}}$
$\mathbf{e}_2$
$\mathcal{O}$
kh
$\mathbf{e}_1$

Figure 4.3: Simulation configuration for lid-driven square cavity flow. Flow within the fluid region, represented by the white area, is driven by the prescribed velocity $\mathbf{u}_\Gamma = U_{\text{lid}}\mathbf{e}_1$ of the upper boundary Γ^{top}, which is referred to as lid. The remaining boundaries $\Gamma \setminus \Gamma^{\text{top}}$ remain impermeable and static. No-slip conditions apply to all boundaries of the fluid region. For further details on notation, see caption to Fig 4.1.

$0.5L, t) = (g\varrho L^2)/(8\mu)$. Numerical results for the transient evolution are in close agreement to the series solution for numerical resolutions $dx/L \geq 10$, i.e. when at least ten particles populate the computation domain along the height of the fluid region (Fig. 4.2). The latter indicates the accuracy of the time stepping stencil and compliance of the numerical method with the no-slip boundary condition. Moreover, we find the relative difference between $U_1(X_2 = 0.5L, t = \infty)$ and the numerically predicted maximum steady-state velocity to be 2.91% for $dx/L = 10$ and 0.16% for $dx/L = 100$. Hence, the interparticle viscous forces accurately represent viscous momentum diffusion and convergence is detected for increasing resolution.

4.2 Lid-driven square cavity flow

We simulate the recirculating flow of a Newtonian fluid within a square-shaped cavity that is driven by the prescribed velocity U_{lid} of the upper lid of the cavity (Fig. 4.3). The lid-driven square cavity flow constitutes a challenging numerical problem that is widely used for benchmark purposes. In particular, the latter is due to singularities that occur at the upper corners, the increasing number of flow vortices for increasing Reynolds numbers and the non-zero Dirichlet boundary condition with respect to fluid velocity at the upper lid. Natural choices for characteristic scales as used in Eq. (3.68) are $L_{\text{ref}} = L$ and $U_{\text{ref}} = U_{\text{lid}}$. We choose $\varrho = 1$ kg/m^3, $U_{\text{lid}} = 1$ m/s and $L = 1$ m and vary the Reynolds number Re by setting fluid viscosity $\mu = (\varrho U_{\text{lid}} L)/\text{Re}$ according to Eq. (2.70). Initial

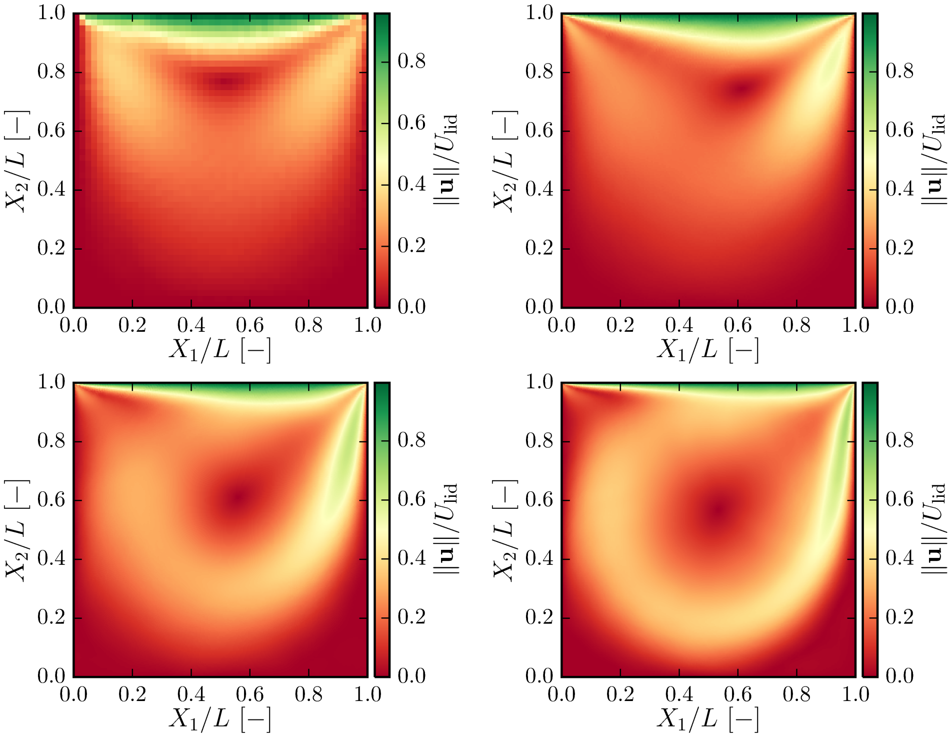

Figure 4.4: Normalized velocity magnitudes during lid-driven square cavity flow for $\text{Re} = 1, 100, 400, 1000$ (from top-left to bottom-right). Plot was generated by linearly interpolating unstructured SPH particle data of particle velocities to points of a regular grid using `matplotlib.mlab.griddata` and subsequently plotting the scalar field of normalized fluid velocity magnitudes.

particle velocities are set to $\mathbf{u}_{0,i} = \mathbf{0}$ and steady-state is detected in the evolution of total kinetic energy. The Dirichlet boundary condition $\mathbf{u}_\Gamma = U_{\text{lid}}\mathbf{e}_1$ for all points $\mathbf{x} \in \Gamma^{\text{lid}}$ of the upper lid is applied by taking into account the prescribed velocity in Eq. (3.48). For all points $\mathbf{x} \in \Gamma \setminus \Gamma^{\text{lid}}$ of the remaining boundaries, the boundary condition $\mathbf{u}_\Gamma = \mathbf{0}$ applies. We measure the numerical resolution in terms of the ratio L/dx_0 and use the quintic kernel W_q.

Steady-state velocity fields (Fig. 4.4) as well as vertical and horizontal velocity profiles (Fig. 4.5) are in general agreement with the well-anticipated benchmark results of Ghia et al. [76]. For $\text{Re} = 1$, a reference computation has been performed using OpenFOAM [206]. The symmetric flow field is reproduced for $\text{Re} = 1$ and velocity profiles are in excellent agreement with reference results even

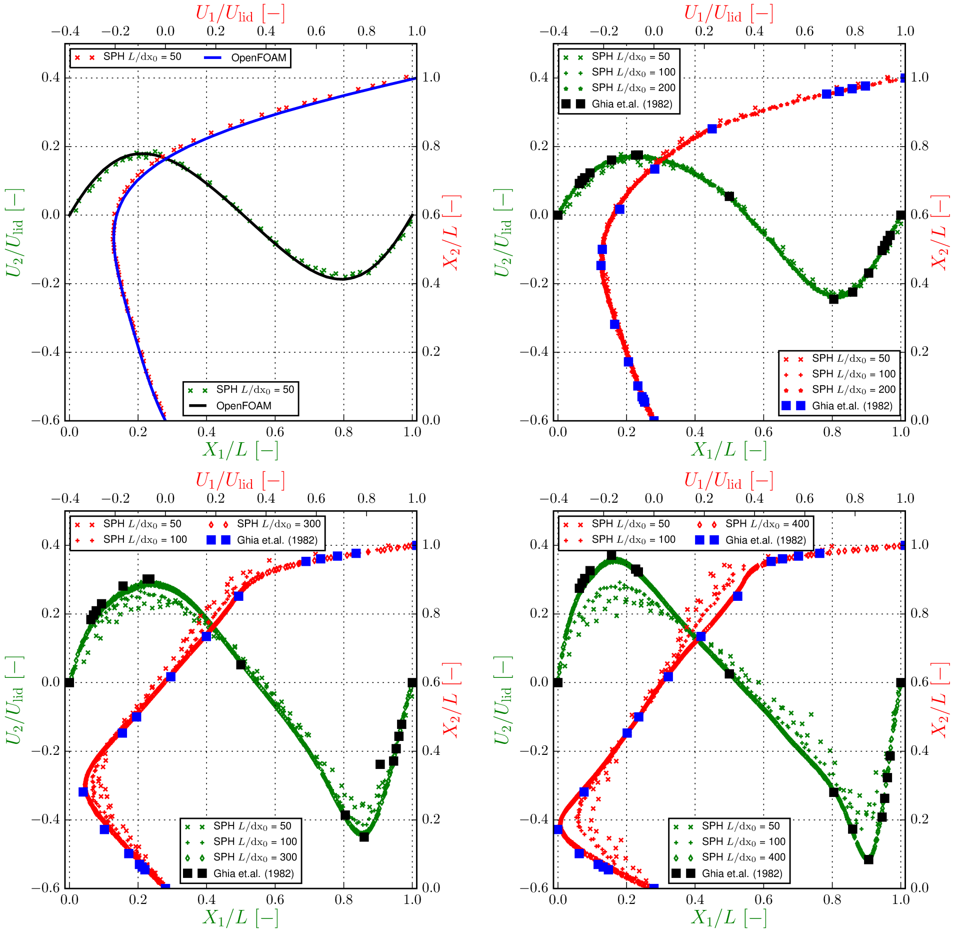

Figure 4.5: Normalized velocity profiles $U_1(X_1/L = 0.5, X_2/L)$ (Red markers and blue lines) and $U_2(X_1/L, X_2/L = 0.5)$ (Green markers and black lines) along vertical and horizontal symmetry lines of the square cavity, respectively, for Re $= 1, 100, 400, 1000$ (from top-left to bottom-right). Cross markers represent velocity components of SPH particles that are located within the narrow region $\pm dx_0$ from the central symmetry lines. Numerical reference results have been adopted from Ghia et al. [76] (Re $= 100, 400, 1000$, square markers) or computed using OpenFOAM [206] (Re $= 1$, solid lines). Numerical resolutions for SPH computations are given in terms of the ratio L/dx_0.

for the lowest considered resolution $L/dx_0 = 50$. For Re = 100, inertial forces move the center of the primary vortex away from the central symmetry line and related velocity profiles are reproduced using SPH simulations for all tested resolutions L/dx_0. For Re = 400 and Re = 1000, the computed velocity profiles deviate from the reference results for the lowest resolution $L/dx_0 = 50$; although profiles of the primary vortex are reproduced with satisfactory accuracy even for the lowest tested resolution. Deviations are attributed to large velocity gradients that appear in close vicinity to the boundaries and the second-order accuracy of the interpolating stencil. For finer numerical resolution, however, a convergence behavior is observed. For $L/dx_0 = 300$ and $L/dx_0 = 400$, velocity profiles for Re = 400 and Re = 1000, respectively, are in excellent agreement with reference results.

4.3 Permeability of sphere packings

We compute the creeping flow of an incompressible, Newtonian fluid through the pore-space of a periodic sphere packing driven by a volumetric acceleration $\mathbf{b}$. We consider sphere packings comprised of equal-sized spheres arranged on the lattice sites of simple (SC), body-centered (BCC) or face-centered (FCC) cubic lattices. Packings are referred to as consolidated (C) if the diameter D of the spheres is large enough to cause overlap or contact of spheres and non-consolidated (NC) if spheres are not in contact with each other. We further introduce the so-called close-touching limit (CTL), which refers to the value of D where initial contact occurs such that a close packing is formed. All spheres are considered static and impermeable and thus represented by ghost particles that account for no-slip and no-penetration on sphere surfaces (Fig. 4.6, top row). Due to periodicity and isotropy of lattice and steady-state flow field, the computation domain can be reduced to a cubic unit-cell of side-length L with periodic boundary conditions applied to all faces of the computation domain. Initial particle velocities are set to $\mathbf{u}_{0,i} = \mathbf{0}$ and fluid viscosity and density are chosen $\mu = 0.001$ Pa s and $\varrho = 1000$ kg/m^3, respectively. The unit-cell side-length is chosen $L = 1$ mm. Simulations are based on the quintic kernel W_q and steady-state is detected in the evolution of total kinetic energy. The initial particle spacing is chosen such that the ratio $L/dx_0 = 60$ for all simulations. Particle spacing is kept constant for all simulations for reasons of simplicity. As discussed in Holmes et al. [96], however, adapting the numerical resolution to an effective pore-throat length scale is more sensible. In contrast to the previous simulation cases, the current benchmark case is simulated in three-dimensional space.

Porosity ϕ is defined as the ratio of pore volume $V_\mathfrak{f}$ to total volume $V = L^3$, i.e. $\phi := V_\mathfrak{f}/V$. We perform simulation sweeps for various porosities $\phi = 0.1, \ldots, 0.9$ and various microstructures (SC, BCC, FCC). For a given porosity and unit-cell

	Non-consolidated ϕ^{NC}	Close-touching D_{CTL}	Consolidated ϕ^{C}
SC	$1-\frac{1}{16}\pi\left(\frac{D}{L}\right)^3$	$D_{\mathrm{CTL}}=L$	$1+\pi\left[\frac{1}{3}\left(\frac{D}{L}\right)^3-\frac{3}{4}\left(\frac{D}{L}\right)^2+\frac{1}{4}\right]$
BCC	$1-\frac{1}{8}\pi\left(\frac{D}{L}\right)^3$	$\frac{2\sqrt{3}}{3}D_{\mathrm{CTL}}=L$	$1+\pi\left[\left(\frac{D}{L}\right)^3-\sqrt{3}\left(\frac{D}{L}\right)^2+\frac{\sqrt{3}}{4}\right]$
FCC	$1-\frac{1}{4}\pi\left(\frac{D}{L}\right)^3$	$\sqrt{2}D_{\mathrm{CTL}}=L$	$1+\pi\left[\frac{8}{3}\left(\frac{D}{L}\right)^3-\frac{10\sqrt{2}}{4}\left(\frac{D}{L}\right)^2+\frac{5\sqrt{2}}{12}\right]$

Table 4.1: Porosity of sphere packings in cubic unit-cells as a function of sphere diameter D and unit-cell side length L. The porosity ϕ^{NC} of non-consolidated packings is applicable when sphere diameters are smaller than or equal to the close-touching limits. If spheres overlap, the porosity of consolidated packings, as given in Hwang [102], is denoted ϕ^{C}.

side length L, the unknown sphere diameter D remains to be defined. For non-consolidated microstructures, porosity is given as $\phi^{\mathrm{NC}} = 1 - N_s(V_s/V)$, where $V_s = \pi D^3/16$ denotes the volume of a single sphere and N_s denotes the total number of spheres a unit cell is comprised of. The unit cell of simple cubic lattices is comprised of one sphere in total, i.e. $N_s^{\mathrm{SC}} = 1$. For body-centered and face-centered lattices, $N_s^{\mathrm{BCC}} = 2$ and $N_s^{\mathrm{FCC}} = 4$, respectively. For consolidated packings, on the other hand, the overlapping volume has to be taken into account in deriving the porosities ϕ^{C} of consolidated packings. Omitting the derivation of ϕ^{C} herein, we adopt the expressions from Hwang [102] and summarize ϕ^{NC}, ϕ^{C} as well as the close-touching limit diameters D_{CTL} in Table 4.3. For given ϕ and L, these expressions give rise to a root-finding problem for the unknown sphere diameters.

For the present benchmark problem, it is our interest to compare SPH estimates of intrinsic permeabilities k_I [m^2] to the benchmark results of Larson & Higdon [119] and to the empirical expression due to Kozeny [111] and Carman [38]. Intrinsic permeability is a crucial hydraulic material parameter of porous materials and defined by Darcy's law. Darcy's law constitutes a coarse-grained model for the flow problem defined above, i.e. the creeping flow of an incompressible, viscous pore fluid through the pore-space of a rigid solid skeleton entirely driven by a hydraulic gradient under isothermal conditions. For the formulation of coarse-grained balance equations, the continuum-mixture theory, where such processes are described at the length scale of Representative Volume Elements (RVE), provides a suitable framework. While omitting a detailed introduction to continuum-mixture theory, for which the reader is referred to Hassanizadeh & Gray [84, 85], Ehlers & Bluhm [64], Renner & Steeb [172], Steeb [191] and references therein, we shall concisely summarize the assumptions that underly

Darcy's law.

To this end, we introduce the relative velocity $\mathbf{w}_\mathfrak{f} := \mathbf{v}_\mathfrak{f} - \mathbf{v}_\mathfrak{s}$, or seepage velocity, which is defined as the difference between phase-specific volume averages of microscopic (local) fluid velocity $\mathbf{v}_\mathfrak{f} := \langle \mathbf{u} \rangle^\mathfrak{f}$ and local solid velocity $\mathbf{v}_\mathfrak{s} := \langle \mathbf{u} \rangle^\mathfrak{s}$. The phase-specific volume-averaging operator is defined $\langle \bullet \rangle^\alpha := V_\alpha^{-1} \int_{\Omega_{\mathrm{RVE}}} \bullet \, dV$, where V_α denotes the total volume of phase α contained within the domain Ω_{RVE} of a Representative Volume Element. Furthermore, the filter velocity or Darcy velocity is defined $\mathbf{q} = \langle \mathbf{u} \rangle$, where the volume-averaging operator $\langle \bullet \rangle = V^{-1} \int_{\Omega_{\mathrm{RVE}}} \bullet \, dV$ applies to the total volume V of Ω_{RVE}. A static solid skeleton implies $\mathbf{u} = \mathbf{0}$, $\forall \, \mathbf{x} \in \Omega_\mathfrak{s}$ such that $\mathbf{q} = \phi \mathbf{w}_\mathfrak{f} = \phi \mathbf{v}_\mathfrak{f}$, where $\phi := V_\mathfrak{f}/V$ has been taken into account.

In the context of continuum-mixture theory, Darcy's law can be derived based on the coarse-grained balance of linear momentum of the pore-fluid which, assuming 1. incompressible phases, 2. quasi-static processes absent of inertia forces and 3. viscous shear stresses in the fluid much smaller than the viscous momentum exchange between pore fluid and solid skeleton [55, 90], reduces to

$$\phi \operatorname{grad} p = \phi \varrho \mathbf{b} + \hat{\mathbf{p}}^\mathfrak{f}_{\mathrm{neq}}. \tag{4.1}$$

The non-equilibrium momentum interaction $\hat{\mathbf{p}}^\mathfrak{f}_{\mathrm{neq}}$ between pore-fluid and solid skeleton accounts for viscous skin friction forces that arise due to relative movement of fluid and solid phase. A suitable constitutive equation remains to be introduced for $\hat{\mathbf{p}}^\mathfrak{f}_{\mathrm{neq}}$. The defining assumption underlying Darcy's law is that $\hat{\mathbf{p}}^\mathfrak{f}_{\mathrm{neq}} \propto \mathbf{w}_\mathfrak{f}$ and, as a result, $\hat{\mathbf{p}}^\mathfrak{f}_{\mathrm{neq}} \propto \mathbf{q}$. As demonstrated in the above references, close to thermodynamic equilibrium, the latter assumption can be written

$$\hat{\mathbf{p}}^\mathfrak{f}_{\mathrm{neq}} = -\frac{\phi \mu}{k_I} \mathbf{q}, \tag{4.2}$$

where the intrinsic permeability k_I is introduced as a proportionality factor that solely depends on properties of the solid skeleton. Substituting Eq. (4.2) into Eq. (4.1), Darcy's law is obtained in the well-anticipated form

$$\mathbf{q} = -\frac{k_I}{\mu} \left(\operatorname{grad} p - \varrho \mathbf{b} \right) = \frac{k_I}{\mu} \mathbf{J}, \tag{4.3}$$

where $\mathbf{J} := -\left(\operatorname{grad} p - \varrho \mathbf{b} \right)$ is referred to as external driving force. Assuming k_I a scalar-valued material property, Eq. (4.3) implies that the filter velocity is aligned in a direction parallel to the external driving force $\mathbf{J}$. For porous materials with an anisotropic pore-space, on the other hand, Darcy's law is written $\mathbf{q} = -\frac{1}{\mu} \mathbf{k}_I \cdot \mathbf{J}$, where $\mathbf{k}_I$ denotes the second-order intrinsic permeability tensor. Since cubic lattice-based microstructures exhibit isotropy, the assumption $\mathbf{k}_I = k_I \mathbf{I}$ is considered reasonable. For the present benchmark problem, flow of the pore-fluid is driven entirely by a volumetric acceleration $\mathbf{b} = -g\mathbf{e}_1$ which implies that $\mathbf{q} = q_1\mathbf{e}_1 = \phi\langle\mathbf{u}\rangle^{\mathfrak{f}} = \phi\langle u_1\rangle^{\mathfrak{f}}\mathbf{e}_1$. Substituting these expressions into Eq. (4.3) yields

$$k_I = \frac{\mu\phi}{\varrho g}\langle u_1\rangle^{\mathfrak{f}} \tag{4.4}$$

for the unknown intrinsic permeability. The phase-specific volume average $\langle u_1\rangle^{\mathfrak{f}}$ is evaluated using a nodal integration over the set of SPH particles $\mathbf{x}_i \in \Omega_{\mathfrak{f}}$. Exploiting the fact that particle volumes $V_i \approx$ const. for quasi-incompressible computations implies that the operator $\langle\bullet\rangle^\alpha$ turns into the arithmetic average

$$\langle\bullet\rangle^\alpha \approx \frac{1}{N_\alpha}\sum_{i:\mathbf{x}_i\in\Omega_\alpha}(\bullet)_i, \tag{4.5}$$

where $N_\alpha = \sum_{i:\mathbf{x}_i\in\Omega_\alpha} 1$ is the total number of particles of phase α. Hence, we evaluate intrinsic permeabilities using

$$k_I = \frac{\mu\phi}{\varrho g}\frac{1}{N_{\mathfrak{f}}}\sum_{i:\mathbf{x}_i\in\Omega_{\mathfrak{f}}} u_{i,1}$$

as soon as we detect steady-state in the evolution of total kinetic energy. The non-zero component of volumetric acceleration was chosen $g = 0.01\mathrm{m/s}^2$, which ensured low Reynolds number flow with negligible inertia forces compliant with Darcy's law.

It is evident from Eq. (4.4) that only when a closed-form expression for the steady-state velocity field is available, one may derive a closed-form expression for k_I. These expressions are only available for simple flow problems such as for creeping flow in cylindrical tubes or between parallel plates (see section 4.1). It is for that reasons, pore-scale resolved numerical computations are required to compute k_I for general microstructures. However, approximative, empirical or heuristic expressions are available for certain microstructures, most notably the Carman-Kozeny equation [38, 111]

$$k_I^{\mathrm{CK}} = \frac{D^2}{180}\frac{\phi^3}{(1-\phi)^2},$$

which is the most widely used heuristic expression for the intrinsic permeability of dense granular media comprised of near-uniform grain sizes with grain diameter D (see Kaviany [108, § 2.4.2] and Steeb [191, Appendix A]). Numerical reference results for the present benchmark problem are available in Larson & Higdon [119], where the governing Stokes flow equation for creeping flow has been solved using a collocation method and Lamb's general solution in spherical

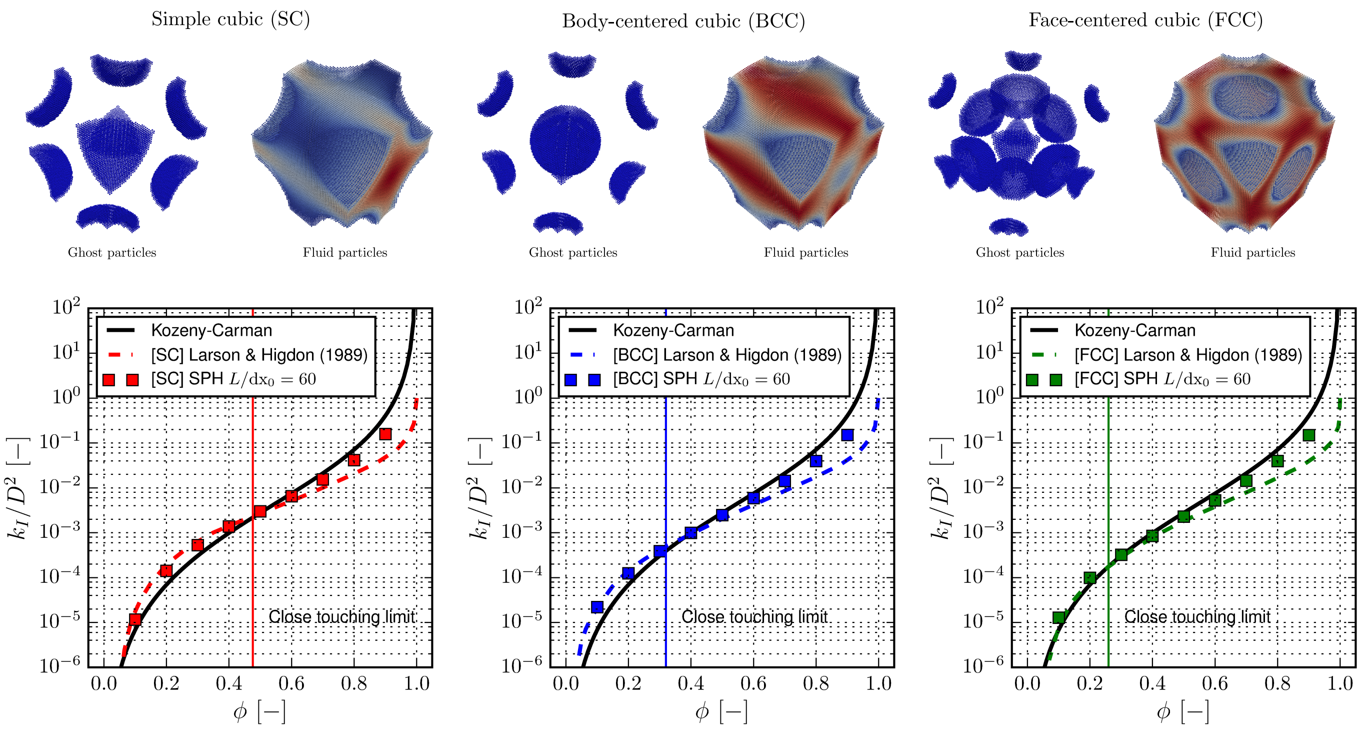

Figure 4.6: Dimensionless permeabilities of sphere packings in periodic cubic unit-cells. (Top Row) Visualization of ghost particles that enforce boundary conditions on static and impermeable solid surfaces and fluid particles colored according to fluid velocity magnitude for $\phi = 0.8$ and microstructures SC, BCC and FCC (from left to right). (Bottom Row) Intrinsic permeabilities k_I normalized by squared sphere diameter D^2 as a function of porosity ϕ for microstructures SC (Red), BCC (Blue) and FCC (Green). Square markers represent SPH results, dashed lines indicate the reference results from Larson & Higdon [119], solid black lines correspond to the Carman-Kozeny expression and vertical solid lines indicate the close-touching limits.

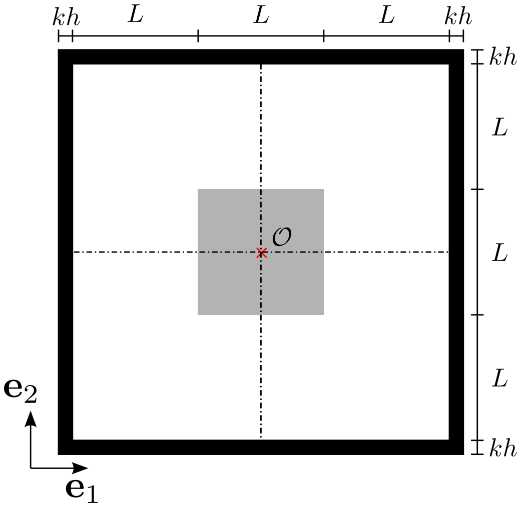

Figure 4.7: Simulation configuration for fully immersed liquid droplet. Black, white and gray areas correspond to fictitious solid phase $\Omega_{\mathfrak{s}}$, wetting phase $\Omega_{\mathfrak{w}}$ and non-wetting phase $\Omega_{\mathfrak{n}}$, respectively. For further details on notation, see caption to Fig 4.1.

coordinates [118].

We find SPH results for normalized intrinsic permeabilities k_I/D^2 to be in close agreement to the numerical reference results for $\phi < 0.6$ irrespective of the lattice structure (Fig. 4.6). Increasing deviations are observed for porosities $\phi > 0.6$, where SPH results consistently overestimate permeabilities. We recall that the numerical resolution ($L/dx_0 = 60$) is kept constant for all simulations. We therefor argue that deviations occur due to the fact that solid surfaces are represented by a prohibitively small of amount of ghost particles for large porosities. As an example, for the simple cubic structure (SC) and a porosity of $\phi = 0.8$, solid spheres are discretized by six particles over the length of the sphere diameter. For the given numerical resolution, however, permeabilities below the close-touching limits are reproduced with satisfactory accuracy. Given the fact that computations below the close-touching limits are more challenging due to the singularities that exist at the sphere contacts, we conclude that these results motivate the use of SPH with respect to flow in complex geometries. We further note that the Carman-Kozeny equation constitutes an excellent approximation for FCC structures below and close to the close-touching limit.

4.4 Fully immersed liquid droplet

A single, square-shaped fluid droplet of side length L is initially suspended in the center of a surrounding fluid, with the total fluid domain being bounded by fictitious ghost particles (Fig. 4.7). During simulation, the system is free to equilibrate in the absence of volumetric acceleration $\mathbf{b} = \mathbf{0}$. The simulation is terminated as soon as fluctuations in total kinetic energy are small enough to assume steady state. In equilibrium, pressure levels within both fluid phases are constant, hence, the equilibrium capillary pressure will be equal at any point of the interface $\Gamma_{\mathfrak{w}\mathfrak{n}}$. Following Eq. (2.77), equilibrium will consequently yield a circular meniscus of constant curvature $\kappa^{\mathfrak{w}\mathfrak{n}} = 1/R$, where R is the radius of the circle which parametrizes the equilibrium meniscus, and equilibrium capillary pressure p_C^{eq}.

The capillary pressure $p_C^{\text{eq}} := p_{\text{eq}}^{\mathfrak{n}} - p_{\text{eq}}^{\mathfrak{w}} = \sigma^{\mathfrak{w}\mathfrak{n}}\kappa^{\mathfrak{w}\mathfrak{n}}$ is independent of fluid density and dynamic viscosity, which are chosen to be $\varrho_0^{\mathfrak{n}} = \varrho_0^{\mathfrak{w}} = 1000$ kg/m^3 and $\mu^{\mathfrak{n}} = \mu^{\mathfrak{w}} = 0.001$ Pa s for the sake of computational efficiency. The interfacial tension is set to $\sigma^{\mathfrak{w}\mathfrak{n}} = 0.01$ N/m in all simulations. Due to the absence of contact lines, the results are independent of the values of $\sigma^{\mathfrak{w}\mathfrak{s}}$ and $\sigma^{\mathfrak{n}\mathfrak{s}}$, which are set to zero. Both fluid phases are modeled to be quasi-incompressible such that the volume of the suspended fluid droplet is required to be conserved, which implies that the equilibrium meniscus radius $R = L/\sqrt{\pi}$. The characteristic length scale is chosen to be $L_{\text{ref}} = R$ in Eq. (3.68), whereas U_{ref} is chosen to be zero stating that advection is not predominant. Initial particle velocities are set to $\mathbf{u}_{0,i} = \mathbf{0}$.

We study the capability of the numerical model to reproduce equilibrium pressure profiles and meniscus shapes for two choices of the kernel $W \in \{W_q, W_w\}$, and various values of the initial particle spacing dx_0, which we measure in terms of the ratio R/dx_0. Irrespective of the choice of W, equilibrium pressure profiles are accurately reproduced for $R/dx_0 = 16$, except in close vicinity to the interface where a smooth transition of particle pressures, rather than a localized pressure jump, is observed (Fig. 4.8). As indicated in section 2.3, the latter is a natural consequence of using numerically diffuse interfaces. The numerical width of interfaces scales with the size of the smoothing kernel compact support kh and, consequently, with dx_0. Pronounced differences in particle distributions can be observed between simulation results based on the quintic kernel W_q, where the well known pairing instability [51, 174] (see section 3.3) can be observed, and the Wendland kernel W_w, where homogeneous, glass-like distributions are observed.

The pairing instability is observed to induce local errors in the direction of the immersed interfacial forces $\tilde{\mathbf{F}}_i^S \propto \mathbf{n}^{\mathfrak{w}\mathfrak{n}}$, which seem negligible when using the Wendland kernel W_w. The latter motivates a quantitative analysis of numerical errors with respect to the numerical estimates of equilibrium capillary pressure. We employ two different approaches for computing capillary pressure, the first of which is based on the difference in volume averaged fluid phase pressures such that

$$P_C^{\text{va}} \equiv \frac{1}{V_{\mathfrak{n}}} \int_{\Omega_{\mathfrak{n}}} p^{\mathfrak{n}} \mathrm{d}v - \frac{1}{V_{\mathfrak{w}}} \int_{\Omega_{\mathfrak{w}}} p^{\mathfrak{w}} \mathrm{d}v \approx \langle p_i \rangle^{\mathfrak{n}} - \langle p_i \rangle^{\mathfrak{w}}, \tag{4.6}$$

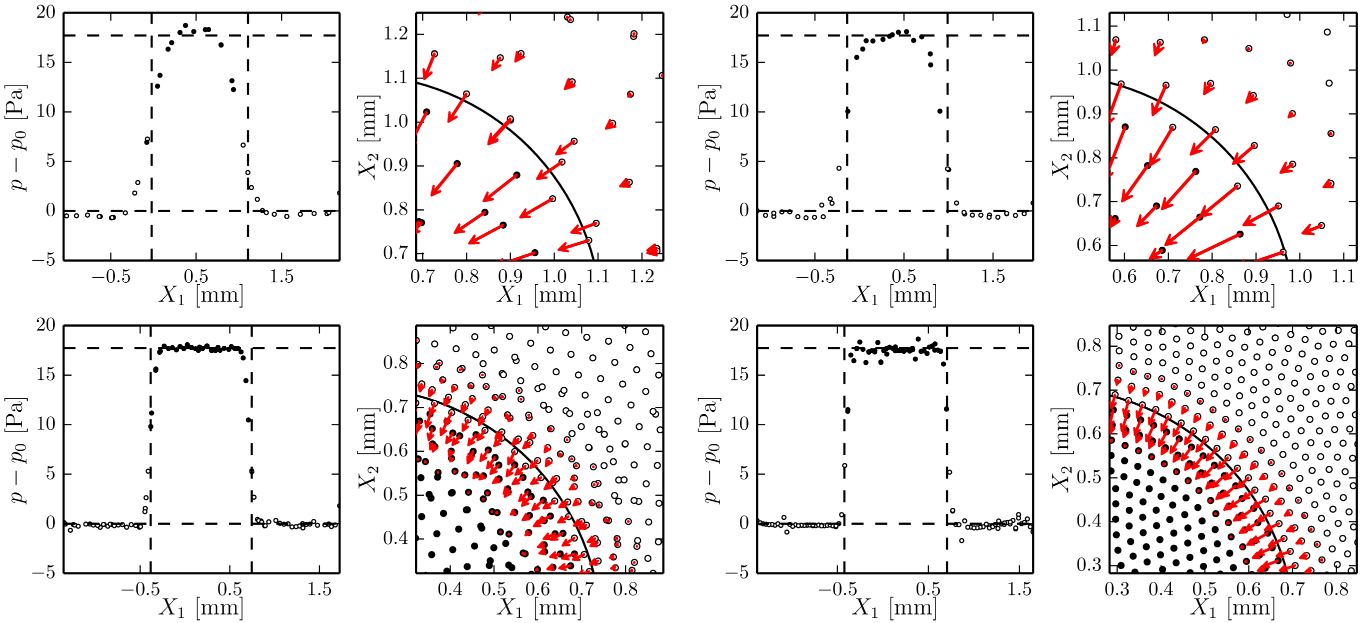

Figure 4.8: Equilibrium pressure profiles and close-up particle plots of a droplet fully immersed in a fluid. Simulation parameters are $L = 1\text{mm}$ in all simulations, and $R/dx_0 = 5$ and $W = W_q$ (top-left), $R/dx_0 = 5$ and $W = W_w$ (top-right), $R/dx_0 = 16$ and $W = W_q$ (bottom-left), $R/dx_0 = 16$ and $W = W_w$ (bottom-right). Filled and open markers represent particles of the droplet and surrounding medium, respectively. Pressure profiles show local particle pressures relative to the background pressure p_0 for all particles placed within a distance dx_0 to the vertical symmetry line. Vertical dashed lines in the pressure plots indicate exact meniscus positions, whereas horizontal dashed lines indicate reference pressure level and exact equilibrium capillary pressure level P_C^{eq}. Lengths and directions of the arrows shown in the particle plots represent magnitude and direction of the interfacial forces $\tilde{\mathbf{F}}_i^S$, whereas the solid line indicates the exact meniscus shape.

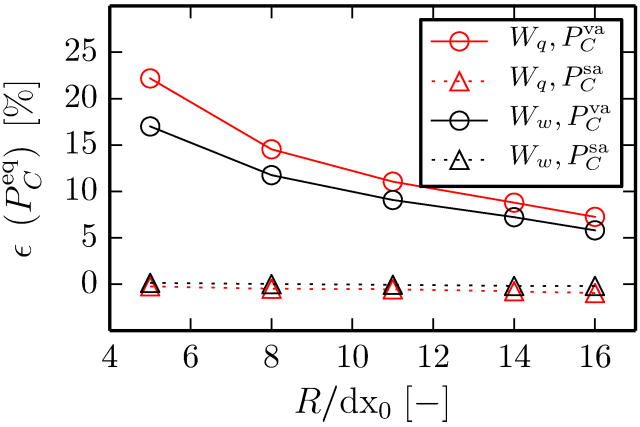

Figure 4.9: Relative errors in numerical estimates P_C^{va} and P_C^{sa} of equilibrium capillary pressure P_C^{eq} plotted as a function of numerical resolution R/dx_0. $L = 1\mathrm{mm}$ in all cases. The relative error is defined to be $\epsilon(\bullet) = 1 - (\bullet)_{\mathrm{exact}}/(\bullet)_{\mathrm{est.}}$, where $(\bullet)_{\mathrm{exact}}$ and $(\bullet)_{\mathrm{est.}}$ represent exact solution and numerical estimate, respectively.

where the operator $\langle\bullet\rangle^\alpha$ denotes the phase-specific arithmetic particle averaging operator as defined in Eq. (4.5). Furthermore, $V_\alpha = \int_{\Omega_\alpha} \mathrm{d}v$ is the total volume occupied by fluid phase α. We denote the volume-averaged capillary pressure with a capital letter P_C. In equilibrium, however, the pressure fields are homogeneous and thus $P_C^{\mathrm{eq}} = p_C^{\mathrm{eq}}$.

The second approach for computing capillary pressure is based on the interfacial average of the interfacial force density and reads

$$\begin{aligned} P_C^{\mathrm{sa}} &:= \frac{1}{A_{\mathfrak{wn}}}\int_{\Gamma_{\mathfrak{wn}}} \sigma^{\mathfrak{wn}}\kappa^{\mathfrak{wn}}\mathrm{d}a \overset{(2.61)}{=} \frac{1}{A_{\mathfrak{wn}}}\int_{\Omega} \sigma^{\mathfrak{wn}}\kappa^{\mathfrak{wn}}\delta^{\mathfrak{wn}}\mathrm{d}v \\ &\overset{(2.68)}{=} \frac{1}{A_{\mathfrak{wn}}}\int_{\Omega} \|\mathbf{f}^{\mathfrak{wn}}\|\mathrm{d}v \overset{(3.62)}{\approx} \frac{1}{A_{\mathfrak{wn}}}\sum_{i:\mathbf{x}_i\in\Omega} \|\tilde{\mathbf{F}}_i^{S,\mathfrak{wn}}\|, \end{aligned}$$

where the total interfacial area

$$\begin{aligned} A_{\alpha\beta} &= \int_{\Gamma_{\alpha\beta}} \mathrm{d}a \overset{(2.61)}{=} \int_{\Omega} \delta^{\alpha\beta}\mathrm{d}v \\ &\overset{(3.62)}{\approx} \sum_{i:\mathbf{x}_i\in\Omega} \|\mathrm{grad}_i\, C^{\alpha\beta}\| V_i \overset{(3.40)}{\approx} \sum_{i:\mathbf{x}_i\in\Omega} \|\mathrm{grad}_i\, C^{\alpha\beta}\| \frac{1}{n_i} \end{aligned} \tag{4.7}$$

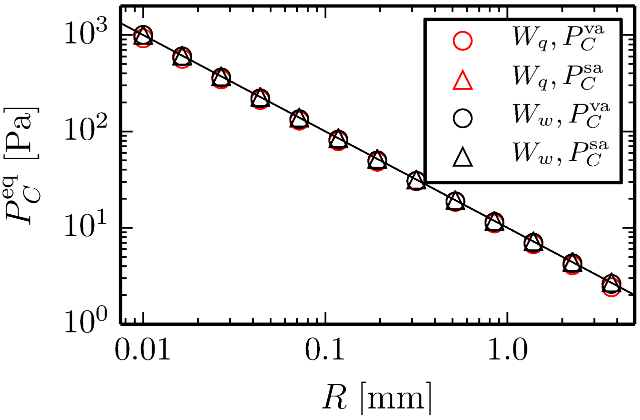

Figure 4.10: Equilibrium capillary pressure estimates P_C^{av} and P_C^{sa} as a function of equilibrium droplet radius R. The exact solution is represented by the solid line. $R/dx_0 = 16$ in all cases. Largest relative error with respect to P_C^{av} is 9.1%, whereas the largest relative error with respect to P_C^{sa} is 2.3%.

of the interface $\Gamma_{\alpha\beta}$ is computed by exploiting the property (2.61) of the surface Dirac distribution. The measures $P_C^{\mathrm{va}} = P_C^{\mathrm{sa}} = P_C^{\mathrm{eq}}$ only in equilibrium and in the absence of numerical errors. Non-equilibrium pressure fields affect the magnitude of P_C^{va}, whereas non-equilibrium meniscus shapes affect the magnitude of P_C^{sa}.

Relative errors in P_C^{va} linearly decrease with increasing numerical resolution for both, W_q and W_w (Fig. 4.9), which is predominantly because the width of the diffuse interface decreases with increasing resolution: For small values of R/dx_0, the number of interfacial particles located within the diffuse interface is large enough to render the volumetric averaging of bulk phase pressures error-prone. A simple remedy would be to exclude interfacial particles in the computation of the arithmetic means in Eq. (4.6). However, in practical applications the number of bulk phase particles will be orders of magnitudes larger as compared to the number of interfacial particles. Errors in P_C^{va} are consistently smaller using W_w because of the size of kernel compact support $kh = 3.4\ dx_0$. Consequently, the width of the diffuse interface is smaller for W_w as compared to W_q, for which $kh = 4.35\ dx_0$ (see section 3.3).

Relative errors in capillary pressure estimates based on the interfacial average P_C^{sa} are well-below 1% for the tested set of simulation parameters, despite the pairing instability of W_q. The latter implies that errors in P_C^{va} are solely due to the underlying averaging procedure rather than a lack of numerical accuracy. The interfacial average based capillary pressure P_C^{sa} is considered to be the

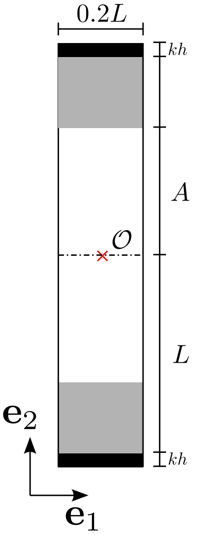

Figure 4.11: Initial simulation configuration (2-dimensional) for layered co-current flow. Black, white and gray areas correspond to fictitious solid phase $\Omega_{\mathfrak{s}}$, non-wetting phase $\Omega_{\mathfrak{n}}$ and wetting phase $\Omega_{\mathfrak{w}}$, respectively. For further details on notation, see caption to Fig 4.1.

preferable method to estimate equilibrium capillary pressure in cases where the total computational domain is small enough such that the number of interfacial particles and bulk phase particles are in the same order of magnitude. Otherwise, the volumetric average based capillary pressure P_C^{va} is preferred for reasons of computationally efficiency.

In order to ensure modeling accuracy with respect to equilibrium pressure profiles across all microscopic length scales of relevance in this contribution (10 µm – cm), simulations are performed for various values of the equilibrium droplet radius R while keeping the resolution $R/dx_0 = 16$ unchanged. Numerical results indicate acceptable margins of numerical error across relevant length scales (Fig. 4.10).

4.5 Layered co-current flow between parallel plates

The flow of two immiscible fluids in layered arrangement between parallel plates is driven by a volumetric acceleration $\mathbf{b} = g\mathbf{e}_1$. The plates are separated by a distance $2L = 1$ mm. The computation domain is periodic in direction of $\mathbf{e}_1$ and bounded by ghost particles that represent the static and impermeable plates in direction of $\mathbf{e}_2$. No-slip is modeled for $X_2 = \pm L$. The wetting phase, occupying the region $A \leq |X_2| \leq L$, is attached to the upper and lower plates, while the non-wetting phase occupies the central region $0 \leq |X_2| \leq A$ (Fig. 4.11). Hence, the saturations

$$S_\alpha := \frac{V_\alpha}{V_\mathfrak{w} + V_\mathfrak{n}} \approx \frac{N_\alpha}{N_\mathfrak{w} + N_\mathfrak{n}}$$

for $\alpha \in \{\mathfrak{n}, \mathfrak{w}\}$ reduce to $S_\mathfrak{w} = A/L$ and $S_\mathfrak{n} = (L{-}A)/L$. We study equilibrium velocity profiles in direction of $\mathbf{e}_2$ and relative permeabilities of each phase as a function of saturations and dynamic viscosity ratio $M := \mu^\mathfrak{n}/\mu^\mathfrak{w}$. In the case of laminar flow, closed-form solutions for equilibrium velocity profiles and relative permeabilities are available [210]. The closed-form solution for the velocity profile reads

$$U_1(X_2) = \begin{cases} \dfrac{g\varrho_0^\mathfrak{n}}{2\mu^\mathfrak{n}} \left[A^2 - (X_2)^2\right] + \dfrac{g\varrho_0^\mathfrak{w}}{2\mu^\mathfrak{w}} \left[L^2 - A^2\right], & \text{if } 0 \leq |X_2| \leq A \\ \dfrac{g\varrho_0^\mathfrak{w}}{2\mu^\mathfrak{w}} \left[L^2 - (X_2)^2\right], & \text{if } A \leq |X_2| \leq L. \end{cases}$$

If the total fluid domain between the plates is considered to be saturated by a single fluid phase α, the closed-form mean velocity in direction of $\mathbf{e}_1$ for laminar flow driven by volumetric acceleration of magnitude g reads $U_{M,1}^\alpha = L^2 \varrho^\alpha g/(3\mu^\alpha)$. We subsequently set the characteristic velocity $U_\text{ref} = \max\left\{U_{M,1}^\mathfrak{w}, U_{M,1}^\mathfrak{n}\right\}$ and the characteristic length scale $L_\text{ref} = 2L$ in evaluating Eq. (3.68). The effects of viscous coupling at the interfaces, with respect to which we intend to validate the numerical model, are most pronounced in the case of viscosity-dominated flow and we set $g = 0.1$ m/s^2, which drives creeping flow with a maximum Reynolds number $\text{Re}_\text{max} < 1$, where

$$\text{Re}_\text{max} := \frac{\max\left\{\varrho_0^\mathfrak{n}, \varrho_0^\mathfrak{w}\right\} U_\text{ref} L_\text{ref}}{\min\left\{\mu^\mathfrak{n}, \mu^\mathfrak{w}\right\}}.$$

Since the equilibrium solutions are independent of capillary effects, we set $\sigma^{\mathfrak{wn}} = \sigma^{\mathfrak{ws}} = \sigma^{\mathfrak{ns}} = 0$. Initial densities are given as $\varrho_0^\mathfrak{n} = \varrho_0^\mathfrak{w} = 1000$ kg/m^3. Simulations are performed for a set of viscosity ratios $M = \{0.01, 0.1, 10.0, 100.0\}$ by appropriate choices of the dynamic viscosities $\mu^\mathfrak{n}$ and $\mu^\mathfrak{w}$, which are chosen in a range 10^{-4} Pa s $< \mu^\alpha < 10^{-1}$ Pa s. Initial particle velocities are set to $\mathbf{u}_{0,i} = \mathbf{0}$ and steady-state is detected in the evolution of total kinetic energy. The initial particle spacing dx_0 is chosen such that the ratio $2L/dx_0 = 45$.

The relative permeability with respect to flow of fluid phase α in direction of $\mathbf{e}_1$ is introduced as the ratio $k_{r,\alpha}(S_\alpha) = Q_{1,S}^\alpha(S_\alpha)/Q_1^\alpha$, where $Q_{1,S}^\alpha$ is the volumetric flow rate of fluid phase α through the region it occupies at a given saturation S_α, whereas Q_1^α is the volumetric flow rate of fluid phase α if it was to saturate the total fluid domain, i.e. for single phase flow. For the given two-dimensional simulation setup, relative permeabilities can be reduced to ratios of volumetric flow rates per unit of length and are subsequently computed as

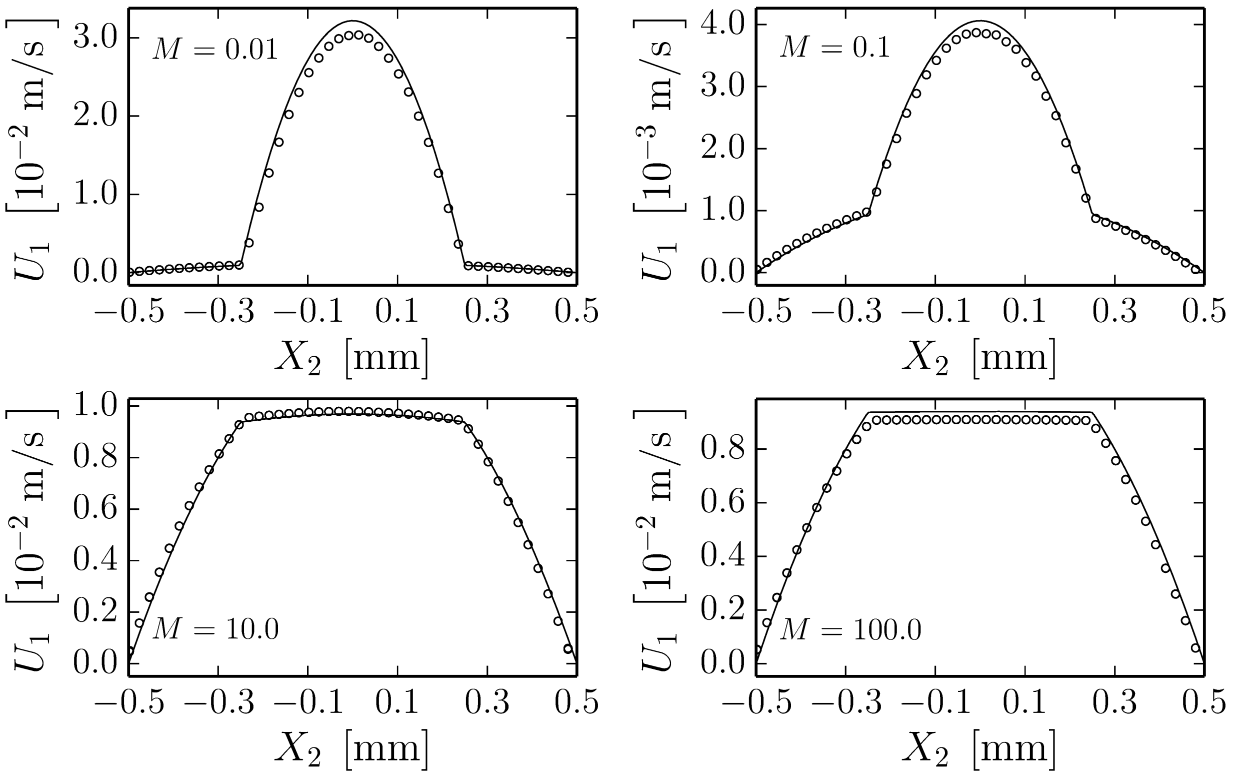

Figure 4.12: Steady-state velocity profiles for $S_\mathfrak{n} = 0.5$ and W_w for all tested values of the dynamic viscosity ratio M. Solid lines indicate closed-form solutions whereas markers represent SPH solutions.

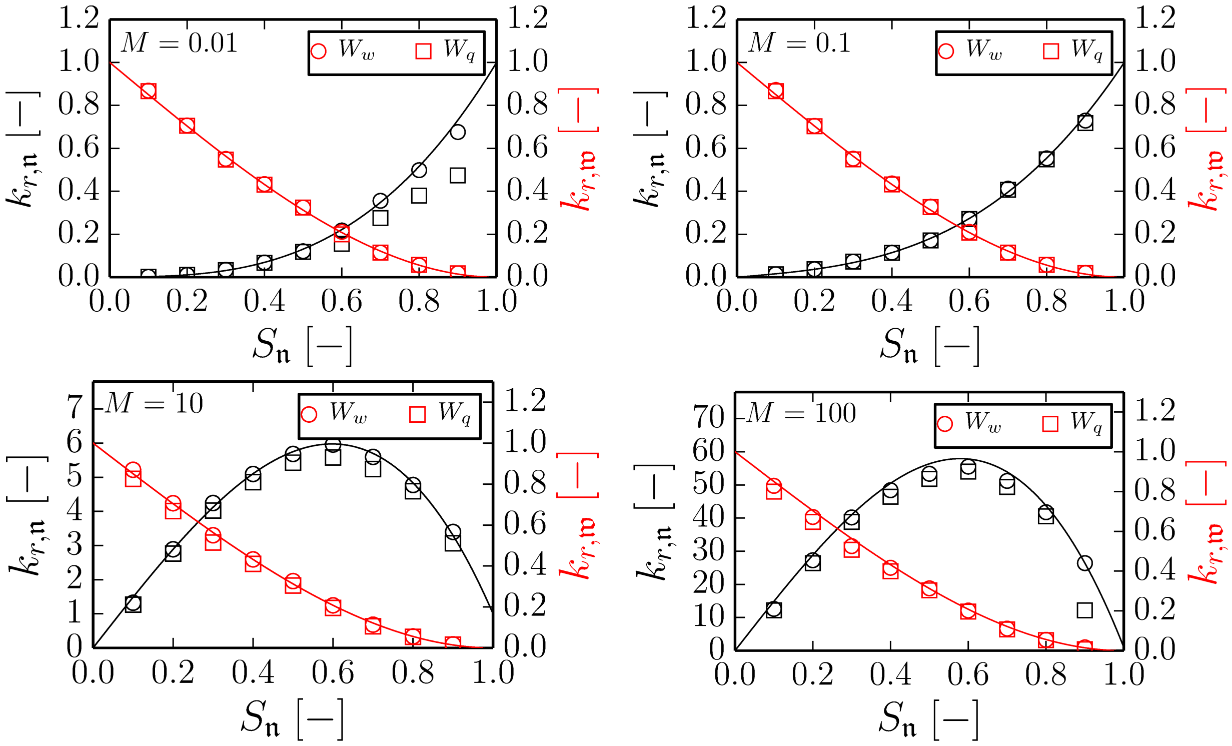

Figure 4.13: Steady-state relative permeabilities as a function of non-wetting phase saturation $S_\mathfrak{n}$ for all tested values of the dynamic viscosity ratio M. Solid lines indicate closed-form solutions whereas markers represent SPH solutions.

$$k_{r,\mathfrak{n}} = \frac{A\langle U_{i,1}\rangle^{\mathfrak{n}}}{LU_{M,1}^{\mathfrak{n}}},\ k_{r,\mathfrak{w}} = \frac{(L-A)\langle U_{i,1}\rangle^{\mathfrak{w}}}{LU_{M,1}^{\mathfrak{w}}}. \tag{4.8}$$

Note that in Eq. (4.8), volumetric flow rates per unit of length are replaced by products of mean velocities and layer thicknesses and the phase-specific averaging operators are defined in Eq. (4.5). Following Yiotis et al. [210], closed-form expressions for relative permeabilities as a function of non-wetting saturation are given by

$$k_{r,\mathfrak{n}} = S_{\mathfrak{n}}\left[\frac{3}{2}M + S_{\mathfrak{n}}^2\left(1-\frac{3}{2}M\right)\right],$$

and

$$k_{r,\mathfrak{w}} = \frac{1}{2}\left(1-S_{\mathfrak{n}}\right)^2\left(2+S_{\mathfrak{n}}\right).$$

The numerical model accurately accounts for viscous coupling at interfaces for both, W_w and W_q, such that equilibrium velocity profiles and relative permeabilities are reproduced within acceptable margins of numerical error (Figs. 4.12 - 4.13). The largest encountered relative errors with respect to relative permeabilities are in the order of 40% and appear for very low and very high values of $S_{\mathfrak{n}}$. The latter is a natural consequence of the fact that velocity profiles exhibit locally large spatial gradients for extremal values of $S_{\mathfrak{n}}$. As the numerical resolution is kept unchanged throughout all simulations, a higher number of particles is expected to increase accuracy in these cases. On the other hand, relative errors with respect to relative permeabilities are below 7% in the range $0.2 < S_{\mathfrak{n}} < 0.8$ for the given numerical resolution and for all tested values of M. Numerical results further reveal the well-known lubrication effect [152], by which $k_{r,\mathfrak{n}}$ is rendered greater than 1 in a certain range of $S_{\mathfrak{n}}$ for $M > 1$. Accurate modeling of co-current laminar flow is crucial with respect to flow in porous media when lubricating wetting films are present as encountered in chapter 6.

4.6 Capillary rise between parallel plates

Two parallel solid plates, vertically aligned along the direction of $\mathbf{e}_2$ and with the inner perimeters being separated by a narrow gap width $D = 10$ mm, are brought in contact with a wetting liquid reservoir (Fig. 4.14). The parallel plates are represented by fictitious ghost particles and the plate thickness is chosen to be twice the compact support radius such that fluid particles on either side of the plates do not spuriously interact with each other. The height of the wetting fluid reservoir is 25 mm, while the remainder of the total fluid domain is occupied

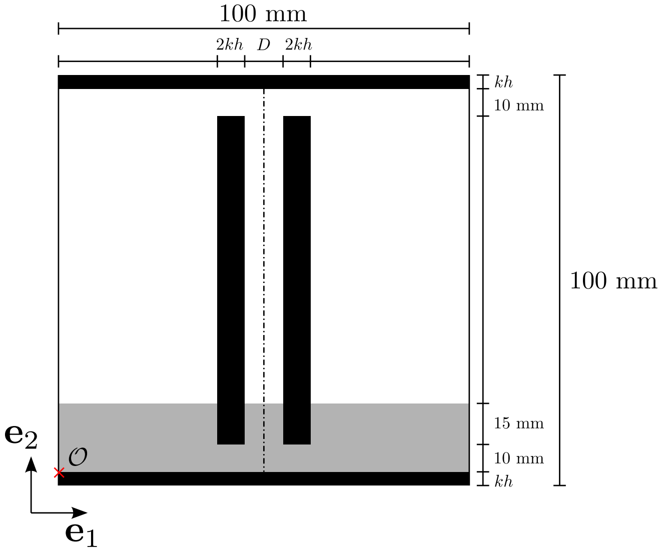

Figure 4.14: Initial simulation configuration for capillary rise between parallel plates. For further details on color coding of bulk phases in schematic, see caption to Fig 4.11.

by particles of the non-wetting phase. The computation domain is bounded by fictitious ghost particles in $\mathbf{e}_2$ direction and periodic in $\mathbf{e}_1$ direction. The gap width D is chosen to be the characteristic length scale $L_{\text{ref}} = D$ in Eq. (3.68), whereas U_{ref} is chosen to be zero following the argument given in section 4.4. A gravitational acceleration $\mathbf{b} = -g\ \mathbf{e}_2$ acts and the system is free to equilibrate during simulation until steady-state is detected in the evolution of total kinetic energy.

For the sake of clarity, we differentiate between the portion of the meniscus which is located in the gap region and the portion of the meniscus of the reservoir region in referring to them as gap meniscus and reservoir meniscus, respectively. Along the direction of $\mathbf{e}_2$, the equilibrium pressure profile in the gap region between the parallel plates is piecewise linear (hydrostatic pressure), exhibiting a jump at points of the gap meniscus. The total curvature of the gap meniscus depends, unlike the total curvature of fully immersed droplets, on the equilibrium contact angle Θ_{eq}, as the presence of contact lines influences the shape of the meniscus. The equilibrium gap meniscus is assumed to be of constant total curvature given that the variation of hydrostatic fluid pressure due to gravity along the curved meniscus is small, rendering the equilibrium pressure difference $p^{\mathfrak{n}} - p^{\mathfrak{w}}$ approximately equal at all points of the gap meniscus. Hence, the gap meniscus is of circular shape and parameterized by a circle of radius $R = 1/\kappa^{\mathfrak{wn}} = D/(2\cos\Theta_{\text{eq}})$ (Fig. 4.15), which leads to

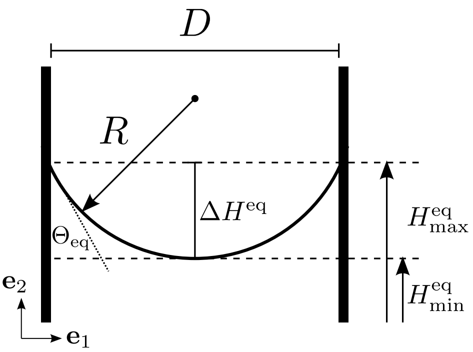

Figure 4.15: Schematic diagram of a meniscus located between two parallel plates that are separated by a narrow gap width D, introducing minimum and maximum capillary rise heights H_{min} and H_{max}, respectively. H_{min} and H_{max} are measured with respect to the reference height H_{ref} of the reservoir.

$$p_C^{\mathrm{eq}} = \frac{2\sigma^{\mathfrak{wn}} \cos \Theta_{\mathrm{eq}}}{D}. \tag{4.9}$$

The width of the reservoir is chosen to be an order of magnitude larger as compared to the gap width, which, together with periodicity in $\mathbf{e}_1$ direction, results in near zero mean curvature of the reservoir meniscus. The equilibrium pressure jump at points of the reservoir meniscus is consequently assumed zero and the mean reference height H_{ref} of the wetting liquid reservoir is introduced.

The interfacial pressure jump across the gap meniscus is the driving force for the wetting liquid to penetrate the gap region. The spontaneous process of wetting liquid penetration is referred to as capillary rise and ends as soon as the difference in mean hydrostatic pressures between points of the gap meniscus and points of the reservoir meniscus counterbalances the interfacial pressure jump p_C^{eq}. Hence, the equilibrium mean capillary rise height, often referred to as Jurin's height, reads

$$H^{\mathrm{eq}} = \frac{2\sigma^{\mathfrak{wn}} \cos \Theta_{\mathrm{eq}}}{\left(\varrho_0^{\mathfrak{w}} - \varrho_0^{\mathfrak{n}}\right) g D}.$$

We emphasize that H^{eq} is a measure of the mean height [35] of the equilibrium gap meniscus with respect to the reference level H_{ref} of the wetting liquid reservoir. In the context of analyzing fully resolved simulation results it is convenient to introduce the lowest point $H^{\mathrm{eq}}_{\mathrm{min}}$ of the equilibrium gap meniscus. A geometric analysis of the circle segment (see Fig. 4.15) yields

$$H^{\mathrm{eq}}_{\mathrm{min}} = H^{\mathrm{eq}} - \frac{1}{2}\Delta H^{\mathrm{eq}} = H^{\mathrm{eq}} - \frac{1}{2}\left(R - \sqrt{R^2 - \frac{D^2}{4}}\right).$$

The numerical prediction of the lowest point $H^{\mathrm{eq}}_{\mathrm{min}}$ is subsequently measured as the difference between the smallest X_2 coordinate among the set of non-wetting particles located in the gap region and the reference height H_{ref}. We study the capability of the numerical model to reproduce $H_{\mathrm{min}}^{\mathrm{eq}}$ and equilibrium gap meniscus shape for two choices of the kernel $W \in \{W_q, W_w\}$, and for various values of the initial particle spacing dx_0, which we measure in terms of the ratio D/dx_0. In all capillary rise simulations, the fluid parameters are chosen to be $\varrho_0^{\mathfrak{n}} = 10$ kg/m^3, $\varrho_0^{\mathfrak{w}} = 100$ kg/m^3 and $\sigma^{\mathfrak{nw}} = 0.01$ N/m; while $g = 0.5$ m/s^2. Since the equilibrium solution is independent of dynamic viscosity, we set $\mu^{\mathfrak{n}} = \mu^{\mathfrak{w}} = 0.001$ Pa s for simplicity. Simulations are performed for a set of equilibrium contact angles $\Theta_{\mathrm{eq}} \in \{15°, 30°, 45°, 60°, 75°\}$. It is $\sigma^{\mathfrak{nw}}$ as well as the difference between the interfacial tensions $\sigma^{\mathfrak{ws}}$ and $\sigma^{\mathfrak{ns}}$ which scales the magnitude of Θ_{eq}. Hence, we choose $\sigma^{\mathfrak{ws}} = 0$ for the sake of computational efficiency and subsequently $\sigma^{\mathfrak{ns}} = \sigma^{\mathfrak{nw}} \cos \Theta_{\mathrm{eq}}$ following Young's equation (2.86). Initial particle velocities are set to $\mathbf{u}_{0,i} = \mathbf{0}$.

Temporal evolutions of H_{min} exhibit equilibrium states for $t > 2$ s (Fig. 4.16). Inertial effects in the dynamic evolution of H_{min} are less pronounced as compared to typical laboratory experiments [215], where air constitutes the non-wetting phase, because the non-wetting phase viscosity introduces a considerable amount of damping.

Irrespective of the choice of the kernel W, equilibrium meniscus shapes are accurately reproduced for all tested values of Θ_{eq}. The numerically predicted gap meniscus is observed to exhibit a mere vertical shift with respect to the curve, that parametrizes the exact gap meniscus for both, $\Theta_{\mathrm{eq}} = 15°$ and $\Theta_{\mathrm{eq}} = 75°$ (Fig. 4.16). The latter indicates that the numerical model adequately accounts for equilibrium effects at contact lines. Consequently, the analysis of numerical errors can be restricted to the analysis of errors in the numerical estimates of $H_{\mathrm{min}}^{\mathrm{eq}}$. Relative errors with respect to $H_{\mathrm{min}}^{\mathrm{eq}}$ decrease with increasing resolution D/dx_0 for all tested values of Θ_{eq}. Errors are consistently smaller using the quintic kernel W_q as compared to W_w (Fig. 4.17), which underlines the often asserted interpolation accuracy of the quintic kernel [98]. For $\Theta_{\mathrm{eq}} < 45°$ and the highest considered numerical resolution, relative errors are below 5% using W_q and below 10% using W_w (Fig. 4.17, top). However, relative errors are observed to be increasingly sensitive to the magnitude of Θ_{eq} for $D/dx_0 > 25$, yielding upper bounds of $\epsilon(H_{\mathrm{min}}^{\mathrm{eq}})$ as large as 18% for $\Theta_{\mathrm{eq}} = 75°$ (Fig. 4.17, bottom).

In an attempt to interpret the latter effect we analyze absolute errors with respect to $H_{\mathrm{min}}^{\mathrm{eq}}$. Absolute errors are observed to be comparatively insensitive to the magnitude of Θ_{eq} for $D/dx_0 > 25$, and respective magnitudes are close to the compact support size kh (Fig. 4.18). We conclude that numerical diffusivity of the solid-fluid interfaces yields an uncertainty with respect to the gap width D in the order of the compact support size and subsequently an uncertainty in capillary rise heights. Relative errors are rendered large for $\Theta_{\mathrm{eq}} > 60°$ since, for the chosen simulation setup, equilibrium rise heights $H_{\mathrm{min}}^{\mathrm{eq}}$ and the length

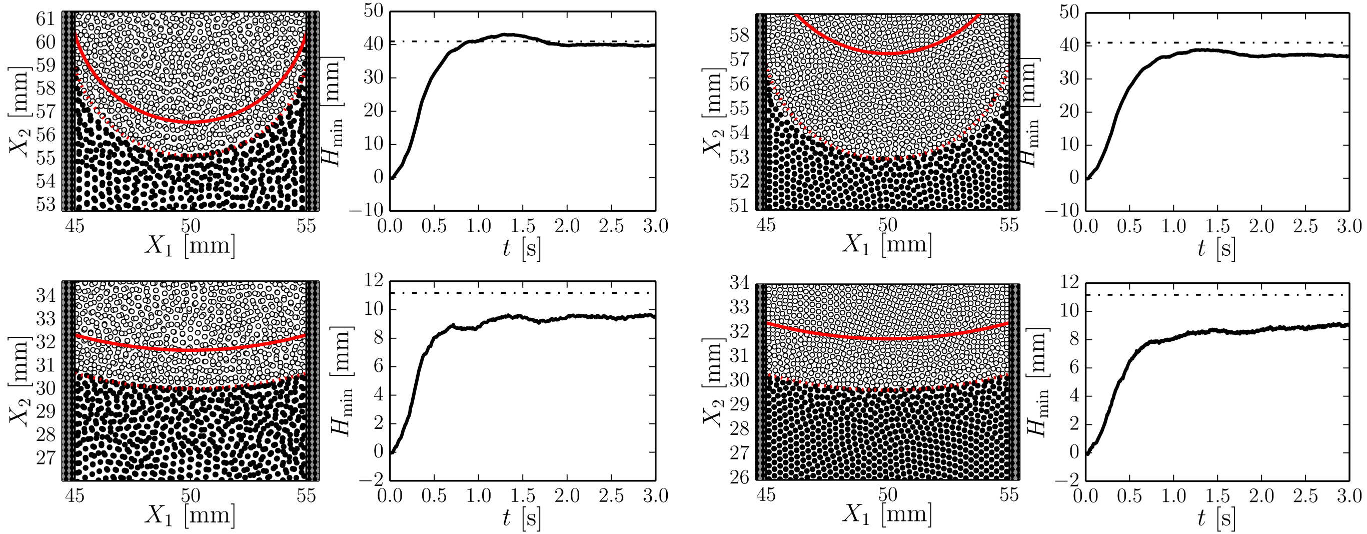

Figure 4.16: Temporal evolution of the lowest point of the gap meniscus $H_{\min}$ and close-up plot of equilibrium particle positions in the vicinity of the gap meniscus. Simulation parameters are $D/dx_0 = 40$ in all simulations and $\Theta_{\text{eq}} = 15°$ and $W = W_q$ (top-left), $\Theta_{\text{eq}} = 15°$ and $W = W_w$ (top-right), $\Theta_{\text{eq}} = 75°$ and $W = W_q$ (bottom-left), $\Theta_{\text{eq}} = 75°$ and $W = W_w$ (bottom-right). Open circle, filled circle and filled diamond markers represent the SPH particle positions of the non-wetting phase, wetting phase and fictitious ghost particles, respectively. Solid red lines in the particle plots indicate the exact position and shape of the gap meniscus, whereas dashed red lines are vertical shifts of the exact meniscus curve to match the numerical estimate of lowest point of the gap meniscus. Horizontal dashed lines in the plots of $H_{\min}$ as a function of time indicate the exact equilibrium solution $H^{\text{eq}}_{\min}$.

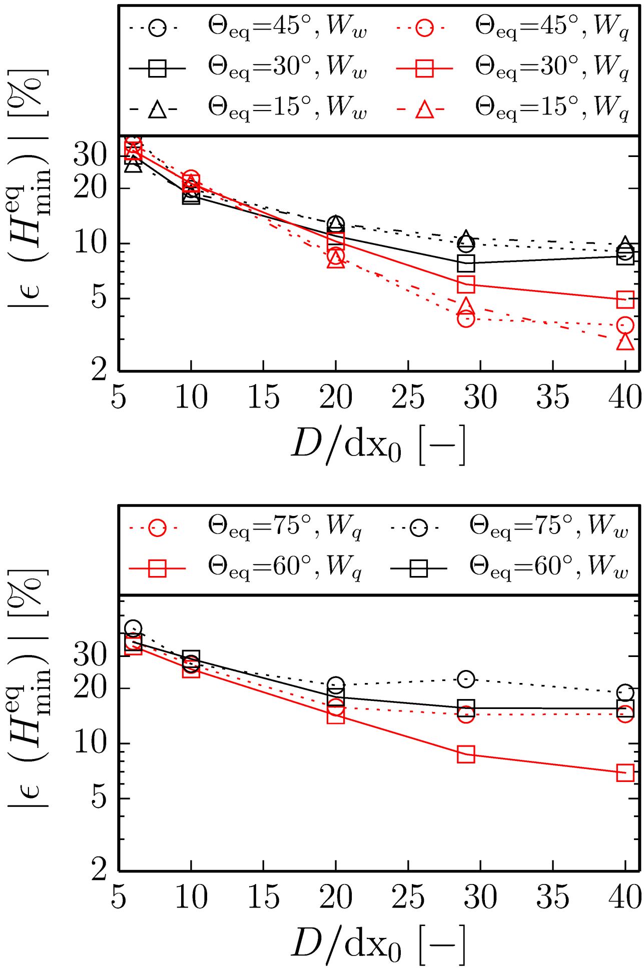

Figure 4.17: Absolute values of relative errors in numerical estimates of $H^{\rm eq}_{\rm min}$ as a function of resolution D/dx_0.

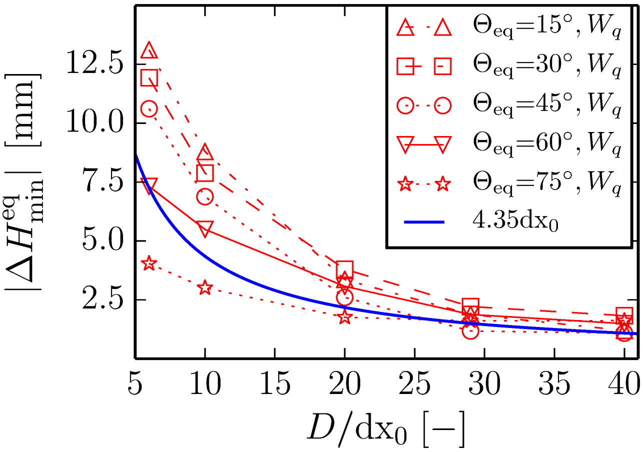

Figure 4.18: Absolute values of the absolute errors in numerical estimates of $H^{\text{eq}}_{\text{min}}$ as a function of resolution D/dx_0, where results for $W = W_w$ are omitted for the sake of clarity. Solid blue line represents the compact support size of the quintic kernel $kh = 4.35\ dx_0$. The absolute error is defined to be $\Delta(\bullet) = (\bullet)_{\text{exact}} - (\bullet)_{\text{est.}}$, where $(\bullet)_{\text{exact}}$ and $(\bullet)_{\text{est.}}$ represent exact solution and numerical estimate, respectively.

scale of numerical uncertainty kh happen to be in the same order of magnitude. Relative errors with respect to $H^{\text{eq}}_{\text{min}}$ are expected to be less pronounced for higher resolutions and smaller gap widths D, since vertical shifts of the meniscus will be less significant given that absolute values of $H^{\text{eq}}_{\text{min}}$ are larger for smaller values of D.

4.7 Oscillating fluid droplet

A circular fluid droplet of the non-wetting phase $\Omega_{\mathfrak{n}}$ with radius $R = 0.2$ m is initially suspended in the center of a surrounding fluid of the wetting phase $\Omega_{\mathfrak{w}}$. The total fluid domain with side lengths $6R$ is bounded by fictitious ghost particles and exhibits a double symmetry in analogy to the simulation setup used in section 4.4 and Hu & Adams [99], Morris [141]. The point of symmetry, which is also the center of the suspended fluid droplet, is chosen to be the point of origin. We study the small-amplitude oscillation of the centered fluid droplet in the absence of gravitational acceleration $\mathbf{b} = \mathbf{0}$ upon excitation due to application of the divergence-free initial velocity field [99, 141]

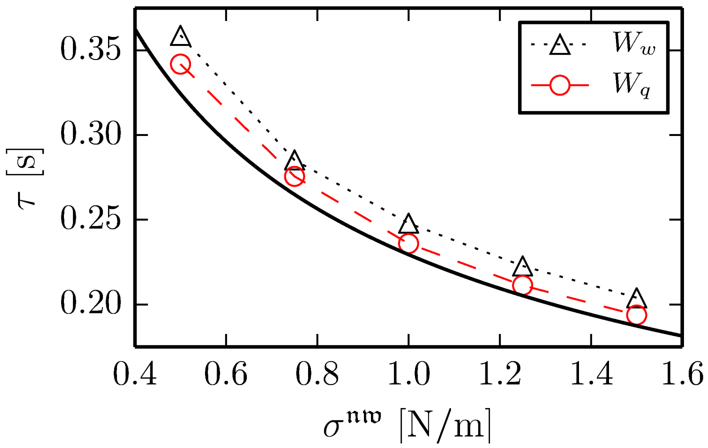

Figure 4.19: Numerical estimates of the period of oscillation as a function of interfacial tension $\sigma^{\mathfrak{w}\mathfrak{n}}$. Solid line represents theoretical prediction according to Eq. (4.11).

$$
\begin{aligned}
U_{0,1} &= U_0 \frac{X_1}{R_0}\left[1 - \frac{X_2^2}{R_0 R}\right] \exp\left(-\frac{R}{R_0}\right), \\
U_{0,2} &= -U_0 \frac{X_2}{R_0}\left[1 - \frac{X_1^2}{R_0 R}\right] \exp\left(-\frac{R}{R_0}\right),
\end{aligned}
\tag{4.10}
$$

to all fluid particles, where $\mathbf{u}_{0,\mathfrak{f}} = U_{0,1}\mathbf{e}_1 + U_{0,2}\mathbf{e}_2$ and $R = \sqrt{X_1^2 + X_2^2}$ denotes the radial distance with respect to the point of origin. Following Hu & Adams [99], Nugent & Posch [151], the period of small-amplitude oscillation of an inviscid, incompressible and circular fluid of infinite extension in the out-of-plane direction, which is embedded in a vapor phase of negligible density, reads

$$
\tau = 2\pi \sqrt{\frac{R^3 \varrho_0^{\mathfrak{n}}}{6\ \sigma^{\mathfrak{w}\mathfrak{n}}}}, \tag{4.11}
$$

as predicted by Lord Rayleigh [170]. In all simulations, the initial density of the droplet $\varrho_0^{\mathfrak{n}} = 1.0$ kg/m^3 and the initial density of the surrounding fluid $\varrho_0^{\mathfrak{w}} = 0.001$ kg/m^3, which results in a density ratio $\varrho_0^{\mathfrak{n}}/\varrho_0^{\mathfrak{w}} = 1000$ and negligible inertial coupling effects between the fluid phases. Furthermore, the dynamic viscosities $\mu^{\mathfrak{n}} = 10.0^{-2}$ Pa s and $\mu^{\mathfrak{w}} = 10.0^{-4}$ Pa s such that viscous coupling effects are expected to be negligible as well. Due to the absence of contact lines,

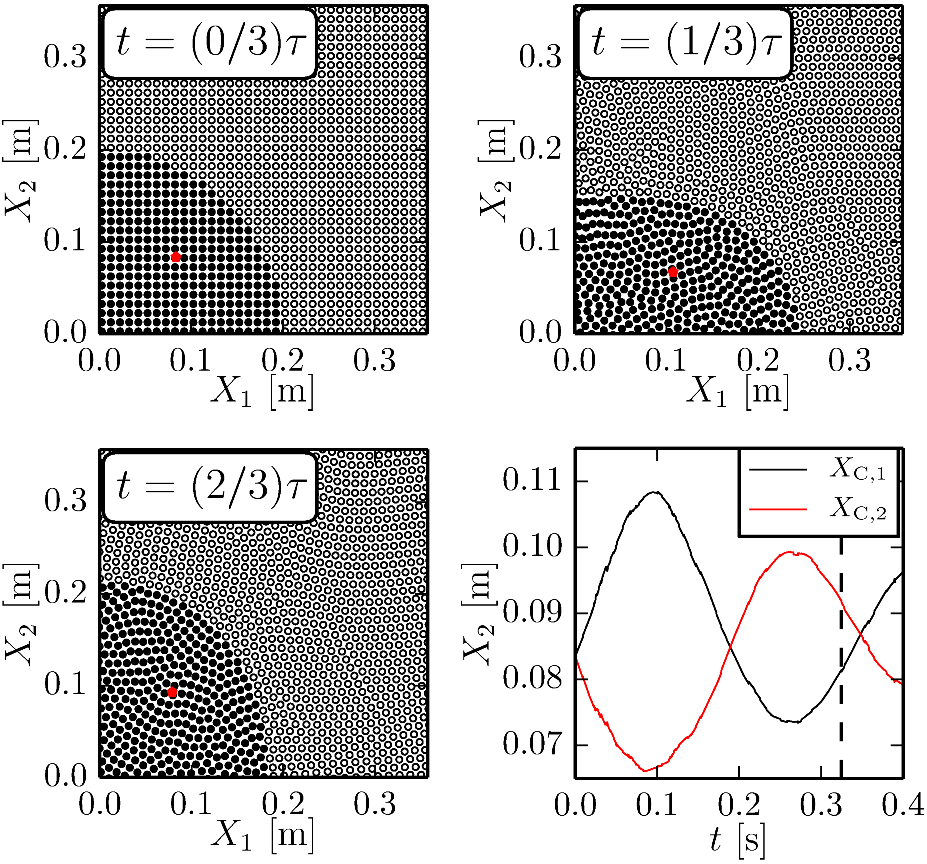

Figure 4.20: Close-up plots of particle positions indicating the mode of oscillation in the upper right-hand quarter $X_1 > 0, X_2 > 0$ at times $t = 0.0$, $t = \tau/3$ and $t = 2\tau/3$ for $\sigma^{\mathfrak{wn}} = 0.5$ N/m and $W = W_w$. Filled and open markers represent particles of the droplet and surrounding medium, respectively, while the red markers indicate the center-of-mass position of the upper right-hand quarter of the droplet. Plot in bottom-right corner shows corresponding center-of-mass coordinates $(X_{C,1}, X_{C,2})$ as a function of time, where the vertical dashed line indicates the predicted value of τ according to Eq. (4.11).

$\sigma^{\mathfrak{ws}} = \sigma^{\mathfrak{ns}} = 0$. The parameters in Eq. (4.10) are chosen as characteristic length scale $L_{\text{ref}} = R_0 = 0.05$ m and characteristic velocity $U_{\text{ref}} = U_0 = 10$ m/s in scaling the numerical speed of sound according to Eq. (2.20). The initial particle spacing dx_0 is chosen such that the ratio $R/dx_0 = 20$. The numerical estimate of the period of oscillation τ is based on the motion of the center-of-mass of the upper right-hand quarter $X_1 > 0, X_2 > 0$ of the fluid droplet (see Fig. 4.20).

Simulations are performed for various values of the interfacial tension $\sigma^{\mathfrak{wn}}$ and results (Fig. 4.19) indicate acceptable margins of errors with respect to Eq. (4.11), despite the fact that fluid viscosity introduces damping and amplitude decay. The largest absolute value of the relative error $|\epsilon(\tau)|$ is 5.3 % and 8.8 % for W_w and W_q, respectively. We conclude that the numerical model adequately accounts for inertial and dynamic effects.

CHAPTER 5

Transition from low to high Reynolds number flow in porous media

---

We numerically analyse fluid flow through porous media up to a limiting Reynolds number of $\mathcal{O}(10^3)$. Due to inertial effects, such processes exhibit a gradual transition from laminar to turbulent flow for increasing magnitudes of Re*. On the macroscopic scale, inertial transition implies non-linearities in the relationship between the effective macroscopic pressure gradient and the filter velocity, typically accounted for in terms of the quadratic Forchheimer equation. However, various inertia-based extensions to the linear Darcy equation have been discussed in the literature - most prominently cubic polynomials in velocity. The numerical results presented in this contribution indicate that inertial transition, as observed in the apparent permeability, hydraulic tortuosity and interfacial drag, is inherently of sigmoidal shape. Based on this observation we derive a novel filtration law which is consistent with Darcy's law at small* Re*, reproduces Forchheimer's law at large* Re *and exhibits higher order leading terms in the weak-inertia regime.*

5.1 Motivation

In the creeping flow or Stokes regime, the linearity

$$-J_1^d := \frac{\partial}{\partial X_1} p - \varrho g = -\frac{\mu}{k_I} q_1 \tag{5.1}$$

between the driving force **J** and the filter velocity **q**, i.e. Darcy's law [14], is well established. The constant of proportionality k_I $\left[\mathrm{m}^2\right]$ is the intrinsic permeability and a scalar-valued material property for homogeneous isotropic porous media. As apparent in Eq.(5.1), we restrict ourselves to macroscopically unidirectional flow, where components of $\mathbf{J} = J_1 \mathbf{e}_1$ and $\mathbf{q} = q_1 \mathbf{e}_1$ are non-zero only in direction $\mathbf{e}_1$. The total driving force J_1 is comprised of the macroscopic pressure gradient as well as an additional volumetric force to account for gravitational acceleration $\mathbf{b} = g \mathbf{e}_1$. The usual notation for density ϱ and dynamic viscosity μ is adopted.

The most prominent extension to Darcy's law in order to account for effects of inertia dates back to Forchheimer [72] and considers a quadratic polynomial in **q**, which, in its modern form due to Ward [205], reads

$$-J_1^q := \frac{\partial}{\partial X_1} p - \varrho g = -\frac{\mu}{k_I} q_1 - \frac{\varrho c_F}{\sqrt{k_I}} q_1^2. \tag{5.2}$$

The non-dimensional coefficient c_F to the quadratic term is referred to as Forchheimer coefficient. The range of validity of Eq.(5.2) remains however an issue of ongoing discussion. It is commonly being reported that the Forchheimer equation consistently overestimates pressure gradients in the so-called weak-inertia regime $\mathcal{O}(10^{-1}) < \mathrm{Re} < \mathcal{O}(10^1)$, where Re is based on the average velocity and a microscopic length scale depending e.g. on the grain size. In particular, various numerical, [e.g., 4, 71, 133, 147, 175], as well as experimental studies, [e.g., 116, 188], articulate the use of a leading cubic term in the weak-inertia regime in the form of

$$-J_1^c := \frac{\partial}{\partial X_1} p - \varrho g = -\frac{\mu}{k_I} q_1 - \frac{\varrho^2 \zeta}{\mu} q_1^3, \tag{5.3}$$

with ζ being a material dependent fitting coefficient. Others have used non-constant Forchheimer coefficients $c_F = c_F(\mathbf{q})$ to account for higher-order contributions, [e.g., 44, 130]. Clearly, the mismatch of the leading terms in Eqs. (5.2) and (5.3) underline a controversy. Using the method of homogenization Balhoff et al. [8] showed that the extension to Darcy's law in the weak-inertia regime has to be considered an infinite series polynomial in filter velocity, which, in the case of microstructures exhibiting isotropy and symmetry in their periodic units, reduces to a cubic polynomial. Considering the fact that flow processes involving effects of weak-inertia are of relevance in many natural, e.g. transitional flow at interfaces between a free flow domain and a porous domain or double-porosity flows in fractured reservoirs, and various technical applications, e.g. flow in catalytic converters, it is of decisive scientific interest to find a general solution for this hydraulic problem.

We state the motivation for this chapter as threefold. We numerically analyze flow phenomena on the scale of the pore network throughout six decades of Reynolds numbers covering the coarse-grained Darcy flow regime, the weak-inertia regime and the strong-inertia regime up to the limit where we observe the onset on non-steady solutions. We thereby characterize effective macroscopic flow properties based on various well established transport coefficients such as the filter velocity, apparent permeability, hydraulic tortuosity and total drag force. We discuss a strong correlation between the latter variables which is, to the best of our knowledge, yet unreported.

A further aspect of this contribution is the use of the mesh-free Lagrangian method Smoothed-Particle Hydrodynamics (SPH) [136] to assess effective transport properties of porous materials with focus on its potential application in digital rock physics. In this context, we compare the predictive capabilities of SPH with respect to established numerical methods. For the latter benchmark purpose, we base our study on a fibrous porous material which is well examined in the literature, e.g. in Narváez et al. [147].

5.2 Methods

We implement a Smoothed Particle Hydrodynamics (SPH) [136] model to simulate pore-scale resolved flow through fibrous porous media as outlined in chapter 3. For validation purposes, the computational domain is chosen in analogy with Narváez et al. [147] (see Fig. 5.1). The fibers have a circular cross section with radius r and are aligned in parallel, such that our computation can be reduced to two dimensions and to flow in a transverse direction only. Furthermore, the fibers are randomly distributed with a constraining minimum pore throat size of $r/2$. The porosity, defined as the ratio of total pore space volume V_F to total volume V, is $\phi = 0.6373$.

The saturand is considered to be a Newtonian fluid and its governing conservation equations for mass and momentum are Eq. (2.11) and Eq. (2.28), respectively. As outlined in section 2.1.4, we consider a barotropic fluid and thus model the local microscopic pressure p as a function of density in terms of a stiff equation of state. The numerical speed of sound chosen large enough such that density fluctuations relative to the initial fluid density ϱ_0 can be neglected. ote that the macroscopic filter velocity $\mathbf{q}$ is related to the local fluid velocity $\mathbf{u} = u_1\mathbf{e}_1 + u_2\mathbf{e}_2$ in terms of an average of $\mathbf{u}$ with respect to the total volume V. We introduce the volume average operator $\langle \bullet \rangle = V^{-1} \int_V \bullet \, dV$ and state concisely $\mathbf{q} = \langle \mathbf{u} \rangle$.

Flow is driven by a volume force applied in direction of the unit vector $\mathbf{e}_1$, i.e. $\mathbf{b} = g\mathbf{e}_1$, which, for the isotropic material at hand, implies that $\mathbf{q}$ is unidirectional, i.e. $\mathbf{q} = q_1\mathbf{e}_1$. Fixing the local fluid properties ϱ_0 and μ in all simulations, the microscopic length scale based Reynolds number $\mathrm{Re} = \varrho_0\|\mathbf{q}\|r/\mu$ is varied by the

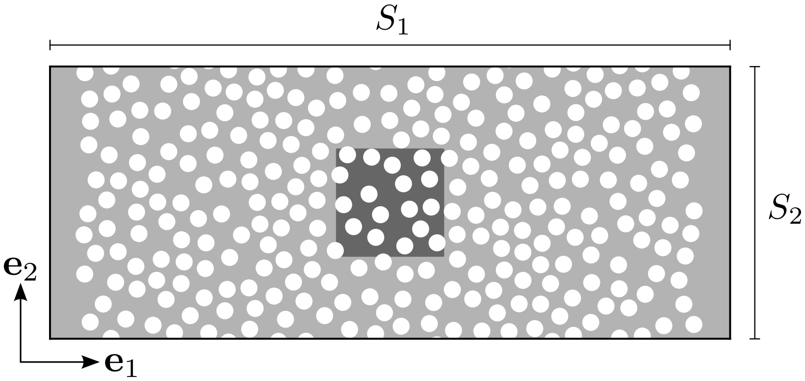

Figure 5.1: Computational domain proposed by Narváez et al. [147]. The domain is periodic in both $\mathbf{e}_1$ and $\mathbf{e}_2$ direction and the domain dimensions satisfy $S_2 = 0.4\ S_1$. The external force is applied in $\mathbf{e}_1$ direction. The fiber count equals 266. The centered dark gray area corresponds to the subdomain for which streamlines are shown in Fig. 5.4. Integration points are initially set up on a Cartesian lattice with 1280 and 512 points in $\mathbf{e}_1$ and $\mathbf{e}_2$ direction, respectively.

choice of g. The characteristic velocity $\|\mathbf{q}\|$ is the magnitude of the filter velocity and $\| \bullet \|$ indicates the L^2 norm. Periodic boundary conditions are applied in $\mathbf{e}_1$ and $\mathbf{e}_2$ direction with respect to facing edges. Additionally, the crucial no-slip and no-penetration boundary condition (2.26) is applied on the solid surfaces. Thus defined boundary value problem is completed by the initial conditions for velocity $\mathbf{u}(t=0) = \mathbf{0}$ and density $\varrho(t=0) = \varrho_0$.

A detailed description of the numerical scheme is available in chapter 3. However, we recall relevant key properties of SPH herein. SPH is a Lagrangian method which implies that the integration positions $\mathbf{x}_i$, also referred to as particles, follow the trajectories of Newton's equation of motion $\dot{\mathbf{x}}_i = \mathbf{u}_i$. This comes with the advantage that, in contrast to Eulerian methods, the non-linear convective term $\operatorname{grad} \mathbf{u} \cdot \mathbf{u}$ is not required to be modeled, which makes SPH comparatively stable at high Re. As outlined in section 3.5, the discrete nodal motion equation for single-phase flow reads

$$m_i \dot{\mathbf{u}}_i = \sum_{j:\mathbf{x}_j \in \Omega_i} \mathbf{F}_{ij}^V - \sum_{j:\mathbf{x}_j \in \Omega_i} \mathbf{F}_{ij}^P + \mathbf{F}_i^G$$

Note how the pressure and viscosity terms in Eq. (2.28) are turned into a summation of inter-particle forces due to local pressure variations $\mathbf{F}_{ij}^P$ and local velocity gradients $\mathbf{F}_{ij}^V$ acting between a particle i and its short-range neighboring particles $j : \mathbf{x}_j \in \Omega_i$ that are located within the compact support domain Ω_i of the smoothing kernel W centered at point $\mathbf{x}_j$. The derivation of the inter-particle accelerations is documented in section 3.5. We may evaluate the total resultant force exerted by the pore fluid on the solid-skeleton surfaces in terms of

$$\mathbf{F}^D = \underbrace{\sum_{i:\mathbf{x}_i\in\Omega_{\mathfrak{s}}}\ \sum_{j:\mathbf{x}_j\in\Omega_{\mathfrak{f}}} \mathbf{F}^P_{ij}}_{\mathbf{F}^D_P} + \underbrace{\sum_{i:\mathbf{x}_i\in\Omega_{\mathfrak{s}}}\ \sum_{j:\mathbf{x}_j\in\Omega_{\mathfrak{f}}} \mathbf{F}^V_{ij}}_{\mathbf{F}^D_V} \tag{5.4}$$

which stems from the summation of inter-particle forces acting on stationary particles i of the solid domain $\Omega_{\mathfrak{s}}$. Following common terminology, the component F^D_1 of the total resultant force acting in direction of the filter velocity is called drag force. In analogy to Eq. (5.4), we additively split the total drag force into the inertia force induced form drag $F^D_{P,1}$ and the viscous shear force induced skin friction $F^D_{V,1}$. The component F^D_2 acting perpendicular to the unidirectional filter velocity fluctuates around zero.

5.3 Results

For the purpose of data validation, we compare our results of the apparent permeability $k_A := \mu q_1/\varrho_0 g$ to results previously published in Narváez et al. [147]. The expression for k_A is derived using the linear Darcy Eq. (5.1) for volume force driven unidirectional filtration, which implies that $k_A = k_I$ only in a limited range of small Re. The data presented in Fig. 5.2 shows that the predictive capability of the SPH model is comparable to the lattice Boltzmann model (LB) and the finite-element model (FEM) used in Narváez et al. [147]. The peak relative difference in k_A between all methods is of the order of 3 %, which is due to numerical discretization. Even though Narváez et al. [147] restrict their analysis to a maximum Re of order 50, we do not question the validity of our data in regimes of larger Re arguing that a careful choice of the numerical speed of sound c will ensure Mach numbers $\mathrm{Ma} = q_1/c$ well below 0.1 as shown in the inset to Fig. 5.2. Artificial compressibility effects are thus considered negligible. In fact, the largest encountered density variation $\Delta\varrho$ relative to the reference density ϱ_0 is of the order of 5 %, which ensures compliance to the quasi-incompressibility constraint.

The onset of non-Darcy flow at $\mathrm{Re} \approx 1$ is observed in terms of an increasing deviation of k_A from the upper asymptote k_I as shown in Fig. 5.2. Furthermore, the dependence of k_A on Re is observed to possess a sigmoidal character with a lower asymptote being reached at $\mathrm{Re} \approx \mathcal{O}(10^3)$. The latter observation is supported by the numerical work of Chaudhary et al. [40], who document an asymptotic behavior of k_A for $\mathrm{Re} > 450$, and the experimental study of Barree

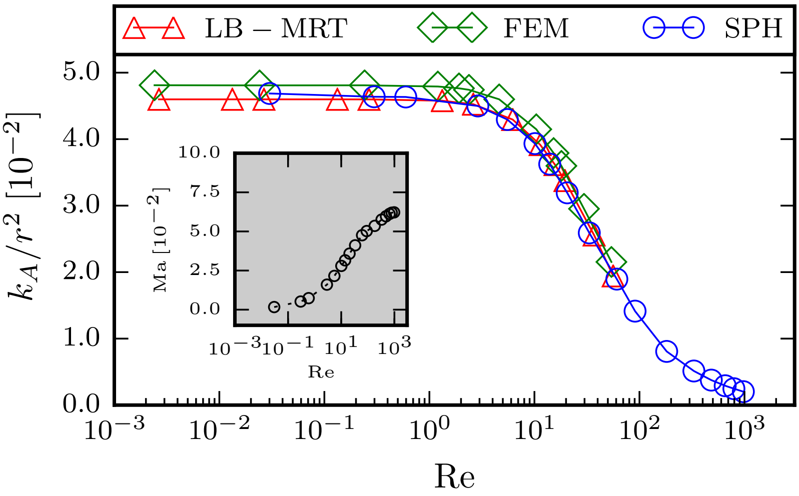

Figure 5.2: Dependence of the non-dimensional apparent permeability on Re as predicted by our SPH calculations compared to reference results for the same pore-space morphology published in Narváez et al. [147]. Non-dimensionalization was performed with respect to the cross-sectional fibre radius r. The inset shows the filter velocity based Mach number.

& Conway [12].

Despite the fact that k_A does highlight the nonlinearity of the effective hydraulic conductivity, it is typically the relationship between the macroscopic external driving force J_1 and the filter velocity q_1 which is of interest in light of effective filtration models. Hence we focus on Fig. 5.3 and observe the well documented gradual transition of J_1 from a linear dependence on q_1 for Re $< \mathcal{O}(10^0)$ to a purely quadratic dependence on q_1 for Re $> \mathcal{O}(10^3)$. While the latter observation is confirmed in various experimental studies [e.g., 27, 61], the use of pore-scale resolved simulations enables the analysis of the correlation between macroscopic effects in terms of J_1 (filled circles) and microscopic mechanisms in terms of the total drag force F_1^D (open circles).

The fact that both data sets superimpose in Fig. 5.3 implies that macroscopic nonlinearities are solely caused by the apparent nonlinearity in the drag forces, which confirms results of the dimensional analysis conducted by Hassanizadeh & Gray [90]. J_1 is proportional to F_1 over the entire range of Re with a constant proportionality factor having a unit of volume. We therefore interpret each term on the right-hand side of the filtration Eqs. (5.1)-(5.3) as averaged microscopic drag per unit of volume.

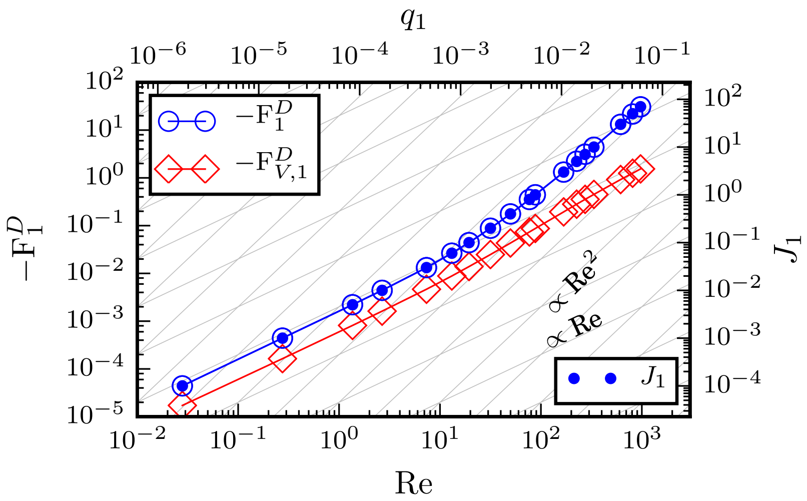

Figure 5.3: Dependence of the total microscopic drag force F_1^D [N], skin friction component $F_{V,1}^D$ [N] and macroscopic external driving force J_1 $\left[\mathrm{N/m^3}\right]$ on Re and the filter velocity q_1 [m/s]. A set of curves scaling either with Re or Re^2 are plotted to indicate scaling properties of F_1^D and J_1.

We further analyze the nonlinearity of F_1^D in terms of its additive decomposition introduced in Eq. (5.4). The skin friction due to viscous shearing, i.e. the component $F_{V,1}^D$, scales approximately linearly in q_1 throughout the analyzed range of Re. While $F_{V,1}^D$ considerably contributes to the total drag F_1^D in the linear regime, we can practically neglect its contribution in the pure quadratic regime where the magnitudes of $F_{V,1}^D$ and F_1^D differ by more than one order. Clearly, the effects of inertia that we measure in terms of the form drag component $F_{P,1}^D$ lead to the nonlinearity of F_1^D and therefore cause the apparent nonlinearity of J_1. The latter observation agrees well with the common understanding of non-Darcy flow at high filter velocities, in which the nonlinearities are attributed to the effects of inertia [e.g., 106].

In an attempt to characterize inertial transition in terms of the microscopic flow field, we analyze the streamlines to the steady-state velocity fields as shown in Fig. 5.4. The subdomain depicted in Fig. 5.4, which corresponds to the dark gray area in Fig. 5.1, is considered large enough to be representative of the entire computation domain. We can clearly highlight that from the onset of inertial transition at Re $\approx$ 1, the simultaneous and strongly interrelated processes of streamline rectification in direction of the applied external force, flow tube narrowing, flow separation and the formation and augmentation of wake eddies take place [see 9, 40]. In the Darcy regime, the irrotational flow is fully attached and viscous dissipation can be attributed to the presence of shear boundary layers adhering to solid surfaces $\Gamma_{\mathfrak{fs}}$. From the onset of flow separation, the flow can no longer be considered irrotational since wake eddies are present. Due to the increase of the local velocity gradient, recirculation in eddies causes further viscous dissipation in free shear layers, which separate irrotational flow from the rotational flow [189].

We quantify the observation of streamline rectification with use of the so-called hydraulic tortuosity T. We note that the definition of T is rather ambiguous in literature [c.f., 60]; however, we adopt the most common definition of T in terms of the ratio of the mean streamline arc length $\langle \mathrm{L}_a \rangle$ to the mean length of streamlines projected onto the direction of filtration $\langle \mathrm{L}_1 \rangle$. It can be readily deduced that $T \geq 1$. We stress the fact that streamlines living in recirculation zones do not contribute to the effective hydraulic conductivity and are thus considered dead space as seen from the perspective of a macroscopic observer. We therefore exclude rotational streamlines in the computation of the hydraulic tortuosity T based on the simple argument that no segment of the streamline should point in negative $\mathbf{e}_1$ direction. Despite the fact that the latter argument successfully allows the differentiation between conductive irrotational streamlines (red) and eddy streamlines (black) as shown in Fig. 5.4, it is not of general validity, e.g. in cases of microscopic non-uniformity. In order to confirm the validity of our data for $\langle \mathrm{L}_a \rangle / \langle \mathrm{L}_1 \rangle$ presented in Fig. 5.5, we further compute the upper-bound estimate $T^M \geq T$ which is due to Duda et al. [60]. T^M is defined as the ratio of the mean velocity magnitude $\langle \|\mathbf{u}\| \rangle$ to the mean velocity in filtration direction $\langle u_1 \rangle$.

The dependence of T on Re is sigmoidal, having two asymptotes in the regimes $\mathrm{Re} < \mathcal{O}(10^0)$ and $\mathrm{Re} > \mathcal{O}(10^3)$ as shown in Fig. 5.5. The upper asymptote is referred to as the diffusional tortuosity $T_{\max}$ and solely depends on the pore-space morphology, since it is an intrinsic property of the porous skeleton for any fully attached Stokes flow. Bo-Ming & Jian-Hua [23] comprehensively show that $T_{\max}$ can be estimated by means of geometric considerations only. Duda et al. [60] document that $T^M = T = T_{\max}$ in the limit of low Re where the absence of eddies is expected, which otherwise have a positive contribution to T^M. Our data confirms the latter assumption within the margins of numerical uncertainty. Focusing on the lower asymptote $T_{\min}$, Fig. 5.5 indicates that the magnitudes of T^M and T can be considered fairly independent of Re. We argue that the existence of a lower asymptote to T must hold for steady flow, since the process of streamline rectification will be truncated by the imposed no-penetration condition on the interface $\Gamma_{\mathfrak{fs}}$. We stress the fact that the latter argument will only hold for steady flow, since we expect an increase of local streamline curvature in non-steady flow, e.g. due to vortex shedding. We conclude that $T_{\min}$, subsequently

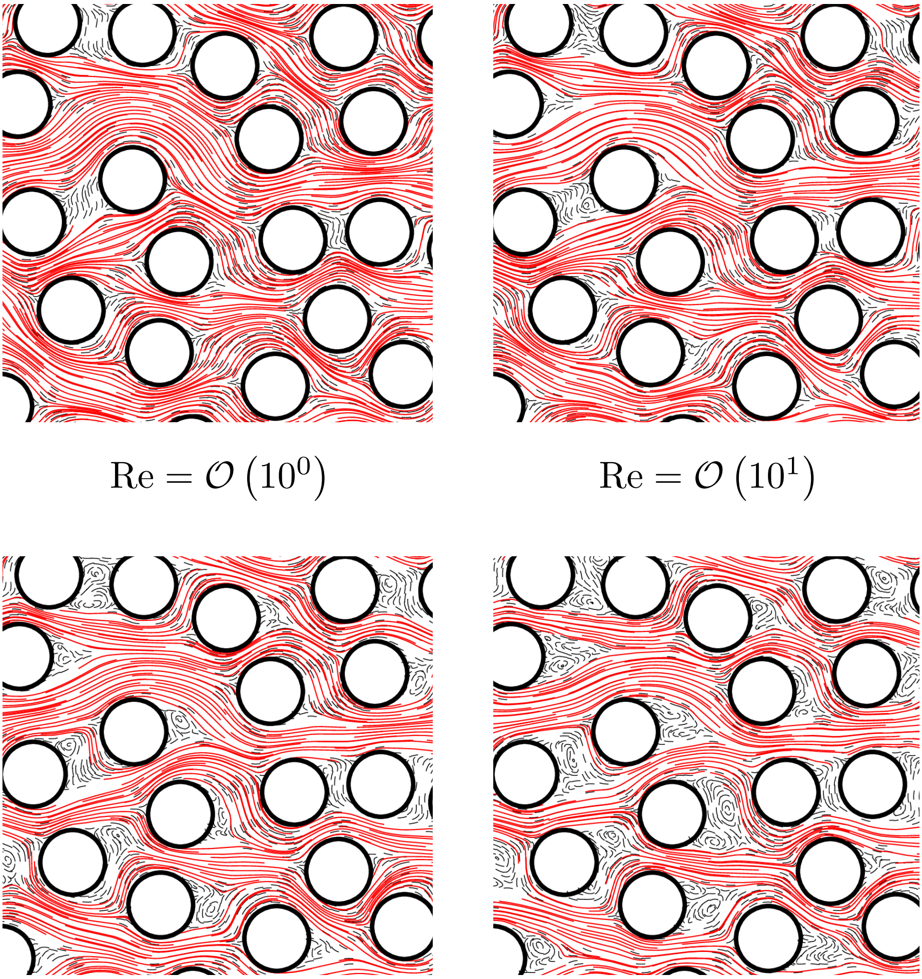

$\mathrm{Re} = \mathcal{O}\left(10^{0}\right)$

$\mathrm{Re} = \mathcal{O}\left(10^{1}\right)$

$\mathrm{Re} = \mathcal{O}\left(5 \cdot 10^{1}\right)$

$\mathrm{Re} = \mathcal{O}\left(10^{2}\right)$

Figure 5.4: Subset streamline figures for various Re. Streamlines are colored black if they live in domains of rotational eddy motion and red otherwise. Only red streamlines contribute to the computation of the mean hydraulic tortuosity. Hence, we evaluate T in the irrotational flow domain only. The depicted subdomain corresponds to the dark gray area in Fig. 5.1.

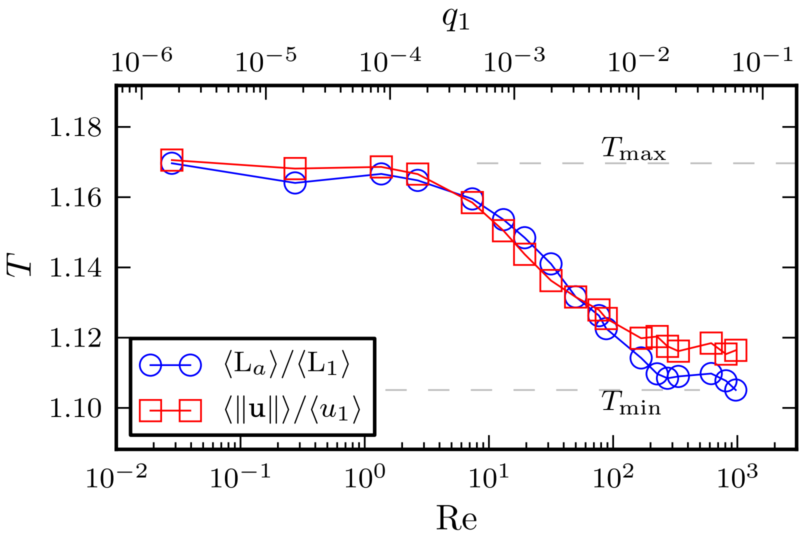

Figure 5.5: Dependence of the hydraulic tortuosity T on Re and the filter velocity q_1. Upper bound estimate of the hydraulic tortuosity following Duda et al. [60] are marked red.

referred to as inertial tortuosity, is the global minimum for T and also an intrinsic property of the porous medium.

5.4 Discussion

The most striking result to emerge from the data discussed so far is that we observe a strong and yet unreported positive correlation between k_A, J_1 and T. Not only do we observe that k_A and T possess sigmoidal characteristics, but we also see that the points of saturation, i.e. where the upper and lower asymptotes are reached, match. Moreover, the very same saturation points $\mathrm{Re} \approx \mathcal{O}(10^0)$ and $\mathrm{Re} \approx \mathcal{O}(10^3)$ are observed to be the bounds within which inertial transition as apparent in J_1 occurs. As previously discussed, the Darcy linearity holds for $\mathrm{Re} < \mathcal{O}(10^0)$ while the pure quadratic dependence holds for $\mathrm{Re} > \mathcal{O}(10^3)$. The latter observation implies a correlation of k_A and T with the rate of J_1. In an attempt to meaningfully analyze our observation, we introduce the normalization operator

$$n_{[0,1]}(f) := \frac{f - \min(f)}{\max(f) - \min(f)}, \tag{5.5}$$

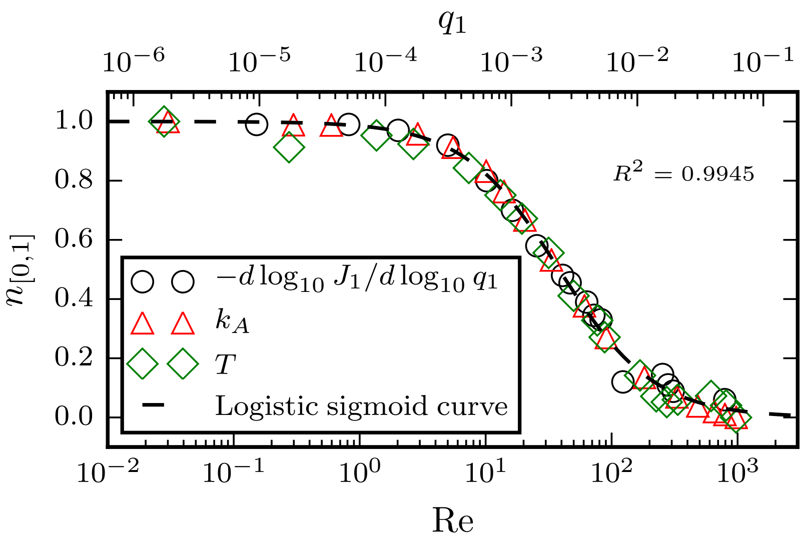

Figure 5.6: Various macroscopic variables normalized according to $n_{[0,1]}$ show a strong correlation with the logistic sigmoid function. The best fitting values with respect to Eq. (5.4) are $\gamma = 1.1475$ and $q_1^i = 2.39 \cdot 10^{-3}$m/s.

which rescales f to be bounded between 0 and 1. The results for $n_{[0,1]}$ applied to k_A, T and the logarithmic derivative, or apparent exponent, $-d\log_{10} J_1/d\log_{10} q_1$ are shown in Fig. 5.7. The logarithmic derivative is inverted in sign for comparative purposes (see Fig. 5.7 for clarity). The analyzed normalizations are confirmed to be equal with high certainty. Hence, we put forward the idea that inertial transition, as measured by means of the discussed macroscopic variables, qualitatively follows the logistic sigmoid curve

$$n_{[0,1]}(f) = \left[1 + \left(\frac{q_1}{q_1^i}\right)^{\gamma}\right]^{-1},$$

with fixed inflection point velocity q_1^i and slope factor γ. Since q_1^i and γ are fixed, Eq. (5.5) implies that the quantitative form of a macroscopic variable of interest can be derived by the knowledge of the corresponding upper and lower asymptotic values only.

Consequently, our intention is to find a macroscopic filtration model $J_1(q_1)$ which satisfies Eq. (5.5) for f being the apparent exponent $-d\log_{10} J_1/d\log_{10} q_1$. For this purpose, we make use of the experimentally and herein numerically validated properties that the upper and lower asymptotes $\min(f)$ and $\max(f)$

to $-d\log_{10} J_1/d\log_{10} q_1$ are -2 and -1, respectively. Reformulation of Eq. (5.5) thus leads to

$$\frac{dJ_1}{dq_1} = \frac{J_1}{q_1}\frac{d\log_{10} J_1}{d\log_{10} q_1} = \frac{J_1}{q_1}\left(2 - n_{[0,1]}\right). \tag{5.6}$$

Direct integration of Eq. (5.6) yields the closed form solution

$$J_1 = Cq_1\left[1 + \left(\frac{q_1}{q_1^i}\right)^{\gamma}\right]^{\frac{1}{\gamma}}, \tag{5.7}$$

where C is the constant of integration. The linearization of Eq. (5.7) for small q_1 reads $J_1 = Cq_1$ such that we can identify C to be the coefficient μ/k_I for consistency with Eq. (5.1). We finally propose the filtration law

$$-J_1^S := \frac{\partial}{\partial X_1}p - \varrho g = -\frac{\mu}{\kappa}q_1\left[1 + \left(\frac{q_1}{q_1^i}\right)^{\gamma}\right]^{\frac{1}{\gamma}} \tag{5.8}$$

for macroscopically steady, fully saturated single-phase flow through porous media based on the empirical observation that inertial transition is inherently sigmoidal in shape.

We find that J_1^S has certain intriguing properties which we discuss subsequently. As already pointed out, the linearization of J_1^S for small q_1 reduces to the Darcy Eq. (5.1). Focusing on the bracket term $[1 + (q_1/q_1^i)^{\gamma}]$ in Eq. (5.8), we see that Darcy linearity holds for filter velocities small enough to satisfy $(q_1/q_1^i)^{\gamma} \ll 1$. Similarly, the pure quadratic dependence $J_1^S = \mu q_1^2/k_I q_1^i$ is recovered if $(q_1/q_1^i)^{\gamma} \gg 1$. We stress the fact that both properties, which in fact result from the presumed asymptotes in Eq. (5.6), hold for any value of $\gamma > 0$. The proposed filtration law depends on γ only in the limited range of Re where inertial transition takes place, the effective width of which increases for smaller values of γ. We conclude that γ dictates the effective width of inertial transition while q_1^i shifts the onset of nonlinearity with respect to q_1 and Re.

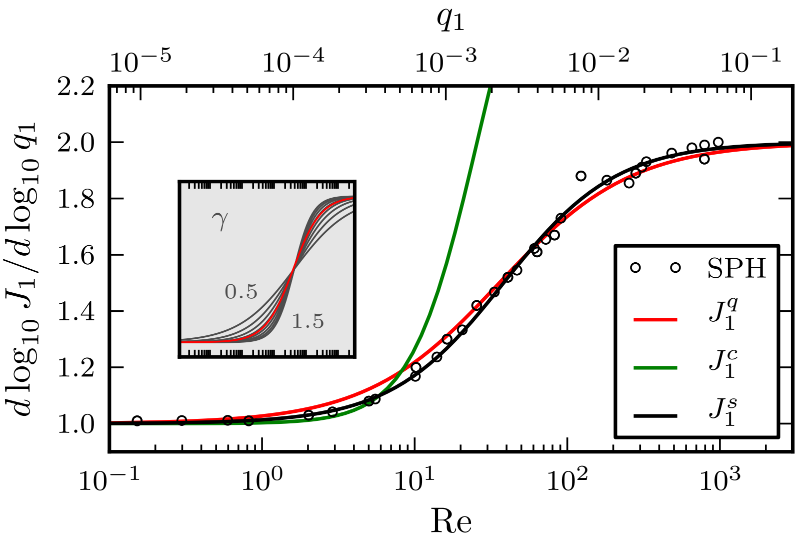

Figure 5.7: The dependence of the apparent exponent $d\log_{10} J_1/d\log_{10} q_1$ on Re and the filter velocity q_1. The red curve is derived using the best fitting Forchheimer Eq. (5.2). The green curve is derived using the best fitting cubic transition Eq. (5.3), with the fitting target being restricted to a maximum Re = 10. The black curve is our postulated phenomenological logistic filtration law. Inset shows the dependence of the logistic curve on γ with the derived Forchheimer function (red) added for reference. Inset axes correlate exactly to the outer axes.

J_1^S reduces to a quadratic polynomial function for $\gamma = 1$, which clearly implies that the Forchheimer Eq. (5.2) is a special case of the proposed filtration Eq. (5.8). The non-dimensional Forchheimer coefficient c_F therefore satisfies $c_F := \mu/\varrho q_1^i \sqrt{k_I}$, which passes dimensional consistency. Hence we can additionally reformulate Forchheimer's law into a form in which the coefficient q_1^i to the quadratic term allows a more accessible interpretation in terms of an inflection point velocity, than c_F.

The structural form of the proposed Eq. (5.8) is not considered a novelty, but rather an application of the Churchill-Usagi asymptotic correlation method. Following Churchill & Usagi [45], if $Y(X)$ is a physical entity describing a transport phenomena and $Y_0(X), Y_1(X)$ are known asymptotes to $Y(X)$ for small and large values of the independent variable X, the expression $Y^\gamma = Y_0^\gamma + Y_1^\gamma$ describes a uniform transition between the asymptotes, with γ being a blending coefficient. The latter expression can be reformulated to read $Y = Y_0[1+(Y_1/Y_0)^\gamma]^{1/\gamma}$ which matches our model Eq. (5.8). The Churchill-Usagi method is successfully used in describing various transport phenomena in fluid mechanics, heat transfer and chemical engineering. In fact, Prieur Du Plessis [164] made use of the correlation method to model inertial flow through granular porous media. By means of volumetrically averaging the Navier-Stokes equations over a cubic periodic cell of closely-packed spheres, Prieur Du Plessis [164] derives expressions for the total drag force in the limit of Re → 0 and Re → ∞ assuming macroscopically laminar flow. The homogenization procedure revealed that drag scales $\propto \mathbf{q}$ in the lower limit and $\propto \mathbf{q}^2$ in the upper limit, which matches our numerical results. Prieur Du Plessis [164] applies the Churchill-Usagi method to correlate the latter asymptotes and derives an expression to cover the complete range of Re and sets $\gamma = 1$ arguing that the experimental results of Ergun [65] indicate so.

We believe that the general validity of the condition $\gamma = 1$ for different porous media is rather questionable in light of phenomenology, e.g. the laminar to turbulent transition in straight tubes is known to be quite discrete while more gradual in less streamlined pore-channels. The latter argument is supported by Chaudhary et al. [40] who emphasize that the specifics of Forchheimer flow, i.e. flow tube narrowing and growth of wake eddies, are dependent on pore geometry. As shown in the following, we find that it is in fact this restrictive property of the Forchheimer law, that several researchers observe the cubic transition Eq. (5.3) to yield better fitting results in the so-called weak-inertia regime $10^0 < \mathrm{Re} < 10^1$ [e.g., 4, 147, 148, 175, 188].

We evaluate the Taylor series expansion of Eq. (5.8) about $q_1 = 0$ to analyse the polynomial order in the weak-inertia regime. Application of the binomial theorem yields the infinite series polynomial

$$\begin{aligned} -TJ_1^S(q_1, 0) &= -\frac{\mu}{\kappa} q_1 \sum_{n=0}^{\infty} \binom{\frac{1}{\gamma}}{n} \left(\frac{q_1}{q_1^i}\right)^{n\gamma} \\ &\approx -\frac{\mu}{\kappa} q_1 \left[1 + \frac{1}{\gamma}\left(\frac{q_1}{q_1^i}\right)^{\gamma}\right] + (\gamma - 1)\, \mathcal{O}\left(q_1^{2\gamma+1}\right) \end{aligned}$$

which shows that the extension to Darcy's law to account for weak-inertia increases in its polynomial order for larger values of γ. The magnitude of the coefficients given by the binomial coefficient however diminish greatly with order for $\gamma > 1$ which is consistent with Balhoff et al. [8].

We further fit the non-linear filtration Eqs. (5.2),(5.3) and (5.8) to our data for $J_1(q_1)$. Regarding the proposed Eq. (5.8), a further optimization is redundant since the free parameters $\gamma = 1.1475$ and $q_1^i = 2.39 \cdot 10^{-3}$m/s are adopted from the logistic function shown in Fig. 5.7 and the permeability k_I can be readily deduced from k_A. We keep the value of k_I fixed, such that the single free parameters c_F and ζ remain to be optimized with respect to Eq. (5.2) and Eq. (5.3), respectively. In the case of the cubic Eq. (5.3), the fitting target is restricted to a maximum

$\text{Re} = 10^1$, since Eq. (5.3) fails in regimes of larger Re as pointed out by Narváez et al. [147]. We find that the results can be conveniently discussed in terms of the logarithmic derivative $d\log_{10} J_1/d\log_{10} q_1$ as shown in Fig. 5.7. We stress the fact that the discrete data points are derived using a midpoint rule, which causes a numerical scattering since the data points are not equispaced in $\log_{10} q_1$. Despite the numerical uncertainty, we clearly observe that the fit to Forchheimer Eq. (5.2) overestimates the apparent exponent of J_1 in the weak-inertia regime. The cause of which can be attributed to the fact that $\gamma > 1$ for the analyzed porous medium as shown in the inset to Fig. 5.7. We can confirm that the fit to the cubic transition Eq. (5.3) yields a smaller residual in the weak-inertia regime compared to Eq. (5.2), but fails for larger values of Re. Concerning the analyzed model material, we thus document the superiority of the proposed logistic filtration Eq. (5.8).

5.5 Summary

We have discussed numerical results for macroscopically steady and unidirectional flow through a rigid fully-saturated fibrous porous medium for Re up to $\mathcal{O}(10^3)$. A strong positive correlation between apparent permeability k_A, hydraulic tortuosity T, total drag force F_1^D and the macroscopic external force J_1 is found. Inertial transition, as apparent in the analyzed macroscopic transport coefficients, can be conveniently modeled in terms of a logistic sigmoid function with the two free parameters q_1^i and γ. The parameter q_1^i dictates the onset of inertial transition, while γ dictates the effective width of inertial transition. We derive a new macroscopic filtration law $J_1^S(q_1)$ consistent with the phenomenological observation of sigmoidal transition. It is found that $J_1^S(q_1)$ can be alternatively derived by application of the Churchill-Usagi asymptotic correlation method with the lower and upper asymptotes to $J_1(q_1)$ inherited from volumetric homogenization or dimensional analysis, [e.g., 164, 189]. The lower asymptote for $\text{Re} \to 0$ to the proposed filtration law is the Darcy equation, while the upper asymptote for $\text{Re} \to \mathcal{O}(10^3)$ is the highest order term of the Forchheimer equation. Setting the blending coefficient $\gamma = 1$, the Forchheimer equation is found to be a special case of $J_1^S(q_1)$. The necessity of using a cubic transition equation in the weak-inertia regime, where the Forchheimer equation is often observed to fail, is quite possibly due to the fact that $\gamma > 1$ for certain pore-space morphologies. It is left open for future work, to find how γ correlates to geometric properties of the pore-space and how $J_1^S(q_1)$ should be extended to account for material anisotropy.

CHAPTER 6

Wetting phase entrapment during primary drainage

We perform pore-scale resolved direct numerical simulations of two-phase flow of immiscible fluids to analyze the mechanisms of wetting phase entrapment during saturation-controlled primary drainage in heterogeneous, partially wettable porous media. At the length scale of pore networks, flow regimes that emerge due to the interplay of viscous and capillary forces have been characterized as viscous fingering, stable displacement and capillary fingering. At the length scales of individual pores, however, the corresponding flow fields and dynamics of fluid-fluid interfaces remain largely unknown. To this end, we study the effect of capillary number (Ca*) and viscosity ratio (*M*) on the formation and entrapment of discrete ganglia of the wetting fluid. During viscous fingering, pore-scale flow fields are reminiscent of Bretherton's coating flow which implies the formation of wetting films. Wetting films render the evolution of fluid-fluid interfacial area non-linear and give rise to non-negligible interfacial viscous momentum coupling. Although macroscopically appearing flat, saturation fronts during stable displacement extend over the length of the capillary dispersion zone. While far from the capillary dispersion zone fluid permeation obeys Darcy's law, frequent fragmentation and coalescence of discrete ganglia renders fluid flow within the capillary dispersion zone complex. Capillary trapping mechanisms are observed dominant for small* Ca*. Using these insights, we map out a tentative phase diagram on the* $\log \mathrm{Ca} - \log \mathrm{M}$ *plane by classifying the morphologies of discrete wetting phase ganglia. We consider the latter a useful complementary extension to the well-anticipated phase diagram of drainage displacement patterns.*

6.1 Introduction

Assessing the stability and evolution of saturation fronts, or, from a pore-scale point of view, interfaces between immiscible bulk fluid phases, is key with respect to understanding, designing and controlling a multitude of subsurface processes such as sequestration of carbon dioxide in geological media, groundwater contamination remediation, or enhanced oil recovery. Depending on the governing capillary number (Ca), viscosity ratio (M), morphological properties of the porous microstructure and boundary conditions, the displacement of an immiscible wetting fluid from a porous medium by a non-wetting fluid, i.e. primary drainage, results in flow regimes as diverse as viscous fingering, stable displacement or capillary finger branching [122]. Yet, traditional coarse-grained continuum models for two-phase flow in porous media assume the same set of balance equations and constitutive relations applicable to all displacement patterns. In particular, a phenomenological extension of Darcy's law is assumed to govern macroscopic momentum balance with relative permeability and capillary pressure functions representing constitutive model inputs [14]. These constitutive relations are considered functions of saturations only and their calibration in light of a particular flow regime typically renders them non-linear and hysteretic [75, 103, 144]. In an attempt to face the latter, contemporary models acknowledge the role of interfacial areas in hysteresis [78, 87–89] or explicitly account for mass-exchange between percolating and non-percolating subphases [91, 93]. Considerable effort has been devoted to studying two-phase flow at the length scale of pore-networks, both experimentally [e.g. 16, 67, 74, 120, 199, 214] and numerically [e.g. 21, 39, 52, 68, 70, 125], providing a reliable set of data for the Ca-M phase diagram of drainage displacement patterns as introduced by Lenormand et al. [122]. However, the pore-scale dynamics of fluid-fluid interfaces and the mechanisms by means of which discrete ganglia form and become trapped remain poorly understood which hampers the development of accurate coarse-grained models.

To this end, recent advances in pore-scale imaging-based characterization methods (see review Bultreys et al. [37]) that enable the fast visualization of two-phase flow at pore-scale resolution, most notably microscopy imaging of thin micro-models [e.g. 6, 107, 135, 214], X-ray computed tomography [e.g. 17, 22, 36, 208] and confocal microscopy [e.g. 49, 112], have provided valuable insights into the interplay of viscous, capillary, gravitational and inertial forces that constitutes the complexity of interface dynamics at the pore-scale. For instance, free-energy driven Haines jumps have been confirmed as dominant displacement mechanism for flow at small capillary numbers [6, 17] and to give rise to inertial oscillations of moving interfaces [135]. Clearly, these observations deviate from the assumptions underlying generalized Darcy flow. Besides experimental approaches, we consider direct numerical simulations to be an important complementary tool for quantitative characterization of multiphase flow in porous media [37, 132].

In this chapter, we present pore-scale resolved direct numerical simulations of two-phase flow in partially wettable porous media of particulate microstructure. Our method of choice is a quasi-incompressible Smoothed-Particle Hydrodynamics model (SPH) [99, 136, 187] which incorporates the Navier-Stokes equations together with the continuum surface force method [30, 115] to account for the interfacial balance equations. Since SPH is a mesh-free particle method, it constitutes an attractive approach to model the formation and fragmentation of moving boundaries, i.e. fluid-fluid interfaces, in complex pore spaces. Disregarding gravity effects, we perform numerical experiments of saturation-controlled primary drainage for various magnitudes of capillary number and viscosity ratio. Rather than studying the emerging displacement patterns at the length scale of pore-networks, we discuss pore-scale flow fields associated with different flow regimes and characterize the mechanisms by means of which wetting phase becomes hydraulically reservoir-disconnected and, ultimately, trapped.

Our results show that for viscous fingering, i.e. when viscous forces dominate and the viscosity of the invading fluid is considerably lower than that of the defending fluid, fluid displacement at the pore-scale is reminiscent of Bretherton's problem [32], i.e. flow of gas bubbles in liquid-filled capillary tubes. The corresponding flow field is such that the less viscous fluid drains through the core of a pore-throat causing the formation of wetting films on solid surfaces. Wetting films are observed to render the evolution of specific fluid-fluid interfacial area non-linear and, as a result, non-equilibrium viscous momentum exchange between both fluid phases, i.e. the Yuster effect [7, 211], non-negligible. For stable displacement, i.e. when viscous forces dominate and the viscosity of the defending fluid is considerably lower than that of the invading fluid, saturation profiles evolve by what might be referred to as travelling shock wave - a well-known solution of the Buckley-Leverett equation [34]. However, rather than being sharp as predicted by the Buckley-Leverett equation, the effects of capillarity render the saturation front diffuse. Pore-scale flow within the diffuse transition zone, or, also referred to as capillary dispersion zone [104, 173, 176], is observed to exhibit a complex array of events including frequent fragmentation and coalescence of discrete ganglia. We measure the width of the capillary dispersion zone and observe that it increases with microstructural heterogeneity. For capillary fingering, i.e. when viscous forces are negligible, fluid displacement is reminiscent of invasion percolation with frequent occurrence of Haines jumps and associated velocity bursts [6, 17, 81, 129, 135]. Trapping of wetting phase is primarily observed in high-curvature domains that are inaccessible to percolation when capillary forces dominate. Motivated by these observations and complementary to the phase diagram of drainage displacement patterns[122], we propose a tentative phase diagram of hydraulically reservoir-disconnected wetting phase based on the morphological properties of discrete ganglia.

6.2 Methods

Governing balance equations, inherent physical assumptions and numerical computation procedures that are relevant for this chapter have been discussed in sections 2.4 and 3.5. In this section, we first discuss methodological benefits and limitations of the SPH method regarding the pore-scale resolved simulation of two-phase flow of immiscible fluids in porous media. Furthermore, we introduce our simulation setup for numerical experiments of saturation-controlled primary drainage and the macroscopic quantities that are relevent for the formulation of coarse-grained models on the Darcy scale.

6.2.1 Methodological benefits and limitations

Advantages of SPH in the context of two-phase flow in porous media include its mesh-free nature since the reproducing kernel approximation (3.17) does not require collocation points to be distributed on grids or meshes. The latter renders spatial discretization of complex pore spaces less computationally expensive as compared to traditional grid or mesh-based methods. The majority of SPH methods use an updated Lagrangian approach. The latter implies that phase indicator fields $C^{\alpha\beta}$ are advected through particle motion simplifying implementation of the CSS method since no interface-tracking method is required. Moreover, the updated Lagrangian formulation simplifies modeling of locally large Reynolds numbers [186] and the formation and fragmentation of interfaces is intrinsically accounted for. The implemented SPH method is additionally compliant to Galilean invariance and total mass and linear momentum conservation in the absence of volumetric sources (see chapter 3).

Disadvantages of SPH include its high computational costs associated with iterative use of neighbor searching algorithms that scale with $\mathcal{O}(N \log N)$ and, in the context of using explicit time integration schemes, time stepping criteria such as the CFL-condition $(3.67)_1$ being rather restrictive. Total number of time iterations for the primary drainage simulations presented hereafter is in the order of $\mathcal{O}(10^6)$. Hence, feasibility of three-dimensional computational domains necessitates highly optimized software and hardware. Furthermore, the application of essential boundary conditions is non-trivial in SPH methods [25] since SPH interpolants generally do not satisfy the Kronecker delta property as discussed in section 3.2.

Difficulties associated with the application of boundary conditions in SPH have minor impact on modeling the no-slip and no-penetration condition (3.46) provided that the discretization length scale dx is smaller that the viscous boundary layer thickness. In particular, implementation of Eq. (3.46) follows what was in Adami et al. [2] and has proven to accurately reproduce parabolic velocity profiles of Poiseuille flow (see section 4.1). However, since the Kronecker delta property is not satisfied, there exists a spatial uncertainty regarding velocity profiles in the order of dx.

The spatial uncertainty dx may be regarded a numerical slip length and gives rise to the movement of contact lines. Since the slip length does not represent a physical parameter, local dynamics of moving contact lines far from equilibrium must be considered artificial. More sophisticated approaches to apply slip boundary conditions in SPH exist [155], however, the physical slip length associated with moving contact lines remains an issue of ongoing research. Moreover, resolutions to Huh and Scirven's paradox other than slip models have been proposed, e.g. molecularly thin precursor films that serve as lubricants for contact lines (see review Popescu et al. [159] and references therein), but not taken into account herein. However, for flow in porous media, energy dissipation due to moving contact lines is assumed negligible as compared to contributions due to interfacial viscous coupling at solid surfaces and menisci. Furthermore, wetting effects near equilibrium can be accurately reproduced using the present SPH model, as shown in Sivanesapillai et al. [187] and section 4.6 where numerical capillary rise heights were shown to converge to analytical solutions for decreasing dx. As to be indicated in section 6.2.2, we herein restrict ourselves to transport processes at macroscopically small Reynolds numbers.

The present model is only applicable to ideal solid surfaces absent of chemical imperfections, surface roughness or dust particles. In the presence of inhomogeneous solid surfaces on the other hand, a phenomenon referred to as contact line hysteresis has to be taken into account. In particular, as a result of surface inhomogeneities, a contact line may be pinned and resist motion unless a threshold force acting on the contact line is overcome. The apparent contact angle of a pinned contact line may thus differ from Young's contact angle Θ and fall into an interval bounded by static receding and advancing contact angles $\Theta_{\mathrm{r,st}}$ and $\Theta_{\mathrm{a,st}}$, respectively, which constitute material parameters. Once the threshold force is overcome, dynamic receding and advancing contact angles may further differ from respective static values. Typical effective continuum models that account for this behavior are reminiscent of static and kinetic friction models as encountered in mechanics of solid materials (see Kurzeja & Steeb [114, § 4] and references therein). It is emphasized that the given approach, however, does not account for inhomogeneous solid surfaces and assumes the validity of Young's Eq. (2.86), i.e. we restrict ourselves to ideal solid surfaces.

Given the numerical costs associated with pore-scale resolved SPH simulations, we restrict ourselves to two-dimensional (2D) IBVPs. The latter implies that curvature of menisci in the out-of-plane direction is not accounted for. However, as recently shown by Ferrari et al. [70] and Kunz et al. [113], simulation results can be regarded representative of flow in thin Hele-Shaw micro-models if one accounts for viscous momentum exchange between bulk fluids and confining walls as well as a constant contribution to capillary pressure due to out-of-plane curvature. In particular, Kunz et al. [113] performed micro-model experiments and equivalent 2D SPH simulations of primary drainage in small microstructures (about 20 grains) and showed quantitative agreement between both regarding the evolution of phase distribution and capillary pressure. On the other hand, Ferrari et al. [70] performed micro-model experiments as well as equivalent 2D and 3D Finite-Volume simulations using what might be referred to as representative microstructures (about 4000 grains). Ferrari et al. [70] reported quantitative agreement between simulations and experiments regarding macroscopic quantities such as interfacial areas, saturation profiles as well as fractal dimensions of unstable fingers. However, they emphasized that sensitivity of unstable flow to initial conditions, boundary conditions and numerical uncertainties yields discrepancies with respect to fluid distribution. Despite the use of different modeling frameworks, physical assumptions that are incorporated in the above references are equivalent to those of the present contribution. However, the above mentioned depth-related modifications to account for Hele-Shaw confinement are not taken into account herein.

Solid surfaces are assumed smooth such that singularities are absent. The latter assumption is implicit to the definition of interfacial curvatures. Surface singularities constitute domains of singular curvature; the drainage of which requires excessively large capillary pressures. Wetting phase trapping due to singular curvatures, e.g. the formation of pendular rings where solid grains come in contact with each other or the presence of wetting phase trapped in corners of pore channels with polygonal cross sections [117], is not considered hereafter. As a result, contributions to macroscopic capillary pressure as well as specific interfacial areas due to wetting phase entrapped in singular domains is not considered herein.

When a gas bubble invades a capillary tube that is initially saturated with a wetting liquid of non-negligible viscosity, a residual wetting film is formed between gas bubble and channel wall resulting in a flow field commonly referred to as core-annular flow. The latter was studied in Bretherton [32] and constitutes a special case of the Landau-Levich-Derjaguin problem [50, § 5.3]. The thickness of the wetting film is typically approximated in the context of the lubrication theory. However, when the thickness of the wetting film is of order $\mathcal{O}(0.1\mu\mathrm{m})$ [190, § 1.2], mutual interaction of meniscus and solid surface separated by the molecularly thin wetting film gives rise to an additional contribution to pressure inside the film referred to as disjoining pressure. Disjoining pressure has a crucial effect on the

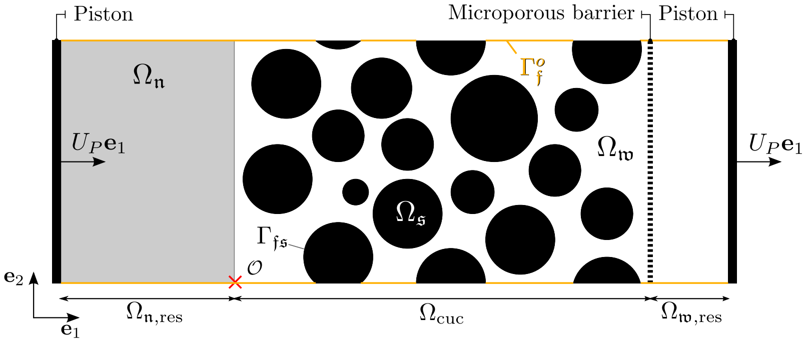
Piston
Microporous barrier
Piston
$\Omega_\mathfrak{n}$
$\Gamma_\mathfrak{f}^o$
$U_P\mathbf{e}_1$
$\Omega_\mathfrak{w}$
$U_P\mathbf{e}_1$
$\Omega_\mathfrak{s}$
$\Gamma_{\mathfrak{f}\mathfrak{s}}$
$\mathcal{O}$
$\mathbf{e}_2$
$\mathbf{e}_1$
$\Omega_{\mathfrak{n},\mathrm{res}}$
Ω_{cuc}
$\Omega_{\mathfrak{w},\mathrm{res}}$

Figure 6.1: Schematic diagram of the simulation setup at initial time $t = 0$. Black, white and gray areas correspond to solid phase $\Omega_\mathfrak{s}$, wetting phase $\Omega_\mathfrak{n}$ and non-wetting phase $\Omega_\mathfrak{w}$, respectively. The outer boundary $\Gamma_\mathfrak{f}$, which is subject to periodic boundary conditions, is highlighted yellow. The point of origin, indicated by the red cross marker, is located in the lower left-hand corner of the microstructure. The position vector $\mathbf{x} := X_1\mathbf{e}_1 + X_2\mathbf{e}_2$.

stability of molecularly thin wetting films. Despite of the fact that we observe the formation of wetting films during viscous fingering, the present model does not take into account the effect of disjoining pressure. We argue that for considered capillary numbers and average pore-throat sizes of order $\mathcal{O}(0.1\mathrm{mm})$, the effect of disjoining pressure is negligible as compared to capillary pressure. Whether or not disjoining pressure effects are negligible for transport in reservoir rocks remains an open question.

While the above discussion of methodological limitations is by no means exhaustive, we believe that it provides an overview of the most crucial restrictions regarding the present direct numerical simulations of immiscible flow in porous media with partial wettability. Indeed, Schmatz et al. [180] recently reported the presence of pinned contact lines as well as molecularly thin wetting films using nanometer-resolved images of mixed-wet reservoir rocks which questions both the assumption of ideal surfaces and negligible disjoining pressure with respect to complex subsurface systems. While the latter limits the applicability of the present model to idealized porous media, we believe that the qualitative significance of the here reported results may motivate further experimental effort.

6.2.2 Simulation Setup

Our simulation setup (Fig. 6.1) for numerical primary drainage experiments resembles what was used earlier in Sivanesapillai et al. [187] and is motivated by laboratory setups as described, for instance, in Moura et al. [143]. The computation domain is comprised of wetting and non-wetting phase reservoirs denoted $\Omega_{\mathfrak{w},\mathrm{res}}$ and $\Omega_{\mathfrak{n},\mathrm{res}}$, respectively, as well as the porous sample domain Ω_{cuc}. The porous sample, also referred to as computational unit cell (CUC), has side lengths $L_W = 20\,\mathrm{mm}$ and $L_H = 15\,\mathrm{mm}$ in direction of the unit vectors $\mathbf{e}_1$ and $\mathbf{e}_2$, respectively. The microstructure exhibits L_H-periodicity in direction of $\mathbf{e}_2$ such that periodic boundary conditions are applied with respect to $\mathbf{e}_2$. The latter avoids boundary effects that otherwise arise due to confinement in direction of $\mathbf{e}_2$. Initially, the sample is completely saturated by the wetting phase. The drainage process is saturation-controlled in that saturation levels inside the porous sample are controlled by imposing the uni-directional advection velocity $\mathbf{U}_P = U_P\,\mathbf{e}_1$ of reservoir pistons by means of which reservoir fluids are displaced into the pore space of the sample. The component of the piston velocity U_P is chosen positive and constant and, as a result, non-wetting phase saturation rates are positive and constant as well.

Three distinct microstructures comprised of disordered packings of polydisperse, non-overlapping hard fibers of circular cross section have been generated using an event-driven particle dynamics algorithm [57, 58]. Pore-throat sizes can be considered normally distributed such that we introduce expectation value, or mean value, m_N and standard deviation v_N of pore-throat size distributions. Our approach to compute pore-throat size and fiber diameter distributions (Table 6.1) of computational unit cells is summarized hereafter. In analogy to what was done in Sivanesapillai et al. [187] and Moura et al. [143], pore-throat size distributions are computed on the basis of a Delaunay triangulation of the center points of the fibers (Fig. 6.2, left column). The pore-throat size between two neighboring fibers is considered equal to the length of the connecting Delaunay edge upon subtracting respective fiber radii. Delaunay edges that intersect the system boundaries are excluded during generation of pore-throat size histograms. Resulting pore-throat size histograms (Fig. 6.2, center column) and fiber diameter histograms (Fig. 6.2, right column) are subsequently fitted to the Gaussian functions $G_N(x) := A_N \exp\left[-(x-m_N)^2/(2v_N^2)\right]$ and $G_F(x) := A_F \exp\left[-(x-m_F)^2/(2v_F^2)\right]$, respectively.

Mean pore-throat size m_N serves as characteristic length scale for the reference capillary pressure

$$P_C^{\mathrm{ref}} := \frac{2\cos\Theta\sigma^{\mathfrak{wn}}}{m_N}.$$

Following Eq. (4.9), P_C^{ref} is the magnitude of the pressure jump across a meniscus that is pinned between two confining walls that a separated by a distance m_N. Fiber diameters are normally distributed as well with corresponding expectation value and standard deviation denoted m_F and v_F, respectively. Averaging the

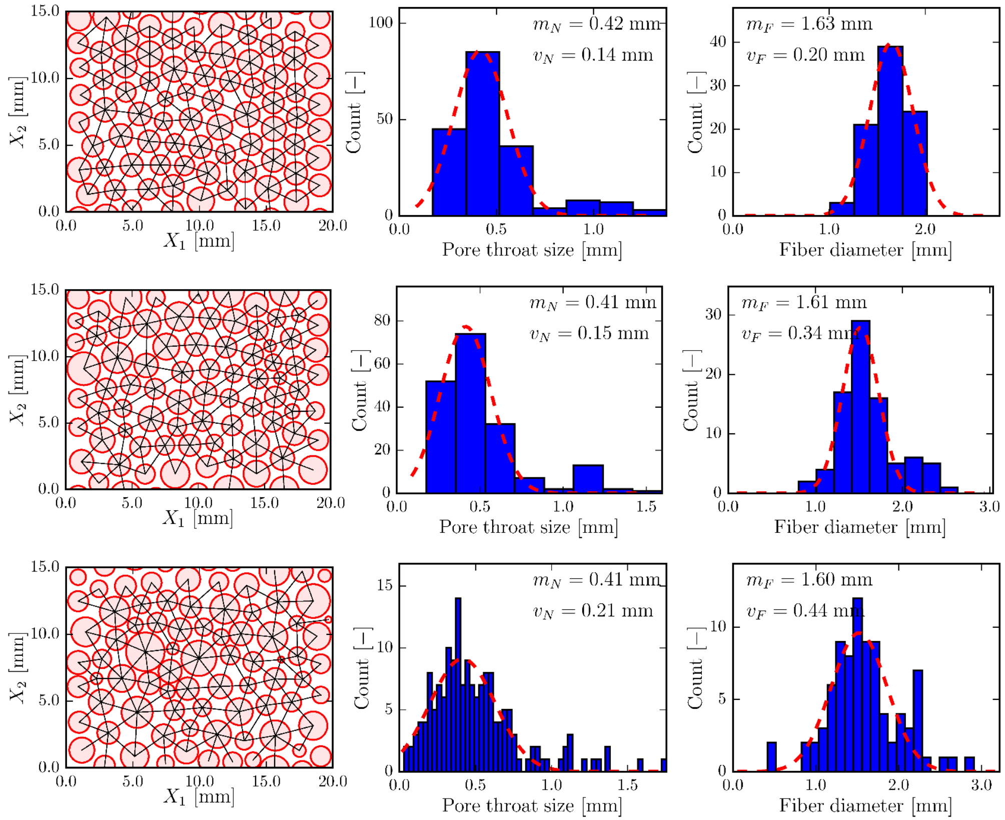

Figure 6.2: Results of statistical analysis of computational unit cells A, B and C (from top to bottom). Black lines in microstructure plots (left column) correspond to Delaunay edges that have been used to generate pore-throat size histograms. Dashed red lines in the pore-throat size (center column) and fiber diameter histograms (right column) correspond to the best fitting Gaussian functions.

Table 6.1: Overview of microstructure parameters. Intrinsic permeabilities k_I were calculated using single-phase flow simulations.

Microstructure	A	B	C
Pore-throat size distribution			
Expectation value m_N [mm]	0.42	0.41	0.41
Standard deviation v_N [mm]	0.14	0.15	0.21
Fiber diameter distribution			
Expectation value m_F [mm]	1.63	1.61	1.60
Standard deviation v_F [mm]	0.20	0.34	0.44
Miscellaneous			
Porosity ϕ_{cuc} [%]	45.5	46.0	44.3
Intrinsic Permeability $k_{I,\text{cuc}}$ $\left[10^{-9}\text{m}^2\right]$	4.41	4.55	4.55
Dimensions $\left[\text{mm}^2\right]$	20×15		
Fiber count	88	85	86

means m_N and m_F among the set of microstructures yields the arithmetic means $\bar{m}_N = 0.413\,\text{mm}$ and $\bar{m}_F = 1.62\,\text{mm}$, respectively. While standard deviations v_N and v_F are chosen different for each microstructure (Table 6.1), expectation values m_N and m_F differ by less than 2.5 % from $\bar{m}_N$ and $\bar{m}_F$, respectively. In other words, microstructures only differ by the degree of heterogeneity defined by the width of pore-throat size and fiber diameter distributions.

The porous sample domain Ω_{cuc}, comprised of approximately 85 fibers, is referred to as computational unit cell given that no extensive study regarding the question whether or not the domain size is representative is performed. However, clipping the sample width L_W by 50 % was observed to yield changes in above expectation values and standard deviations of less than 10 %. In other words, we consider the domain size large enough to study pore-scale effects related to the length scale of microstructure heterogeneity.

The magnitude of piston velocity U_P is chosen such that the mixed capillary number

$$\text{Ca} := \frac{\mu^{\mathfrak{n}} U_P}{\sigma^{\mathfrak{wn}}} \tag{6.1}$$

takes the desired value. We refer to Ca as mixed capillary number since its derivation incorporates a macroscopic characteristic velocity as well as a pore-scale characteristic length scale. Primary drainage processes are studied for the set of mixed capillary numbers $\mathrm{Ca} = \{10^{-2}, 10^{-3}, 10^{-4}, 10^{-5}\}$. The maximum mixed Reynolds number

$$\max(\mathrm{Re}) := \frac{\max\{\varrho_0^{\mathfrak{n}}, \varrho_0^{\mathfrak{w}}\}\, U_P\, m_N}{\min\{\mu^{\mathfrak{n}}, \mu^{\mathfrak{w}}\}},$$

where, in analogy to Ca, the macroscopic characteristic velocity U_P as well as the pore-scale characteristic length scale m_N have been incorporated. For all simulation cases, the maximum mixed Reynolds number is within the range $0.6 < \max(\mathrm{Re}) < 0.8$. The latter is achieved by setting fluid densities $\varrho_0^{\mathfrak{f}} = \varrho_0^{\mathfrak{n}} = \varrho_0^{\mathfrak{w}}$ and choosing initial fluid density $\varrho_0^{\mathfrak{f}}$ such that time step widths are maximized and $\max(\mathrm{Re})$ minimized. In other words, fluid densities were parameterized such that computational resources could be minimized. However, since Re is of order $\mathcal{O}(0.1)$, we conclude that inertial effects are negligible in a macroscopic sense and, with gravity forces being absent, the parameterization of fluid densities is expected to play a minor role with respect to saturation profiles. In spite of the latter, the occurrence of Haines jumps and pressure bursts [17, 135] as well as rapid meniscus reconfigurations [69] render spatially and temporally local inertial effects non-negligible, in particular, regarding the dynamics of capillary fingering. We therefor point out that the implemented SPH model was previously shown in Sivanesapillai et al. [186] and chapter 5 to accurately reproduce effective hydraulic properties for high velocity transport in porous media for Re up to order $\mathcal{O}(10^3)$.

Fluid viscosities are chosen such that the viscosity ratio

$$\mathrm{M} := \frac{\mu^{\mathfrak{n}}}{\mu^{\mathfrak{w}}}$$

takes the desired value. The simulated set of viscosity ratios is $\mathrm{M} = 10^{-1}$, 10^0 and 10^1 by considering the viscosity 2-tuples $\log_{10}(\mu^{\mathfrak{n}}, \mu^{\mathfrak{w}}) = (-4, -3)$, $(-3, -3)$ and $(-3, -4)$ [Pa s], respectively. The fluid-fluid interfacial tension is chosen $\sigma^{\mathfrak{wn}} = 5\,\mathrm{N/mm}$ whereas Young's contact angle $\Theta = 30°$, which is achieved by means of setting the fluid-solid interfacial tensions $\sigma^{\mathfrak{ws}} = 0$ and $\sigma^{\mathfrak{ns}} = \sigma^{\mathfrak{nw}} \cos\Theta$ following Young's equation (2.86). Since the contact angle is fixed for all simulations, effects related to variations in solid surface wettability are not studied herein.

Following typical laboratory setups, a microporous barrier that separates the porous sample and wetting phase reservoir is introduced. The microporous barrier exhibits a regular pattern of narrow pore channels with size $8\,dx < m_N$, such that capillary forces prevent the non-wetting phase to enter the wetting phase reservoir easily. Simulations are halted as soon as the non-wetting phase penetrates the microporous barrier, i.e. at breakthrough. Choice of the numerical resolution dx depends on mean pore-throat size m_N as well as governing dimensionless numbers Ca and M. For Ca $= 10^{-2}$ and M $= 10^{-1}$, the pore-scale flow field resembles a core-annular flow giving rise to thin wetting films which require a fine numerical resolution to ensure numerical accuracy. Hence, for the latter case we choose $dx = \bar{m}_N/19 = 21.7\,\mu\mathrm{m}$ which leads to wetting films being represented by approximately 4 particles in direction of film thickness. For all remaining cases, we choose $dx = \bar{m}_N/14 = 29.5\,\mu\mathrm{m}$. It was previously shown in Sivanesapillai et al. [187] and chapter 4 that the incorporated choices of dx can reproduce local pressure, menisci and velocity profiles with reasonable accuracy. The total number of SPH particles is approximately $6 \cdot 10^5$. Average computation time for a single time step was $0.6\,s$ using a moderately optimized code running 6 threads in parallel on an Intel® Xeon® CPU E5-1650. The total number of time steps varied between $1.1 \cdot 10^6$ for small and $1.6 \cdot 10^5$ for large capillary numbers.

6.2.3 Macroscopic Quantities

Using the shorthand notations $\Omega_\alpha^{\mathrm{cuc}} := \Omega_\alpha \cap \Omega_{\mathrm{cuc}}$ and $\Gamma_{\alpha\beta}^{\mathrm{cuc}} := \Gamma_{\alpha\beta} \cap \Omega_{\mathrm{cuc}}$, we introduce

$$V := \int\limits_{\Omega_{\mathrm{cuc}}} \mathrm{d}v, \quad V_\alpha := \int\limits_{\Omega_\alpha^{\mathrm{cuc}}} \mathrm{d}v \quad \text{and} \quad A_{\alpha\beta} := \int\limits_{\Gamma_{\alpha\beta}^{\mathrm{cuc}}} \mathrm{d}a = \int\limits_{\Omega_{\mathrm{cuc}}} \delta^{\alpha\beta} \mathrm{d}v,$$

which denote total volume, total phase volume and total interfacial area contained within the porous sample domain Ω_{cuc}, respectively. Since the majority of macroscopic quantities is defined with respect to the domain of the porous sample, the subscript $(\bullet)_{\mathrm{cuc}}$ is dropped for the sake of simplifying notation whenever unambiguously possible. In the context of numerical computations, surface integrals are evaluated by taking into account Eq. (2.61) and Eq. (4.7), i.e. total interfacial area $A_{\alpha\beta}$ is equal to the volume integral of $\delta^{\alpha\beta}$. Total fluid volume within Ω_{cuc} is denoted $V_\mathfrak{f} := V_\mathfrak{w} + V_\mathfrak{n}$, such that sample porosity $\phi := V_\mathfrak{f}/V$. Sample wetting phase saturation, non-wetting phase saturation and specific interfacial areas are thus defined

$$S_\mathfrak{w} := \frac{V_\mathfrak{w}}{V_\mathfrak{f}}, \quad S_\mathfrak{n} := \frac{V_\mathfrak{n}}{V_\mathfrak{f}}, \quad a_{\mathfrak{wn}} := \frac{A_{\mathfrak{wn}}}{V}, \quad a_{\mathfrak{ns}} := \frac{A_{\mathfrak{ns}}}{V}$$

respectively. Saturation profiles $S_{\mathfrak{w},\Delta X_1}$ in direction of $\mathbf{e}_1$ are generated by means of computing wetting phase saturations in vertical slices of the sample domain. The width of a vertical slice is denoted ΔX_1. Similarly, mean pressure profiles $\bar{p}_{\Delta X_1}$ in direction of $\mathbf{e}_1$ are generated by computing arithmetic means of fluid pressures in vertical slices of the sample domain. Residual wetting phase saturation $S_\mathfrak{w}^B$ is computed at breakthrough, i.e. when the non-wetting phase penetrates the microporous barrier.

In analogy to microscopic capillary pressure p_C, sample domain averaged macroscopic capillary pressure is traditionally defined

$$P_C^{\mathrm{cuc}} := \frac{1}{V_{\mathfrak{n}}} \int\limits_{\Omega_{\mathfrak{n}}^{\mathrm{cuc}}} p^{\mathfrak{n}} \mathrm{d}v - \frac{1}{V_{\mathfrak{w}}} \int\limits_{\Omega_{\mathfrak{w}}^{\mathrm{cuc}}} p^{\mathfrak{w}} \mathrm{d}v. \tag{6.2}$$

However, the definition of macroscopic capillary pressure remains ambiguous. In particular, typical laboratory setups define macroscopic capillary pressure as the difference between inlet and outlet reservoir pressures. In the context of our simulation setup, the latter is defined

$$P_C^{\mathrm{res}} := \frac{1}{V_{\mathfrak{n},\mathrm{res}}} \int\limits_{\Omega_{\mathfrak{n},\mathrm{res}}} p^{\mathfrak{n}} \mathrm{d}v - \frac{1}{V_{\mathfrak{w},\mathrm{res}}} \int\limits_{\Omega_{\mathfrak{w},\mathrm{res}}} p^{\mathfrak{w}} \mathrm{d}v, \tag{6.3}$$

where $V_{\alpha,\mathrm{res}} := \int_{\Omega_{\alpha,\mathrm{res}}} \mathrm{d}v$ denotes total reservoir volumes. Rather than Eq. (6.3), a more appropriate representation of laboratory measurements would be to consider the difference in mean pressures as averaged over the exposed contact area of pressure sensors.

It is intuitively understood that above measures of macroscopic capillary pressure are equivalent to each other if and only if $\Omega_{\mathfrak{n}}^{\mathrm{cuc}} \cup \Omega_{\mathfrak{n},\mathrm{res}}$ and $\Omega_{\mathfrak{w}}^{\mathrm{cuc}} \cup \Omega_{\mathfrak{w},\mathrm{res}}$ represent path-connected spaces and, additionally, if pressure fields within each of the above domains are uniform as to make volume averages independent of the averaging domain. The requirement of path-connection is clearly unmet in the presence of hydraulically reservoir-disconnected trapped phases. As pointed out by Hassanizadeh & Gray [88], P_C^{res} is hence expected to lose significance with respect to the definition of P_C^{cuc} near residual saturations where path-connection becomes increasingly questionable. The latter was indicated in pore-scale resolved numerical simulations of Sivanesapillai et al. [187]. On the other hand, the requirement of pressure uniformity is unmet in the presence of non-equilibrium conditions, i.e. due to inertial or viscous momentum exchange, as well as gravity, i.e. due to a hydrostatic pressure field, in which case pressure fields are rendered non-uniform. The latter was studied theoretically in Nordbotten et al. [149] and observed in pore-scale resolved numerical simulations of Ferrari & Lunati [68].

Following Sivanesapillai et al. [186] and Eq. (5.4), we compute the total viscous drag force, i.e. skin friction, acting between pore fluids and solid phase by summing viscous particle interaction forces that act between the set of particles that represent solid surface, i.e. fictitious ghost particles, and fluid phase such that

$$\mathbf{F}_{\mathfrak{f}\mathfrak{s}}^{V} := \sum_{i:\mathbf{x}_i \in \Omega_{\mathfrak{s}}^{\mathrm{cuc}}} \sum_{j:\mathbf{x}_j \in \Omega_{\mathfrak{f}}^{\mathrm{cuc}}} \mathbf{F}_{ij}^{V}.$$

Furthermore, we compute the total viscous interaction force acting between non-wetting and wetting phase as

$$\mathbf{F}^V_{\mathfrak{wn}} := \sum_{i:\mathbf{x}_i \in \Omega^{\mathrm{cuc}}_{\mathfrak{w}}} \; \sum_{j:\mathbf{x}_j \in \Omega^{\mathrm{cuc}}_{\mathfrak{n}}} \mathbf{F}^V_{ij}.$$

Interfacial viscous coupling implies $\mathbf{F}^V_{\mathfrak{wn}} = -\mathbf{F}^V_{\mathfrak{nw}}$. It is well anticipated that the viscous drag force $\mathbf{F}^V_{\mathfrak{fs}}$ gives rise to the Darcian term in coarse-grained models of fluid flow in porous media. On the other hand, the effect of fluid-fluid viscous coupling, i.e. the Yuster effect [7, 211], which we measure in terms of $\mathbf{F}^V_{\mathfrak{wn}}$, is typically not accounted for in classical coarse-grained models of two phase flow.

6.3 Results

The overarching goal of the present contribution is to report pronounced disparities in the mechanisms of wetting phase entrapment during primary drainage as observed for different flow regimes (Fig. 6.3), i.e. capillary fingering, viscous fingering and stable displacement [122]. In an attempt to elucidate the underlying interface dynamics, in this section, we phenomenologically study pore-scale resolved flow fields that we find representative of the observed entrapment mechanisms. The relevance of accounting for the latter differences in coarse-grained, percolation-based and pore-network-based models of two-phase flow is indicated by quantifying their impact on macroscopic quantities as introduced in section 6.2.3.

6.3.1 Capillary Fingering Regime: On the Role of Microstructural Simplicity

At sufficiently small capillary numbers, the pressure drop across the porous sample due to viscous drag becomes negligible as compared to the magnitude of pressure jump across menisci. As a result, pressure fields within path-connected subsets of $\Omega_{\mathfrak{w}}$ and $\Omega_{\mathfrak{n}}$ are homogeneous and, recalling Eq. (2.77), menisci are of constant mean curvature. The evolution of fluid phase distribution during primary drainage at small capillary numbers is greatly sensitive to microstructure in that the non-wetting phase will percolate the pore-space through preferential flow paths. Preferential flow paths exhibit the lowest capillary resistance to drainage. Since threshold capillary pressures ($\sim \sigma^{\mathfrak{wn}}/m_N$) scale with the inverse of pore-throat sizes, heterogeneous microstructures yield ramified fluid-fluid interfaces [122]. An individual branch of a ramification pattern, hereafter referred to as capillary finger, may exhibit loops that enclose undrained high-curvature domains. A capillary finger loop implies trapping of the enclosed wetting phase,

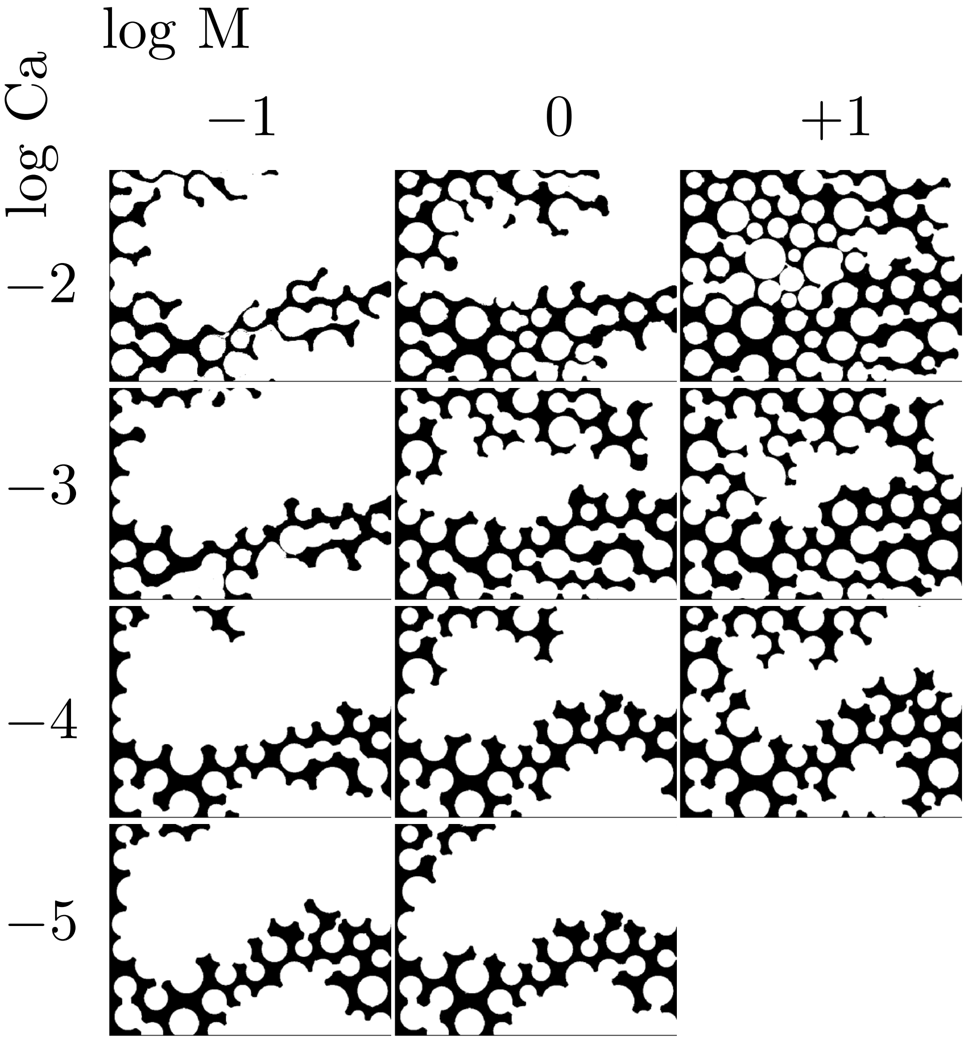

Figure 6.3: Non-wetting phase distribution at breakthrough for microstructure C. Domain $\Omega_{\mathfrak{n}}$ is colored black whereas both $\Omega_{\mathfrak{s}}$ and $\Omega_{\mathfrak{w}}$ are colored white.

i.e. hydraulic disconnection from the wetting phase reservoir $\Omega_{\mathfrak{w},\mathrm{res}}$. The latter mechanism is referred to as capillary trapping. In accordance to laboratory experiments of Zhang et al. [214], capillary fingering was observed for $\mathrm{Ca} \leq 10^{-4}$ within the range of simulated viscosity ratios (Fig. 6.3).

While the pore-scale capillary statics associated with low capillary number drainage is deemed understood, i.e. Eqs. (2.77) and (2.86), the formulation of computationally efficient models applicable to reservoir-scale problems remains a challenge. On the one hand, the latter is due to the fact that the algebraic relation between P_C^{cuc} and $S_{\mathfrak{w}}$, which serves as constitutive input to traditional coarse-grained models [14], is generally nonlinear and hysteretic [75, 144]. Indeed, the $P_C^{\mathrm{cuc}} = P_C^{\mathrm{cuc}}(S_{\mathfrak{w}})$ relation can depend on a broad array of factors, such as contact angle hysteresis [94], heterogeneous wetting properties [43], solid matrix deformation, and temperature dependency [82]. On the other hand, further modeling challenges arise due to changes in fluid phase distribution being predominantly discrete in time rather than gradual. In particular, discrete pore-filling events, commonly referred to as Haines jumps [81], are spontaneous processes since they imply a release of free energy as a meniscus transitions from a narrow pore-throat to a comparatively wide pore-body. Haines jumps have been identified as dominant displacement mechanism at small Ca [17], to give rise to locally non-negligible inertial effects despite small mixed Reynolds numbers [69, 135], to give rise to measurable acoustic signals [54] and to be associated with an intrinsic time scale independent of macroscopic flow rates [6, 135].

Though not focus of the present study, the above phenomena are reproduced in our fully resolved simulations and affect their interpretation. In particular, we frequently observe the occurrence of cooperative pore-filling events (Fig. 6.4) during low capillary number drainage in accordance to what was reported in Armstrong & Berg [6] and Berg et al. [17]. The attribute of a Haines jump as being a cooperative event applies if the geometrically necessary mass flux for the drainage of a pore exceeds the external mass flux from $\Omega_{\mathfrak{n},\mathrm{res}}$ to $\Omega_{\mathfrak{n}}^{\mathrm{cuc}}$. The required mass flux is subsequently collectively supplied from partially saturated pore-throats that may be as distant from the event location as multiple pore-body sizes.

A pore-filling event is accompanied by a sudden decrease in macroscopic capillary pressure as the energetically favorable pore-body is drained and subsequent increase of the latter as the capillary finger proceeds to drain an adjacent pore-throat. In accordance to Måløy et al. [129], the latter gives rise to high-frequency content in the $P_C(S_{\mathfrak{w}})$ signal (Fig. 6.5). While both the sample-averaged P_C^{cuc} and the reservoir-averaged P_C^{res} exhibit qualitatively equivalent behavior, quantitative differences are attributed to transient effects during Haines jumps and, most notably, the presence of trapped wetting phase that does not contribute to P_C^{res}. The latter is manifested by the fact that the difference $P_C^{\mathrm{cuc}} - P_C^{\mathrm{res}}$ is ob-

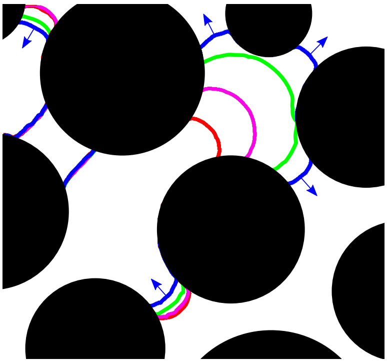

Figure 6.4: Evolution of $\Gamma_{\mathfrak{wn}}$ during a Haines jump as observed in a subdomain of microstructure B having size 4.5 mm × 4.5 mm for $\mathrm{Ca} = 10^{-5}$ and $\mathrm{M} = 10^{-1}$. Arrows indicate direction of interfacial velocity. Menisci are initially located in pore-throats (Red contours) whereas an additional pore-body is observed to be drained post-event (Blue contours). Retraction of menisci from adjacent pore-throats suggests cooperative pore-filling. Despite it is not connected to the advancing finger, a pore-throat meniscus located near the upper edge of the plot retracts as well. Meanwhile, the trapped wetting cluster observed in the upper left-hand corner remains static. Time increment between superimposed contour plots amounts to 0.45 s. Plot was generated by linearly interpolating unstructured SPH particle data of phase indicator field $C^{\mathfrak{wn}}$ to points of a regular grid using `matplotlib.mlab.griddata` and subsequently plotting contour lines $C^{\mathfrak{wn}} = 0.5$.

served to increase as breakthrough is approached. Nonetheless, these differences are observed negligible for practical purposes which supports the assumption that macroscopic capillary pressure at low capillary number is mainly due to the difference in uniform pressure levels present throughout reservoir-connected regions.

We subdivide $P_C(S_{\mathfrak{w}})$ curves into a pre-entry and post-entry regime (Fig. 6.5). Initially, $\Gamma_{\mathfrak{wn}}$ is a flat surface and $a_{\mathfrak{wn}}(t_0) = 50\,\mathrm{m}^{-1}$ is equal to the height of the sample (15 mm) divided by sample area (200 mm^2). During the pre-entry regime, the meniscus comes in contact with the solid phase and enters the pore-space through the largest pore-throat. The latter is evidenced by the fact that $a_{\mathfrak{wn}}$ decreases by the amount of wetted solid surface area whereas P_C increases by the amount of the required entry capillary pressure. In accordance to Moura et al. [143], we interpret the pre-entry regime as a boundary effect that is sensitive to initial conditions. During the post-entry regime on the other hand, percolation of all analyzed microstructures is observed to occur at a constant mean value of macroscopic capillary pressure when high-frequency fluctuations are filtered. The normalized capillary pressure plateau is located at a level $P_C/P_C^{\mathrm{ref}} \approx 0.3$ which implies that capillary fingers percolate through a preferential network with characteristic length scales nearly three times the mean pore-throat size m_N. Furthermore, $a_{\mathfrak{wn}}$ is observed to scale linearly with $S_{\mathfrak{w}}$ throughout the post-entry regime which is consistent with earlier experimental and numerical investigations

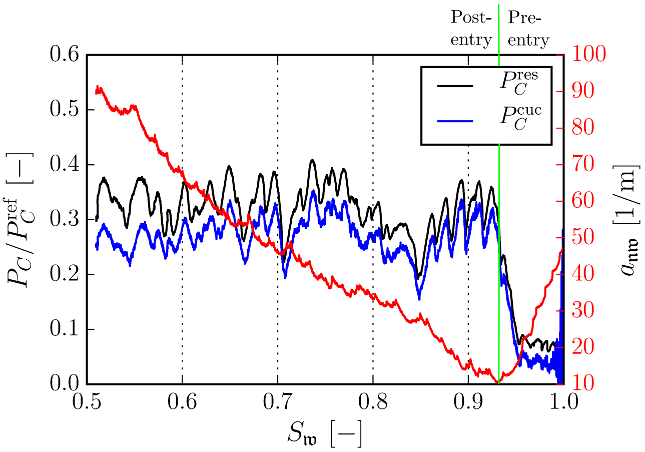

Figure 6.5: Normalized $P_C(S_{\mathfrak{w}})$ and $a_{\mathfrak{w}\mathfrak{n}}(S_{\mathfrak{w}})$ for primary drainage in microstructure C at $\mathrm{Ca} = 10^{-5}$ and $\mathrm{M} = 10^{0}$. Capillary pressures are normalized using the reference capillary pressure P_C^{ref}.

[42, 124, 179, 213, 214]. The boundary effect whereby P_C increases near residual saturation, referred to as clogging regime in Moura et al. [143], is not observed as the penetration of the microporous barrier occurred prior to its clogging.

Percolation at constant P_C and constant $\mathrm{d}a_{\mathfrak{w}\mathfrak{n}}/\mathrm{d}S_{\mathfrak{w}}$ motivates our notion of microstructural simplicity with respect to drainage as defined hereafter. In particular, contrary to Moura et al. [143] who hypothesize general validity of percolation at statistically constant P_C for sufficiently large sample domains, we consider the latter to result from the property of simulated microstructures of being poorly graded. Considering low capillary number drainage in closed systems as isothermal process at constant chemical potentials, the differential expression for the Helmholtz free energy reads

$$dF := \sum_{\alpha\beta} \sigma^{\alpha\beta} \mathrm{d}A_{\alpha\beta} - \sum_{\alpha} p_\alpha \mathrm{d}V_\alpha. \tag{6.4}$$

Taking into account solid phase rigidity, i.e. $\mathrm{d}V_{\mathfrak{n}} = -\mathrm{d}V_{\mathfrak{w}}$ and $\mathrm{d}A_{\mathfrak{n}\mathfrak{s}} = -\mathrm{d}A_{\mathfrak{w}\mathfrak{s}}$, as well as Young's equation (2.86), Eq. (6.4) is reformulated to read

$$p_{\mathrm{eq}}^{\mathfrak{n}} - p_{\mathrm{eq}}^{\mathfrak{w}} = \sigma^{\mathfrak{w}\mathfrak{n}} \left(\frac{\mathrm{d}A_{\mathfrak{n}\mathfrak{w}}}{\mathrm{d}V_{\mathfrak{n}}} + \cos\Theta \frac{\mathrm{d}A_{\mathfrak{n}\mathfrak{s}}}{\mathrm{d}V_{\mathfrak{n}}} \right) \tag{6.5}$$

at equilibrium ($\mathrm{d}F = 0$). If phase pressures are uniform and trapped phases absent, equilibrium macroscopic capillary pressure is expected equal to equilib-

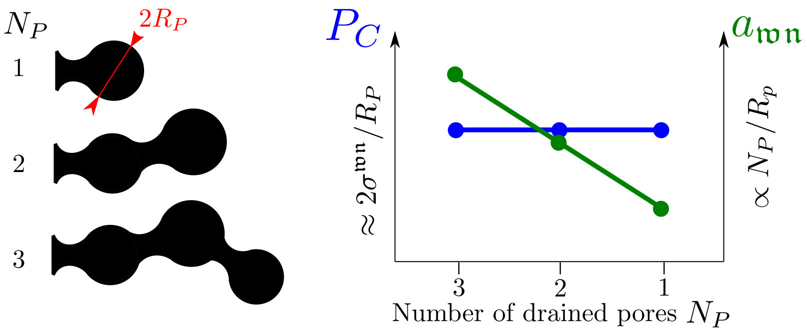
N_P
$2R_P$
1
2
3
P_C
$a_{\mathfrak{wn}}$
$\approx 2\sigma^{\mathfrak{wn}}/R_P$
$\propto N_P/R_p$
3
2
1
Number of drained pores N_P

Figure 6.6: The shape of capillary fingers in the present, poorly graded microstructures resembles a chain of nearly-monodisperse spheres of mean radius R_P that are hydraulically connected to each other. In a reasonable approximation, specific area $a_{\mathfrak{wn}}$ is proportional to the surface-area-to-volume ratio of spheres (3D) or circles (2D) multiplied by the number of drained pores $N_P \propto S_{\mathfrak{w}}$. As a result, $a_{\mathfrak{wn}}$ increases linearly with non-wetting phase saturation. Since $R_P \approx$ const. due to microstructural simplicity, $P_C \approx$ const..

rium microscopic capillary pressure, i.e. $P_C^{\text{eq}} = p_C^{\text{eq}} = p^{\mathfrak{n}}_{\text{eq}} - p^{\mathfrak{w}}_{\text{eq}}$. As interfacial material parameters remain constant, percolation at constant P_C hence implies that the bracket term on the RHS of Eq. (6.5) is constant or, as a special case, both $\mathrm{d}A_{\mathfrak{nw}}/\mathrm{d}V_{\mathfrak{n}}$ and $\mathrm{d}A_{\mathfrak{ns}}/\mathrm{d}V_{\mathfrak{n}}$ are constant. Both conditions are related to intrinsic morphological properties of preferential flow paths and, while the former condition is considered rather restrictive, we may deduce two situations for which the latter applies: During the drainage of a bundle of capillary tubes, $A_{\mathfrak{nw}}$ as well as $\mathrm{d}A_{\mathfrak{ns}}/\mathrm{d}V_{\mathfrak{n}}$ are constant, since, on the one hand, total cross sectional area ($\sim A_{\mathfrak{nw}}$) of tubes remain constant, and, on the other hand, the wetted portion of lateral surface area of tubes ($\sim A_{\mathfrak{ns}}$) scales linearly with $V_{\mathfrak{n}}$. The second situation, which applies to our simulations, is when the shape of capillary fingers resembles that of connected, nearly-monodisperse spheres (Fig. 6.6).

While microstructural simplicity enables intuitive interpretation of $P_C(S_{\mathfrak{w}})$ and $a_{\mathfrak{wn}}(S_{\mathfrak{w}})$ curves, the evolution of saturation profiles during capillary fingering is less accessible to interpretation. The latter is asserted to the great sensitivity of invasion percolation to local features of the microstructure. However, saturation profiles do offer evidence that capillary fingers may propagate in a direction opposite to macroscopic mass flux (Fig. 6.7) as previously observed in experiments [112, 214]. The latter is attributed to the fact that not only the intrinsic velocity magnitude of a Haines jump is independent of macroscopic mass flux [6, 135], but also the direction in which a meniscus proceeds during an event is independent of the direction of macroscopic mass flux.

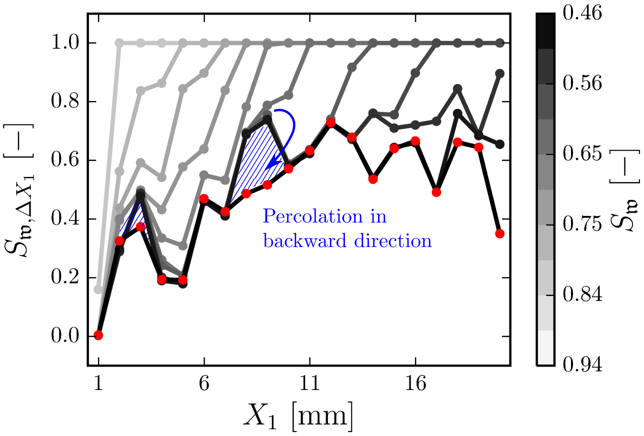

Figure 6.7: Evolution of saturation profiles in direction of $\mathbf{e}_1$ for microstructure A at Ca = 10^{-5} and M = 10^0. Width of vertical slices $\Delta X_1 = L_W/20$. Red markers indicate residual saturation profile at breakthrough.

6.3.2 Viscous Fingering Regime: On the Role of Wetting Film Formation

Viscous fingering occurs when a less viscous fluid displaces a more viscous fluid (M $<$ 1) at sufficiently large capillary numbers. While invasion percolation is considered a suitable stochastic model for capillary fingering, viscous fingering is stochastically reminiscent of diffusion-limited aggregation (DLA) [121, 131, 156]. In contrast to DLA models where fractal growth of particle aggregates is due to Brownian particle motion [209], viscous fingers evolve in the presence of flow-field perturbations. Any perturbation of fluid velocity normal to the meniscus will open a flow path of reduced viscous resistance for the less viscous fluid resulting in the promotion of unstable finger growth, i.e. the Saffman-Taylor instability [177]. Sensitivity of unstable flow to local perturbations challenges the accuracy of numerical predictions [70]. However, statistical predictability of displacement patterns is assumed possible if simulation domains are of representative size. For instance, Ferrari et al. [70] recently reproduced fractal dimensions of viscous fingers using direct numerical simulations. However, due to the limited size of the present sample domain it is inferred that statistical characterization of displacement patterns on the length scale of pore-networks is not insightful herein. Instead, we study the impact of wetting films on macroscopic quantities and entrapment mechanisms. As to be quantified in section 6.4, we consider the formation of wetting films a major trapping mechanism during viscous fingering.

The creeping motion of a long gas bubble through a narrow flow channel that is initially saturated with a viscous liquid, i.e. Bretherton's problem [32], implies a core-annular flow and, as a result, the formation of a liquid film. Lubrication theory [50, § 5.3], in particular the balance between film depth-integrated viscous force and meniscus-integrated interfacial force, predicts the thickness of liquid films $\sim m_N \mathrm{Ca}_{\mathrm{m}}^{2/3}$, where the microscopic capillary number Ca_{m} incorporates a characteristic microscopic velocity rather than U_P in Eq. (6.1). Liquid films that arise due to core-annular flow must be differentiated from molecularly thin precursor films that emerge in the presence of contact lines and, in contrast to the former, depend on solid surface wettability properties [159]. Despite of the fact that lubrication theory has provided accurate predictions for liquid film thickness in curved and narrow flow channels [145], the complexity of pore-networks is expected to necessitate either laboratory experiments or direct numerical simulations to study core-annular flow in porous media. Experiments indeed confirm the presence of thin wetting films following primary drainage of densely packed glass beads at $\mathrm{M} \approx 0.2$ [112].

If sufficient numerical resolution is provided, i.e. the discretization length scale must be significantly smaller that the expected wetting film thickness, the present direct numerical simulations reveal the underlying core-annular flow field. Menisci are of spherical shape near finger tip regions whereas menisci curvatures of wetting films are determined by the morphology of the wetted solid surface (Fig. 6.8). While curvature matching between the latter limiting cases, a prerequisite for the applicability of lubrication theory, is considered possible for as long the finger tip is located within a pore-throat (Fig. 6.8, t_0), transition from spherical tip to wetting film is observed less obvious when the finger proceeds to percolate through a pore-body (Fig. 6.8, $t_0 + 0.6\,\mathrm{ms}$). Hence, even at the pore-scale, viscosity affects meniscus shapes and we conclude that the assumptions of mean curvature flow do not generally apply for viscous fingering. For viscosity-dominated, dynamic flow conditions, the latter casts doubt on the use of pore-network models which require menisci shapes as model input. In two-dimensional microstructures, the formation of a viscous finger loop implies entrapment of wetting films. While the latter is not expected to hold always true for three-dimensional microstructures where flow through hydraulically reservoir-connected wetting films might constitute a relevant transport mechanism [169], the conclusions drawn below are expected to apply independent of spatial dimensionality.

Following Nordbotten et al. [150], we consider our choice of material parameters for $\mathrm{Ca} = 10^{-2}$ and $\mathrm{M} = 10^{-1}$ a rough representation of a carbon dioxide (CO_2)-water system in deep sedimentary formations which implies that core-annular flow might constitute a relevant transport mechanism during supercritical CO_2 sequestration. In particular, the modeled non-wetting phase has small but non-negligible viscosity ($\mu^{\mathrm{n}} = 0.1\,\mathrm{mPa\,s}$). For non-negligible viscous extra

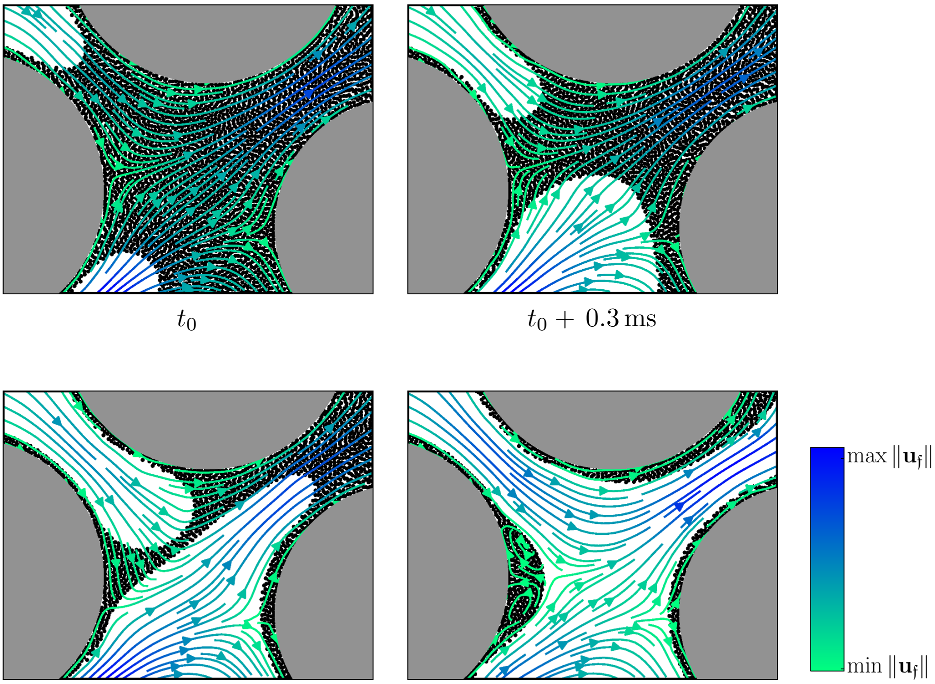

t_0 $t_0 + 0.3\,\mathrm{ms}$

$t_0 + 0.6\,\mathrm{ms}$ $t_0 + 0.9\,\mathrm{ms}$

Figure 6.8: Wetting film entrapment as observed in a subdomain of microstructure A having size 2.4 mm × 1.9 mm for $\mathrm{Ca} = 10^{-2}$ and $\mathrm{M} = 10^{-1}$. Solid phase domain is colored gray whereas wetting phase SPH particles are represented by black markers. Non-wetting phase SPH particles are omitted for improved visibility. Streamlines are colored according to the magnitude of local fluid velocity. Streamlines were generated by linearly interpolating unstructured SPH particle data of fluid velocity to points of a regular grid and subsequently using `matplotlib.pyplot.streamplot` [59].

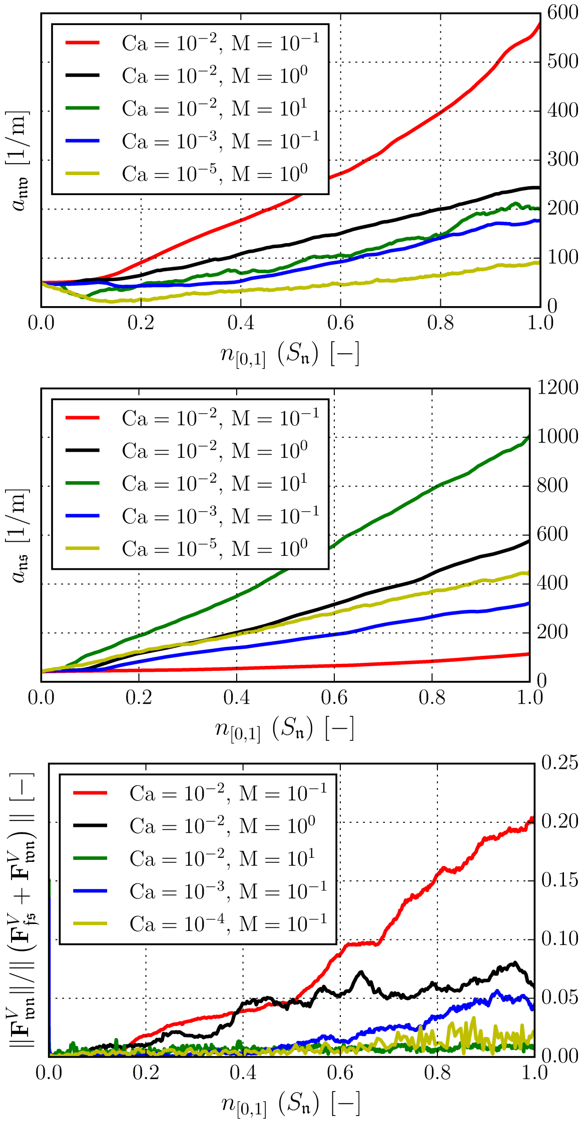

Figure 6.9: Evolution of specific interfacial areas $a_{\mathfrak{wn}}$ (top) and $a_{\mathfrak{ns}}$ (middle) as well as ratio of total viscous interaction force to total resistance force (bottom) for microstructure C. The normalization operator $n_{[0,1]}(f) := (f - \min(f))/(\max(f) - \min(f))$.

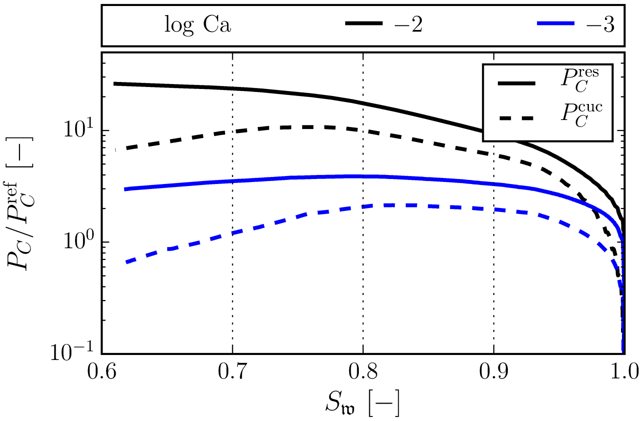

Figure 6.10: Normalized $P_C^{\mathrm{cuc}}(S_{\mathfrak{w}})$ (dashed lines) and $P_C^{\mathrm{res}}(S_{\mathfrak{w}})$ (solid lines) for primary drainage in microstructure C at $\mathrm{M} = 10^{-1}$ and various capillary numbers Ca (color coded).

stresses, the following results furthermore indicate that the effects of interfacial viscous coupling are ubiquitous. Since interfacial viscous coupling induces fluid flow within the wetting film region, the dynamic profile of a trapped wetting film is observed non-uniform, i.e. the film is not of constant thickness. Instead, the interface of an entrapped wetting film exhibits a ridge in the wake region of the wetted solid fiber where recirculating fluid flow takes place (Fig. 6.8, $t_0 + 0.9\,\mathrm{ms}$). Not only does the presence of wetting films imply a decrease in the effective channel width accessible for advective fluid transport, but also a change in apparent boundary conditions for the percolating fluid phase. In particular, before drainage the kinematic no-slip boundary condition (3.46) applies with respect to the percolating wetting phase whereas after drainage the dynamic interfacial viscous coupling condition applies with respect to the percolating non-wetting phase. Despite of the fact that streamline patterns before (Fig. 6.8, t_0) and after drainage (Fig. 6.8, $t_0 + 0.9\,\mathrm{ms}$) are rather comparable to each other due to laminar flow, the dynamic boundary condition is expected to affect energy dissipation as evidenced by the presence of recirculating flow within wetting film ridges.

It is intuitively understood that wetting film formation has considerable effect on the evolution of specific interfacial areas. For $\mathrm{Ca} = 10^{-2}$ and $\mathrm{M} = 10^{-1}$, $a_{\mathfrak{wn}}$ is observed to increase non-linearly with $S_{\mathfrak{n}}$ and its magnitude at breakthrough is found nearly six times the corresponding value for capillary fingering (Fig. 6.9, top). The latter difference is expected to be even more pronounced for domain sizes large enough such that fractal branching can be statistically reproduced.

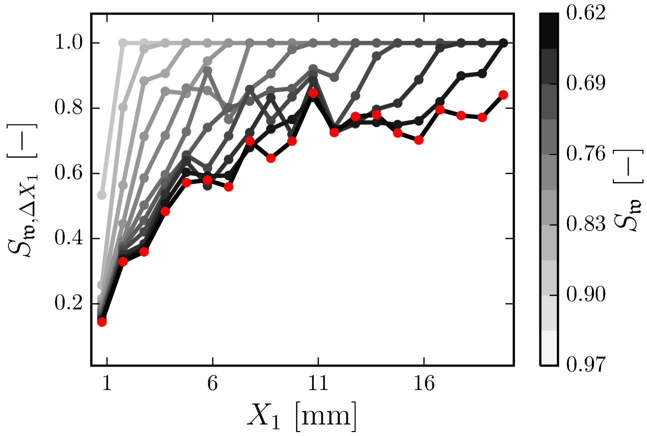

Figure 6.11: Evolution of saturation profiles in direction of $\mathbf{e}_1$ for microstructure C at Ca $= 10^{-2}$ and M $= 10^{-1}$. Width of vertical slices $\Delta X_1 = L_W/20$. Red markers indicate residual saturation profile at breakthrough.

On the other hand, as solid surfaces are coated with wetting films, the specific interfacial area $a_{\mathfrak{ns}}$ formed between non-wetting phase and solid phase is observed negligible for viscous fingering as compared to other displacement mechanisms (Fig. 6.9, middle). For creeping flow at sufficiently large capillary numbers we expect the total resistance force against drainage to be additively comprised of total solid-fluid viscous drag force $\mathbf{F}^V_{\mathfrak{fs}}$, i.e. Darcian drag, and interface-integrated viscous coupling force between wetting and non-wetting fluid phase $\mathbf{F}^V_{\mathfrak{wn}}$. A major implication of wetting film formation with respect to coarse-grained or pore-network modeling is that $\mathbf{F}^V_{\mathfrak{wn}}$ contributes considerably to the total resistance force (Fig. 6.9, bottom). As $a_{\mathfrak{wn}}$ increases non-linearly, the contribution of fluid-fluid viscous coupling to total resistance is observed to increase in a qualitatively similar manner. At breakthrough, nearly one fifth of total resistance is due to viscous coupling. On the other hand, viscous coupling is indeed observed negligible for Ca $\leq 10^{-4}$ as well as for M $> 10^0$. These results cast doubt on the calibration of relative permeability functions, which, by definition, are related to momentum exchange between solid and fluid phases only.

In contrast to low capillary number displacement, considerable differences between sample-averaged P_C^{cuc} and reservoir-averaged P_C^{res} exist during viscous fingering (Fig. 6.10). The latter is attributed to viscous pressure drops across porous sample and microporous barrier as well as the presence of trapped wetting phase. Besides pronounced quantitative differences, P_C^{cuc} and P_C^{res} exhibit qualitative differences as well. In agreement with Ferrari & Lunati [68], the increasing amount of trapped wetting phase as breakthrough is approached leads to significant decrease of P_C^{cuc} which does not apply for P_C^{res}. Disregarding fluctuations that are likely artifacts related to small widths ΔX_1 of the averaging slices, saturation profiles are observed smooth and monotonically increasing functions of X_1 (Fig. 6.11). In particular, saturation overshoots as observed in the context of unstable, gravity-driven fingering during unsaturated flow [53] are absent.

6.3.3 Stable Displacement Regime: On the Role of the Capillary Dispersion Zone

In contrast to viscous fingering, viscosity stabilizes interfacial perturbations when a more viscous fluid displaces a less viscous fluid (M > 1) at sufficiently large capillary numbers. The latter gives rise to compact patterns of non-wetting phase distribution, stochastically referred to as anti-DLA patterns [121, 156], and interfaces that macroscopically appear as being flat. Residual wetting phase saturations at breakthrough $S_{\mathfrak{w}}^B$ are significantly lower for compact patterns as compared to fractal or ramification patterns. Stable displacement is hence desirable during enhanced oil recovery (EOS) due to optimal sweeping efficiency. In our simulations, compact patterns are observed for M > 1 and Ca $> 10^{-3}$ (Fig. 6.3). Compared to other displacement mechanisms, it is intuitively understood that compact patterns give rise to large amount of specific interfacial area $a_{\mathfrak{ns}}$ formed between non-wetting phase and solid phase (Fig. 6.9, middle). While large mixed capillary numbers Ca imply that capillarity effects are macroscopically negligible, the latter does not apply at smaller length scales. On the contrary, capillarity greatly affects pore-scale interfacial dynamics within the capillary dispersion zone [104, 173, 176].

Disregarding boundary effects, saturation profiles $S_{\mathfrak{w},\Delta X_1}$ that arise during stable displacement are sigmoidal in shape and, in a rough approximation, upper and lower asymptotes to sigmoidal profiles can be considered the equilibrium states $S_{\mathfrak{w}}^u = 1$ and $S_{\mathfrak{w}}^l = S_{\mathfrak{w}}^B \approx 0$, respectively (Fig. 6.12). Considerable saturation gradients are observed only in a localized transition zone which is referred to as capillary dispersion zone. Since we associate macroscopic saturation gradients with the presence of microscopic interfaces, sigmoidal profiles evidence compact patterns. However, rather than being sharp as one would anticipate on the basis of the Buckley-Leverett equation [34] and its admissible shock wave solutions, capillarity is observed to regularize the shock wave within the capillary dispersion zone. Nevertheless, the temporal evolution of saturation profiles is indeed reminiscent of a travelling wave solution which, in consistency with the Buckley-Leverett equation, suggests that a hyperbolic conservation law macroscopically governs the evolution of wetting phase saturation during stable displacement.

We define the width $L_C(t)$ of the capillary dispersion zone as spatial differ-

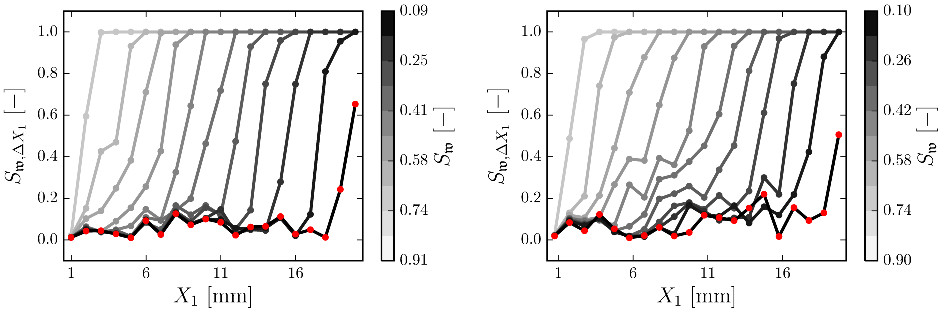

Figure 6.12: Evolution of saturation profiles in direction of $\mathbf{e}_1$ for microstructure A (left) and C (right) at $\mathrm{Ca} = 10^{-2}$ and $\mathrm{M} = 10^1$. Among the set of tested microstructures, microstructure A exhibits the narrowest fiber diameter distribution and microstructure C the widest. Width of vertical slices $\Delta X_1 = L_W/20$. Red markers indicate residual saturation profile at breakthrough.

ence between both points where saturation profiles $S_{\mathfrak{w},\Delta X_1}(X_1, t)$ approach the equilibrium asymptotes. In formal terms, L_C is computed as

$$L_C(t) := \max\left\{\underset{X_1}{\operatorname{argmin}}\left(S_{\mathfrak{w},\Delta X_1} - S^B_{\mathfrak{w},\Delta X_1}\right)\right\} - \min\left\{\underset{X_1}{\operatorname{argmax}}\left(S_{\mathfrak{w},\Delta X_1} - 1\right)\right\},$$

where $S^B_{\mathfrak{w},\Delta X_1}(X_1)$ denotes residual saturation profiles at breakthrough (Fig. 6.12, red markers). While equilibrium asymptotes $S^u_{\mathfrak{w}}$ and $S^l_{\mathfrak{w}}$ as well as residual wetting phase saturations $S^B_{\mathfrak{w}}$ are observed barely sensitive to properties of the microstructures, the width $L_C(t)$, on the other hand, appears to increase with the degree of microstructure heterogeneity. In an attempt to quantify the latter, we compute the temporal average of $L_C(t)$, hereafter denoted $\bar{L}_C$. In order to avoid boundary artifacts, we consider the averaging window for $\bar{L}_C$ equal to the time frame during which the capillary dispersion zone is entirely contained within the porous sample domain. We observe the latter to be the case for $0.3 < S_{\mathfrak{w}}(t) < 0.7$. In spite of the fact that more data and larger simulation domains are required to gain statistical confidence, the average width of the capillary dispersion zone is found to increase linearly with standard deviation v_F of fiber diameter distribution (Fig. 6.13). In particular, $\bar{L}_C \approx 14\, v_F\, m_F$ yields a reasonable fit to the present data. We emphasize that drainage rate, viscosities and intrinsic permeabilities, which are expected to affect $L_C(t)$ as well, are kept constant. Moreover, microstructures A, B and C only differ by the degree of heterogeneity expressed in terms of v_F and v_N while porosities and expectation values m_F and m_N remain unchanged (Table 6.1). If further experimental support is provided, the

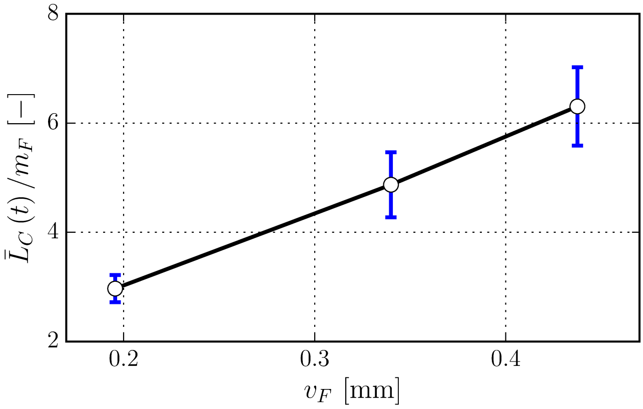

Figure 6.13: Average width $\bar{L}_C$ of capillary dispersion zone during stable displacement as a function of standard deviation v_F of fiber diameter distribution. Blue error bars correspond to standard deviations of $L_C(t)$. $\bar{L}_C$ as well as standard deviations are normalized with respect to mean fiber diameter m_F.

latter would imply the existence of an intermediate length scale, i.e. a mesoscopic capillary dispersion length scale, between pore-scale ($\sim m_F$) and Darcy scale which depends on the second central moment of the grain size distribution. Proper characterization of the latter is considered crucial since, as discussed in the remainder of this section, hydraulic disconnection of wetting phase and ganglion dynamics [176] during stable displacement are processes that are local to the capillary dispersion zone.

In an attempt to improve our understanding of capillary dispersion, we discuss the evolution of mean fluid pressure profiles $\bar{p}_{\Delta X_1}$ in time (Fig. 6.14, solid lines). Mean pressure profiles are found to be continuous, piecewise linear functions composed of two line segments. Each line segment can be intuitively attributed to Darcy flow of wetting and non-wetting phase, respectively. While the kink point, i.e. the point where both segments are connected to each other, moves downstream as non-wetting saturation increases, slopes of line segments appear rather invariant to the level of saturation. Clearly, the latter is due to the fact that intrinsic permeability, bulk viscosities and macroscopic flux remain constant during drainage. Since the viscosity of the defending wetting fluid is lower, the corresponding slope downstream of the kink point is lower as well. While all of the above is consistent with the macroscopic assumption that fluid permeation obeys Darcy's law, a prerequisite for the applicability of the Buckley-Leverett equation, a broad fluid pressure distribution is found within the capillary dispersion zone which we attribute to transient pore-scale events, ganglion dynamics and the

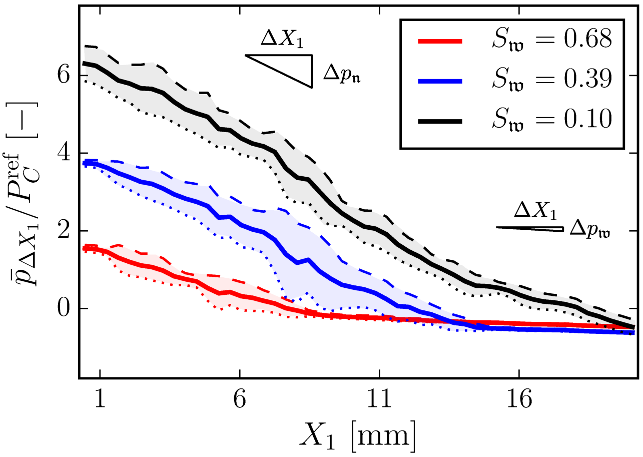

Figure 6.14: Normalized pressure profiles in direction of $\mathbf{e}_1$ for microstructure C at Ca $= 10^{-2}$ and M $= 10^1$. Solid lines represent average fluid pressures $\bar{p}_{\Delta X_1}$ within vertical slices of width $\Delta X_1 = L_W/50$. Dotted and dashed lines correspond to lower and upper bounds to fluid pressure distribution within vertical slices, respectively. Bounds are defined $\bar{p}_{\Delta X_1} \pm 1.5 v_{p,\Delta X_1}$ where $v_{p,\Delta X_1}$ denotes standard deviation of fluid pressure within a vertical slice. Resulting bounds envelope 87 % of pressure data.

presence of trapped wetting phase. The latter is most pronounced when the entire capillary dispersion zone is contained within the sample domain (Fig. 6.14, shaded blue area).

We have identified three distinct pore-scale events and corresponding flow fields that frequently occur near the saturation front and within the capillary dispersion zone (Fig. 6.15). A trapping mechanism that frequently takes place at the saturation front is the formation of wetting caps due to overlap of adjacent menisci (Fig. 6.15, top). Following Motealleh et al. [142] and Holtzman & Segre [97], the latter is referred to as Melrose event. In contrast to the overlapping mechanism described in Holtzman & Segre [97], however, for sufficiently large contact angles, we observe the point of overlap to be located at some distance downstream from the solid surface whereby the enclosed wetting phase becomes trapped. The equilibrium shape of the trapped region is a spherical cap. While, in principle, the wetting cap trapping mechanism is considered possible during capillary fingering as well, fractal branching of capillary fingers is expected to render menisci overlaps, i.e. Melrose events, rather unlikely.

In close vicinity of the saturation front, local saturation of the less viscous wetting fluid is comparatively high and, as apparent in the mean pressure profiles (Fig. 6.14, kink points), the local viscous pressure drop is negligible. Due to the resulting local dominance of capillary forces, capillary pressure thresholds govern flow near the saturation front. Hence, along with wetting cap trapping, capillary trapping mechanisms, i.e. high curvature trapping mechanisms, initially contribute to hydraulic disconnection of the wetting phase near the saturation front. In particular, we frequently observe trapping in the form of pendular bridges (Fig. 6.15, middle, $t_0 \rightarrow t_0 + 1.5\,\mathrm{ms}$). However, as the saturation front further advances, the viscous pressure drop across a trapped wetting cluster increases due to higher viscosity of the surrounding non-wetting phase. The latter leads to mobilization and, eventually, fragmentation of trapped wetting clusters. Strictly speaking, the latter implies that the terms hydraulic disconnection and trapping have to be differentiated from each other. In the present microstructures, the most frequent type of fragmentation is identified to be the transition of pendular bridges into multiple wetting caps (Fig. 6.15, middle, $t_0 + 10.7\,\mathrm{ms} \rightarrow t_0 + 12.2\,\mathrm{ms}$).

Even more intriguingly, wetting caps that are of spatial extent large enough such that respective viscous pressure drops exceed contact line pinning forces are observed to move along solid surfaces and eventually coalescence with other disconnected clusters (Fig. 6.15, bottom). The latter gives rise to a repetitive sequence of events by which the motion of hydraulically disconnected wetting phase, i.e. ganglion dynamics, occurs. On the other hand, if the size of a wetting cap falls below a critical threshold size where the viscous pressure drop exceeds the contact line pinning forces, mobilization does not occur. These results are consistent with earlier experimental observations [49]. We emphasize that a quantitatively accurate model for ganglion dynamics requires an accurate model for contact line pinning and dynamic contact angles. However, the present model, as more thoroughly discussed in section 6.2.1, incorporates a numerical contact line slip length and, moreover, advancing and receding contact angles are assumed equal to Young's contact angle. Nevertheless, we believe that our results provide qualitative evidence for the complexity of features that lead to saturation shock front regularization as well as broad fluid pressure distribution within the capillary dispersion zone.

6.4 Discussion

Not only does the complex interplay of viscous and capillary forces result in a rich diversity of macroscopic displacement patterns, but, as phenomenologically shown in section 6.3, the underlying pore-scale flow fields and trapping mechanisms exhibit pronounced disparities as well: In accordance to lubrication theory, core-annular flow is a displacement mechanism that applies to viscous fingering and implies the formation of wetting films. Invasion percolation through prefer-

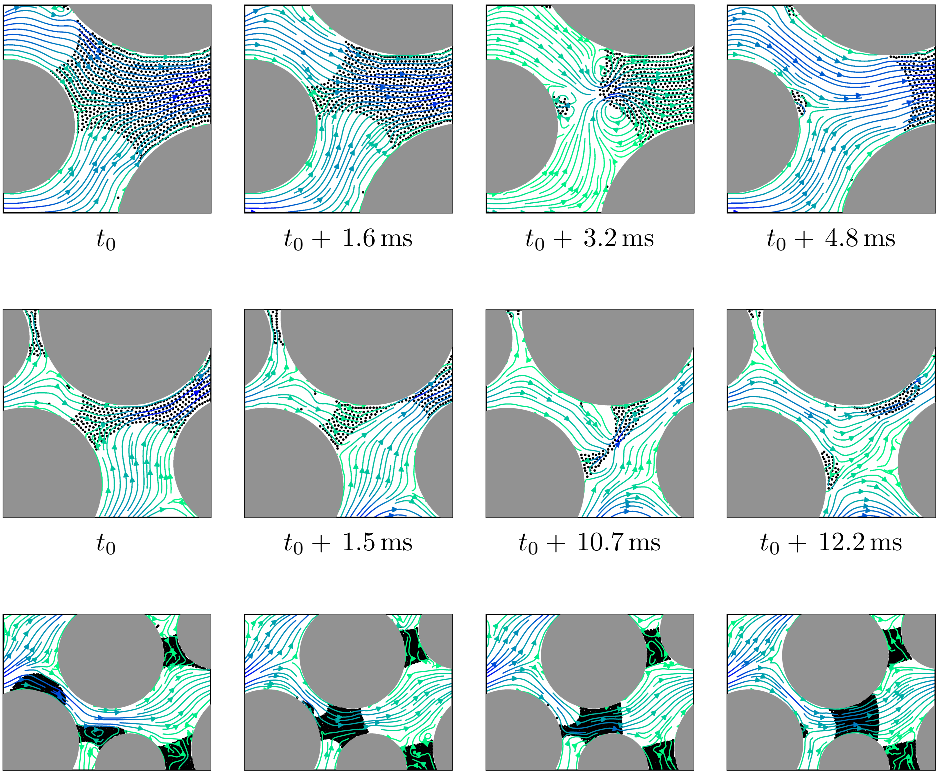

t_0 $t_0 + 1.6\,\mathrm{ms}$ $t_0 + 3.2\,\mathrm{ms}$ $t_0 + 4.8\,\mathrm{ms}$

t_0 $t_0 + 1.5\,\mathrm{ms}$ $t_0 + 10.7\,\mathrm{ms}$ $t_0 + 12.2\,\mathrm{ms}$

t_0 $t_0 + 3.2\,\mathrm{ms}$ $t_0 + 6.4\,\mathrm{ms}$ $t_0 + 9.6\,\mathrm{ms}$

Figure 6.15: Pore-scale interfacial dynamics during stable displacement at $\mathrm{Ca} = 10^{-2}$ and $\mathrm{M} = 10^{1}$. For details on visual representation of streamlines and bulk phases, see caption to Fig. 6.8. (top) Wetting phase entrapment in form of a wetting cap due to menisci overlap at saturation front as observed in a subdomain of microstructure B having size 2 mm × 2 mm. (middle) Fragmentation of a pendular bridge into multiple wetting caps as observed in a subdomain of microstructure C having size 2 mm × 2 mm. Time increments between plots are non-uniform. For $t_0 \rightarrow t_0 + 1.5\,\mathrm{ms}$, the depicted subdomain is located near the saturation front, whereas for $t_0 + 10.7\,\mathrm{ms} \rightarrow t_0 + 12.2\,\mathrm{ms}$ it is within the capillary dispersion zone. (bottom) Wetting phase ganglion dynamics by a sequence of fragmentation and coalescence events within the capillary dispersion zone as observed in a subdomain of microstructure C having size 4 mm × 3 mm.

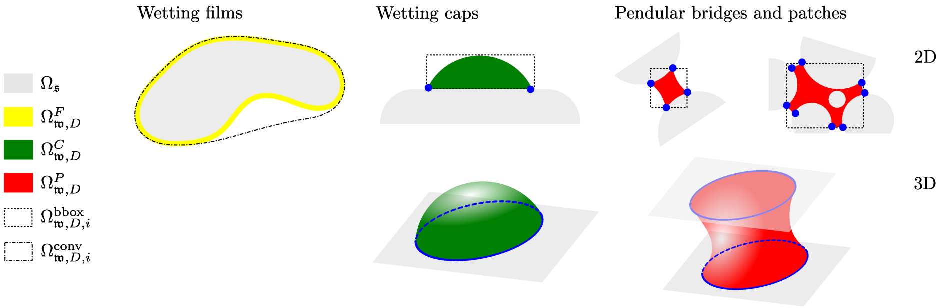
Wetting films
Wetting caps
Pendular bridges and patches
2D
3D
$\Omega_{\mathfrak{s}}$
$\Omega^{F}_{\mathfrak{w},D}$
$\Omega^{C}_{\mathfrak{w},D}$
$\Omega^{P}_{\mathfrak{w},D}$
$\Omega^{\text{bbox}}_{\mathfrak{w},D,i}$
$\Omega^{\text{conv}}_{\mathfrak{w},D,i}$

Figure 6.16: Schematic diagram of the proposed classification of hydraulically reservoir-disconnected wetting phase clusters into wetting films $\Omega^{F}_{\mathfrak{w},D}$ (yellow), wetting caps $\Omega^{C}_{\mathfrak{w},D}$ (green) and pendular clusters $\Omega^{P}_{\mathfrak{w},D}$ (red). Blue markers indicate contact points (2D) whereas blue lines indicate contact lines (3D). Minimum bounding box $\Omega^{\text{bbox}}_{\mathfrak{w},D,i}$ (dashed line) and convex hull $\Omega^{\text{conv}}_{\mathfrak{w},D,i}$ (dash-dot line) serve to identify cluster set membership.

ential flow paths of least capillary resistance gives rise to high curvature trapping mechanisms during capillary fingering. Coalescence of menisci along the macroscopically flat saturation front, i.e. Melrose events, gives rise to the formation of wetting caps during stable displacement. In attempt to quantify the above, we introduce the following classification of hydraulically reservoir-disconnected wetting phase. We emphasize that the following hypothesis is expected to hold only for partially wettable solid surfaces.

Following Hilfer [91, 92] and without loss of generality one may express the region of the pore-space or total bulk fluid phase as

$$\Omega_{\mathfrak{f}} = \Omega_{\mathfrak{w},C} \cup \Omega_{\mathfrak{w},D} \cup \Omega_{\mathfrak{n},C} \cup \Omega_{\mathfrak{n},D},$$

where $\Omega_{\alpha,C}$ and $\Omega_{\alpha,D}$ denote hydraulically reservoir-connected (percolating) and reservoir-disconnected (non-percolating) subsets of fluid phases $\Omega_{\alpha} \in \{\Omega_{\mathfrak{n}}, \Omega_{\mathfrak{w}}\}$, respectively. By definition, reservoir domains and reservoir-disconnected domains are disjoint sets, i.e. $\Omega_{\alpha,D} \cap \Omega_{\alpha,\text{res}} = \emptyset$, and, furthermore, $\Omega_{\alpha,C} \cap \Omega_{\alpha,D} = \emptyset$ as well. In the following, we study the properties of $\Omega_{\mathfrak{w},D}$ as breakthrough is reached after saturation-controlled primary drainage. Provided that solid surfaces are partially wettable, we hypothesize that $\Omega_{\mathfrak{w},D}$ can be further subdivided such that

$$\Omega_{\mathfrak{w},D} = \Omega^{F}_{\mathfrak{w},D} \cup \Omega^{C}_{\mathfrak{w},D} \cup \Omega^{P}_{\mathfrak{w},D} \cup \Omega^{S}_{\mathfrak{w},D}, \tag{6.6}$$

where $\Omega^{F}_{\mathfrak{w},D}$, $\Omega^{C}_{\mathfrak{w},D}$, $\Omega^{P}_{\mathfrak{w},D}$ and $\Omega^{S}_{\mathfrak{w},D}$ denote pairwise disjoint domains occupied by wetting films, wetting caps, pendular clusters and trapped wetting phase in singular curvature domains, respectively (Fig. 6.16). As more thoroughly discussed in section 6.2.1, surface singularities such as corners and grain contacts are absent herein such that $\Omega^{S}_{\mathfrak{w},D} = \emptyset$. The total volume and saturation of a domain $\Omega^{\mathfrak{t}}_{\mathfrak{w},D}$, where the superscript $\mathfrak{t} \in \{F, C, P, S\}$, is defined

$$V^{\mathfrak{t}}_{\mathfrak{w},D} := \int\limits_{\Omega^{\mathfrak{t}}_{\mathfrak{w},D}} \mathrm{d}v, \quad S^{\mathfrak{t}}_{\mathfrak{w},D} := \frac{V^{\mathfrak{t}}_{\mathfrak{w},D}}{V_{\mathfrak{f}}}, \quad \forall\, \mathfrak{t} \in \{F, C, P, S\},$$

respectively. Moreover, each region $\Omega^{\mathfrak{t}}_{\mathfrak{w},D}$ is comprised of a number $N^{\mathfrak{t}}_{\mathfrak{w},D}$ of individual clusters such that

$$\Omega^{\mathfrak{t}}_{\mathfrak{w},D} := \bigcup_{i=1}^{N^{\mathfrak{t}}_{\mathfrak{w},D}} \Omega^{\mathfrak{t}}_{\mathfrak{w},D,i}, \quad \forall\, \mathfrak{t} \in \{F, C, P, S\}.$$

Individual clusters are mutually disjoint, i.e. $\Omega^{\mathfrak{t}}_{\mathfrak{w},D,i} \cap \Omega^{\mathfrak{t}}_{\mathfrak{w},D,j} = \emptyset$ for all $i \neq j$.

In the context of imaging-based experimental techniques, e.g. X-ray computed tomography or confocal microscopy, the identification of individual clusters is considered possible using image segmentation methods [22, 49, 112, 208]. Using the present direct numerical simulation approach on the other hand, individual clusters can be identified based on the connectivity of the binary phase indicator field $C^{\mathfrak{wn}}$. Since we attempt to quantify saturations $\Omega^{\mathfrak{t}}_{\mathfrak{w},D}$, we require unique properties by means of which the set membership of an individual cluster $\Omega^{\mathfrak{t}}_{\mathfrak{w},D,i}$ to either one of the subsets in Eq. (6.6) can be identified.

An unambiguous definition of the set membership of a cluster is provided by studying three-phase contact lines that are adjacent to a cluster. It is intuitively understood that no contact lines are formed by wetting films. On the other hand, wetting caps form a single contact line loop whereas pendular clusters form at least two contact line loops (Fig. 6.16, blue lines). In two-dimensional computations, the latter implies that wetting caps form precisely two contact points whereas pendular clusters form at least four (Fig. 6.16, blue markers). A pendular cluster that forms the minimum number of two contact line loops is referred to as pendular bridge. As pendular clusters may form a larger number of contact line loops, further topological classification of pendular clusters, e.g. with the use of Betti numbers [208], is considered sensible. However, topological classification of pendular clusters is not further discussed herein. Despite of the fact that the above provides an intuitive definition of set membership, the implementation of image analysis algorithms to count contact line loops is considered rather non-trivial. Hence, we implement alternative criteria for the identification of cluster set membership.

We denote the region and volume of the convex hull [10] that envelopes all

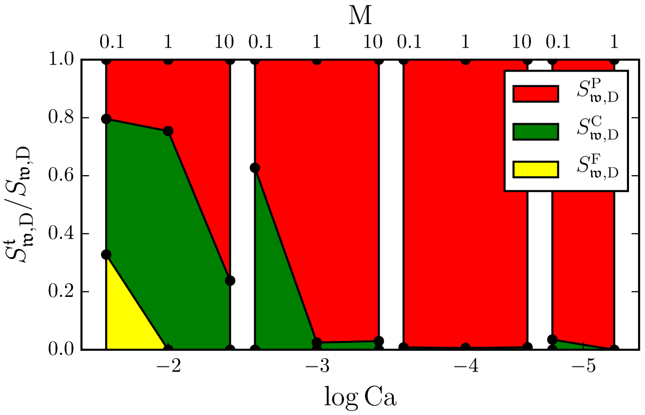

Figure 6.17: Quantitative analysis of $\Omega_{\mathfrak{w},D}$ in terms of constituent saturations $S^F_{\mathfrak{w},D}$, $S^C_{\mathfrak{w},D}$ and $S^P_{\mathfrak{w},D}$ at breakthrough for microstructure C. Constituent saturations are normalized with respect to total saturation of reservoir-disconnected wetting phase $S_{\mathfrak{w},D}$ and represented by a stacked area chart. Black markers indicate computed data points. Areas are highlighted in color according to the color code introduced in Fig. 6.16.

points of a cluster as

$$\Omega^{\mathrm{conv}}_{\mathfrak{w},D,i} := \mathrm{conv}\left(\Omega^{\mathrm{t}}_{\mathfrak{w},D,i}\right), \quad V^{\mathrm{conv}}_{\mathfrak{w},D,i} := \int\limits_{\Omega^{\mathrm{conv}}_{\mathfrak{w},D,i}} \mathrm{d}v,$$

respectively. In addition to the convex hull, we make use of the minimum bounding box $\Omega^{\mathrm{bbox}}_{\mathfrak{w},D,i}$ of a cluster according to Freeman & Shapira [73]. Though not unambiguous, we identify a cluster as wetting film if the ratio of cluster volume $V^{\mathrm{t}}_{\mathfrak{w},D,i}$ to its convex hull volume is lower than a critical threshold value. For the present particulate microstructures $V^{\mathrm{t}}_{\mathfrak{w},D,i}/V^{\mathrm{conv}}_{\mathfrak{w},D,i} < 0.1$ has proven a stable criterion. However, the critical threshold value is expected to depend on the morphology of the microstructure as well as capillary number. If the wetting film criterion is not met, the cluster is either a member of $\Omega^C_{\mathfrak{w},D}$ or $\Omega^P_{\mathfrak{w},D}$. We differentiate wetting caps from pendular clusters using the local capillary pressure difference $P^{\mathrm{bbox}}_{C,i}$ within the region of the minimum bounding box $\Omega^{\mathrm{bbox}}_{\mathfrak{w},D,i}$. In particular, the bounding box capillary pressure $P^{\mathrm{bbox}}_{C,i}$ is computed by considering the pressure averaging domains to be the bulk volumes contained within $\Omega^{\mathrm{bbox}}_{\mathfrak{w},D,i}$, i.e. using $\Omega^{\mathrm{cuc}}_{\alpha} \cap \Omega^{\mathrm{bbox}}_{\mathfrak{w},D,i}$ in place of $\Omega^{\mathrm{cuc}}_{\alpha}$ in Eq. (6.2).

Since the meniscus of a wetting cap is convex, the respective bounding box capillary pressure is positive, i.e. $P_{C,i}^{\mathrm{bbox}} > 0$. On the other hand, pendular cluster menisci are concave such that $P_{C,i}^{\mathrm{bbox}} < 0$. In summary, our approximative approach to identify cluster set membership reads

$$\Omega_{\mathfrak{w},D,i}^{\mathrm{t}} \in \begin{cases} \Omega_{\mathfrak{w},D}^{F} & \text{if } V_{\mathfrak{w},D,i}^{\mathrm{t}}/V_{\mathfrak{w},D,i}^{\mathrm{conv}} < 0.1, \\ \Omega_{\mathfrak{w},D}^{C} & \text{if } V_{\mathfrak{w},D,i}^{\mathrm{t}}/V_{\mathfrak{w},D,i}^{\mathrm{conv}} > 0.1 \text{ and } P_{C,i}^{\mathrm{bbox}} > 0, \\ \Omega_{\mathfrak{w},D}^{P} & \text{if } V_{\mathfrak{w},D,i}^{\mathrm{t}}/V_{\mathfrak{w},D,i}^{\mathrm{conv}} > 0.1 \text{ and } P_{C,i}^{\mathrm{bbox}} < 0. \end{cases} \tag{6.7}$$

Though readily implemented into our direct numerical simulation approach, the set of criteria outlined in Eqs. (6.7) fails if the viscous pressure drop across $\Omega_{\mathfrak{w},D,i}^{\mathrm{bbox}}$ dominates over local capillary pressure and, on the other hand, if the critical threshold value is not properly calibrated. Nevertheless, due to length scales of bounding boxes being small enough to render viscous contributions to $P_{C,i}^{\mathrm{bbox}}$ negligible and due to the simplicity of present microstructures that renders results relatively insensitive to the choice of the critical threshold value, Eqs. (6.7) have proven to be suitable approximations herein (Fig. 6.18).

Despite of the sparsity of data, the quantitative analysis of saturations $S_{\mathfrak{w},D}^{F}$, $S_{\mathfrak{w},D}^{C}$ and $S_{\mathfrak{w},D}^{P}$ at breakthrough is consistent with the our phenomenological discussion of pore-scale flow fields in section 6.3 (Fig. 6.17). At sufficiently small capillary numbers, invasion percolation results in hydraulically reservoir-disconnected wetting clusters being predominantly present in the form of pendular clusters, i.e. $\Omega_{\mathfrak{w},D} \approx \Omega_{\mathfrak{w},D}^{P}$ for $\mathrm{Ca} \leq 10^{-4}$. On the other hand, wetting caps considerably contribute to residual wetting phase saturation at breakthrough for $\mathrm{Ca} \geq 10^{-3}$. The formation of wetting films is indeed observed a relevant trapping mechanism for $\mathrm{Ca} = 10^{-2}$ and $\mathrm{M} = 10^{-1}$, i.e. for viscous fingering. These results indicate that the governing flow regime becomes not only apparent in the macroscopic patterns formed by non-wetting phase distribution but also in the composition of $\Omega_{\mathfrak{w},D}$ following Eq. (6.6). If further experimental support is provided, the proposed classification of hydraulically reservoir-disconnected wetting clusters may constitute a useful extension to complement the phase diagram of displacement patterns as introduced in Lenormand et al. [122].

6.5 Summary and Conclusions

Using fully resolved direct numerical simulations, we studied the effect of capillary number and viscosity ratio on the pore-scale dynamics of fluid-fluid interfaces during primary drainage in partially wettable porous media of particulate microstructure. At the length scale of individual pores, pore-scale flow fields and trapping mechanisms as observed for the three basic flow regimes exhibit profound differences. We draw the following conclusions from this work:

Viscous fingering (Ca = 10^{-2}, M = 10^{-1})

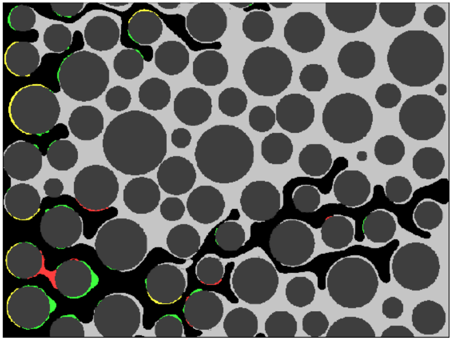

Stable displacement (Ca = 10^{-2}, M = 10^{1})

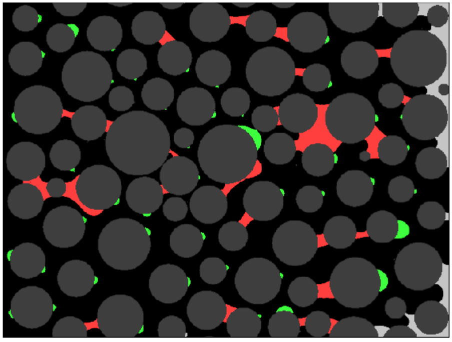

Capillary fingering (Ca = 10^{-5}, M = 10^{0})

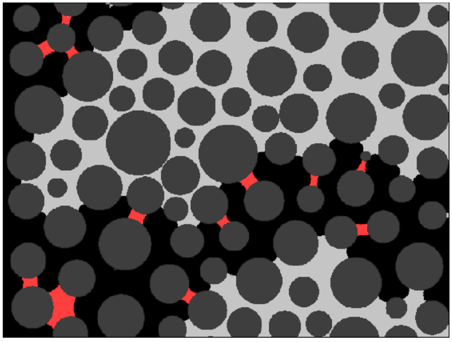

Figure 6.18: Fluid phase distribution at breakthrough for microstructure C. Domain $\Omega_{\mathfrak{s}}$ is colored dark gray, $\Omega_{\mathfrak{n},C}$ colored black and $\Omega_{\mathfrak{w},C}$ colored light gray. Hydraulically reservoir-disconnected clusters are highlighted in color according to cluster set membership and the color code introduced in Fig. 6.16. Cluster set memberships were identified using the approximative criteria in Eqs. (6.7). Individual clusters are identified by linearly interpolating unstructured SPH particle data of phase indicator field $C^{\mathfrak{wn}}$ to points of a regular grid using `matplotlib.mlab.griddata` [59] and subsequently using `skimage.measure.label` [202] to identify connected domains. Thin wetting films are observed to coat solid surfaces for Ca = 10^{-2} and M = 10^{-1} (left). A significant number of wetting caps are observed for Ca = 10^{-2} and M = 10^{1} (middle). For Ca = 10^{-5} and M = 10^{0} (right), hydraulically reservoir-disconnected wetting phase is observed to be solely present in the form of pendular clusters.

1. During viscous fingering,
    1.1. the pore-scale flow field resembles Bretherton's coating flow and implies the formation of wetting films.
    1.2. wetting films significantly contribute to specific fluid-fluid interfacial area and give rise to non-negligible interfacial viscous momentum coupling.
    1.3. the calibration of relative permeability functions, which by definition are related to viscous momentum exchange between solid and fluid phases only, should be reconsidered.
2. During stable displacement,
    2.1. saturation fronts extend over the finite width of capillary dispersion zones.
    2.2. fluid permeation obeys Darcy's law far from the saturation front. On the other hand, ganglion dynamics renders two-phase flow within the capillary dispersion zone complex.
    2.3. the width of the capillary dispersion zone is observed to increase linearly with standard deviation of fiber diameter, or grain size, distribution when material properties, boundary conditions, porosity and intrinsic permeability are kept constant.
    2.4. trapped wetting caps form due to menisci overlaps and fragmentation of pendular clusters.
3. During capillary fingering,
    3.1. our simulations confirm the occurrence of cooperative pore-filling events.
    3.2. percolation at constant macroscopic capillary pressure implies linear evolution of specific fluid-fluid interfacial area if the pore-space exhibits microstructural simplicity.
    3.3. pendular clusters are formed in high-curvature domains.

CHAPTER 7

Summary and Outlook

In this thesis we investigated non-Darcian fluid flow in porous media using pore-scale resolved direct numerical simulations. Exploiting its mesh-free and Lagrangian nature, we applied Smoothed Particle Hydrodynamics methods to study high velocity and two-phase immiscible flow in particulate porous media. We articulate the goals of this contribution as threefold: 1. to identify microscopic flow patterns that give rise to the deviation of the macroscopic constitutive behavior from classical Darcian solutions. 2. to calibrate constitutive models for flow processes beyond Darcy's law and 3. to assess the predictive capabilities, advantages and limitations of SPH methods with respect to pore-scale resolved fluid flow simulations.

Localization of interfacial effects renders simulation results sensitive to particle disorder and, as a result, sensitive to the kernel function. Kernel functions that lack non-negativity of the kernel Fourier transform, such as the quintic B-spline, are prone to the particle pairing instability [51] - a spurious zero energy mode due to which interpolation accuracy at interfaces is impaired. Kernel functions with positive Fourier transform, such as Wendland kernels [207], are thus preferable for two-phase simulations. As to avoid the notorious tensile instability of weakly-compressible SPH [138, 194], which occurs if particles experience negative principal stresses or pressures, we have furthermore used a constant positive background pressure upon which all pressure perturbations occur. Anticipating the results of Morris [139], however, background pressures are kept small enough as to avoid the long wavelength instability that is observed in the numerical dispersion relation for overly large background pressures. On the basis of an extensive validation procedure, we demonstrated the ability of SPH methods to reproduce key features of creeping, inertial and capillary flows. While we understand boundary conditions in SPH being satisfied in a "weak" sense only, i.e. over the domain of the interpolation kernel compact support, the critical velocity Dirichlet boundary condition as well as the equilibrium contact angle condition are found to be reproduced with satisfactory accuracy. Weak compliance to boundary conditions, however, gives rise to non-equilibrium contact line motion which, while it does bypass the Huh-Scriven paradox [101], must be considered artificial far from thermodynamic equilibrium. While the physical implementation of contact line slippage is left open for future investigations, macroscopic seepage velocities in the present work were kept small enough as to avoid large non-equilibrium perturbations at contact lines. In spite of the above, we shall recall that the proposed discrete SPH equations are compliant to Galilean invariance as well as total mass and linear momentum conservation.

The inertial transition from low to high Reynolds number flow in porous media as measured on the effective macroscale is found decisively influenced by microstructure. In particular, we have reported a strong correlation between the macroscopically measurable quantities apparent permeability and effective hydraulic gradient as well the microscopically measurable quantities total drag force and hydraulic tortuosity. Indeed, these quantities fall on the same sigmoidal curve when normalized appropriately and plotted over seepage velocity. Flow tube narrowing and streamline rectification gives rise to sigmoidal transition of hydraulic tortuosity. On the other hand, the increase of form drag is due to eddies that form in the low-pressure wakes of flow path obstacles and observed subject to sigmoidal transition as well. The sigmoidal transition function consists of four free parameters: Two asymptotes, the inflection point as well as a steepness parameter which controls the width of transition. We argue that the width of inertial transition is influenced by microstructure recalling that the laminar-turbulent transition in simple conduits is rather discrete while more gradual in tortuous conduits. On the basis of these empirical observations, we have proposed a novel macroscopic constitutive model for inertial transition that can, alternatively, be derived using the asymptotic correlation method of Churchill & Usagi [45]. While the model is of empirical character, it is consistent with Darcy's model for small flow rates, reproduces Forchheimer's model for large rates and exhibits higher-order leading terms that depend on the steepness parameter for intermediate flow rates. The proposed model is put forward as an empirical resolution to the notorious weak-inertia regime in which the hydraulic gradient has been observed to vary with the cube of the flow rate. How the steepness parameter depends on microstructure is left open for future investigations. It is most-likely, however, that this parameter depends on the geometric tortuosity of flow conduits.

We have discussed primary drainage in porous media of particulate microstructure for various points of the $(\mathrm{Ca}, \mathrm{M})$ phase diagram. In an attempt to meet the question, whether or not pore-scale flow topologies associated with different macroscopic displacement patterns are equivalent, we have characterized the entrapment of wetting phase. Our results show that for viscous fingering fluid displacement at the pore-scale is reminiscent of Bretherton's problem [32], i.e. flow of gas bubbles in saturated capillary tubes. The corresponding flow pattern is such that the less viscous fluid drains through the core of a pore-throat causing the formation of wetting lubrication layers on solid surfaces. The latter is found to render non-equilibrium momentum exchange between both fluid phases, i.e. the Yuster effect [211], non-negligible and the evolutoin of specific interfacial area non-linear. The latter casts doubt on the classical use of relative permeability functions, which, by definition, are related to momentum exchange between solid and fluid phases only. For stable displacement, saturation profiles evolve by what might be referred to as traveling shock wave - a well known solution to the hyperbolic Buckley-Leverett (BL) equation [34]. However, rather than being sharp as predicted by the BL equation, pore-scale simulations reveal the saturation front to be diffuse. Pore-scale flow patterns within this capillary dispersion zone were observed to exhibit complex events such as frequent fragmentation and coalescence of hydraulically isolated wetting clusters. The latter implies that capillarity regularizes the saturation front. We have found a strong correlation between the width of the capillary dispersion zone and the standard deviation of the pore-throat size distribution which motivates further investigations. For capillary fingering fluid displacement is indeed reminiscent of invasion percolation with frequent pore-scale events singular in time, such as Haines jumps and associated velocity bursts [17, 81, 135]. The evolution of interfaces during capillary fingering is governed by the free energy balance comprised of pressure-volume work and interfacial tension-interfacial area work. Trapping of wetting phase was observed to primarily occur in high-curvature domains that are energetically inaccessible to percolation. The latter casts doubt on coarse-grained models that do not explicitly take into account the evolution of interfacial areas [89]. We argue that these results speak in favor of effective macroscopic models that are augmented by balance equations for the transport and evolution of interfaces [78, 87, 89]. Furthermore, pore-scale resolved simulations are found a feasible approach to calibrate such models in future investigations.

List of Figures

2.1 Schematic representation of motion and configurations 8
2.2 Domains and boundaries for single phase flow in porous media . . 15
2.3 Motion of surfaces embedded in three-dimensional space 18
2.4 Schematic representation of a material volume with internal interface 21
2.5 Schematic representation of the concept of interface-excess densities 23
2.6 Interpretation of flux terms in transport theorem for surfaces . . . 26
2.7 On the assumption of negligible interface-excess mass density . . . 27
2.8 Schematic representation of the phase indicator field 37
2.9 Schematic diagram of multi-phase flow in porous media 39
2.10 Concurrent force system acting on a three-phase contact line . . . 44
2.11 Reduced interfacial force density at solid-fluid interfaces 48

3.1 Schematic of the nodal integration 55
3.2 Kernel functions and their one-dimensional Fourier transforms . . 58
3.3 Typical equilibrium particle distributions and pairing instability . 60
3.4 Error convergence study of discrete reproducing approximations . . 66
3.5 Schematic of compact kernel support domain truncation 68
3.6 Schematic of the ghost particle approach 68
3.7 Visualization of boundary inconsistencies at free surfaces 69
3.8 Error convergence study of zeroth order complete gradient operator 72
3.9 Periodic boundary condition using minimum image convention . . 77
3.10 Schematic of fictitious ghost velocities adjacent to Dirichlet boundary 78
3.11 Fixed ghost particles in the vicinity of Dirichlet boundaries 80

4.1 Simulation configuration for Poiseuille flow 92
4.2 Evolution of transient velocity profiles during Poiseuille flow 93
4.3 Simulation configuration for lid-driven square cavity flow 94
4.4 Velocity magnitude fields during lid-driven square cavity flow . . . 95
4.5 Vertical and horizontal velocity profiles for lid-driven cavity flow . 96

4.6 Permeabilities of sphere packings in periodic cubic unit-cells 101
4.7 Simulation configuration for fully immersed liquid droplet 102
4.8 Equilibrium shape and pressure profiles of fully immersed droplets 104
4.9 Numerical errors for capillary pressure of fully immersed droplets . 105
4.10 Numerical estimates for capillary pressure of fully immersed droplets 106
4.11 Initial simulation configuration for layered co-current flow 107
4.12 Steady-state velocity profiles during co-current flow 109
4.13 Steady-state relative permeabilities during co-current flow 110
4.14 Simulation configuration for capillary rise between parallel plates . 112
4.15 Schematic diagram of a meniscus located between two parallel plates 113
4.16 Time evolution and equilibrium meniscus shapes for capillary rise . 115
4.17 Relative errors in numerical estimates of capillary rise height . . . 116
4.18 Absolute errors in numerical estimates of capillary rise height . . . 117
4.19 Period of oscillation of immersed droplet versus interfacial tension 118
4.20 Computing the period of oscillation of an oscillating fluid droplet . 119

5.1 Computational domain for high velocity flow simulations 124
5.2 Non-dimensional apparent permeability as function of Re 126
5.3 Total microscopic drag force and skin friction as function of Re . . 127
5.4 Rectification of streamlines for increasing Re 129
5.5 Hydraulic tortuosity as function of Re 130
5.6 Correlation between permeability, tortuosity and interfacial drag . 131
5.7 Fitting Forchheimer model, cubic model and logistic filtration model 133

6.1 Computational domain for primary drainage simulations 143
6.2 Statistical analysis of computational unit cells 145
6.3 Overview of drainage displacement patterns on $\log \mathrm{Ca} - \log \mathrm{M}$ plane 151
6.4 Evolution of menisci during cooperative pore-filling event 153
6.5 Evolution of capillary pressure and interfacial area at low Ca . . . 154
6.6 Schematic of capillary fingering in poorly graded microstructures . 155
6.7 Evolution of saturation profiles during capillary fingering 156
6.8 Flow fields during wetting field entrapment for viscous fingering . . 158
6.9 Evolution of interfacial areas and interfacial momentum exchange . 159
6.10 Evolution of macroscopic capillary pressure during viscous fingering 160
6.11 Evolution of saturation profiles during viscous fingering 161
6.12 Evolution of saturation profiles during stable displacement 163
6.13 Width of capillary dispersion zone for simulated microstructures . 164
6.14 Evolution of pressure profiles during stable displacement 165
6.15 Pore-scale interfacial dynamics during stable displacement 167
6.16 Morphological classification of discrete wetting phase clusters . . . 168
6.17 Tentative phase diagram of discrete wetting phase ganglia 170

6.18 Fluid phase and discrete ganglia distribution at breakthrough . . . 172

List of Tables

4.1 Porosity of (non)-consolidated sphere packings in cubic unit-cells . 98
6.1 Overview of microstructure parameters for drainage simulations . . 146

List of Algorithms

1 Schematic simulation initialization and time-stepping algorithm . . 89
2 Schematic particle force computation algorithm 90

Bibliography

[1] S. Adami, X. Hu, and N. Adams. A new surface-tension formulation for multi-phase SPH using a reproducing divergence approximation. *J. Comput. Phys.*, 229(13):5011–5021, 2010.

[2] S. Adami, X. Hu, and N. Adams. A generalized wall boundary condition for smoothed particle hydrodynamics. *J. Comput. Phys.*, 231(21):7057–7075, 2012.

[3] B. Ahrenholz, J. Tölke, P. Lehmann, A. Peters, A. Kaestner, M. Krafczyk, and W. Durner. Prediction of capillary hysteresis in a porous material using lattice-Boltzmann methods and comparison to experimental data and a morphological pore network model. *Adv. Water Resour.*, 31:1151–1173, 2008.

[4] J. S. Andrade, U. M. S. Costa, M. P. Almeida, H. A. Makse, and H. E. Stanley. Inertial effects on fluid flow through disordered porous media. *Phys. Rev. Lett.*, 82:5249–5252, Jun 1999.

[5] R. Aris. *Vectors, Tensors and the Basic Equations of Fluid Mechanics*. Dover Publications, New York, NY, USA, 1990.

[6] R. T. Armstrong and S. Berg. Interfacial velocities and capillary pressure gradients during haines jumps. *Phys. Rev. E*, 88:043010, 2013.

[7] M. Ayub and R. G. Bentsen. Interfacial viscous coupling: a myth or reality? *J. Petrol. Sci. Eng.*, 23(1):13–26, 1999.

[8] M. Balhoff, A. Mikelić, and M. F. Wheeler. Polynomial filtration laws for low reynolds number flows through porous media. *Transp. Porous Med.*, 81(1):35–60, 2009.

[9] M. T. Balhoff and M. F. Wheeler. A predictive pore-scale model for non-darcy flow in porous media. *SPE Journal*, pages 579–587, 2009.

[10] C. B. Barber, D. P. Dobkin, and H. Huhdanpaa. The quickhull algorithm for convex hulls. *ACM Trans. Math. Softw.*, 22(4):469–483, 1996.

[11] G. I. Barenblatt and G. G. Chernyi. On moment relations on surfaces of discontinuity in dissipative media. *J. Appl. Math. Mech. (PMM)*, 27(5): 1205–1218, 1963.

[12] R. D. Barree and M. W. Conway. Beyond beta factors: A complete model for darcy, forchheimer, and trans-forchheimer flow in porous media. In *Paper SPE 89325 presented at the SPE Annual Technical Conference and Exhibition, Houston, 26–29 September*, 2004.

[13] G. Batchelor. *An Introduction to Fluid Dynamics.* Cambridge University Press, New York, NY, USA, 2000.

[14] J. Bear. *Dynamics of Fluids in Porous Media.* Dover Publications, New York, NY, USA, 1988.

[15] T. Belytschko, Y. Krongauz, J. Dolbow, and C. Gerlach. On the completeness of meshfree particle methods. *Int. J. Numer. Meth. Eng.*, 43:785–819, 1998.

[16] V. Berejnov, N. Djilali, and D. Sinton. Lab-on-chip methodologies for the study of transport in porous media: energy applications. *Lab Chip*, 8: 689–693, 2008.

[17] S. Berg, H. Ott, S. A. Klapp, A. Schwing, R. Neiteler, N. Brussee, A. Makurat, L. Leu, F. Enzmann, J.-O. Schwarz, M. Kersten, S. Irvine, and M. Stampanoni. Real-time 3d imaging of haines jumps in porous media flow. *P. Natl. Acad. Sci. USA*, 110(10):3755–3759, 2013.

[18] B. Berkowitz and I. Balberg. Percolation theory and its application to groundwater hydrology. *Water Resour. Res.*, 29(4):775–794, 1993.

[19] F. Bierbrauer, P. Bollada, and T. Phillips. A consistent reflected image particle approach to the treatment of boundary conditions in smoothed particle hydrodynamics. *Comput. Method. Appl. M.*, 198(41âĂŞ44):3400–3410, 2009.

[20] M. J. Blunt. Flow in porous media – pore-network models and multiphase flow. *Curr. Opin. Colloid. In.*, 6(3):197–207, 2001.

[21] M. J. Blunt and H. Scher. Pore-level modeling of wetting. *Phys. Rev. E*, 52:6387–6403, 1995.

[22] M. J. Blunt, B. Bijeljic, H. Dong, O. Gharbi, S. Iglauer, P. Mostaghimi, A. Paluszny, and C. Pentland. Pore-scale imaging and modelling. *Adv. Water Resour.*, 51:197–216, 2013.

[23] Y. Bo-Ming and L. Jian-Hua. A geometry model for tortuosity of flow path in porous media. *Chin. Phys. Lett.*, 21(8):1569–1571, 2004.

[24] J. Bonet. Variational and momentum preservation aspects of smooth particle hydrodynamic formulations. *Comput. Method. Appl. M.*, 180:97–115, 1999.

[25] J. Bonet and S. Kulasegaram. Correction and stabilization of smooth particle hydrodynamics methods with applications in metal forming simulations. *Int. J. Numer. Meth. Eng.*, 47(6):1189–1214, 2000.

[26] D. Bonn, J. Eggers, J. Indekeu, J. Meunier, and E. Rolley. Wetting and spreading. *Rev. Mod. Phys.*, 81:739–805, 2009.

[27] K. Boomsma and D. Poulikakos. The effects of compression and pore size variations on the liquid flow characteristics in metal foams. *J. Fluids Eng.*, 124(1):263–272, 2001.

[28] R. M. Bowen. Incompressible porous media models by use of the theory of mixtures. *Int. J. Eng. Sci.*, 18(9):1129 – 1148, 1980.

[29] R. M. Bowen. Compressible porous media models by use of the theory of mixtures. *Int. J. Eng. Sci.*, 20(6):697 – 735, 1982.

[30] J. Brackbill, D. Kothe, and C. Zemach. A continuum method for modeling surface tension. *J. Comput. Phys.*, 100(2):335–354, 1992.

[31] T. Breinlinger, P. Polfer, A. Hashibon, and T. Kraft. Surface tension and wetting effects with smoothed particle hydrodynamics. *J. Comput. Phys.*, 243(0):14–27, 2013.

[32] F. P. Bretherton. The motion of long bubbles in tubes. *J. Fluid Mech.*, 10: 166–188, 3 1961.

[33] L. Brookshaw. A method of calculating radiative heat diffusion in particle simulations. *P. Astron. Soc. Aust.*, 6:207–210, 1985.

[34] S. E. Buckley and M. C. Leverett. Mechanism of fluid displacement in sands. *AIME Transactions*, 146(1):107–116, 1942.

[35] J. W. Bullard and E. J. Garboczi. Capillary rise between planar surfaces. *Phys. Rev. E*, 79:011604, 2009.

[36] T. Bultreys, M. A. Boone, M. N. Boone, T. De Schryver, B. Masschaele, D. Van Loo, L. Van Hoorebeke, and V. Cnudde. Real-time visualization of haines jumps in sandstone with laboratory-based microcomputed tomography. *Water Resour. Res.*, 51(10):8668–8676, 2015.

[37] T. Bultreys, W. D. Boever, and V. Cnudde. Imaging and image-based fluid transport modeling at the pore scale in geological materials: A practical introduction to the current state-of-the-art. *Earth-Sci. Rev.*, pages 1–97, 2016.

[38] P. Carman. Fluid flow through granular beds. *T. I. Chem. Eng. Lond.*, 15: 155–166, 1937.

[39] J. F. Chau and D. Or. Linking drainage front morphology with gaseous diffusion in unsaturated porous media: A lattice boltzmann study. *Phys. Rev. E*, 74:056304, 2006.

[40] K. Chaudhary, M. B. Cardenas, W. Deng, and P. C. Bennett. The role of eddies inside pores in the transition from darcy to forchheimer flows. *Geophys. Res. Lett.*, 38(24):L24405, 2011.

[41] C. Chen and J. J. Jiao. Numerical simulation of pumping tests in multilayer wells with non-darcian flow in the wellbore. *Ground Water*, 37(3):465–474, 1999.

[42] L. Chen and T. C. G. Kibbey. Measurement of air − water interfacial area for multiple hysteretic drainage curves in an unsaturated fine sand. *Langmuir*, 22(16):6874–6880, 2006.

[43] P. Chiquet, D. Broseta, and S. Thibeau. Wettability alteration of caprock minerals by carbon dioxide. *Geofluids*, 7(2):112–122, 2007.

[44] C. Chukwudozie and M. Tyagi. Pore scale inertial flow simulations in 3-d smooth and rough sphere packs using lattice boltzmann method. *AIChE J.*, 59(12):4858–4870, 2013.

[45] S. W. Churchill and R. Usagi. A general expression for the correlation of rates of transfer and other phenomena. *AIChE J.*, 18(6):1121–1128, 1972.

[46] P. W. Cleary. Modelling confined multi-material heat and mass flows using SPH. *Appl. Math. Model.*, 22(12):981 – 993, 1998.

[47] A. Colagrossi, B. Bouscasse, M. Antuono, and S. Marrone. Particle packing algorithm for SPH schemes. *Comput. Phys. Commun.*, 183(8):1641–1653, 2012.

[48] R. Courant, K. Friedrichs, and H. Lewy. Über die partiellen Differenzengleichungen der mathematischen Physik. *Mathematische Annalen*, 100:32–74, 1928.

[49] S. S. Datta, T. S. Ramakrishnan, and D. A. Weitz. Mobilization of a trapped non-wetting fluid from a three-dimensional porous medium. *Phys. Fluids*, 26(2):022002, 2014.

[50] P. de Gennes, F. Brochard-Wyart, and D. Quere. *Capillarity and Wetting Phenomena: Drops, Bubbles, Pearls, Waves.* Springer, New York, NY, USA, 2004.

[51] W. Dehnen and H. Aly. Improving convergence in smoothed particle hydrodynamics simulations without pairing instability. *Mon. Not. R. Astron. Soc.*, 425(2):1068–1082, 2012.

[52] M. M. Dias and A. C. Payatakes. Network models for two-phase flow in porous media part 1. immiscible microdisplacement of non-wetting fluids. *J. Fluid Mech.*, 164:305–336, 3 1986.

[53] D. A. DiCarlo. Experimental measurements of saturation overshoot on infiltration. *Water Resour. Res.*, 40(4), 2004. W04215.

[54] D. A. DiCarlo, J. I. G. Cidoncha, and C. Hickey. Acoustic measurements of pore-scale displacements. *Geophys. Res. Lett.*, 30(17), 2003. 1901.

[55] S. Diebels, W. Ehlers, and B. Markert. Neglect of the fluid extra stresses in volumetrically coupled solid-fluid problems. *Z. Angew. Math. Mech.*, 81 (S3):521–522, 2001.

[56] S. Diehl, G. Rockefeller, C. L. Fryer, D. Riethmiller, and T. S. Statler. Generating optimal initial conditions for smooth particle hydrodynamics simulations, 2012.

[57] A. Donev, S. Torquato, and F. H. Stillinger. Neighbor list collision-driven molecular dynamics simulation for nonspherical hard particles. I. Algorithmic details. *J. Comput. Phys.*, 202(2):737–764, 2005.

[58] A. Donev, S. Torquato, and F. H. Stillinger. Neighbor list collision-driven molecular dynamics simulation for nonspherical hard particles.: II. Applications to ellipses and ellipsoids. *J. Comput. Phys.*, 202(2):765–793, 2005.

[59] M. Droettboom, J. Hunter, E. Firing, T. A. Caswell, P. Elson, D. Dale, J.-J. Lee, D. McDougall, B. Root, A. Straw, and et al. matplotlib: v1.4.3, 2015.

[60] A. Duda, Z. Koza, and M. Matyka. Hydraulic tortuosity in arbitrary porous media flow. *Phys. Rev. E*, 84:036319, Sep 2011.

[61] N. Dukhan and I. Minjeur, Carel A. A two-permeability approach for assessing flow properties in metal foam. *J. Porous Mat.*, 18(4):417–424, 2011.

[62] A. Dziubek. Equations for two-phase flows: A primer. *Meccanica*, 47(8): 1819–1836, 2012.

[63] D. Edwards, H. Brenner, and D. Wasan. *Interfacial Transport Processes and Rheology.* Butterworth-Heinemann series in chemical engineering. Butterworth-Heinemann, Stoneham, MA, USA, 1991.

[64] W. Ehlers and J. Bluhm, editors. *Porous Media: Theory, Experiments and Numerical Applications.* Springer, Berlin, Germany, 2002.

[65] S. Ergun. Fluid flow through packed columns. *Chem. Eng. Prog.*, 48(2): 89–94, 1952.

[66] P. Español and M. Revenga. Smoothed dissipative particle dynamics. *Phys. Rev. E*, 67:026705, 2003.

[67] M. Ferer, C. Ji, G. S. Bromhal, J. Cook, G. Ahmadi, and D. H. Smith. Crossover from capillary fingering to viscous fingering for immiscible unstable flow: Experiment and modeling. *Phys. Rev. E*, 70:016303, 2004.

[68] A. Ferrari and I. Lunati. Direct numerical simulations of interface dynamics to link capillary pressure and total surface energy. *Adv. Water Resour.*, 57: 19–31, 2013.

[69] A. Ferrari and I. Lunati. Inertial effects during irreversible meniscus reconfiguration in angular pores. *Adv. Water Resour.*, 74(0):1–13, 2014.

[70] A. Ferrari, J. Jimenez-Martinez, T. L. Borgne, Y. Méheust, and I. Lunati. Challenges in modeling unstable two-phase flow experiments in porous micromodels. *Water Resour. Res.*, 51(3):1381–1400, 2015.

[71] M. Firdaouss, J.-L. Guermond, and P. Le Quéré. Nonlinear corrections to darcy's law at low reynolds numbers. *J. Fluid Mech.*, 343:331–350, 7 1997.

[72] P. Forchheimer. Wasserbewegung durch Boden. *Zeitschrift des Vereines Deutscher Ingenieure*, 45:1736–1741 & 1781–1788, 1901.

[73] H. Freeman and R. Shapira. Determining the minimum-area encasing rectangle for an arbitrary closed curve. *Commun. ACM*, 18(7):409–413, July 1975.

[74] O. I. Frette, K. J. Måløy, J. Schmittbuhl, and A. Hansen. Immiscible displacement of viscosity-matched fluids in two-dimensional porous media. *Phys. Rev. E*, 55:2969–2975, Mar 1997.

[75] O. v. Genabeek and D. H. Rothman. Macroscopic manifestations of microscopic flows through porous media: Phenomenology from simulation. *Annu Rev Earth Pl Sc*, 24(1):63–87, 1996.

[76] U. Ghia, K. Ghia, and C. Shin. High-re solutions for incompressible flow using the navier-stokes equations and a multigrid method. *J. Comput. Phys.*, 48(3):387 – 411, 1982.

[77] R. A. Gingold and J. J. Monaghan. Smoothed particle hydrodynamics - theory and application to non-spherical stars. *Mon. Not. R. Astron. Soc.*, 181:375–389, 1977.

[78] W. Gray and S. Hassanizadeh. Averaging theorems and averaged equations for transport of interface properties in multiphase systems. *Int. J. Multiphas. Flow*, 15(1):81–95, 1989.

[79] M. Griebel, S. Knapek, and G. Zumbusch. *Numerical Simulation in Molecular Dynamics: Numerics, Algorithms, Parallelization, Applications.* Springer-Verlag, Berlin, Germany, 2007.

[80] H. Gvirtzman and P. V. Roberts. Pore scale spatial analysis of two immiscible fluids in porous media. *Water Resour. Res.*, 27(6):1165–1176, 1991.

[81] W. B. Haines. Studies in the physical properties of soil. v. the hysteresis effect in capillary properties, and the modes of moisture distribution associated therewith. *J. Agric. Sci.*, 20:97–116, 1 1930.

[82] N. S. Hanspal and D. B. Das. Dynamic effects on capillary pressure – saturation relationships for two-phase porous flow: Implications of temperature. *AIChE J.*, 58(6):1951–1965, 2012.

[83] D. Harvie, M. Davidson, and M. Rudman. An analysis of parasitic current generation in volume of fluid simulations. *Appl. Math. Model.*, 30(10):1056–1066, 2006.

[84] M. Hassanizadeh and W. G. Gray. General conservation equations for multi-phase systems: 1. averaging procedure. *Adv. Water Resour.*, 2:131 – 144, 1979.

[85] M. Hassanizadeh and W. G. Gray. General conservation equations for multi-phase systems: 2. mass, momenta, energy, and entropy equations. *Adv. Water Resour.*, 2:191 – 203, 1979.

[86] M. Hassanizadeh and W. G. Gray. General conservation equations for multi-phase systems: 3. constitutive theory for porous media flow. *Adv. Water Resour.*, 3(1):25 – 40, 1980.

[87] S. M. Hassanizadeh and W. G. Gray. Toward an improved description of the physics of two-phase flow. *Adv. Water Resour.*, 16(1):53–67, 1993.

[88] S. M. Hassanizadeh and W. G. Gray. Thermodynamic basis of capillary pressure in porous media. *Water Resour. Res.*, 29(10):3389–3405, 1993.

[89] S. Hassanizadeh and W. G. Gray. Mechanics and thermodynamics of multiphase flow in porous media including interphase boundaries. *Adv. Water Resour.*, 13(4):169–186, 1990.

[90] S. Hassanizadeh and W. Gray. High velocity flow in porous media. *Transp. Porous Med.*, 2(6):521–531, 1987.

[91] R. Hilfer. Macroscopic equations of motion for two-phase flow in porous media. *Phys. Rev. E*, 58:2090–2096, Aug 1998.

[92] R. Hilfer. Macroscopic capillarity without a constitutive capillary pressure function. *Physica A*, 371(2):209–225, 2006.

[93] R. Hilfer and H. Besserer. Macroscopic two-phase flow in porous media. *Physica B Condens. Matter*, 279(1-3):125–129, 2000.

[94] M. Hilpert and A. Ben-David. Infiltration of liquid droplets into porous media: Effects of dynamic contact angle and contact angle hysteresis. *Int. J. Multiphas. Flow*, 35(3):205–218, 2009.

[95] M. Hirschler, P. Kunz, M. Huber, F. Hahn, and U. Nieken. Open boundary conditions for ISPH and their application to micro-flow. *J. Comput. Phys.*, 307:614–633, 2016.

[96] D. W. Holmes, J. R. Williams, and P. Tilke. Smooth particle hydrodynamics simulations of low reynolds number flows through porous media. *Int. J. Numer. Anal. Met.*, 35(4):419–437, 2011.

[97] R. Holtzman and E. Segre. Wettability stabilizes fluid invasion into porous media via nonlocal, cooperative pore filling. *Phys. Rev. Lett.*, 115:164501, Oct 2015.

[98] J. Hongbin and D. Xin. On criterions for smoothed particle hydrodynamics kernels in stable field. *J. Comput. Phys.*, 202(2):699–709, 2005.

[99] X. Hu and N. Adams. A multi-phase SPH method for macroscopic and mesoscopic flows. *J. Comput. Phys.*, 213(2):844–861, 2006.

[100] M. Huber, F. Keller, W. Säckel, M. Hirschler, P. Kunz, S. Hassanizadeh, and U. Nieken. On the physically based modeling of surface tension and moving contact lines with dynamic contact angles on the continuum scale. *J. Comput. Phys.*, 310:459–477, 2016.

[101] C. Huh and L. Scriven. Hydrodynamic model of steady movement of a solid/liquid/fluid contact line. *J. Colloid Interf. Sci.*, 35(1):85–101, 1971.

[102] C.-O. Hwang. *A New Fluid Permeability Estimation in Periodic Grain Consolidation Models and Nonoverlapping and Overlapping Mono-sized Sphere Models of Porous Media.* PhD thesis, The University of Southern Mississippi, 1999.

[103] G. R. Jerauld and S. J. Salter. The effect of pore-structure on hysteresis in relative permeability and capillary pressure: Pore-level modeling. *Transp. Porous Med.*, 5(2):103–151, 1990.

[104] G. R. Jerauld, H. T. Davis, and L. E. Scriven. Stability fronts of permanent form in immiscible displacement. *SPE Journal*, pages 1–9, 1984.

[105] V. Joekar Niasar, S. M. Hassanizadeh, L. J. Pyrak-Nolte, and C. Berentsen. Simulating drainage and imbibition experiments in a high-porosity micromodel using an unstructured pore network model. *Water Resour. Res.*, 45 (2):W02430, 2009.

[106] D. D. Joseph, D. A. Nield, and G. Papanicolaou. Nonlinear equation governing flow in a saturated porous medium. *Water Resour. Res.*, 18(4): 1049–1052, 1982.

[107] N. K. Karadimitriou and S. M. Hassanizadeh. A review of micromodels and their use in two-phase flow studies. *Vadose Zone J.*, 11(3), 2012.

[108] M. Kaviany. *Principles of Heat Transfer in Porous Media.* Springer, New York, NY, USA, 1995.

[109] T. Kohl, K. F. Evans, R. J. Hopkirk, R. Jung, and L. Rybach. Observation and simulation of non-darcian flow transients in fractured rock. *Water Resour. Res.*, 33(3):407–418, 1997.

[110] P. Koumoutsakos. Multiscale flow simulations using particles. *Annu. Rev. Fluid Mech.*, 37(1):457–487, 2005.

[111] J. Kozeny. Über kapillare Leitung des Wassers im Boden. *Sitzber. Akad. Wiss., Wien*, 136:271–306, 1927.

[112] A. T. Krummel, S. S. Datta, S. Münster, and D. A. Weitz. Visualizing multiphase flow and trapped fluid configurations in a model three-dimensional porous medium. *AIChE J.*, 59(3):1022–1029, 2013.

[113] P. Kunz, I. Zarikos, N. Karadimitriou, M. Huber, U. Nieken, and S. Hassanizadeh. Study of multi-phase flow in porous media: Comparison of sph simulations with micro-model experiments. *Transp. Porous Med.*, 2015.

[114] P. S. Kurzeja and H. Steeb. Variational formulation of oscillating fluid clusters and oscillator-like classification. I. Theory. *Phys. Fluids*, 26(4): 042106, 2014.

[115] B. Lafaurie, C. Nardone, R. Scardovelli, S. Zaleski, and G. Zanetti. Modelling merging and fragmentation in multiphase flows with SURFER. *J. Comput. Phys.*, 113(1):134–147, 1994.

[116] J. L. Lage, B. V. Antohe, and D. A. Nield. Two types of nonlinear pressure-drop versus flow-rate relation observed for saturated porous media. *J. Fluids Eng.*, 119:700–706, 1997.

[117] M. Lago and M. Araujo. Threshold pressure in capillaries with polygonal cross section. *J. Colloid Interf. Sci.*, 243(1):219–226, 2001.

[118] H. Lamb. *Hydrodynamics.* Cambridge Univ. Press, New York, NY, USA, 6 edition, 1932.

[119] R. E. Larson and J. J. L. Higdon. A periodic grain consolidation model of porous media. *Phys. Fluids A*, 1(1):38–46, 1989.

[120] R. Lenormand. Flow through porous media: Limits of fractal patterns. *Proc. R. Soc. Lond. A*, 423(1864):159–168, 1989.

[121] R. Lenormand. Liquids in porous media. *J. Phys. Condens. Matter*, 2(S): SA79, 1990.

[122] R. Lenormand, E. Touboul, and C. Zarcone. Numerical models and experiments on immiscible displacements in porous media. *J. Fluid Mech.*, 189: 165–187, 4 1988.

[123] R. LeVeque. *Finite Volume Methods for Hyperbolic Problems.* Cambridge University Press, New York, NY, USA, 2002.

[124] H. Liu, A. J. Valocchi, C. Werth, Q. Kang, and M. Oostrom. Pore-scale simulation of liquid co_2 displacement of water using a two-phase lattice Boltzmann model. *Adv. Water Resour.*, 73:144–158, 2014.

[125] H. Liu, Y. Zhang, and A. J. Valocchi. Lattice boltzmann simulation of immiscible fluid displacement in porous media: Homogeneous versus heterogeneous pore network. *Phys. Fluids*, 27(5):052103, 2015.

[126] M. Liu and G. Liu. Smoothed particle hydrodynamics (SPH): an overview and recent developments. *Arch. Comput. Method E*, 17(1):25–76, 2010.

[127] W. K. Liu, S. Jun, and Y. F. Zhang. Reproducing kernel particle methods. *Int. J. Numer. Meth. Fluids*, 20(8–9):1081–1106, 1995.

[128] L. B. Lucy. A numerical approach to the testing of the fission hypothesis. *Astron. J.*, 82:1013–1024, 1977.

[129] K. J. Måløy, L. Furuberg, J. Feder, and T. Jøssang. Dynamics of slow drainage in porous media. *Phys. Rev. Lett.*, 68:2161–2164, 1992.

[130] S. Mattis, C. N. Dawson, C. E. Kees, and M. W. Farthing. Numerical modeling of drag for flow through vegetated domains and porous structures. *Adv. Water Resour.*, 39:44–59, 2012.

[131] P. Meakin. Diffusion-controlled cluster formation in 2-6-dimensional space. *Phys. Rev. A*, 27:1495–1507, Mar 1983.

[132] P. Meakin and A. M. Tartakovsky. Modeling and simulation of pore-scale multiphase fluid flow and reactive transport in fractured and porous media. *Rev. Geophys.*, 47(3):RG3002, 2009.

[133] C. C. Mei and J.-L. Auriault. The effect of weak inertia on flow through a porous medium. *J. Fluid Mech.*, 222:647–663, 1 1991.

[134] N. Metropolis, A. W. Rosenbluth, M. N. Rosenbluth, A. H. Teller, and E. Teller. Equation of state calculations by fast computing machines. *J. Chem. Phys.*, 21(6):1087–1092, 1953.

[135] F. Moebius and D. Or. Interfacial jumps and pressure bursts during fluid displacement in interacting irregular capillaries. *J. Colloid Interf. Sci.*, 377 (1):406–415, 2012.

[136] J. J. Monaghan. Smoothed particle hydrodynamics. *Rep. Prog. Phys.*, 68 (8):1703–1759, 2005.

[137] J. Monaghan. An introduction to SPH. *Comput. Phys. Commun.*, 48(1): 89–96, 1988.

[138] J. Monaghan. SPH without a tensile instability. *J. Comput. Phys.*, 159(2): 290 – 311, 2000.

[139] J. P. Morris. A study of the stability properties of smooth particle hydrodynamics. *Publ. Astron. Soc. Aust.*, 13:97–102, 1996.

[140] J. P. Morris and P. J. Fox. Modeling low reynolds number incompressible flows using SPH. *J. Comput. Phys.*, 136:214–226, 1997.

[141] J. P. Morris. Simulating surface tension with smoothed particle hydrodynamics. *Int. J. Numer. Meth. Fluids*, 33(3):333–353, 2000.

[142] S. Motealleh, M. Ashouripashaki, D. DiCarlo, and S. Bryant. Mechanisms of capillary-controlled immiscible fluid flow in fractionally wet porous media. *Vadose Zone J.*, 9(3):610–623, 2009.

[143] M. Moura, E.-A. Fiorentino, K. J. Måløy, G. Schäfer, and R. Toussaint. Impact of sample geometry on the measurement of pressure-saturation curves: Experiments and simulations. *Water Resour. Res.*, 51(11):8900–8926, 2015.

[144] J. C. Muccino, W. G. Gray, and L. A. Ferrand. Toward an improved understanding of multiphase flow in porous media. *Rev. Geophys.*, 36(3): 401–422, 1998.

[145] M. Muradoglu and H. A. Stone. Motion of large bubbles in curved channels. *J. Fluid Mech.*, 570:455–466, 1 2007.

[146] F. Murnaghan. The compressibility of media under extreme pressures. *Proc. Natl. Acad. Sci. USA*, 30:244–247, 1944.

[147] A. Narváez, K. Yazdchi, S. Luding, and J. Harting. From creeping to inertial flow in porous media: a lattice boltzmann – finite element study. *J. Stat. Mech. Theor. Exp.*, 2013(02):P02038, 2013.

[148] D. A. Nield and A. Bejan. *Convection in Porous Media*, volume XXIV. Springer, third edition, 2006.

[149] J. M. Nordbotten, M. A. Celia, H. K. Dahle, and S. M. Hassanizadeh. Interpretation of macroscale variables in darcy's law. *Water Resour. Res.*, 43(8), 2007. W08430.

[150] J. Nordbotten, M. Celia, and S. Bachu. Injection and storage of CO2 in deep saline aquifers: Analytical solution for CO2 plume evolution during injection. *Transp. Porous Med.*, 58(3):339–360, 2005.

[151] S. Nugent and H. A. Posch. Liquid drops and surface tension with smoothed particle applied mechanics. *Phys. Rev. E*, 62:4968–4975, 2000.

[152] A. Odeh. Effect of viscosity ratio on relative permeability. *Trans. AIME*, 216:346–353, 1959.

[153] F. Ott and E. Schnetter. A modified SPH approach for fluids with large density differences, 2003.

[154] C. Pan, M. Hilpert, and C. T. Miller. Lattice-Boltzmann simulation of two-phase flow in porous media. *Water Resour. Res.*, 40(1):W01501, 2004.

[155] W. Pan, J. Bao, and A. M. Tartakovsky. Smoothed particle hydrodynamics continuous boundary force method for navier-stokes equations subject to a robin boundary condition. *J. Comput. Phys.*, 259:242–259, 2014.

[156] L. Paterson. Diffusion-limited aggregation and two-fluid displacements in porous media. *Phys. Rev. Lett.*, 52:1621–1624, Apr 1984.

[157] D. Pelletier, Steven Dufour. Computations of multiphase flows with surface tension using an adaptive finite element method. *Numer. Heat Tr. A-Appl.*, 40(4):335–362, 2001.

[158] C. S. Peskin. Numerical analysis of blood flow in the heart. *J. Comput. Phys.*, 25(3):220–252, 1977.

[159] M. N. Popescu, G. Oshanin, S. Dietrich, and A.-M. Cazabat. Precursor films in wetting phenomena. *J. Phys. Condens. Matter*, 24(24):243102, 2012.

[160] M. L. Porter, D. Wildenschild, G. Grant, and J. I. Gerhard. Measurement and prediction of the relationship between capillary pressure, saturation, and interfacial area in a NAPL-water-glass bead system. *Water Resour. Res.*, 46(8):W08512, 2010.

[161] M. L. Porter, E. T. Coon, Q. Kang, J. D. Moulton, and J. W. Carey. Multicomponent interparticle-potential lattice Boltzmann model for fluids with large viscosity ratios. *Phys. Rev. E*, 86:036701, 2012.

[162] J. Pozorski and A. Wawrenczuk. SPH computation of incompressible viscous flows. *J. Theor. App. Mech.*, 40(4):917–937, 2002.

[163] J. P. Price. *Magnetic fields in Astrophysics*. PhD thesis, Institute of Astronomy, University of Cambridge, Cambridge, UK, 8 2004.

[164] J. Prieur Du Plessis. Analytical quantification of coefficients in the ergun equation for fluid friction in a packed bed. *Transp. Porous Med.*, 16(2): 189–207, 1994.

[165] M. Prodanović and S. L. Bryant. A level set method for determining critical curvatures for drainage and imbibition. *J. Colloid Interf. Sci.*, 304(2):442–458, 2006.

[166] N. J. Quinlan, M. Basa, and M. Lastiwka. Truncation error in mesh-free particle methods. *Int. J. Numer. Meth. Eng.*, 66(13):2064–2085, 2006.

[167] A. Q. Raeini, M. J. Blunt, and B. Bijeljic. Modelling two-phase flow in porous media at the pore scale using the volume-of-fluid method. *J. Comput. Phys.*, 231(17):5653–5668, 2012.

[168] A. Raeini, B. Bijeljic, and M. Blunt. Numerical modelling of sub-pore scale events in two-phase flow through porous media. *Transp. Porous Med.*, 101 (2):191–213, 2014.

[169] T. Ransohoff and C. Radke. Laminar flow of a wetting liquid along the corners of a predominantly gas-occupied noncircular pore. *J. Colloid Interf. Sci.*, 121(2):392–401, 1988.

[170] L. Rayleigh. On the capillary phenomena of jets. *P. R. Soc. London*, 29 (196–199):71–97, 1879.

[171] P. C. Reeves and M. A. Celia. A functional relationship between capillary pressure, saturation, and interfacial area as revealed by a pore-scale network model. *Water Resour. Res.*, 32(8):2345–2358, 1996.

[172] J. Renner and H. Steeb. *Handbook of Geomathematics*, chapter Modeling of Fluid Transport in Geothermal Research, pages 1–55. Springer Berlin Heidelberg, Berlin, Heidelberg, 2014.

[173] A. Riaz and H. A. Tchelepi. Linear stability analysis of immiscible two-phase flow in porous media with capillary dispersion and density variation. *Phys. Fluids*, 16(12):4727–4737, 2004.

[174] M. Robinson. *Turbulence and Viscous Mixing using Smoothed Particle Hydrodynamics*. PhD thesis, Department of Mathematical Science, Monash University, Melbourne, Australia, 7 2009.

[175] S. Rojas and J. Koplik. Nonlinear flow in porous media. *Phys. Rev. E*, 58: 4776–4782, 1998.

[176] M. Rücker, S. Berg, R. T. Armstrong, A. Georgiadis, H. Ott, A. Schwing, R. Neiteler, N. Brussee, A. Makurat, L. Leu, M. Wolf, F. Khan, F. Enzmann, and M. Kersten. From connected pathway flow to ganglion dynamics. *Geophys. Res. Lett.*, 42(10):3888–3894, 2015. 2015GL064007.

[177] P. G. Saffman and G. Taylor. The penetration of a fluid into a porous medium or hele-shaw cell containing a more viscous liquid. *Proc. R. Soc. Lond. A*, 245(1242):312–329, 1958.

[178] R. Scardovelli and S. Zaleski. Direct numerical simulation of free-surface and interfacial flow. *Annu. Rev. Fluid Mech.*, 31:567–603, 1999.

[179] C. E. Schaefer, D. A. DiCarlo, and M. J. Blunt. Experimental measurement of air-water interfacial area during gravity drainage and secondary imbibition in porous media. *Water Resour. Res.*, 36(4):885–890, 2000.

[180] J. Schmatz, J. L. Urai, S. Berg, and H. Ott. Nanoscale imaging of pore-scale fluid-fluid-solid contacts in sandstone. *Geophys. Res. Lett.*, 42(7): 2189–2195, 2015. 2015GL063354.

[181] I. Schoenberg. Contributions to the problem of approximation of equidistant data by analytic functions. *Quart. Appl. Math.*, 4:45–99, 1946.

[182] Z. Sen. Non-darcian flow in fractured rocks with a linear flow pattern. *J. Hydrol.*, 92(1):43 – 57, 1987.

[183] P. R. Shapiro, H. Martel, J. V. Villumsen, and J. M. Owen. Adaptive Smoothed Particle Hydrodynamics, with Application to Cosmology: Methodology. *Astrophys. J. Suppl.*, 103:269, 04 1996.

[184] D. Shepard. A two-dimensional interpolation function for irregularly-spaced data. In *Proceedings of the 1968 23rd ACM national conference*, ACM '68, pages 517–524, 1968.

[185] Y. Shikhmurzaev. *Capillary Flows with Forming Interfaces.* Chapman and Hall/CRC, Boca Raton, FL, USA, 2007.

[186] R. Sivanesapillai, H. Steeb, and A. Hartmaier. Transition of effective hydraulic properties from low to high reynolds number flow in porous media. *Geophys. Res. Lett.*, 41(14):4920–4928, 2014.

[187] R. Sivanesapillai, N. Falkner, A. Hartmaier, and H. Steeb. A CSF-SPH method for simulating drainage and imbibition at pore-scale resolution while tracking interfacial areas. *Adv. Water Resour.*, 2015.

[188] E. Skjetne and J. Auriault. New insights on steady, non-linear flow in porous media. *Eur. J. Mech, B-Fluid*, 18(1):131–145, 1999.

[189] E. Skjetne and J.-L. Auriault. High-velocity laminar and turbulent flow in porous media. *Transp. Porous Med.*, 36(2):131–147, 1999.

[190] V. Starov, M. Velarde, and C. Radke. *Wetting and Spreading Dynamics.* Surfactant Science Series. CRC Press, Boca Raton, FL, USA, 2007.

[191] H. Steeb. *Non-Equilibrium Processes in Porous Media.* PhD thesis, Saarland University, 2008. Habilitation thesis.

[192] E. M. Stein and G. Weiss. *Introduction to Fourier Analysis on Euclidean Spaces.* Princeton Univ. Press, Princeton, NJ, USA, 1971.

[193] P. Steinmann. On boundary potential energies in deformational and configurational mechanics. *J. Mech. Phys. Solids*, 56(3):772–800, 2008.

[194] J. Swegle, D. Hicks, and S. Attaway. Smoothed particle hydrodynamics stability analysis. *J. Comput. Phys.*, 116(1):123–134, 1995.

[195] A. M. Tartakovsky and P. Meakin. A smoothed particle hydrodynamics model for miscible flow in three-dimensional fractures and the two-dimensional Rayleigh – Taylor instability. *J. Comput. Phys.*, 207(2):610–624, 2005.

[196] A. M. Tartakovsky and P. Meakin. Pore scale modeling of immiscible and miscible fluid flows using smoothed particle hydrodynamics. *Adv. Water Resour.*, 29(10):1464–1478, 2006.

[197] A. M. Tartakovsky and A. Panchenko. Pairwise force smoothed particle hydrodynamics model for multiphase flow: Surface tension and contact line dynamics. *J. Comput. Phys.*, 305:1119–1146, 2016.

[198] A. M. Tartakovsky, P. Meakin, and A. L. Ward. Smoothed particle hydrodynamics model of non-aqueous phase liquid flow and dissolution. *Transp. Porous Med.*, 76(1):11–34, 2009.

[199] M. Theodoropoulou, V. Sygouni, V. Karoutsos, and C. Tsakiroglou. Relative permeability and capillary pressure functions of porous media as related to the displacement growth pattern. *Int. J. Multiphas. Flow*, 31(10-11): 1155–1180, 2005.

[200] J. Thomas. *Numerical Partial Differential Equations: Finite Difference Methods.* Graduate Texts in Mathematics. Springer, New York, NY, USA, 1995.

[201] S. O. Unverdi and G. Tryggvason. A front-tracking method for viscous, incompressible, multi-fluid flows. *J. Comput. Phys.*, 100(1):25–37, 1992.

[202] S. van der Walt, J. L. Schönberger, J. Nunez-Iglesias, F. Boulogne, J. D. Warner, N. Yager, E. Gouillart, T. Yu, and the scikit-image contributors. scikit-image: image processing in Python. *PeerJ*, 2:e453, 6 2014.

[203] D. Violeau. *Fluid Mechanics and the SPH Method: Theory and Applications.* Oxford University Press, Oxford, UK, 2012.

[204] D. Violeau and B. D. Rogers. Smoothed particle hydrodynamics (sph) for free-surface flows: past, present and future. *Journal of Hydraulic Research*, 54(1):1–26, 2016.

[205] J. Ward. Turbulent flow in porous media. In *Journal of the Hydraulics Division, Proceedings of the American Society of Civil Engineers*, number 5 in HY5, pages 1–12, 1964.

[206] H. G. Weller, G. Tabor, H. Jasak, and C. Fureby. A tensorial approach to computational continuum mechanics using object-oriented techniques. *Comput. Phys.*, 12(6):620–631, 1998.

[207] H. Wendland. Piecewise polynomial, positive definite and compactly supported radial functions of minimal degree. *Adv. Comput. Math.*, 4(1):389–396, 1995.

[208] D. Wildenschild and A. P. Sheppard. X-ray imaging and analysis techniques for quantifying pore-scale structure and processes in subsurface porous medium systems. *Adv. Water Resour.*, 51:217–246, 2013.

[209] T. A. Witten and L. M. Sander. Diffusion-limited aggregation. *Phys. Rev. B*, 27:5686–5697, May 1983.

[210] A. G. Yiotis, J. Psihogios, M. E. Kainourgiakis, A. Papaioannou, and A. K. Stubos. A lattice Boltzmann study of viscous coupling effects in immiscible two-phase flow in porous media. *Colloid. Surf. A*, 300(1-2):35–49, 2007.

[211] S. Yuster. Theoretical considerations of multiphase flow in idealized capillary systems. In *World Petroleum Cong.*, pages 437–445, 1951.

[212] S. Zahedi, M. Kronbichler, and G. Kreiss. Spurious currents in finite element based level set methods for two-phase flow. *Int. J. Numer. Meth. Fluids*, 69(9):1433–1456, 2012.

[213] C. Zhang, C. J. Werth, and A. G. Webb. A magnetic resonance imaging study of dense nonaqueous phase liquid dissolution from angular porous media. *Environ. Sci. Technol.*, 36(15):3310–3317, 2002.

[214] C. Zhang, M. Oostrom, T. W. Wietsma, J. W. Grate, and M. G. Warner. Influence of viscous and capillary forces on immiscible fluid displacement: Pore-scale experimental study in a water-wet micromodel demonstrating viscous and capillary fingering. *Energy Fuels*, 25(8):3493–3505, 2011.

[215] B. Zhmud, F. Tiberg, and K. Hallstensson. Dynamics of capillary rise. *J. Colloid Interf. Sci.*, 228(2):263–269, 2000.

Curriculum Vitae - Rakulan Sivanesapillai

Place and Date of Birth: Herne, Germany | September 12, 1985

Professional Occupation

02/2016 - present	Research associate Chair of Continuum Mechanics, Inst. of Applied Mechanics, Universität Stuttgart, Germany
01/2015 - 01/2016	Research associate Chair of Continuum Mechanics, Inst. of Mechanics, Ruhr-Universität Bochum, Germany
02/2012 - 12/2014	Research associate Interdisciplinary Centre for Advanced Materials Simulation, Ruhr-Universität Bochum, Germany
04/2010 - 10/2010	Internship Polyurethane Materials Research & Technology Bayer MaterialScience AG, Leverkusen, Germany
04/2009 - 03/2010	Student assistant Chair of Continuum Mechanics, Inst. of Mechanics, Ruhr Universität Bochum, Germany

University Education

06/2013 - 09/2015	UA Ruhr SiMiDe Graduate School Certified member of graduate school “Simulation-based Microstructure Design”
08/2012 - 04/2016	RUB Research School Certified member of university-wide graduate school
09/2006 - 11/2011	Mechanical Engineering Major: Applied mechanics Diploma (Dipl. Ing.) in November 2011 Ruhr Universität Bochum, Germany

School Education

06/1996 - 06/2005	Pestalozzi Gymnasium, Herne, Germany Higher School Certificate (Abitur) in June 2005

Civil Service

07/2005 - 03/2006	St. Anna Hospital, Herne, Germany

Mitteilungen aus dem Institut für Mechanik
RUHR-UNIVERSITÄT BOCHUM
Nr. 166, August 2016

ISBN 978-3-935892-44-5